Strål
säkerhets
myndigheten
Swedish Radiation Safety Authority

Forskning

APRI-10 - Slutrapport

2022:02

Författare: Patrick Isaksson [1], Christian Linde [1], Henrik Glänneskog [2], Johan Ljung [3], Weimin Ma [4], Sevostian Bechta [4], Walter Villanueva [4], Andrei Komlev [4], Seyed Mohsen Hoseyni [4], Yangli Chen [4], Peng Yu [4], Qiang Guo [4], Hongdi Wang [4], Yan Xiang [4], Boshen Bian [4], Yucheng Deng [4], Dmitry Grishchenko [4], Alexander Konovalenko [4], Sergey Galushin [4], Sergey Yakush [5], Mikhail Davydov [6], Christian Ekberg [7], Fredrik Espegren [7], Anna-Elina Pasi [7]
[1] SSM, [2] Vattenfall, [3] RAB, [4] KTH, [5] IPM RAS, [6] EREC, [7] Chalmers

Rapportnummer: 2022:02
ISSN: 2000-0456
Tillgänglig på: www.ssm.se

SSM perspektiv

Bakgrund

Strålsäkerhetsmyndigheten (SSM) har sedan början på 1990-talet finansierat forskning inom svåra haverier, då dåvarande SKI finansiellt bidrog till en professur och utvecklandet av avdelningen för kärnkraftsäkerhet på KTH. Inriktningen har varit att studera och verifiera den svenska haverihanteringen vid svårt haveri samt att delta i och bevaka den internationella forskningen inom området.

Forskningen har bedrivits som treåriga projekt med namnet APRI (Accident Phenomena of Risk Importance). Föreliggande slutrapport avser APRI-10.

Resultat

APRI-10 har gett en ökad förståelse för bland annat följande fenomen och processer:

- härddegraderingsförloppet i reaktortanken,
- tankgenomsmältningsmode,
- kylbarhet av härdrester i inneslutningen,
- ångexplosionsfenomenet, och
- osäkerhetskvantifiering avseende utmaningar mot inneslutningen som sista barriär.

Resultaten har uppnåtts via experimentella undersökningar, modellutveckling och simuleringar. Simuleringar har bestått av Melcorberäkningar där Melcor har kopplats till andra koder för att studera specifika frågeställningar som exempelvis tankgenomsmältning eller härdresters kylbarhet. Även CFD-koder har ingått i APRI-forskningen.

Relevans

Forskningen och resultaten bedöms ha hög relevans för myndigheten. Relevansen består dels i att förstå och bedöma den säkerhetsredovisning tillståndshavarna presenterar, dels att förstå och granska den haverihantering tillståndshavarna har utvecklat. Vidare så kopplar relevansen till beredskapsuppdraget myndigheten har där haveriförlopp och källterm vid en händelse ska uppskattas. Myndighetens förståelse handlar både om fenomenen i sig och de simuleringskoder som används inom området svåra haverier.

Behov av vidare forskning

Ansvarig handläggare ser behov av fortsatt forskning inom området. Området svåra haverier är multidisciplinärt där SSM valt att finansiera vad som bedöms vara nyckelfrågor för den svenska haverihanteringsstrategin. Även om förståelsen och upplösningen succesivt blir bättre återstår betydande osäkerheter.

Projektinformation

Kontaktperson SSM: Patrick Isaksson
Referens: SSM2018-2914 / 7030246-00 (2022: 4530065)

Strål
säkerhets
myndigheten

Swedish Radiation Safety Authority

Författare: Patrick Isaksson [1], Christian Linde [1], Henrik Glänneskog [2], Johan Ljung [3], Weimin Ma [4], Sevostian Bechta [4], Walter Villanueva [4], Andrei Komlev [4], Seyed Mohsen Hoseyni [4], Yangli Chen [4], Peng Yu [4], Qiang Guo [4], Hongdi Wang [4], Yan Xiang [4], Boshen Bian [4], Yucheng Deng [4], Dmitry Grishchenko [4], Alexander Konovalenko [4], Sergey Galushin [4], Sergey Yakush [5], Mikhail Davydov [6], Christian Ekberg [7], Fredrik Espegren [7], Anna-Elina Pasi [7]

[1] SSM
[2] Vattenfall
[3] RAB
[4] KTH
[5] IPM RAS
[6] EREC
[7] Chalmers

2022:02

APRI-10 - Slutrapport

Datum: Februari 2022
Rapportnummer: 2022:02 **ISSN:** 2000-0456
Tillgänglig på www.stralsakerhetsmyndigheten.se

APRI

Forskningsprojektet APRI-10 har genomförts i samarbete mellan följande organisationer:

- Strålsäkerhetsmyndigheten (SSM)
- Forsmarks Kraftgrupp AB (FKA)
- OKG Aktiebolag (OKG)
- Ringhals AB (RAB)

Projektet har varit underställd en styrgrupp med representanter från SSM och kraftbolagen enligt följande:

Mauritz Gärdinge, OKG (ordförande)
Ola Jonsson, OKG
Patrick Isaksson, SSM
Christian Linde, SSM
Staffan Dittmer, RAB
Anders Henoch, RAB
Johan Olofsson, RAB
Margareta Tanse Larsson, FKA
Eric Ramenblad, FKA
Henrik Glänneskog, Vattenfall AB (projektledare)

Arbetet har genomförts i projektform med deltagande från parterna och andra svenska och utländska uppdragstagare och samarbetspartners.

Redaktörer:

Patrick Isaksson, SSM
Henrik Glänneskog, Vattenfall AB

Personer som har bidragit till olika avsnitt:

Patrick Isaksson, SSM
Christian Linde, SSM
Henrik Glänneskog, Vattenfall
Johan Ljung, RAB
Weimin Ma, KTH
Sevostian Bechta, KTH
Walter Villanueva, KTH
Andrei Komlev, KTH
Seyed Mohsen Hoseyni, KTH
Yangli Chen, KTH
Peng Yu , KTH
Qiang Guo, KTH
Hongdi Wang, KTH
Yan Xiang, KTH
Boshen Bian, KTH
Yucheng Deng, KTH
Sergey Yakush, IPM RAS
Dmitry Grishchenko, KTH
Alexander Konovalenko, KTH
Sergey Galushin, KTH
Mikhail Davydov, EREC
Christian Ekberg, Chalmers
Fredrik Espegren, Chalmers
Anna-Elina Pasi, Chalmers

SAMMANFATTNING

Svåra haverier handlar om och avser de händelser och scenarion som leder till omfattande härdskador i en kärnreaktor. Verkliga händelser är haverierna i Three Mile Island 1979, Tjernobyl 1986 samt Fukushima 2011. Svåra haverier präglas av komplexa och ofta samspelande fenomen under extrema förhållanden. Smälttemperaturen för urandioxid är tex. närmare 3000 K. Haveriförloppen kan vara våldsamma och sker typiskt under en kort tidsrymd (timskala) när processerna väl har startat och riskerar att leda till stora utsläpp av radioaktiva ämnen med åtföljande stora hälsokonsekvenser för omgivningen och ekonomiska konsekvenser för samhället i stort.

Kunskap och förståelse om de fenomen och processer som kan uppträda vid ett svårt haveri i en kärnreaktor är en viktig förutsättning för att bland annat kunna genomföra riskstudier och för att förstå anläggningsresponsen vid ett svårt haveri. Kunskap och förståelse för området är även väsentlig för att kunna utforma rutiner och instruktioner för haverihantering i händelse av ett haveri samt inte minst för att kunna dimensionera en effektiv beredskapsplanering. Forskningsområdet svåra haverier omfattar många forskningsdiscipliner och innefattar experiment, modellutveckling och simuleringar. Trots betydande forskningsinsatser råder det fortfarande stora osäkerheter inom området, vilket är en följd av områdets komplexitet och svårigheterna att genomföra experiment under realistiska förhållanden.

Sedan början på 80-talet har kraftbolagen och myndigheten i Sverige samarbetat inom forskningsområdet svåra haverier. Samarbetet i början var framför allt knutet till att utveckla en haverihanteringsstrategi och en implementering av konsekvenslindrande system som en följd av händelserna i TMI-2. Sedan början på 90-talet har samarbetet delvis ändrat karaktär och inriktats mer på fenomenologiska frågor av riskdominerande betydelse. Samarbetet har bedrivits i projektform och inom ett ramverk kallat APRI (Accident Phenomena of Risk Importance), som har löpt i treårsperioder. Under åren 2018-2020 har samarbetet fortsatt inom forskningsprogrammet APRI-10.

Syftet med forskningssamarbetet har bland annat varit att minska osäkerheterna i de studerade fenomenen för att kunna verifiera att de lösningar som har valts i den svenska strategin för haverihantering ger ett tillräckligt skydd för omgivningen. För att nå syftet har forskningsprogrammet omfattat dels forskningsaktiviteter på KTH och Chalmers inom området svåra haverier, dels inkluderat en uppföljning av den internationella forskningen inom svåra haverier och utvärdering av resultaten.

KTH:s avdelning för kärnkraftsäkerhet har stått för huvudarbetet under APRI-10 och bedrivit en experimentell forskning inom så kallade coriumrelaterade frågor. Med corium avses den smälta av både kärnbränsle och strukturmaterial i härden som smälter samman under ett svårt haveri och som består av urandioxid från kärnbränslet, zirkonium från kärnbränslets kapsling och i förekommande fall bränsleboxar, samt järn från det stål som utgör material för patronuppställningsplatta, härdgaller etc. Det har de senare åren blivit möjligt att visuellt via robotar se hur sluttillståndet i tre havererade Fukushimareaktorerna ser ut, och tillståndet har delvis överraskat forskarvärlden och medfört ett ökat intresse och fokus på coriumfrågor. I de bilder som förmedlats från Fukushima Daiichi reaktorer nummer 2 och 3 framträder dels att hela strukturer som styrstavsledrör och handtag till bränsleboxar har letat sig ner till inneslutningen från härden dels att genomträngning av reaktortanken har skett på ett flertal ställen. Det som är styrande för förloppet är hur olika material växelverkar med varandra beroende på sammansättning och temperatur. Den modell som har varit arbetshypotes inom exempelvis ARPI-samarbetet innan händelserna i Fukushima var att härdrester antogs samlas i tankbotten för att där smälta samman till en stor smältpöl som därefter antogs frigöras via ett tankgenombrott i

en genomföring i botten på tanken. Observationerna från Fukushima medför att den modell som tidigare har varit utgångspunkt för APRI kan behöva revideras. Förloppet i samband med tankgenomsmältning har en stor påverkan på det fortsatta skeendet i inneslutningen och är allt annat än en ren akademisk fråga. Observationerna från Fukushima har också pekat på att de modeller för härddegradering och tankgenombrott som är implementerade i de integrala simuleringskoderna för svåra haverier (MAAP, MELCOR, ASTEC) dels är grova och dels ger olika resultat trots att de i grunden bygger på samma experiment och data. Här efterfrågas mer fysikaliska modeller, vilket i sin tur fordrar mer experiment. Kodutvecklarna har själva initierat olika aktiviteter för att belysa och kartlägga skillnaderna i resultat. Mot bakgrund av beskrivningen ovan har KTH-NPS under APRI-10 fortsatt studera coriumfrågor ur följande tre aspekter: 1) härddegradering och kylning av smälta i härdrester (dvs. fasta härdrester), 2) förfinade modeller och simuleringar av smältpölens genomträngning av reaktortanken, 3) smältans växelverkan och kylbarhet i det vatten som antas finnas under reaktortanken enligt den svenska haverihanteringsstrategin i samband med tankgenomsmältning. Experimenten har skapat insikter kring bl.a. återsmältning av stelnad smälta i och utanför tanken, interaktion mellan smälta och tankvägg, vätgasgenerering vid fragmentering av smältdroppar i vatten. Fortsatta studier kring corium rekommenderas med fokus på hur multi-komponent corium uppträder i nedre tankbotten, förbättrad modellering av tankgenomträngning med kopplade termo-mekaniska koder samt fortsatta experiment rörande formation och karaktäristik av härdrester och grusbäddens kylbarhet.

KTH:s avdelning för kärnteknik har under APRI-10 avslutat de studier och arbete med ROAAM+ som påbörjades i samband med APRI-8 och fortsatte under APRI-9. ROAAM är en metodik som har utvecklats av professor Theofanous i USA för att tillämpas för hantering av mycket osannolika händelser med mycket stora konsekvenser, vilket är karaktäristiskt för svåra haverier. ROAAM-metodiken bygger på både deterministiska och probabilistiska metoder och anger både kvantitativa och kvalitativa sannolikhetskriterier som den genomförda analysen värderas mot. KTH-NE har utvecklat metoden och kallar den ROAAM+. ROAAM+ beskriver ett ramverk för ett svårt haveri i en kokvattenreaktor inklusive den svenska haverihanteringsstrategin. Ramverket bygger på en mycket stor mängd simuleringar och sofistikerad osäkerhetshantering. Under APRI-10 har APRI-deltagarna deltagit i två workshops där ROAAM+ har tillämpas i ett digitalt verktyg via enkla GUI. KTH-NE har även inom APRI-10 demonstrerat att ROAAM+ kan tillämpas för att förbättra PSA nivå 2-studierna med avseende på till exempel hantering av epistemiska osäkerheter (”modellosäkerheter”). Det rekommenderas att haveriscenarier med möjliga framgångsrika haveriåtgärder beaktas i PSA-analysen samt att en högre upplösning av olika former av inneslutningsbrott modelleras.

Chalmers avdelning för kärnkemi har under APRI-10 bedrivit forskning som syftar till att kartlägga kemin hos grundämnet tellur, vilket är en viktig fissionsprodukt ur radiologisk synpunkt. Tellurens betydelse för omgivningskonsekvenserna framgick tydligt i Fukushima där tellur i sig själv är problematiskt men även är en modernuklid till det radiologiskt viktiga ämnet jod. Forskningen har syftat till att öka kunskapen bl.a. om hur tellur transporteras och interagerar med ytor av olika material som förekommer i inneslutningen. Studier har även genomförts som rör tellurs beteende i vattenlösning. Liksom forskningen om jod, rör det sig om att förstå vilka processer som påverkar flyktigheten för dessa ämnen och hur de påverkas av de betingelser som kan råda vid haveriförhållanden, t.ex. höga temperaturer, varierande ånghalt eller oxidativ miljö. De experimentella resultaten utgör viktig kunskap för möjligheten att bygga beräkningsmodeller också för dessa ämnen. Det rekommenderas att tellurkemin vid temperaturer som är representativa för primärkretsen studeras samt att eventuella reaktioner med borsyra som då sker bör undersökas för att utröna om och på vilket sätt dessa påverkar flyktigheten för tellur.

Uppföljningen av den internationella forskningen har främjat utbyte av kunskap och erfarenheter samt har gett tillgång till en mängd information och data om olika fenomen av betydelse för händelseförlopp vid svåra haverier. Detta är viktigt för att erhålla en god bedömningsgrund av de utsläppsbegränsande åtgärderna i svenska kärnkraftsreaktorer.

INNEHÅLLSFÖRTECKNING

1. INLEDNING

Kunskap om de fenomen som kan uppträda vid svåra haverier i en kärnkraftsanläggning är en viktig förutsättning för att kunna förutse anläggningens beteende, för att kunna utforma rutiner och instruktioner för haverihantering, för beredskapsplaneringen samt för att få god kvalitet på haverianalyser och riskstudier.

De svenska deltagarna, SSM och kärnkraftsföretagen i Sverige har under en följd av år samarbetat inom forskningsområdet svåra reaktorhaverier. Detta har skett inom projekten FILTRA, RAMA, RAMA II, RAMA III, HAFOS, APRI, APRI 2, APRI 3, APRI 4, APRI 5, APRI 6, APRI 7, APRI 8 och APRI 9.

FILTRA- och RAMA-projekten var knutna till processen att utforma, genomföra och verifiera de haveriförebyggande och konsekvenslindrande åtgärder som 1989 införts vid samtliga kärnkraftverk.

I projekten HAFOS, APRI, APRI 2, APRI 3, APRI 4, APRI 5, APRI 6, APRI 7, APRI 8 och APRI 9 var en viktig uppgift att följa internationell forskning rörande svåra härdhaverier. En annan uppgift var att stödja eget arbete inom Sverige där KTH genomfört forskning avseende härdsmälteförlopp och Chalmers undersökt de kemiska förhållandena i inneslutningen.

APRI 10-projektet har i stora drag haft samma inriktning som tidigare APRI-projekt.

1.1 Kort historik

Sedan början på 1980-talet har kärnkraftsföretagen i Sverige och myndigheten samarbetat inom forskningsområdet svåra reaktorhaverier. Samarbetet var i början framför allt knutet till att förstärka skyddet mot omgivningskonsekvenser efter ett svårt reaktorhaveri genom att bl.a. ta fram system för filtrerad tryckavlastning av reaktorinneslutningen. Sedan början på 1990-talet har samarbetet delvis ändrat karaktär och inriktats mer på fenomenologiska frågor av riskdominerande betydelse.

I början av 1986 beslutade regeringen att som villkor för fortsatt drift skulle utsläppsbegränsande åtgärder vidtas vid reaktorerna i Forsmark, Oskarshamn och Ringhals. Åtgärderna skulle vara genomförda senast vid utgången av 1988. I anslutning till dessa regeringsbeslut[1] uppdrog regeringen åt dåvarande Statens kärnkraftinspektion (SKI) att utöver redovisning av beslut som myndigheten fattat med anledning av regeringens nya driftsvillkor även redovisa en bedömning av behovet av fortsatta insatser inom området svåra haveriförlopp.

Efter myndighetens granskning av de åtgärder som vidtagits vid berörda anläggningar konstaterades i ett beslut[2] av den 19 december 1988 att de mål som regeringen angivit som villkor för fortsatt drift hade uppfyllts. I myndighetens beslut pekades emellertid också på att tillståndshavarna även fortsättningsvis behövde följa de forsknings- och utvecklingsinsatser som bedrevs och dra slutsatser om vilka ytterligare säkerhetshöjande åtgärder som bör komma ifråga vid de egna anläggningarna.

I slutet av 1990-talet förtydligades myndighetens allmänna krav på utsläppsbegränsande åtgärder genom föreskrifterna SSMFS 2008:1 om säkerhet i kärntekniska anläggningar. I föreskrifterna ställdes krav på att radiologiska olyckor skall förebyggas genom en för varje anläggning anpassad grundkonstruktion med flera barriärer och ett anpassat djupförsvar. Bestämmelserna

---

[1] Regeringsbeslut 14 ”Uppdrag att redovisa det fortsatta arbetet att begränsa utsläpp vid svåra reaktorhaverier”. Industridepartementet 1986-02-27.

[2] SKI-beslut ”Utsläppsbegränsande åtgärder vid kärnkraftverken i Forsmark, Oskarshamn och Ringhals”. SKI 1988-12-19.

om djupförsvar innehåller bl.a. krav på att utsläpp av radioaktiva ämnen till omgivningen skall förhindras och begränsas genom anordningar och förberedda åtgärder. I föreskrifterna infördes även krav på att säkerheten vid en anläggning fortlöpande skall analyseras och bedömas på ett systematiskt sätt, och i allmänna råd pekades på att bl.a. forskningsresultat särskilt bör beaktas vid sådan fortlöpande analys och bedömning.

Genom föreskrifterna SSMFS 2008:17 om konstruktion och utförande av kärnkraftsreaktorer har myndigheten sedan ytterligare förtydligat och skärpt kraven i vissa avseenden. Även svåra haverier med större härdskador skall beaktas när det gäller konstruktionen av inneslutningsfunktionen, instrumentering för övervakning av anläggningens tillstånd, samt för att kunna uppnå ett stabilt sluttillstånd med reaktorn så att den inte utgör ett hot mot omgivningen på lång sikt. I konsekvensutredningen[3] av föreskrifterna konstaterades att dessa krav, som inte fanns då reaktorerna konstruerades, tillkom i viss omfattning genom regeringsbeslutet om utsläppsbegränsande åtgärder 1986.

Den svenska strategin för haverihantering innebär att inneslutningarna försetts med förstärkt inneslutningskylning, tryckavlastning och filtrering av utsläpp. Den svenska strategin för att hantera en härdsmälta – att låta en härdsmälta falla ner i djupt vatten i inneslutningen – har visat sig ur ett internationellt perspektiv vara ovanlig. Endast i ett fåtal andra reaktorer i världen tillämpas denna strategi aktivt. Eftersom den svenska strategin är ovanlig, finns det mycket lite internationell forskning som direkt belyser denna. Dock bedrivs internationell forskning om fenomen som kan inträffa under ett svårt haveri även i ett svenskt verk.

Det finns kvarvarande osäkerheter förknippade med den svenska strategin som behöver belysas ytterligare genom forskning. Genom den svenska strategin undviks troligen en stor inledande interaktion mellan betong och smälta. Å andra sidan kan ångexplosioner inträffa när smältan faller i djupt vatten. Forskningen på svåra haverier inriktas nu på att visa om de lösningar som har valts ger ett tillräckligt skydd för omgivningen, vilket vi idag håller för troligt med vissa osäkerheter som nämnts ovan. Utgående från regeringens och myndighetens beslut i slutet av 1980-talet har myndigheten och tillståndshavarna tillsammans fortsatt att bedriva forskning om svåra haverier och följa upp internationell forskning.

1.2 Projektets syfte

Projektet syftar till att visa om de lösningar som har valts i den svenska strategin för haverihantering ger ett tillräckligt skydd för omgivningen. Detta sker genom att få fördjupad kunskap om dels viktiga fenomen vid härdsmälteförlopp, dels mängden radioaktivitet som kan släppas ut till omgivningen vid ett svårt haveri.

För att nå syftet och i enlighet med rekommendationerna från APRI 9 (SSM rapport 2018:16) har projektet arbetat med följande uppgifter:

- att följa den internationella forskningen inom svåra haverier och utvärdera resultaten för att erhålla en god bedömningsgrund av de utsläppsbegränsande åtgärderna i svenska kärnkraftsreaktorer,
- att fortsätta att stödja forskningen på KTH och Chalmers om svåra haverier,
- att speciellt studera vissa fenomen som t ex smältans kylbarhet i reaktortanken och i reaktorinneslutningen samt haverikemi,

---

[3] Konsekvensutredning av Statens kärnkraftinspektions förslag till föreskrifter (SKIFS 2004:2) om konstruktion och utförande av kärnkraftsreaktorer, Statens kärnkraftinspektion 2004-10-07.

1.3 Organisation och arbetsformer

Projektet har bedrivits under åren 2018 - 2020 med en total kostnadsram på 19,8 MSEK. SSM har bidragit med ungefär 1/3 och kärnkraftsföretagen med 2/3 till denna budget. Under projektperioden har styrgruppen hållit 19 möten utöver de två uppföljningsmöten per år som har hållits på KTH (MSWI). De årliga Chalmersmötena ingår i de 19.

Arbetet inom projektet har varit uppdelat i 7 delprojekt med var sin delprojektledare.

Deltagande i BIP 3 – Behaviour of Iodine Project

Delprojektledare har varit Christian Linde SSM. En redogörelse för denna verksamhet ges i avsnitt 2.1.

Deltagande i STEM 2 – Source Term Evaluation and Mitigation

Delprojektledare har varit Christian Linde SSM. En redogörelse för denna verksamhet ges i avsnitt 2.2.

Deltagande i ESTER – Experiments on Source Term for Delayed Releases

Delprojektledare har varit Christian Linde SSM. En redogörelse för denna verksamhet ges i avsnitt 2.3.

Uppföljning av Fukushima-händelsen

Delprojektledare har varit Patrick Isaksson, SSM. En redogörelse för denna verksamhet ges i avsnitt 6.

KTH:s forskning inom svåra haverier

Forskningen vid KTH beskrivs i kapitel 3 och 4 och har följts upp av styrgruppen genom två möten per år.

Under APRI 6 och APRI 7 bedrev KTH forskning med syfte att reducera osäkerheter i kvantifieringen av fenomen vid svåra haverier. Det visade sig dock att frågor om smältans kylbarhet och ångexplosioner var svårbehandlade med endast deterministiska verktyg på grund av komplexa beroenden mellan flertalet fenomen under haveriets förlopp. Under APRI 8 och APRI 9 vidareutvecklade därför KTH metoden ROAAM+ (Risk Oriented Accident Analysis Methodology Framework for Safety Analysis of Severe Accident Issues in Nordic BWRs), som bygger på ROAAM-metoden vilken ursprungligen utvecklades av professor T. Theofanous, och som kombinerade deterministiska och probabilistiska analysmetoder så att osäkerheter av olika karaktäristik kunde behandlas på ett sammanhängande sätt. Det ramverk som etablerades i och med ROAAM+ identifierade dock flera områden där återigen deterministiska studier behövde klargöra gränsvärden och begränsande mekanismer för vissa haverifenomen i en referensanläggning. Under APRI 10 påbörjades därför experiment för att skapa insikter kring bl.a. återsmältning av stelnad smälta i och utanför tanken, interaktion mellan smälta och tankvägg, vätgasgenerering vid ångexplosioner, fragmentering av smältdroppar i vatten m.m.

Chalmers forskning inom svåra haverier

Forskningen vid Chalmers beskrivs i kapitel 5 och har följts upp av styrgruppen genom ett möte per år. Forskningen under perioden har framför allt behandlat tellurkemi.

1.4 Erfarenhetsutbyte och seminarier

Ett slutwebbinarium med ca. 60 deltagare arrangerades i APRI:s regi den 27 -28 januari 2021. Seminariets syfte var att presentera det arbete som utförts och de resultat som erhållits inom projektet APRI 10. Ett annat syfte med seminariet var också att ge möjlighet till diskussioner mellan representanter för kraftverken och de som deltagit i APRI:s arbete.

1.5 Ekonomi och rapportering

Ekonomiskt har en viss omfördelning skett mellan olika delprojekt men den totala budgetramen har innehållits. De olika delprojekten har genererat publicerade artiklar, reserapporter och dylikt vilket framgår av referenslistan i varje kapitel.

2. INTERNATIONELL FORSKNING INOM SVÅRA HAVERIER

2.1 BIP - Behaviour of Iodine Project

Forskningsprogrammet OECD/NEA BIP (*Behaviour of Iodine Project*) startades år 2007 i syfte att undersöka separata effekter i jods beteende under svåra haveriförhållanden och för att använda resultaten i analytiska modelleringsstudier. Det experimentella arbetet har utförts av *Canadian Nuclear Laboratories* (CNL) i Chalk River, nordväst om Ottawa i Kanada, som tidigare organiserade under *Atomic Energy of Canada Limited* (AECL). Där finns anläggningar med kobolt-60-bestrålare (Gammaceller), aktiva laboratorier för att utföra jod-131-spårstudier, specialiserade laboratorier för ytvetenskap och omfattande anläggningar för hantering av aktiva prover (s.k. *hot cells*).

2.1.1. BIP-1

Den första fasen av BIP genomfördes under åren 2007-2011 med en budget på ca en miljon euro. Förutom värdlandet Kanada deltog Belgien, Finland, Frankrike, Japan, Korea, Nederländerna, Schweiz, Spanien, Storbritannien, Sverige, Tyskland och USA.

I BIP-1 försökte projektdeltagare kombinera internationella resurser för att skapa en samlad förståelse för beteendet hos jod och andra fissionsprodukter.

De specifika tekniska målen var att:

- kartlägga den totala processen för organisk jodbildning genom att kvantifiera bidragen från olika processer som sker i homogen vattenfas och i den vattenfas som befinner sig i färgporer, samt från heterogena processer som sker på ytor
- mäta hastighetskonstanter för adsorption och desorption av jod på inneslutningsytor som en funktion av temperatur, relativ fuktighet och bärargasens sammansättning
- tillhandahålla försöksdata till deltagarna, för användning vid utveckling och validering av modeller.

Inom ramen för BIP-1 hade gruppen framgångsrikt utfört mer än 50 tester som behandlade adsorptionen av jod på ytor och bildandet av organiska jodformer från bestrålad färg.

Tre typer av epoxifärg testades tillsammans med några stål- och mineralprover. Färg har hög kapacitet för adsorption av jod i både vatten- och i gasfas, medan adsorptionen på stål är mycket lägre. För de tre testade epoxifärgerna var avsättningshastigheterna inom en storleksordning. Värmebehandling, förbestrålning och färgålder hade små effekter på deponeringsgraden. Relativ luftfuktighet visade sig ha störst påverkan på joddeponeringsgraden på målade ytor. Deponeringshastigheterna ökade när den relativa luftfuktigheten ökade men effekten av temperaturen var liten när fukthalten hölls konstant.

Även om goda framsteg uppnåddes beträffande förståelsen för bildandet av metyljodid från bestrålad färg, så förstod man inte mekanismen. En mer detaljerad mekanistisk förståelse för bildandet av metyljodid från bestrålad färg blev därför målet för BIP-2.

2.1.2. BIP-2

BIP-2 genomfördes under åren 2011-2014 med en budget på 0,9 miljoner euro. Samtliga länder från BIP-1 deltog förutom Nederländerna och Schweiz.

I BIP-2 studerades samma processer som i BIP-1, med syftet att nå en förbättrad förståelse för bildandet av organisk jod vid bestrålning av målade ytor. De specifika tekniska målen för uppföljningsprojektet BIP-2 var följande:

- att få en mer detaljerad och mekanistisk förståelse för *jods adsorption och desorption på inneslutningsytor* med hjälp av nya experiment med väl karakteriserade inneslutningsfärger och färgbeståndsdelar, samt med hjälp av ny instrumentering (spektroskopiska metoder)
- att få en mer detaljerad och mekanistisk förståelse för *bildning av organisk jod* med hjälp av nya experiment med väl karakteriserade inneslutningsfärger och färgbeståndsdelar och ny instrumentering (kromatografiska metoder)
- att utveckla en gemensam förståelse för hur man *extrapolerar resultat* från studier på experimentskala till förhållanden på reaktorskala.

Epoxifärg är en komplex blandning av polymera föreningar och det är svårt att veta var och hur jod interagerar och hur metyljodid bildas. I syfte att isolera påverkan från olika funktionella grupper i epoxifärgens kemiska struktur, så användes polymerprover med enkla och representativa strukturer (såsom t.ex. amidgrupper) som modellföreningar. Proverna exponerades för gasformig elementär jod (I_2) och bestrålades för att bestämma hastigheten för bildning av metyljodid. Försök utfördes också med färg som var förexponerad med klorgas (Cl_2) eller med nitrösa gaser (NO_x) i syfte att simulera effekten av reaktiva gaser som förväntas bildas i inneslutningen vid ett svårt haveri.

Ett antal analytiska tekniker användes för att studera ytinteraktionen mellan jod och epoxifärg. Svepelektronmikroskopi (SEM) användes för att bestämma färgytans morfologi, energidispersiv röntgenspektroskopi (XEDS) användes för att mäta jods penetrationsdjup i färgskiktet och gaskromatografi/masspektroskopi (GC/MS) användes för att studera frisättningen av lösningsmedel från åldrad epoxifärg.

Slutrapporteringen av BIP-2 ingår i den rapport som gavs ut efter det internationella expertmötet *International Iodine Workshop* som hölls i Marseille inom OECD-NEA/NUGENIA-SARNET i mars 2015 (NEA/CSNI/R(2016)5).

2.1.3. BIP-3

Kartläggningen av jods beteende har fortsatt i det tredje BIP-programmet (BIP-3) som genomfördes under åren 2016-2019 med en budget på en miljon euro. Förutom värdlandet Kanada, deltog Belgien, Finland, Frankrike, Japan, Korea, Schweiz, Storbritannien, Sverige, Tyskland och U.S.A.

BIP-3 har haft följande huvudmål:

- att förbättra möjligheten att simulera jods adsorption och desorption på ytor i reaktorinneslutningen,
- att förutsäga metyljodids uppförande (bildande och sönderfall) under haveriförhållanden,
- att undersöka hur åldring av målade ytor inverkar på dessa processer,
- att undersöka inverkan från klorgas (Cl_2) och nitrösa gaser (NO_x).

Naturligt åldrande och simulerat åldrande genom förbestrålning till högre doser eller genom termisk härdning, tycktes alla minska jodens depositionshastighet på målade ytor. Termisk härdning i närvaro av ånga hade störst påverkan. Kombinerad åldring (förbestrålning och härdning) gav en additiv effekt på deponeringshastigheten som minskade med ungefär en storleksordning.

Förexponering av färgytan med klorgas (Cl_2) och nitrösa gaser (NO_x).under fuktiga förhållanden ledde till en signifikant minskning av den inledande deponeringshastigheten för jod, men effekten avtog med tiden för deponering.

En betydande produktion av metyljodid visade sig uppstå i försöken genom interaktionen mellan jod och den O-ring av silkongummi som användes i tätningen av försöksuppställningen. Denna oförutsedda effekt påverkade inte de generella slutsatserna ovan, men detta visar att bestrålning av andra polymera material än färg kan bidra till den sammanlagda produktionen av organisk jod.

Hastigheten för deponering av jod på en glasyta är två till tre storleksordningar lägre än för en målad yta, medan deponering på silikongummi sker med liknande hastighet som deponeringen på en målad yta.

Produktionen av metyljodid vid bestrålning av målade ytor minskar med ökat åldrande av ytan.

Hastigheten för deponering av jod och hastigheten för produktion av metyljodid följer samma trender, men effekten av åldring är måttlig liksom effekten av att förexponera ytan med reaktiva gaser.

I anslutning till projektet har ett antal organisationer deltagit i en analytisk arbetsgrupp som har analyserat resultaten från försöken med olika beräkningskoder; CNL (LIRIC V3.3), GRS (COCOSYS V3), IRSN (ASTEC V2.1.1.1), NNL (INSPAIR), Tractebel (ASTEC V2.1.1.1) och VTT (ASTEC V2.1.1.0).

En slutrapport från BIP-3 förväntas bli tillgänglig under år 2022.

2.2 STEM - Source Term Evaluation and Mitigation

Forskningsprogrammet OECD/NEA STEM (*Source Term Evaluation and Mitigation*) inleddes år 2011 i syfte att förbättra förmågan att uppskatta storleken på källtermen i samband med en radiologisk nödsituation och för att reducera osäkerheterna rörande vissa kemiska fenomen kopplade till de båda fissionsprodukterna jod och rutenium. Det experimentella arbetet i STEM-1 och i fortsättningsprojektet STEM-2 utfördes av IRSN (*L'Institut de Radioprotection et de Sûreté Nucléaire*) i Cadarache, Frankrike. Frågeställningarna i STEM angränsar till BIP-programmet och många partners har därför deltagit i båda programmen,

2.2.1. STEM-1

STEM-1 genomfördes under åren 2011-2015 med en budget på 3,5 miljoner euro. Förutom värdlandet Frankrike, deltog Kanada, Tjeckien, Finland, Tyskland, Korea och U.S.A. Sverige deltog inte i STEM-1, men har genom deltagandet i det fortsättningsprojektet STEM-2 även fått tillgång till resultaten från det första projektet

Det första STEM-projektet behandlade tre huvudfrågor:

- Frigörande av jod i det medellånga perspektivet, speciellt med fokus på stabiliteten hos jodaerosoler och partiklar under bestrålning och det resulterande sönderfall som leder till bildande av gasformig jod.
- Interaktion mellan jod och målade ytor under bestrålning i ett kort och ett medellångt perspektiv, däribland processer för bildandet av organisk jod.
- Kemin för transport av rutenium i primärsystemet med fokus på karakterisering av olika former av rutenium, i synnerhet fördelningen mellan gas och kondenserade former.

Resultaten från det första STEM-projektet som avslutades år 2015, har gett ökad förståelse av nyckelfenomen inom jodkemin och har lett till förbättrade modeller, t.ex. för beräkningskoden ASTEC (*Accident Source Term Evaluation Code*) där förbättringar har införts avseende i) interaktionen mellan elementär jod och metyljodid under bestrålning, ii) bildandet och radiolytiskt sönderfall av jodoxider i gas- och i aerosolform, iii) radiolytisk omvandling av gasformig elementär jod till metyljodid, och iv) interaktionen mellan elementär jod och stål eller aerosoler.

Ruteniumresultaten har lett till implementering i ASTEC av en preliminär modell för ruteniumtransport i primärsystemet. Detta har gett en första möjlighet att implementera en källterm för rutenium i verktyget för probabilistisk säkerhetsanalys PSA nivå 2, vilket ledde till slutsatser om att de radiologiska konsekvenserna av rutenium kan vara signifikanta.

Resultaten från STEM-1 bidrog tillsammans med slutsatserna från det internationella expertmöte (*International Iodine Workshop*) som hölls i Marseille inom OECD-NEA/NUGENIA-SARNET i mars 2015, till identifiering av fortsatta frågeställningar bl.a. om jods uppförande. Detta ledde till fortsättningsprojektet STEM-2 där SSM har deltagit för APRI:s räkning.

Slutsatserna från det första STEM-projektet sammanfattas i en slutrapport från OECD/NEA (NEA/CSNI/R(2018)6) som publicerades i mars 2020.

2.2.2. STEM-2

Den andra fasen av OECD/NEA STEM-projektet (STEM-2) genomfördes under åren 2016-2020 med en budget på 2,48 miljoner euro. I STEM-2 deltog samtliga länder från det första STEM-projektet, samt Japan, Storbritannien och Sverige.

I STEM-2 var syftet att genomföra ytterligare experimentella undersökningar av beteendet hos jod och ruthenium. Centrala frågor rörde åldringseffekter på målade ytor vid höga stråldoser (>100-1000 kGy), jodoxiders sönderfall till flyktiga jodformer och ruteniumtransport i primärsystemet.

STEM-2 har haft följande fokusområden:

- *Åldringseffekter på målade ytor* Denna testserie innehöll experiment för att undersöka åldringseffekter vid höga stråldoser (>100-1000 kGy), vilket motsvarar den förväntade dosen vid en LOCA-transient. Vid försöken har kinetiken för frigörande från epoxifärg av både elementär jod och metyljodid mätts och jämförts med frigörelser från normalbestrålade ytor. Åldringens påverkan på målade ytors interaktion med jod har även studerats inom BIP-3 (*Behaviour of Iodine Project 3*). Den generella slutsatsen är att flyktigheten för deponerad jod är lägre från åldrade än från nyare ytor.
- *Sönderfall av jodoxider* Sönderfall av jodoxider (I_xO_y) hade tidigare uppmärksammats av det första STEM-projektet som en källa till bildning av elementär jod (I_2).
    - *Radiolytiskt inducerat sönderfall* I testserien har kinetiken för frigörelse av elementär jod och metyljodid mätts under försöken vid bestrålning av jodoxid på ett färgprov. Ytterligare några tester har genomförts för att studera hydrolys av jodoxider under icke-radiolytiska betingelser. Försöken visade att gammabestrålning är en viktig orsak till jodoxiders sönderfall, men även att den termiska instabiliteten är påtaglig vid höga temperaturer.
    - *Kemiskt inducerat sönderfall av jodoxider* I denna serie har de potentiella reaktionerna mellan jodoxider och kolmonoxid (CO), vätgas (H_2), samt metangas (CH_4) undersökts i syfte att undersöka om detta kan påverka jods flyktighet genom omvandling av jodoxiderna till elementär jod eller till metyljodid. Tillsats av CO eller H_2 till gasflödet leder till en fördröjning av starttidpunkten för frigörelse av jod, men den totala frigörelsen påverkas inte kraftigt.
- *Radiolytisk oxidation av jodaerosoler i multikomponentblandning* Liksom övriga testserier undersöktes här hur källtermen för flyktiga jodformer påverkas av radiolytisk oxidation av jod i aerosolform, som förväntas transporteras från primärsystemet till inneslutningen vid ett haveri. I tre försök har man utgått från silverjodid, cesiumjodid/cesiummolybdat och cesiumjodid/cesiummolybdat/tenndioxid. Förångningen från bestrålad silverjodid är begränsad, men betydande för de övriga fallen. Resultaten indikerar att det är troligt att det bildas flyktiga molybden-jod-föreningar.
- *Rutenium* I syfte att komplettera observationer från det första STEM-projektet gällande ruteniumtransport från primärsystemet, genomfördes en ny testserie under ytterligare variation av betingelser. Det hade tidigare konstaterats att fördelningen mellan olika former av rutenium är avgörande för flyktigheten där ruteniumtetroxid (RuO_4) är en identifierad form med hög flyktighet. Även graden av återförgasning av deponerat material är en viktig parameter. I testerna har en yta av rostfritt stål använts för deponeringen. Förhöjda oxidativa betingelser har använts för att efterlikna de betingelser som uppstår genom radiolys av luft vid ett haveri. Inverkan av ånga på ruteniumtetraoxidens uppförande samt inverkan av representativa gaser och/eller aerosoler har också studerats. IRSN har gjort jämförelser med de tidigare försök som har utförts av VTT/Chalmers. Det har förekommit en del oväntade olikheter bland resultaten, men man konstaterar att olikheter i vissa betingelser kan förklara utfallen.

I anslutning till projektet har ett antal organisationer deltagit i en analytisk arbetsgrupp som har analyserat resultaten från försöken med olika beräkningskoder: GRS (COCOSYS V3), IRSN (ASTEC V2.1.1.1), KINS (RAIM V1.5), NNL (INSPAIR) och VTT (ASTEC V2.1.1.0).

En slutrapport från STEM-2 förväntas bli tillgänglig under år 2022.

2.3 ESTER - Experiments on Source Term for Delayed Releases

Forskningsprogrammet OECD/NEA ESTER (*Experiments on Source Term for Delayed Releases*) är ett nytt projekt inom området källterm som startade i november 2020 och pågår till och med juni 2024. ESTER leds av IRSN i samarbete med CEA (*Commissariat à l`énergie atomique et aux énergies alternatives*). Den totala budgeten uppgår till 3,144 miljoner euro. Förutom värdlandet Frankrike, deltar Finland, Japan, Korea, Sverige, Tyskland och U.S.A.

ESTER fokuserar på två av de rekommendationer för ytterligare studier, som kom fram ur det internationella expertmötet *WGAMA Source Term Workshop* som hölls på OECD/NEA i Paris den 21-22 januari 2019. Rekommendationerna rör återmobilisering av deponerade fissionsprodukter samt organisk jod.

2.3.1. Återmobilisering av deponerade fissionsprodukter

Återmobilisering av deponerade fissionsprodukter kan ha en potentiellt stor påverkan på källtermen i fördröjda utsläpp efter ett haveri. Sådana utsläpp kan begränsa möjligheterna till beredskapsåtgärder på platsen och påverka hanteringen av haveriet i långtidsförloppet. Det kan även föranleda behov av uppdateringar av probabilistiska analysmodeller PSA nivå 2 och 3.

Återmobiliseringsförsöken i ESTER kommer att studeras i tre faser:

1) Analytiska tester av enskilda fissionsprodukter (jod, cesium, molybden och bor). Försöken utförs i IRSN:s CHROMIA plattform som har en rad analytiska tekniker för kemisk analys och för karakterisering av aerosoler, bl.a. EPICUR-uppställningen som genererar och mäter radioaktiv jod i olika former i realtid under betingelser som efterliknar förhållandena i reaktorns primärsystem under ett svårt haveri.
2) Semi-integrala tester för att studera kopplade effekter mellan olika fissionsprodukter. Försöken utförs i IRSN:s CHIP-uppställning som kan generera blandningar med upp till sju olika ämnen och återmobilisera dessa i transportförsök som studeras i realtid.
3) Autentiska tester med deponerat material från bestrålat bränsle. Försöken utförs av CEA med bränsle från det tidigare projektet VERDON2. CEA:s VERDON-laboratorium är utrustat med två heta celler och en handskbox för provpreparering, experiment och analys. I försöksuppställningen CRACOUCASS ingår en rörugn som är försedd med bl.a. pyrometer, kamera och gammaspektrometrar som ger möjlighet att studera kinetiken för förångning och deponering av materialet.

2.3.2. Organisk jod

Organisk jod antas kunna bildas på fler sätt än vad som är känt idag. Studier har sedan länge dominerats av jods interaktion med målade ytor, men denna process bedöms inte på egen hand kunna förklara de mängder av organisk jod som uppmättes i det s.k. Phébusprogrammet som genomfördes under åren 1988-2010. Phébus innehöll experimentella studier av härddegradering, nedsmältning och transport av fissionsprodukter i en inneslutning under ett realistiskt haveriscenario. Ett antal försök kommer därför att genomföras i ESTER-programmet för att studera ytterligare reaktionsvägar, bl.a. gasfasreaktioner mellan metan och olika former av jod. Andra flyktiga kolföreningar såsom aceton och etylen kommer också att studeras. I de sista försöken kommer även polymert kabelmaterial att användas. EPICUR-uppställningen används för dessa försök. Den ger möjlighet att variera temperatur och bärargas för transportförsöken.

2.4 THAI – Thermal-hydraulics, Hydrogen, Aerosols, and Iodine

Det övergripande målet med THAI-programmet (*Thermal-hydraulics, Hydrogen, Aerosols, and Iodine*) har varit att ta itu med öppna frågor om fenomen kopplade till vätgas, jod och aerosoler i inneslutningen vid svåra haverier i lättvattenreaktorer. Förståelsen för de processer som äger rum under sådana händelser är avgörande för möjligheten att kunna utvärdera vilka utmaningar som kan uppstå mot inneslutningens integritet (vätgas), samt för att bestämma storleken på mängden luftburen radioaktivitet (jod och aerosoler) i inneslutningen vid svåra haverier.

Det experimentella arbetet har utförts av Becker Technologies GmbH i Eschborn, Tyskland, som driver programmets experimentanläggning THAI (*Thermal-hydraulics, Hydrogen, Aerosols, and Iodine*) som efter den senaste modernisering har fått benämningen THAI+.

THAI-programmets olika faser har genom åren bidragit med värdefulla data för utveckling av förståelsen för hur och under vilka betingelser som vätgas deflagrerar (förbränns). Ytterligare data har genererats som har använts för att bättre beskriva hur prestanda för passiva autokatalytiska rekombinatorer (PAR) påverkas under olika försvårande betingelser och hur de bäst kan användas för att effektivt minska vätgashalten under ett haveri. Beträffande fissionsprodukter har THAI-programmet kartlagt samspelet mellan gasformig jod och olika typer av aerosoler, samt undersökt huruvida PAR kan integrera jod och därigenom påverka källtermen.

Parallellt med det experimentella programmet har ett omfattande analytiskt arbete utförts, som har innefattat kodberäkningar för att bedöma förberedande försök och stödja utformning av nya tester, samt för att utvärdera resultaten och extrapolera dessa till reaktorbetingelser. Projektet har bidragit till validering och vidareutveckling av avancerade LP- (*Lumped Parameter Code*) och CFD-koder (*Computational Fluid Dynamics*) som används för reaktortillämpningar, t.ex. genom att tillhandahålla experimentella data för ”benchmark”-beräkningar med olika koder. Liksom många andra OECD/NEA-program bidrar THAI också till att upprätthålla kompetens inom reaktorsäkerhet och till att främja internationellt samarbete.

2.4.1. THAI-1

En första etapp (THAI-1) genomfördes under åren 2007-2009 med en budget på 2,8 miljoner euro. Förutom värdlandet Tyskland, deltog Finland, Frankrike, Kanada, Korea, Nederländerna, Schweiz och Ungern. Totalt genomfördes över 70 försök. Nedan redovisas projektets olika testområden med huvudsakliga slutsatser för respektive område:

- *Jämförelser mellan helium och vätgas:* Tester bekräftade att helium kan användas istället för vätgas vid undersökningar av flödesdynamiska fenomen i inneslutningsatmosfären. Beräkningar med olika beräkningskoder (både av LP- och CFD-typ) visade att stora framsteg skett i modelleringen av stratifiering och omblandning.
- *Vätgasförbränning:* Genom att variera olika parametrar såsom initialtryck och -temperatur, ånghalt, förbränningsriktning och gasernas spatiala fördelning kunde deras inflytande på tryck- och temperaturförlopp, flamfrontspropagering och förbränningens fullständighet bestämmas.
- *Vätgasrekombinatorer (PAR):* Kunskapsbasen kring olika PAR-typers prestanda under typiska svåra haveriförhållanden ökade markant som ett resultat av testerna. Detta gäller både aktiveringen av PAR-enheterna, deras rekombineringshastighet och potentialen för PAR-inducerad antändning av gasblandningen. En särskilt viktig slutsats var att PAR-inducerad antändning bara är möjlig i ett relativt begränsat område i Shapirodiagrammet.

- *Interaktion mellan metalljodider och PAR-utrustning:* Test visade att cesiumjodid kan brytas ner och omvandlas till gasformig jod i en omfattning som kan påverka källtermen till inneslutningen.
- *Förgiftning av PAR-utrustning*: Test visade att aerosoler och jod inte förefaller leda till förgiftning som påverkar PAR-enheternas prestanda i någon större utsträckning.
- *Nedtvättning av luftburna partiklar (aerosoler):* Test visade att svagt lutande ytor utsätts för nedtvättning av partiklar av cesiumjodid (CsI) i en tidskala som varierar från minuter till timmar. Tidsskalan och även omfattningen/ effektiviteten beror på vattenflödet och ytans egenskaper.

Det experimentella arbetet kompletterades med analysverksamhet genom att en analytisk arbetsgrupp etablerades med målsättningen att utvärdera testresultaten för att validera och vidareutveckla modeller och analysverktyg.

Slutsatserna från det första THAI-projektet sammanfattas i en slutrapport från OECD/NEA (NEA/CSNI/R(2010)3) som publicerades i juni 2010.

2.4.2. THAI-2

En andra etapp (THAI2) genomfördes under åren 2011-2014 med en budget på 3,6 miljoner euro. Förutom värdlandet Tyskland, deltog Finland, Frankrike, Japan, Kanada, Korea, Nederländerna, Schweiz, Storbritannien, Sverige, Tjeckien och Ungern. Totalt genomfördes 16 försök. Nedan redovisas projektets olika testområden med huvudsakliga slutsatser för respektive område:

- *Frigörelse av gasformig jod vid s.k. ”flashing”:* Försöket syftade till att undersöka hur gasformig jod kan frigöras vid snabb förångning (”flashing”) av en jetstråle i samband med ett tubbrott i en ånggenerator. Testet misslyckades då man trots ansträngningar med förberedande analyser inte fick rätt kemiska förhållanden för att kunna dra relevanta slutsatser. Ingen gasformig jod detekterades i THAI-behållaren (halterna hamnade under instrumenteringens detektionsgräns) då injicerad molekylär jod snabbt reagerade med stålet i förvaringsbehållarens vägg vid uppvärmningen innan försöket påbörjades.
- *Deponering av elementär jod (I_2) på aerosolpartiklar:* Experimenten visade tydligt skillnaden mellan reaktiva (metalliskt silver) och icke-reaktiva (tenndioxid) aerosolers förmåga att påverka inventariet av gasformig jod. Minskningen av gasformig jod var betydligt effektivare (ca 25 gånger snabbare) med silveraerosoler, som möjliggör s.k. kemisorption, jämfört med tenndioxid, som endast tillåter svagare s.k. fysisorption.
- *Vätgasförbränning i samband med sprinkling:* Försöken har gett kunskap om sprinklingens inverkan på förbränningsförloppet. Med något enstaka undantag visar försöken att sprinkling har en dämpande effekt på det resulterande, maximala trycket vid förbränning. Sprinklingens nedkylning av reaktionszonen är den dominerande effekten, men maximala tryck och temperaturer reduceras även eftersom den ånga som produceras via förångning av vattendropparna fungerar som en värmesänka.
- *Vätgasrekombinering med PAR vid låg syrgashalt:* Försöken har utökat databasen för rekombinatorernas prestanda med resultat från försök under nya förhållanden. Testerna visar att rekombinering startar vid mycket låga syrgashalter. Rekombineringshastigheten styrs då främst av syrgasdiffusion genom katalysatorns yta, dvs. genom

tillgången på syrgas. Vid höga syrgashalter blir tillgången på vätgas styrande. Ökningen i effektivitet (γ, förbrukningsgrad av vätgas) blir därför väldigt liten vid ökande syrgashalt. Förbrukningsgraden γ planar ut vid 50-70 %.

Även i THAI2 etablerades en analytisk arbetsgrupp för att samla den analytiska verksamhet som bedrivits av deltagarna för bl.a. utveckling och validering av både beräkningskoder och modeller.

Slutsatserna från det THAI-2 sammanfattas i en slutrapport från OECD/NEA (NEA/CSNI/R(2016)8) som publicerades i februari 2017.

2.4.3. THAI-3

Den tredje etappen (THAI-3) löpte under perioden februari 2016 – juli 2019 med en budget på 4,75 miljoner euro. Förutom värdlandet Tyskland, deltog Belgien, Finland, Frankrike, Indien, Japan, Kanada, Kina, Korea, Luxemburg, Schweiz, Slovakien, Storbritannien, Sverige, Tjeckien och Ungern.

I denna etapp har projektet använt den utökade anläggningsutformningen THAI+ med en ny behållare (PAD – parallel attachable drum) kopplad till den ursprungliga THAI-behållaren, se Figur 2.4.1

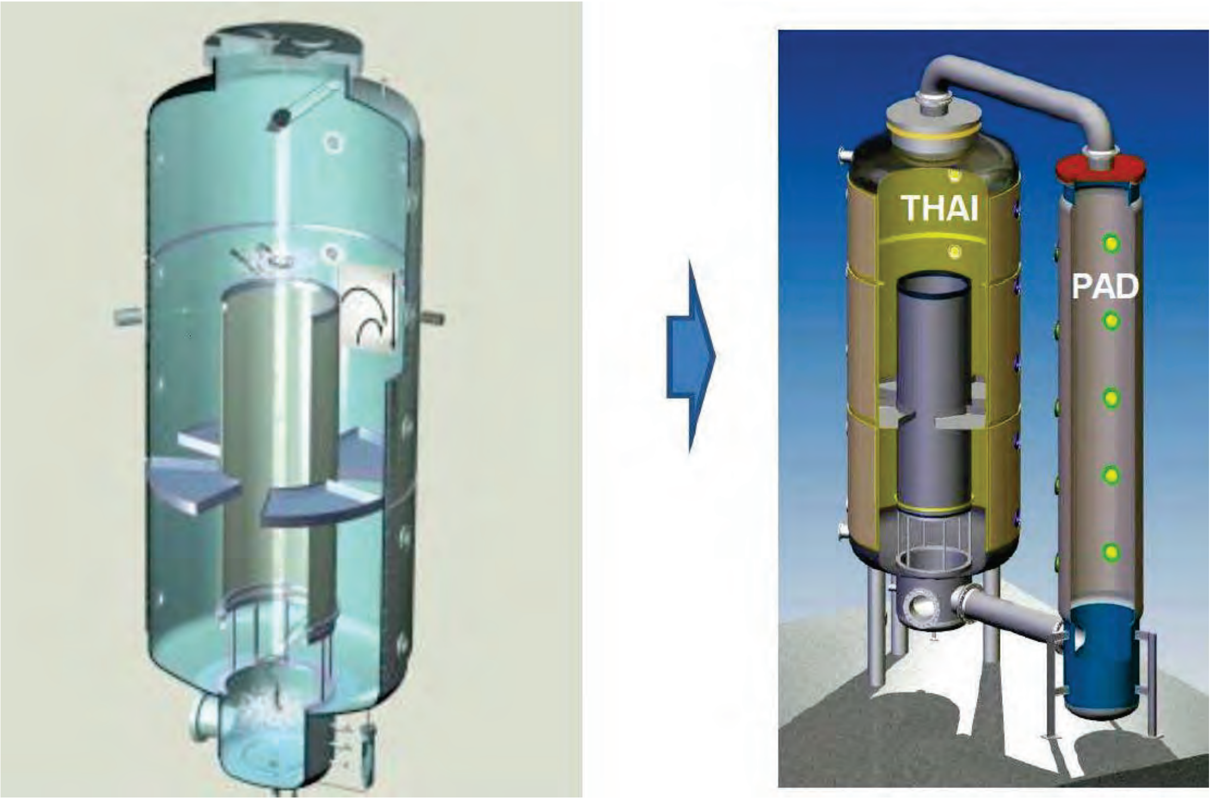

Figur 2.4.1 Den ursprungliga anläggningen THAI (vänster) och den nyligen utökade THAI+ (höger)

Projektet har undersökt följande fyra huvudsakliga frågeställningar:

- *Vätgasrekombinering med PAR under motströmsförhållanden:* Syftet har varit att kartlägga hur PAR-enheternas uppstartsbeteende och prestanda påverkas av motströmsflöde, samt hur prestandan påverkas av PAR-enhetens utformning såsom skorstenshöjd. Bland slutsatserna kan nämnas att kapaciteten hos Areva:s PAR inte påverkas nämnvärt av motströmsflöde. Effekterna av motströmsflöde är samma vid högre som vid lägre omgivningstryck, medan PAR-inducerad antändning sker något tidigare vid ett högre omgivningstryck. Utformningen av skorstenen i Areva:s PAR-enheter (den är inte öppen rakt uppåt) förhindrar effektivt inträngning av motströmflödet in i PAR-enheten. Motströmflöde uppstår endast vid väldigt låga vätgaskoncentrationer.

- *Vätgasförbränning i två förbundna utrymmen*: I dessa försök har man utnyttjat THAI+-anläggningens båda separata utrymmen som står i förbindelse med varandra. Försök har syftat till att undersöka hur förbränningsförloppet (såsom flamfrontspropagering) påverkas av dels strömningsförhållanden under konvektiva förhållanden, dels stratifierade förhållanden med en vätgaskoncentrationsgradient, samt varierande ånghalt och temperatur. Höga flamutbredningshastigheter observerades särskilt i de smala rör som förbinder de båda utrymmena. Turbulenta förhållanden uppstod då blandningen antändes efter att den hade satts i rörelse genom ett påtvingat flöde mellan utrymmena.
- *Fissionsprodukters återinträde i atmosfären från vattenfas vid förhöjda temperaturer:* Försöksserien har syftat till kartläggning av hur fissionsprodukter (både aerosoler och flyktig jod) kan återföras (via s.k. ”re-entrainment”) till inneslutningsatmosfären vid förhöjda temperaturer i kondensationsbassäng/sump, antingen genom kontinuerlig uppvärmning till kokning eller genom kokning som induceras genom trycksänkning (såsom vid filtrerad tryckavlastning). Inverkan av olika hydrodynamiska förhållanden, olika kemiska förhållanden (såsom pH-värde och tillsatser) samt av egenskaper hos gasflödet till vattenbassängen (t.ex. massflöde och andel icke-kondenserbara gaser) har undersökts. Bland slutsatserna kan lyftas att överföringen av aerosoler till gasfasen ökar med ökande temperatur, vilket är förväntat. Överföringen är mindre då flödet i nedblåsningsröret består av ren luft än för en blandning av luft och ånga. Man uppnådde en stabil stratifiering av elementär jod (I_2) i gasfasen med högre koncentrationer av gasformig jod högre upp i behållaren. Jod från gasfasen deponerade troligtvis på stålväggarna, varifrån den kan frigöras i en senare fas. Den ökade överföringen av elementär jod från sump till gasfas vid kokning gav ett gasformigt jodinventarium som var cirka 100 gånger högre än då vattnet inte kokade.
- *Återinträde i atmosfären av deponerade aerosoler och jod i samband med vätgasförbränning*: Syftet har varit att undersöka frigörelse av fördeponerade aerosoler och olika former av jod från ytor i samband med vätgasförbränning, samt hur målade ytor kan påverkas av förbränningen. Deponerade aerosoler såsom cesiumjodid (CsI) frigjordes till största delen i samma kemiska form vid vätgasförbränning, men i mindre partikelstorlekar, vilket gav en hög partikelkoncentration i atmosfären. Försöken med deponerad elementär jod (I_2) visade också att en signifikant mängd frigjordes vid vätgasförbränning. Den frigjorda joden utgjordes i detta fall till övervägande del av gasformig organisk jod, som hade bildats genom kemisk interaktion med färgytan. Jod frigjordes även i aerosolform i former som inte kunde karakteriseras i försöken. Resultaten från denna försöksserie lämnar utrymme för fortsatta studier av påverkan från förbränning på jod som är deponerad på målade ytor.

En slutrapport från THAI-3 förväntas bli tillgänglig under år 2023.

2.5 THEMIS - THAI Experiments on Mitigation measures

Forskningsprogrammet OECD/NEA THEMIS (*THAI Experiments on Mitigation measures, and source term issues to support analysis and further Improvement of Severe accident management measures*) leds av Becker Technologies GmbH (BT) som driver experimentanläggningen THAI+ (*Thermal-hydraulics, Hydrogen, Aerosols, and Iodine*) i Eschborn, Tyskland, i samarbete med Framatome i Erlangen och GRS (*Gesellschaft für Anlagen- und Reaktorsicherheit gGmbH*) i Köln. THEMIS genomförs under åren 2020-2024 med en budget på 5,05 miljoner euro. Förutom värdlandet Tyskland, deltar preliminärt Belgien, Finland, Frankrike, Japan, Kanada, Kina, Korea, Ryssland, Schweiz, Slovakien, Spanien, Storbritannien och Sverige.

Anläggningen (THAI+) är densamma som användes i det tidigare projektet THAI-3, se Figur 2.4.1. Den består av en större behållare (ca 60 kubikmeter) av rostfritt stål med en mindre parallell behållare (ca 18 kubikmeter) som kan trycksättas och vattenfyllas för olika typer av experiment. I behållarna finns instrumentering för mätning av bl.a. tryck, temperatur och flödeshastigheter, som kan anpassas för studier av olika haverifenomen. Med hjälp av höghastighetskameror kan man även följa experimentella förlopp i detalj och studera bl.a. förbränning av gasblandningar och partikelfördelning i luftburna aerosoler.

2.5.1. THEMIS-programmet

Fokus för THEMIS ligger på studier av processer och fenomen som inträffar i den sena fasen av ett svårt haveri t.ex. betong-smälta-interaktioner (MCCI – *Molten Corium Concrete Interactions*), genererering av brännbara gasblandningar innehållande vätgas (H_2) och kolmonoxid (CO), gasblandningarnas påverkan på vätgasrekombinatorer (PAR), samt källtermsrelaterade frågor kopplade till aerosoler och fördröjda utsläpp av fissionsprodukter. Frågeställningarna är hämtade från det expertmöte om källtermsforskning (*WGAMA Source Term Workshop*), som hölls på OECD/NEA i Paris den 21-22 januari 2019. Frågeställningarna kommer att studeras experimentellt i fem planerade försöksserier:

2.5.1.1. Topic 1: ”PAR performance behaviour in H_2-CO containing atmosphere”

I den första försöksserien studeras prestanda hos passiva autokatalytiska rekombinatorer (PAR) i en atmosfär innehållande vätgas (H_2) och kolmonoxid (CO). PAR-utrustningen har som uppgift att katalysera omvandlingen av vätgas till vattenånga. Den PAR-utrustning från Framatome som används i försöksserien har en platinabeläggning som även katalyserar omvandlingen av kolmonoxid (CO) till koldioxid (CO_2). Syftet är att förstå atmosfärens påverkan på t.ex. PAR-utrustningens rekombinationsstart, rekombinationshastighet och effektivitet i utarmningen av brännbara gaser, samt PAR-förgiftning och PAR-inducerad antändning av gasblandningen.

2.5.1.2. Topic 2: ”Combustion and flame propagation behaviour for H_2-CO-steam-air atmosphere”

I den andra försöksserien studeras förbränning och flamutbredning i en gasblandning innehållande vätgas (H_2), kolmonoxid (CO), ånga och luft. Syftet är att förstå hur den koldioxid (CO_2) som bildas vid förbränning påverkar flammans utbredningshastighet i olika riktningar. I samband med en MCCI kan gasblandningen förväntas vara ofullständigt blandad. I försöken studeras därför även flamutbredning i en stratifierad (skiktad) gasblandning där förbränning startar genom gnistbildning på olika nivåer.

2.5.1.3. Topic 3: ”IOx behaviour in containment atmosphere including interaction with “nuclear background aerosol” and thermal stability”

I den tredje försöksserien studeras jodoxiders (IO_x) beteende i inneslutningsatmosfär, inklusive interaktion med ”nukleär bakgrundsaerosol” och termisk stabilitet. Försöken ska efterlikna förväntade haveriförhållanden där atmosfären innehåller små aerosolpartiklar som genereras i samband med degraderingen av härden. Dessa luftburna partiklar utgör den bakgrundsaerosol som förväntas kunna utgöra kärnpunkter för bildandet av aerosoler av jodoxider (IO_x). Syftet med försöken är att studera aerosolpartiklarnas uppbyggnad över tid, samt att studera jodoxidernas stabilitet vid de temperaturer som förväntas råda i reaktorinneslutningen under haveriförhållanden.

2.5.1.4. Topic 4: ”Fission products retention in water pools: Pool Scrubbing”

I den fjärde försöksserien studeras effekter på kvarhållandet av fissionsprodukter i vattenbassänger under betingelser som innefattar gasbubblor som passerar genom vattenvolymen, s.k. ”pool scrubbing”. Denna serie efterliknar scenarier under ett haveri där ång-/gasblandningar blåses ned i en vattenfas, t.ex. i en kondensationsbassäng eller en skrubber.

2.5.1.5. Topic 5: ”PAR interaction with IOx and fine nuclear aerosol in H2-CO containing atmosphere”

I den femte och sista försöksserien studeras PAR-utrustningens interaktion med oxiderade former av jod (IO_x) och interaktion med fin nukleär aerosol i en atmosfär innehållande vätgas (H_2) och kolmonoxid (CO). Denna serie kan ses som ett integralt test som kombinerar förhållandena från den första och den tredje försöksserien. Försöken inkluderar bildandet av jodoxider (IOx) genom oxidation av elementär jod (I_2), jodoxidernas interaktion med vätgas (H_2) och kolmonoxid (CO), PAR-utrustningens påverkan på den luftburna andelen av jodoxider (IO_x), samt processer som kan medföra reduktion av dessa med återbildande av flyktig elementär jod (I_2) som följd.

3. KTH – DEP. OF NUCLEAR POWER SAFETY - RESEARCH ON SEVERE ACCIDENTS

3.1 Research goal, approach and activities at KTH/NPS

The goal of severe accident research at the Division of Nuclear Power Safety of KTH (KTH/NPS) during APRI-10 is to help resolve severe accident issues, which remain or emerge in Swedish nuclear power plants, through development and application of knowledge base for severe accident risk assessment and management. The specific objectives are as follows:

- Fill the knowledge gaps regarding severe accident phenomena influencing corium melt explosivity in water, steam explosion energy and debris bed coolability;
- Improve quality of models and tools used in severe accident analyses; and
- Study limiting mechanism/conditions, which can reduce steam explosion and debris re-melting risks.

Both experimental and analytical approaches were adopted in the research for deterministic studies on several accident phenomena related to:

- Missing links in quantification of melt ejection conditions from the RPV ⇒ to obtain knowledge on in-vessel debris/molten pool behavior and vessel failure mode (e.g., vessel breach vs penetration failure; creep vs melt-through; ablation vs plug);
- Metal melt jet fragmentation in water;
- Effect of metallic debris oxidation on debris coolability;
- Quench of debris bed prior to steady-state coolability;
- Effect of melt oxidation on steam explosion; and
- Limiting and suppression mechanisms of steam explosion.

Accordingly, the research activities at KTH/NPS were divided into five topical areas:

- In-vessel debris behavior and vessel failure;
- Quenching and oxidation of ex-vessel debris bed;
- Mechanisms of ex-vessel fuel-coolant interactions;
- Development of models for deterministic analyses; and
- MISTEE experiment toward prototypical materials.

The APRI-10 activities at KTH/NPS capitalized on the previous knowledge base of severe accident phenomena and scenarios, which was developed and obtained in the past national and international research programs. In particular, the APRI-10 research had synergetic collaborations with the recent EU project IVMR, NKS project SPARC SSM projects and Japanese NRA project.

This report summarized the key achievements in the topical areas. More detailed descriptions of the research activities can be found in the references [1]~[28], including publications under review and to be submitted by the end of APRI-10, and some technical presentations of project review meetings.

3.2 In-vessel debris behavior and vessel failure

The study on in-vessel debris behavior and vessel failure during severe accident is aiming at providing knowledge to the missing links in quantification of melt ejection conditions from the reactor pressure vessel (RPV). Two interconnected issues are of great interest: (i) evolution of multi-composition corium in the lower head (e.g., debris remelting, melt infiltration, crust dynamics, physicochemical interactions); and (ii) pressure vessel failure mode (e.g., lower head breach vs penetration failure; creep vs melt-through; ablation vs plug).

For the first issue, the SIMECO-2 and REMCOD/MRSPOD facilities have been developed at KTH/NPS to investigate multi-composition debris remelting and melt infiltration in debris beds, respectively.

For the second issue, the research emphasis was placed on development and qualification of coupling approaches for thermo-mechanical simulations important to RPV failure analysis during severe accidents.

The main achievements and findings in this topical area are described as follows.

3.2.1. Development of SIMECO-2 test facility – for the study of evolution/progression of multi-composition corium in the lower head

The SIMECO-2 test facility [1] has been co-supported by the EU project IVMR [29], APRI-10 and SSM, with the original objective to study heat transfer of stratified melt pools under volumetric heating and high temperature (average temperature of melt pool up to 650°C). Below is the information and status of the facility.

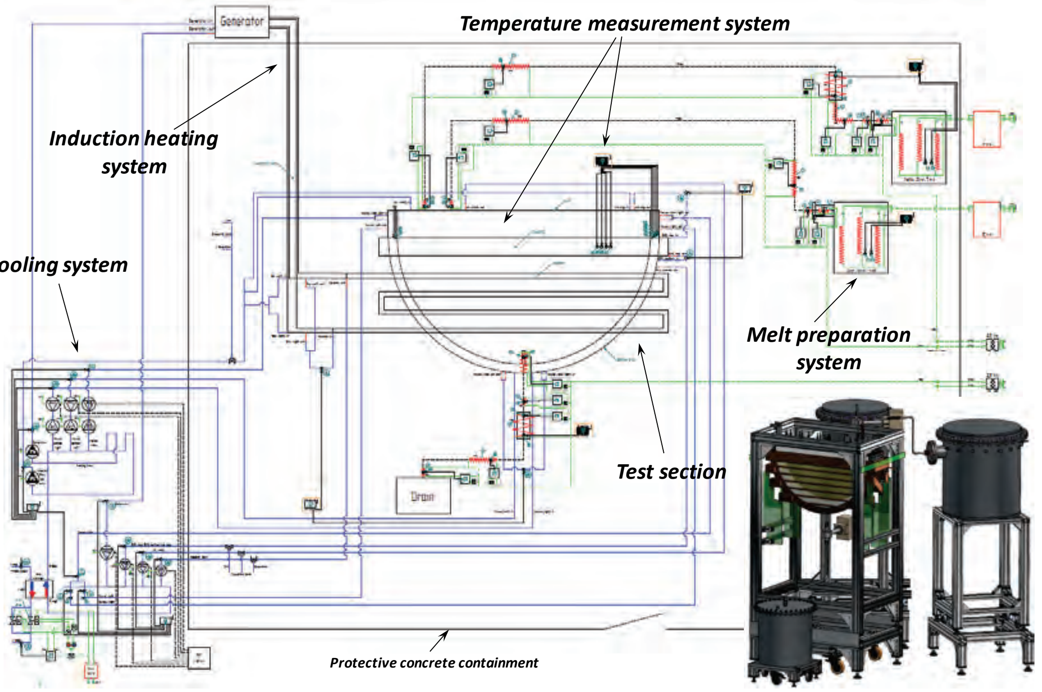

Figure 3.1: Schematic of SIMECO-2 test facility.

Figure 3.1 is the schematic of the SIMECO-2 test facility, including a 3D sketch of test section and melt preparation system. The facility is composed of the following parts:

- Test section (see Table 3.1);
- Induction heating system including high frequency generator (output power up to 150 kW, and frequency range of 200-500 kHz), inductor, top and bottom electromagnetic screens (EMS);
- Melt preparation and transport system, including two melting tanks for respective preparations of initial salt and metal melts, a sump tank for draining materials after experiment, high temperature valve (operational temperature up to 700 °C) and piping system with PID-controlled heaters;

- Temperature measurement system including wireless (Wi-Fi) connection for TC and RTD sensors and FBG probes;
- Cooling system (up to 150 kW cooling capacity); and
- Data acquisition system (DAS).

As a protective measure for safety of experiment, most parts of the facility are located inside the containment at KTH/NPS laboratory.

Table 3.1: Features of SIMECO-2 test section

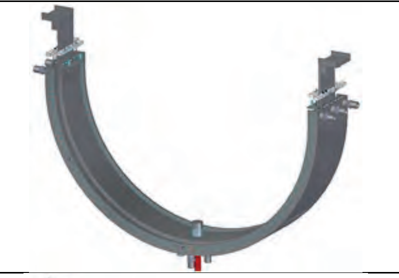	The vessel representing a slice of the RPV lower head of a typical PWR1000 with the geometrical scaling factor of ~4.5, with the following dimensions: diameter of 1000 mm, height of 500 mm and width of 120 mm.
	Visually transparent double walls made of fused quartz to contain debris bed or melt pool heated by induction (simulating heat generating oxidic melt layer). Such arrangement allows visual observation of melt behavior, such as remelting, crust formation, layer inversion, mixing and stratification, as well as possible measurement of melt velocities by e.g. PIV method.
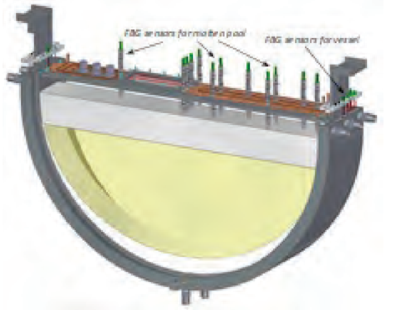	Temperature measurement system based on FBG sensors
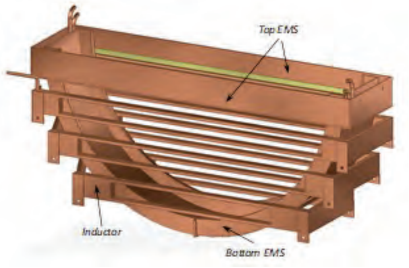	Contactless induction heating system, including inductor with windows for visual observation, top and bottom electromagnetic screens (EMS) for vessel protection.

For selecting proper simulant materials of immiscible corium compositions (oxide and metal) to be employed in SIMECO-2 experiment, salt systems based on the components of NaCl, LiCl, KCl, CsCl, $CeCl_3$, $BaCl_2$, $MgCl_2$, $CaCl_2$ and Na_2SO_4 had been studied during the design process of SIMECO-2, including small-scale experiments. As a result, the CsCl-KCl-LiCl system (Figure 3.2) and the Al-Mg system (Figure 3.3) were selected to reproduce some features of complex behavior of stratified molten pool during IVR, in particular:

- formation of stratified pool including two immiscible liquids with different densities allowing top metal layer and bottom salt layer;
- high thermal conductivity of top metal simulant layer affecting heat focusing on the interface between the metal melt and RPV wall; and

- layer inversion after small change of relative densities of layers.

These two systems of materials chosen are particularly suitable to simulate a typical configuration of two-layer corium pool in the lower head assumed for the IVR strategy.

This is the first time induction heating is applied for heating of molten salt layer in a slice geometry, and therefore extensive simulations have been conducted to cover different design options and operational regimes of the induction heating system, through a collaboration with the group of Prof. D. Lopukh from Saint Petersburg Electrotechnical University [2]. Figure 3.4 illustrated (a) the domain in the simulations, including vessel, inductor, top and bottom EMS of ½ test section; and (b) the volumetric current density distribution (power distribution) of induction heating.

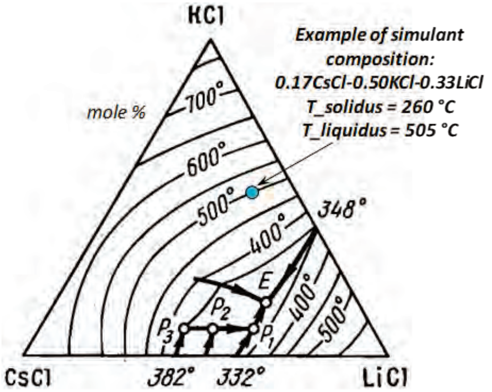

Figure 3.2: Phase diagram of CsCl-LiCl-KCl [30] with indication of suitable simulant composition.

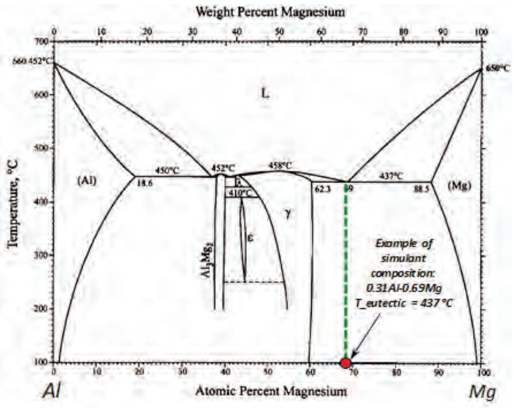

Figure 3.3: Phase diagram of Al-Mg [31] with indication of suitable simulant composition.

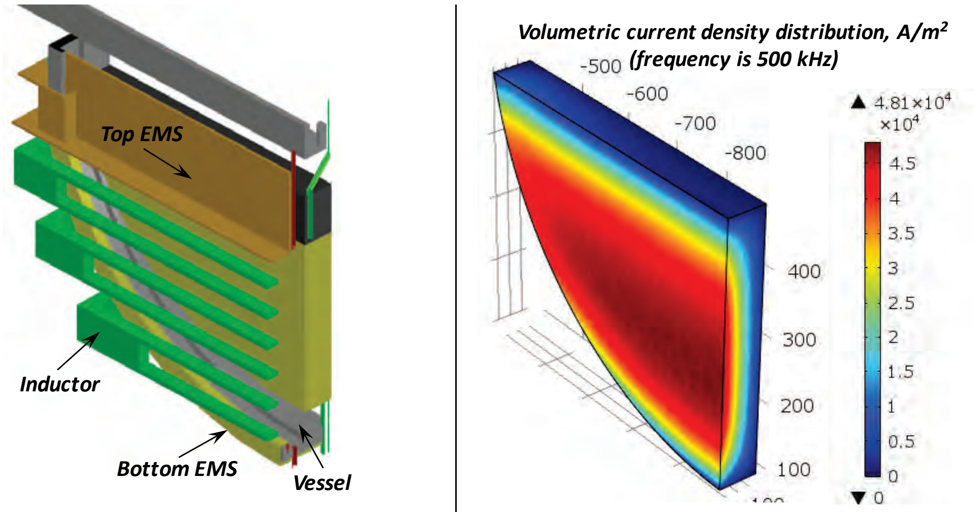

(a) (b)

Figure 3.4: Simulated domain (a) and current density distribution in the salt layer (b).

Many other pre-test analyses and simulations, including CFD [32] and Phase-change Effective Convectivity Model (PECM) previously developed at KTH/NPS [33], have been performed to support the facility design and get a preliminary understanding about thermal condition of a stratified molten pool, such as required heating power, temperature and heat flux distributions in the test vessel, crust profile, heat losses, etc. Figure 3.5 shows the temperature distribution on the middle plane of a stratified pool in SIMECO-2 predicted by the PECM.

A recent simulation [3] was to address the effect of internal radiation on natural convective heat transfer in a volumetrically heated molten pool of SIMECO-2 using a modified PECM. The simulation results show that internal radiation was quantitatively visible, but it did not play a dominant role in heat transfer and energy distribution under the temperature range of melt to be employed in the SIMECO-2 experiment.

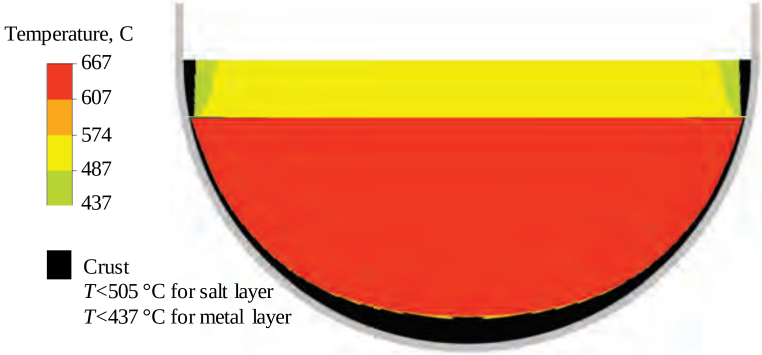

Figure 3.5: Predicted temperature distribution of two-layer pool in SIMECO-2 and interfacial crust shape with metallic layer (Al-Mg) on top and oxidic layer (salt) at bottom.

The usage of induction heating in the experiment leads to additional requirements to the temperature measurement system, including selection of proper temperature sensors and line of signal transfer from the sensors to the DAS. It is necessary to minimize the effect of the strong electromagnetic field from the inductor on the signals of temperature sensors. For this purpose, two types of temperature sensors are applied in the facility: (i) optical multipoint temperature sensors based on Fiber Bragg Grating (FBG) for measurement of temperatures in the molten salt pool and the steel vessel, and (ii) thermocouples and RTD probes with wireless transmitters for monitoring of temperatures in the tanks for melt preparation and drainage, the cooling lines and the metal layer of a stratified pool, as well as the high-temperature valve.

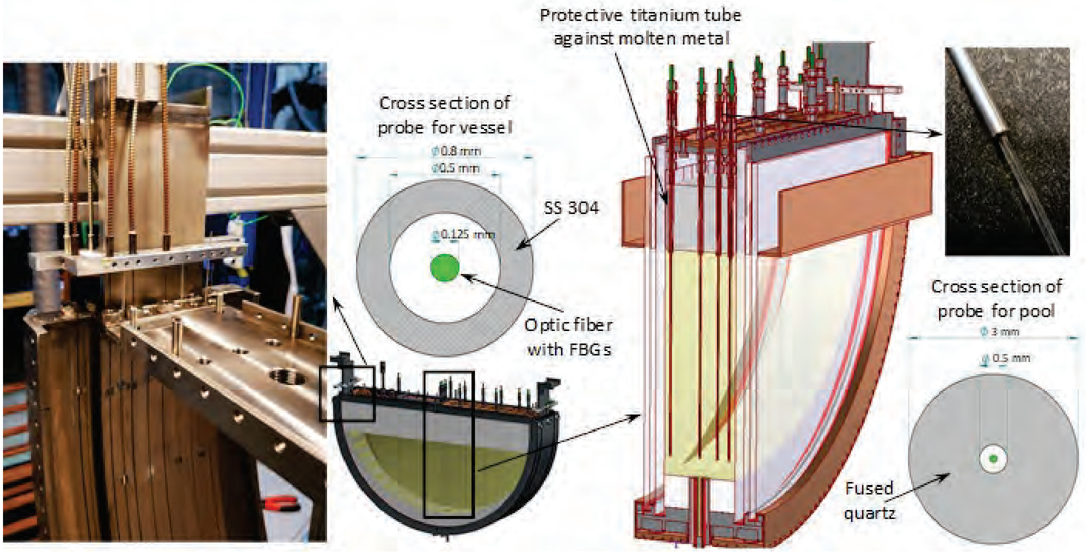

Figure 3.6: FBG probes for measurement of temperature in vessel and molten pool.

FBG is a novel method of temperature measurement, which is based on the registration of reflected light shift on Bragg gratings caused by thermal expansion. The main advantage of FBG probes is that they are not affected by electromagnetic field.

There are two diameters of FBG sensors applied in the SIMECO-2 facility: 0.8mm probes installed in the vessel wall for measurement of temperatures on the “hot” side toward to the crust and on the “cold” side toward cooling channel, whose values are used for calculation of heat flux through the vessel wall; and 3mm probes installed in the lid and immersed to the salt pool (Figure 3.6). The technical characteristics of the FBG probes are provided in Table 3.2.

Table 3.2: Parameters of FBG probes

Parameter	*Probe for vessel*	*Probe for pool*
Maximum operating temperature (°C)	150 (cold-side probe); 450 (hot-side probe)	700
Number of measurement points	up to 23 (from 0° to 90° of polar angle)	up to 13
Outer diameter of probe (mm)	0.8	3.0
Material of protective tube	SS (AISI 304)	SiO_2 (fused quartz)
Thickness of protective tube (mm)	0.15	1.25
Reproducibility (°C)	±2 (cold-side probe); ±3 (hot-side probe)	±4
Accuracy (°C)	±2 (cold-side probe); ±3 (hot-side probe)	±4

The salt and metal melts will be prepared outside of the test section in respective melting tanks (Figure 3.7) and then transported to the test section.

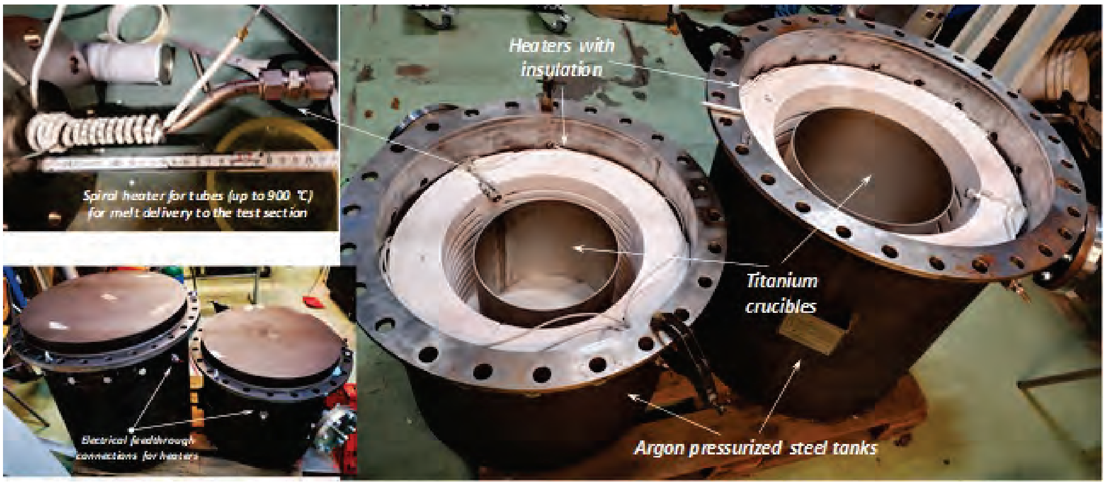

Figure 3.7: Melting tanks for preparation of salt and metal melts.

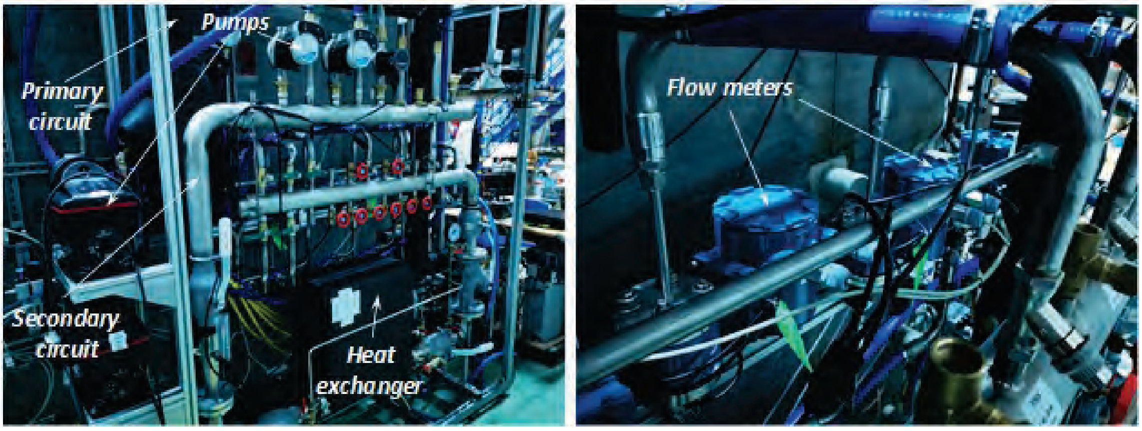

Figure 3.8: Cooling system for SIMECO-2 facility.

The SIMECO-2 facility requires several cooling functions. In order to provide reliable cooling capacities for the SIMECO-2 facility, KTH/NPS has significantly reconstructed the laboratory and installed a new cooling hub with a continuous cooling capacity up to 150 kW. Seven flow meters are installed in the main cooling loops (Figure 3.8) for precise registration of water flow rates through the cooled elements, which are necessary for thermal balance calculation.

In summary, the SIMECO-2 facility is still under construction, due to many technical difficulties encountered. The main components and systems of the facility is in place, for which intensive testing and assembling works are being carried out. It is expected that the facility will be commissioned by the end of year 2020. After its successful commissioning, it will become a valuable and unique facility for KTH/NPS to investigate the evolution and heat transfer of multi-composition debris bed (in addition to molten pool heat transfer) in the lower head, because SIMECO-2 is a first-of-its-kind infrastructure featuring high operational temperature, transparent visualization and novel instrumentation.

3.2.2. REMCOD/MRSPOD experiment – for the study of evolution/progression of multi-composition corium in the lower head

Under the primary support of the Nuclear Regulation Authority (NRA) in Japan, the REMCOD/ MRSPOD test facilities have been developed to study the thermal-hydraulic characteristics of molten metal penetration into debris beds [34][35].

The REMCOD facility has a rectangular container with four separate compartments accommodating different particulate beds (~300×75×26 mm each), for which heating is provided from one side of the facility by thermal resistance heaters, and visualization of molten metal penetration in the debris beds is realized from the other side which is made of transparent glass. The REMCOD facility has provided a wealth of information regarding melt interaction with the porous debris bed. However, some limitations were also identified regarding the facility, such as one-dimensional melt penetration, significant wall effect, low operating temperature and limited temperature control. To overcome these drawbacks, the MRSPOD facility was developed by placing a quartz tube in a high temperature tube furnace, which can reach high temperature inside furnace up to 1000°C, with well-controlled conditions and instruments. The quartz tube (120mm in diameter and 1300mm in length) was employed to accommodate a particulate bed and enable the visual property of the test section.

After the completion of the NRA tasks, our research was directed to development and validation of models using the experimental data [4] as well as interpretation of the results for insights [5]. The experimental approaches and expertise gained also provide the foundation for further investigation toward reducing the gap between prototypical materials and simulants in the experiment, so as to advance the understanding of molten metal (Zr/Fe) infiltration in oxidic (UO_2-ZrO_2) debris beds. Since the work has been well documented in [4][5][34], it will not be repeated here.

3.2.3. Coupled thermo-mechanical analysis of RPV failure

As the physical barrier to contain the core, the failure of the reactor pressure vessel (RPV) due to corium attack during a severe accident is the transition point from in-vessel to ex-vessel progression of accident. Therefore, the prediction of RPV failure is important to analysis of accident progression and assessment of severe accident mitigation strategies. For instance, the assessment of ex-vessel corium coolability and melt retention strategy adopted in some light reactors (LWRs) requires the information of RPV failure characteristics (e.g. time and mode of RPV failure), since the failure time and mode determine the melt release location and conditions (amount, composition and superheat).

Since the structural performance of RPV is highly affected by the thermal loads from the corium, the RPV failure is a coupled thermo-mechanical problem per se, whose solution is determined by the combination of heat transfer of decay-heated corium in the lower head of RPV with creep of the lower head under the thermal and mechanical loads of the corium.

Our study on this topic was focused on two aspects: (i) determination of the initial state of corium in the lower head: and (ii) development and qualification of coupling approach for RPV failure analysis.

The initial state of corium in the lower head is an important starting point for debris evolution in the lower head, and it is determined by corium relocation from the core to the lower head. The MELCOR code was chosen to provide such information. For this purpose, a sensitivity study of MELCOR nodalization was performed for simulation of in-vessel severe accident progression in a boiling water reactor [6]. In a separate study, the thermal loads from the MELCOR were also directly employed in vessel creep analysis [7].

The development of a coupling approach for RPV failure analysis was based on the latest multiphysics platform of ANSYS Workbench. The new approach facilitates transient simulation of complex geometries, addition of advanced models as well as reduction of user effect. For instance, the newly developed three-stage modified theta-projection model [8] was employed as creep model in the validation work below.

The general procedures of the thermo-mechanical coupling approach can be summarized as follows:

(a) Heat transfer simulations of debris bed/melt pool and vessel wall in ANSYS Fluent with a special attention paid to turbulence modelling of melt pool,
(b) Transient thermal load transfer from ANSYS Fluent to ANSYS Structural in ANSYS Workbench with use of an extension tool,
(c) Structural analysis of the vessel in ANSYS Structural where a special attention was paid to the creep modelling of vessel steel.

The heat transfer of a debris bed/melt pool can be estimated by the simplified method of PECM [33] implemented in ANSYS Fluent. A more mechanistic method can simulate the melt pool heat transfer by turbulent modeling of natural convection driven by internal heat source. For this reason, the SST model was employed in the present study, which is a combination of k-ε and k-ω equations and recommended by ANSYS for most industrial heat transfer problems.

As shown in Figure 3.9 where fluid and structure correspond to respective melt pool and RPV wall, two methods could be used to realize the transfer of transient temperature from conjugate heat transfer analysis to mechanical analysis. The conjugate heat transfer analysis is for calculating thermal load of the melt pool, while the mechanical analysis is for the calculation of the structure (vessel wall) behavior under the thermal load. In the first method (Figure 3.9a), transient thermal loads in the vessel wall are transferred and mapped into the mechanical simulation domain. After the structural domain reads the essential thermal loads, a structural analysis of this domain is performed. In the second method (Figure 3.9b), transient thermal loads at the surface of vessel wall are mapped to the boundary of the structural domain, and then under this boundary condition a coupled thermo-mechanical analysis of the structural domain is conducted. To distinguish these two methods, the former is termed the former as volume loads mapping (VLM) and the latter as surface loads mapping (SLM).

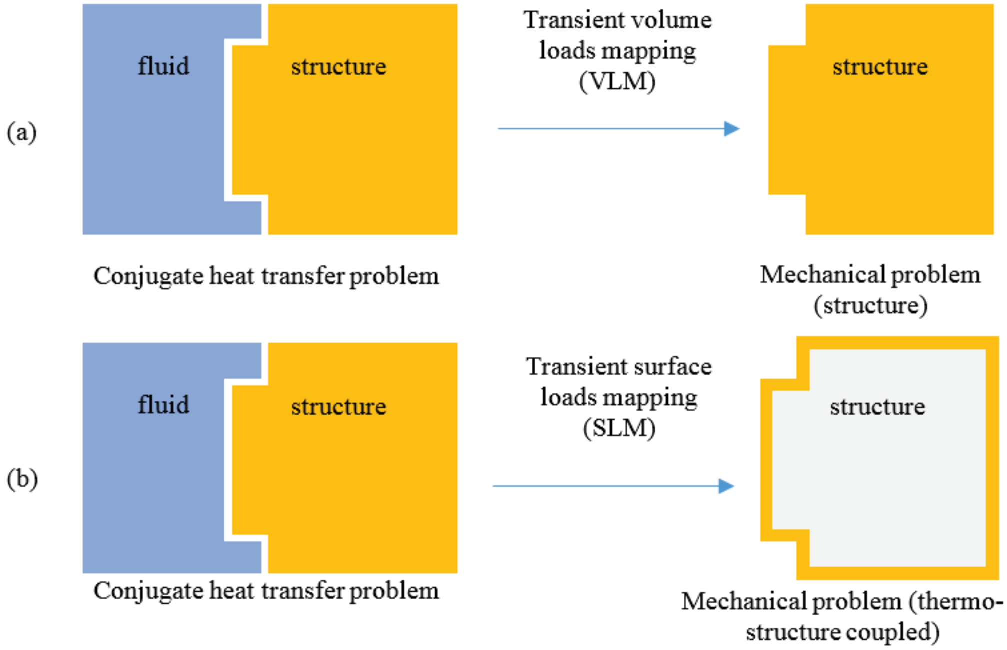

Figure 3.9: Two methods of thermal load transfer for thermo-mechanical coupling approach: (a) volume loads mapping, (b) surface loads mapping.

As a validation of the coupling approach, the volume loads mapping (VLM) was employed in the simulation [9] for the FOREVER-EC2 experiment [36], which was conducted in, 2001 to investigate the vessel creep phenomena under thermal and mechanical loads. A 1:10 scaled-down RPV with 406mm diameter and 15-mm-thick wall was employed in the experiment. The lower head was made of French reactor steel (16MND5) while the upper cylindrical shell was made of German Steel (15Mo3). A binary mixture of 30% CaO-70% B_2O_3 was used as melt simulant of corium in the lower head. During the experiment, the melt pool was heated by a special designed heater to maintain a maximum pool temperature up to 1300 °C. No external cooling was applied and the pressure in the vessel was maintained at 25 bar during the experiment. The natural convection in melt pool was modeled with the SST turbulence model with a well-resolved boundary layer, while the creep deformation for the vessel made of 16MND5 steel was analyzed with the three-stage creep model recently developed by Yu et al. [8]. The validation work demonstrated the well-posed capability of the coupling approach for prediction of the key parameters of interest, including temperature profile, total displacement of vessel bottom point and the evolution of wall thickness profile in the experiment [9].

For comparison purposes, a comparative study was performed by using either VLM or SLM in the coupling approach for the FOREVER-EC2 experiment and a reactor case [10].

Figure 3.10 shows the calculated temperature fields of the FOREVER-EC2 experiment. A thermal stratification Figure 3.10a) is seen in the molten pool, which is an expected phenomenon of natural convection driven by volumetric heat source. The highest temperature is 1609 K. In the lower head region covered by melt as in Figure 3.10b, temperature generally increases with polar angle and decreases when the polar angle is approaching 90°. It further decreases with the height in the cylindrical shell. The highest temperature of the vessel is 1364 K.

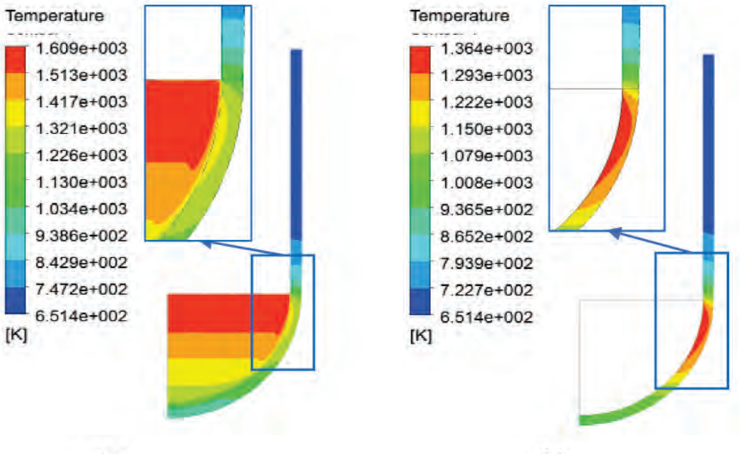

(a) (b)

Figure 3.10: Temperature distribution: (a) global, (b) local vessel.

Figure 3.11 shows the temperature profiles of the external vessel along the polar angle in comparison with experimental data. Regions with a polar angle larger than 90° are those in the cylindrical shell of the vessel. It also shows the temperature profile increases with time until reaching a steady state (after 4975 s). The steady-state results agree well with the experimental data, except for the bottom of the lower head and the uppermost cylindrical shell. In addition to possible modelling uncertainties, the discrepancy in bottom temperature of the lower head may be caused by the crust and gap possibly formed there in the experiment but not modelled in simulations.

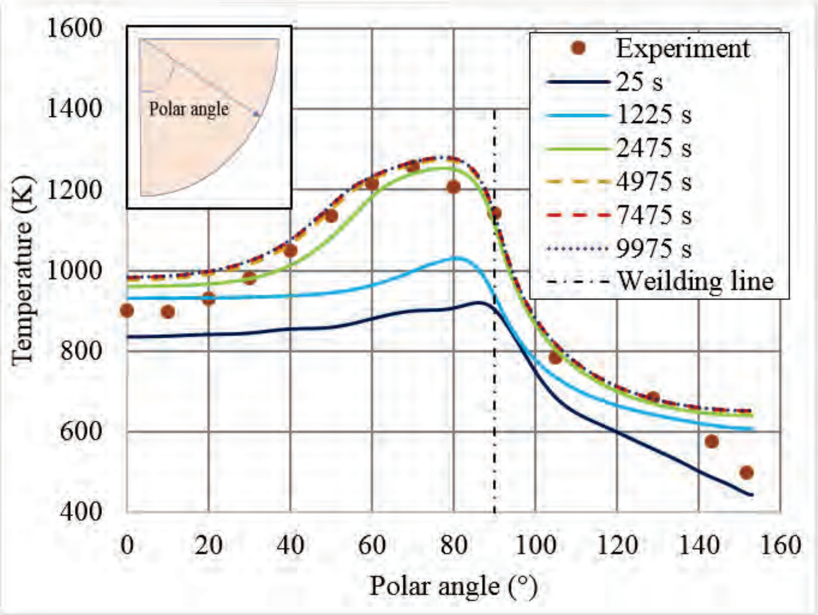

Figure 3.11: Temperature profiles of external vessel surface along the vessel polar angle.

In the mechanical analysis, the VLM predicts a failure time of 23959 s and the SLM of 22445 s: both are close to the experimental failure time 24180 s. Figure 3.12 is the creep strain fields at failure time. Both VLM and SLM predicts the maximum creep strains at same location where the temperature is high (cf. Figure 3.10). This is related to the fact that creep behavior is driven by high temperature. The maximum values also close to each other: 0.393 in VLM and 0.366 in SLM. Figure 3.13 presents the total deformation of the vessel bottom point in the vertical direction. Similar trend is seen in the VLM, SLM and experimental data, i.e., the deformation increases with time and reaches a drastic acceleration at the end. Both simulations with VLM and SLM agree well with the experimental data, though both slightly underpredict the value of total deformation.

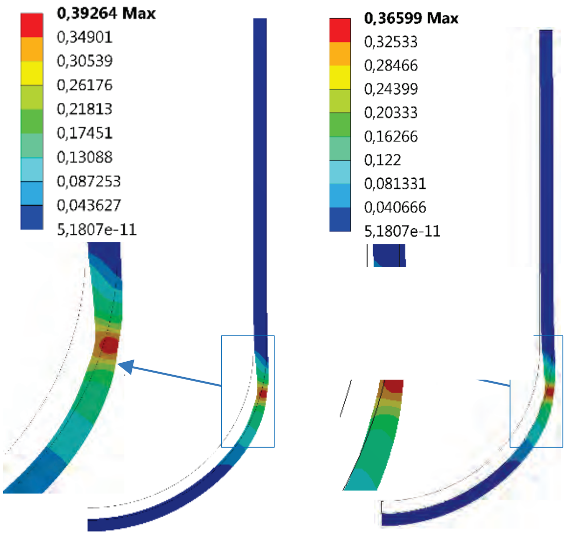

(a) (b)

Figure 3.12: Creep strain fields at failure time: (a) VLM (b) SLM.

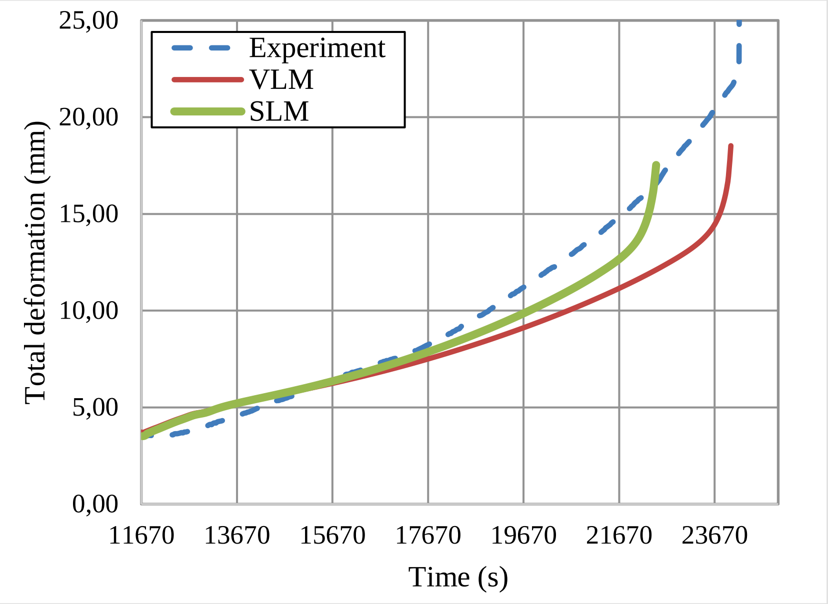

Figure 3.13: Total deformation in vertical direction of the vessel bottom point.

For the reactor case, the coupling approach was employed to simulate the vessel failure during a hypothetical severe accident for a reference BWR initiated by SBO. Assuming the corium distribution being homogeneous, the total amount of corium relocated in the lower head was considered to form a 1.9 m corium melt pool/debris bed. Figure 3.14a illustrates the computational domain of the conjugate heat transfer, and in this case the PECM was used for the calculation. A computational domain with a height of 2.3 m was assumed in the simulations, where the 1.9 m corium pool high was covered by a 0.4 m thick layer of water injected the late phase of accident sequence. Under the implementation of PECM, the water layer was damped with artificially high heat capacity and high conductivity such that it would efficiently remove heat from the corium and keep its saturation temperature. For the corium part below water, a volumetric heat source 1.1 MW/m^3 was adopted as the nuclear decay heat. Without the insulation on the external vessel wall, a very small heat loss of 20 W/m^2 was applied. Melting and solidification of the corium were also considered with a solidus temperature of 2750 K and a liquidus temperature of 2770 K. The initial corium temperature was set as 1100 K. For the mechanical analysis (Figure 3.14b), an inner pressure of 3.15 bar and an outer pressure of 2.48 bar were assumed. For the region covered by corium, an extra hydrostatic pressure was added on the vessel wall. A 2-m-long vessel extension was assumed in addition to standard gravity.

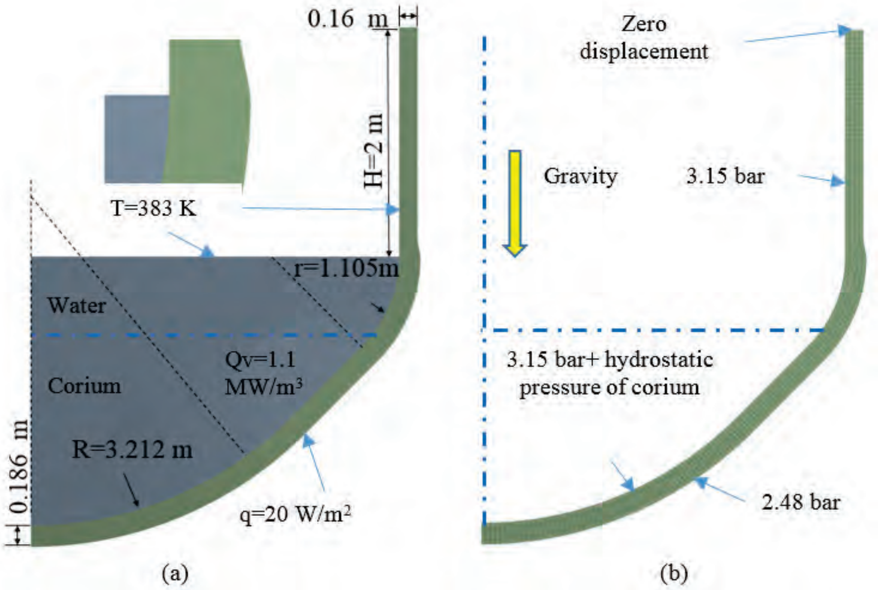

Figure 3.14: Computational domains and boundary conditions: (a) conjugate heat transfer analysis, (b) mechanical analysis.

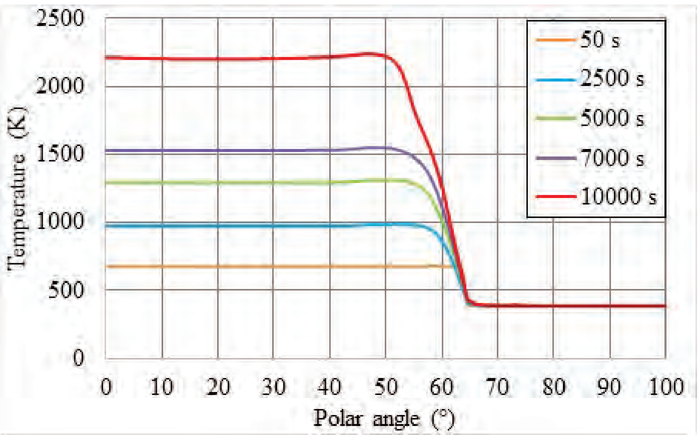

Figure 3.15: Temperature profiles of inner vessel wall along the vessel polar angle.

Figure 3.15 presents the wall temperature profile along the inner vessel surface at 50 s, 2500 s, 7500 s and 10000 s. The temperature increased with time for the vessel surface in contact with corium and the profile was flat because a large portion of the corium was still in solidus status. It also indicated that for the surface in contact with water, the temperature was basically unchanged due to the upward heat removal by water.

The predicted RPV failure time was 9869 s by VLM and 9650 s by SLM. Like the FOREVER-EC2 case above, the VLM predicted a slightly later failure time than the SLM in the reactor case. Figure 3.16a compares the maximum creep strain developments with time. Before 9000 s, the predicted values by VLM and SLM are close to each other. Afterward, the creep acceleration occurred, and the strain increased drastically. The acceleration of the VLM occurred 200 s later than that of the SLM, which agreed with the predicted later failure time. Similar trend was observed for the total deformation in vertical direction of vessel bottom point as shown in Figure 3.16b. The deformations of VLM and SLM were close except that the acceleration of VLM occurred slightly later than that of SLM. Overall, the results of VLM agreed well with those of SLM.

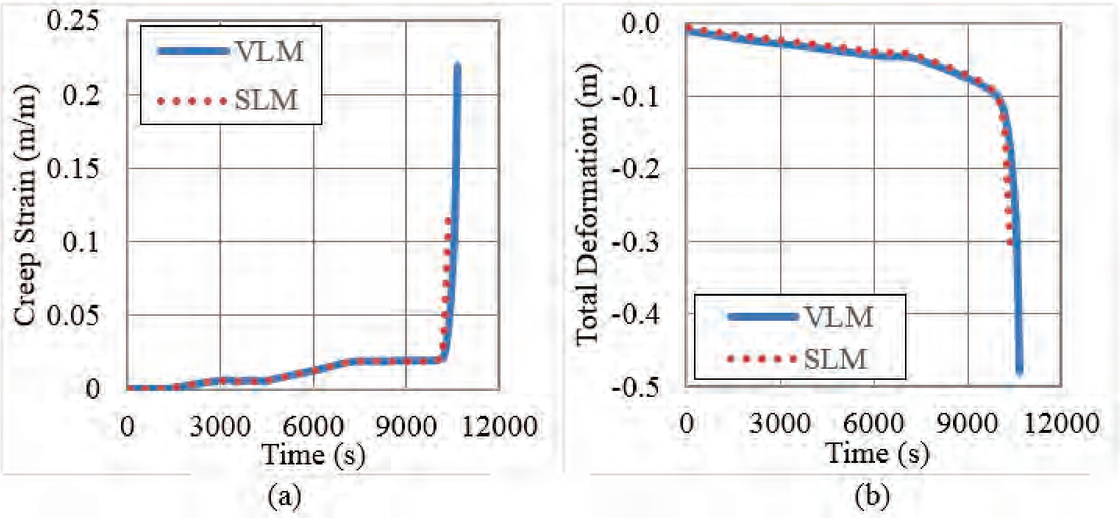

Figure 3.16: Results of structural analysis: (a) creep strain and (b) total deformation in vertical direction of vessel bottom point.

Table 3.3 lists the number of CPU cores and corresponding costs of computational time for each simulation. All the simulations were done in a Lenovo P700 workstation equipped with 2 Intel Xeon E5-2630 v3 processors (8 cores per processor) and 32 G RAM. For the simulations of FOREVER-EC2, the SLM employed twice the parallel CPU cores and spent 28.6 % more time compared with the VLM. For the simulations of the reactor case, both VLM and SLM employed the same number of parallel CPU cores, but the VLM only took 1/3 of the computational time of the SLM. As a result, it can be concluded that the VLM has a much higher computational efficiency than the SLM. The reason is that a structural analysis is performed in the VLM method while a coupled thermo-structural analysis is performed in the SLM method (cf. Figure 3.9); a standalone structural analysis is computed faster than a coupled thermo-structural analysis.

Table 3.3: Comparison of computational efficiency

Case	FOREVER-EC2		BWR	
	VLM	SLM	VLM	SLM
Number of CPU cores	4	8	4	4
Computational time (hours)	2.1	2.7	1.8	7.2

In summary, the coupling approach developed on ANSYS Workbench was proven to be capable of predicting RPV failure using either VLM or SLM method, but the VLM was recommended due to its computational efficiency. Since it is insensitive to geometry, the coupling approach can be further considered to the applications with more complex geometries such as a BWR lower head with a forest of penetrations (CRGTs and IGTs) modelled in detail.

3.3 Quenching and oxidation of ex-vessel debris bed

Motivated by interest in ex-vessel debris bed coolability, an extensive program of experimental studies on two-phase flow and heat transfer in a variety of particulate debris beds had been carried out previously at KTH/NPS. Analytical studies including development of models has also been performed, e.g., in the recent work [11] at KTH/NPS the MEWA code was validated against experiments and then applied to investigate the coolability of ex-vessel debris beds with cylindrical, conical and truncated conical shapes assumed to form under severe accident scenarios of a boiling water reactor. The simulations showed that the dryout power density of a prototypical debris bed was roughly inversely proportional to the bed's height regardless of the bed's shape [11].

To assess the coolability of a debris bed, it is important to identify the dryout heat flux at the top surface or dryout power density in the bed, since it is usually considered as the maximum heat removal capacity under thermal equilibrium. Hence, the dryout condition has been extensively investigated in many experimental and analytical studies. However, the dryout is concerned with the long-term coolability of a debris bed. In a more realistic scenario, the high-temperature corium debris is initially dry and will go through a quenching process, where the thermal equilibrium is no longer valid everywhere. As observed in the DEFOR-E experiment [37], the temperature of the debris bed from melt coolant interaction still remained higher than the saturation temperature of water for more than 100 s after settling down to the bottom of water pool, far behind the melt-coolant-interaction time of 10 s. In a reactor situation with decay heat, such ‘‘dry zone” of debris bed will continue to heat up before the arrival of quench front due to the insufficient cooling capacity, and consequently starts remelting if the temperature exceeds the solidus temperature. Therefore, the assessment of the probability of the successful quenching of a high-temperature debris bed is also important and necessary since it is the prerequisite for achieving long-term coolability of debris bed. In the quenching process, the temperature difference between solid particles and fluid (steam and liquid water) is large and involving oxidation phenomenon, and flow patterns and heat transfer mechanisms during this process are complex, making it difficult to cover by experimental measurement and modeling. Since little work has been done regarding quenching studies of a prototypical debris bed, a recent study [12] was performed at KTH/NPS to fill this knowledge gap in the severe accident area.

The focus was a heap-like debris bed formed in the pedestal during a hypothetical severe accident of a Nordic boiling water reactor (BWR). The MEWA code was employed to simulate the quenching process of the ex-vessel debris bed. The MEWA code, previously named WABE and now as a module of the COCOMO code, is developed by University of Stuttgart to simulate the transient boil-off and quenching behaviors of debris beds during a severe accident [38]. The latest development of the code capabilities includes modeling of oxidation and remelting of debris beds.

Before addressing the prototypical debris bed, the code was validated against the latest experimental results obtained from the PEARL experiment at IRSN [39]. The comparisons of the predicted results against the experimental data in terms of several key parameters, such as velocity of the quench front and production rate of steam, show a good agreement. The simulation also shows that a top-quenching phenomenon occurs as the water from the bypass gradually accumulates atop of the bed. Such top-quenching was not detected in the experiment, most probably because the top quenching layer is too thin to be covered by the single thermocouple installed in the region near the top. More details of the validation work can be found in [12][13].

After the validation against the PEARL experiment, the MEWA code was applied to the investigation on the quenching of an ex-vessel debris bed for a reference Nordic-type boiling water reactor (BWR), which features a reactor cavity filled with a deep water pool as a severe accident mitigation strategy. The thermal power of the BWR is 2100 MW, and the diameter of the pedestal (reactor cavity) is 9 m. During a hypothetical severe accident, about 180t molten corium is assumed to discharge into the reactor cavity as the result of the failure of the reactor vessel wall five hours after the occurrence of the accident. Due to fuel coolant interactions (FCI), a heap-like debris bed is assumed to form on the cavity floor. According to the previous studies at KTH/NPS, the mean porosity and the effective particle diameter of the debris bed are set as 42% and 1.75mm, respectively. The diameter of the debris bed is 8 m and the repose angle of the cone is chosen as 30°, yielding the bed height of 2 m. The decay heat power is estimated to be 14.5 MW according to the Way-Wigner formula, which corresponds to a specific power of 109W/(kgUO2) if the corium has 75% of UO2. Initial temperature of the debris bed (filled with steam) is assumed to be 1273 K because the water inside the bed is boiled off due to the high temperature. It is also assumed that the water in the pool surrounding the debris bed is saturated (407 K) at the ambient pressure of 3 bar. Only half of the conical bed is simulated due to axial symmetry.

There are two types of debris bed considered in the study: (i) a debris bed without Zr, representing an accident scenario where Zircaloy contained in the corium has been completely depleted before it arrives at the bottom of the pedestal; and (ii) a debris bed with Zr, for the case where Zircaloy remains in the settled debris bed, and therefore further oxidation will take place during the quenching process. Other possible metal component such as stainless steel is not considered.

The oxidation of the Zircaloy will not only generate heat which contribute to heat-up of the debris bed, but also produce hydrogen which may affect the thermal-hydraulics and cause combustion risk, as described by;

$$\mathrm{Zr} + 2\mathrm{H_2O} \rightarrow \mathrm{ZrO_2} + 2\mathrm{H_2}, \quad \Delta H = -547 kJ/mol \tag{1}$$

The oxidation reaction is limited by the availability of steam and controlled by the diffusion process of oxygen through the ZrO_2 layer, which is approximately governed by a parabolic kinetic law:

$$\frac{\mathrm{d}X^2}{\mathrm{d}t} = K_{oxi} \tag{2}$$

where X is the thickness of ZrO_2 layer or the total oxygen mass gain in ZrO_2 layer, and the kinetic constant K_{oxi} is temperature-dependent which is usually given as an Arrhenius formulation:

$$K_{oxi} = A \cdot \exp\left(-\frac{B}{RT}\right) \tag{3}$$

The values of the empirical parameters A and B in Eq. (3) are determined from experiments [39].

3.3.1. Quenching of a debris bed without Zr

In the case of quenching of a debris bed without Zr, the corium of the debris bed is assumed to consist of 75% UO_2 and 25% ZrO_2 (the other possible component such as stainless steel is not considered).

The development of the profiles of the bed temperature and liquid fraction, as well as the velocity fields of the liquid and steam were plotted in Figure 3.17.

Time=842s

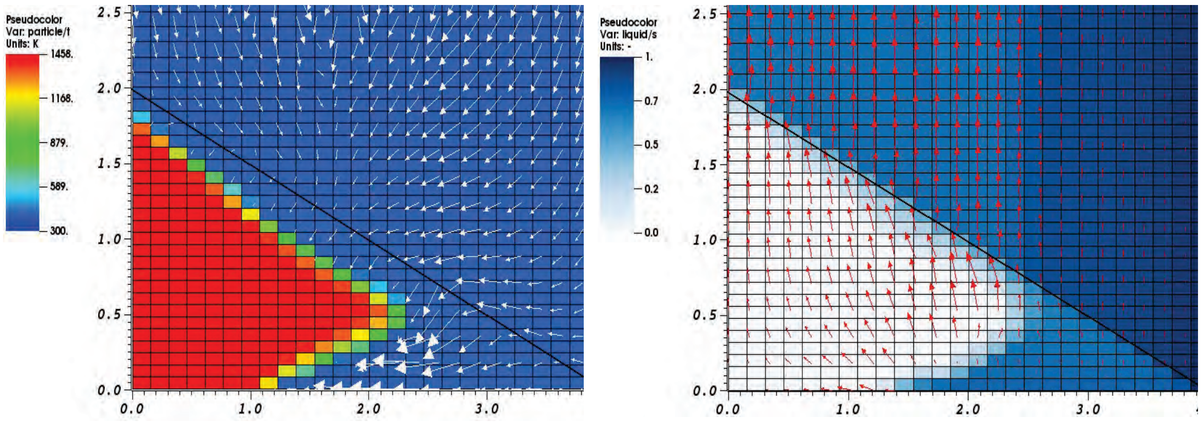

Time=2000s

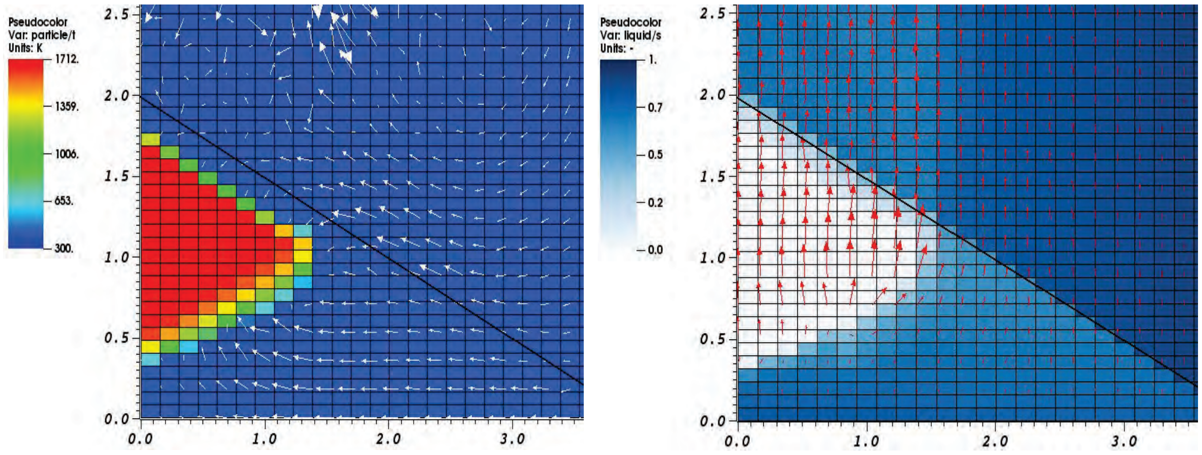

Time=4810s

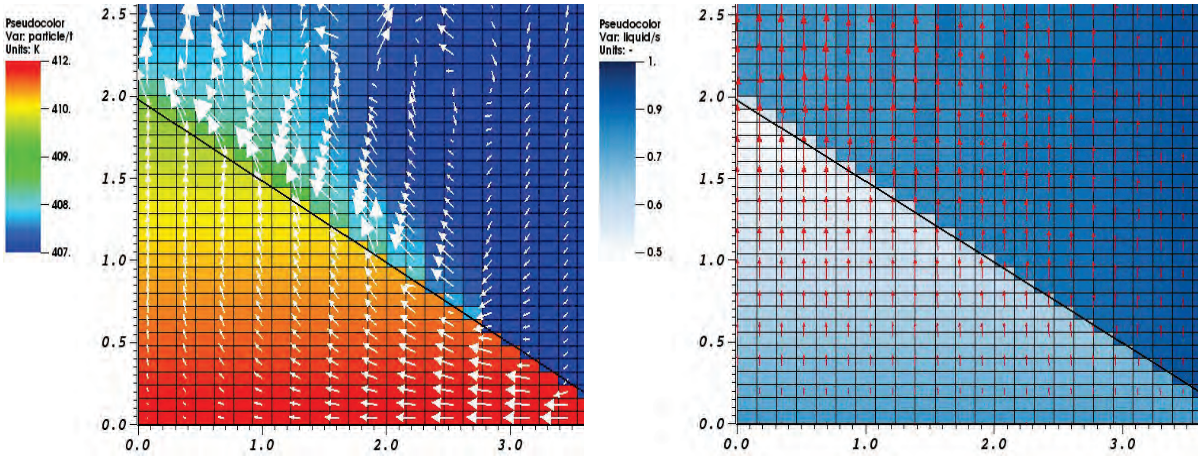

Figure 3.17: Quenching of the 75% UO_2+25% ZrO_2 debris bed by top-flooding: debris temperature and liquid velocity (left); liquid fraction and steam velocity (right).

From the graphs it clearly shows that the propagation of the quenching front of the conical debris bed by top-reflooding features a multi-dimensional pattern, which starts with the lateral infiltration of water from the bottom since the downward flow of water is hindered by the upward flow of steam. The transverse ingression of water at a higher elevation is also blocked by the steam generated below until the lower part has been quenched. Meanwhile the upward flow of water is gradually increasing, especially after the transverse water flow reaches the centerline. Finally, a coolable steady state is reached after about 4800 seconds, with the bed temperature stabilized at about 411 K which is slightly higher than the saturated temperature of water.

The highest temperature of the bed during the whole quenching process is 2067K, which is much lower than the melting point (~2800K) of the corium (UO_2 + ZrO_2) in this case.

3.3.2. Quenching of a debris bed with Zr

If not all the zircaloy is consumed when the ex-vessel debris bed is formed, the oxidation of the zircaloy during the quenching process is necessary to be taken into account. In addition to the heat and hydrogen that will be released during this chemical reaction, it is also worth of being noted that the inclusion of zircaloy in the corium will lead to a lower melting temperature (~2100 K). Here we assume that the initial composition of the corium debris bed is 75% UO_2 + 15% ZrO_2 + 10% Zr.

Generally, the quenching process of the Zr contained debris bed is quite similar to that of the oxidic debris bed above, but a non-coolable state is finally yielded due to the oxidation of Zr component, as shown in Figure 3.18. The temperature of the unquenched zone rises up to 3000 K at 2090 s (Figure 3.18a), which far exceeds the liquidus temperature of the corium and consequently should lead to remelting and relocation. This is mainly attributed to the extra release of large amount of heat from Zr oxidation. Furthermore, the oxidation process has been intensified as the result of the positive temperature feedback.

To further explore the transient process of heat-up, three representative locations (marked in Figure 3.18a) were probed, whose evolutions of temperature are plotted in Figure 3.18b. It is observed that only the location C can be successfully quenched after a modest temperature increase (<250 K), with its temperature remained always below the melting point during the whole quenching process, while both the location A and the location B have experienced a dramatic increase of temperature up to 2000 K. The explanation for the difference of behavior can be found in [12].

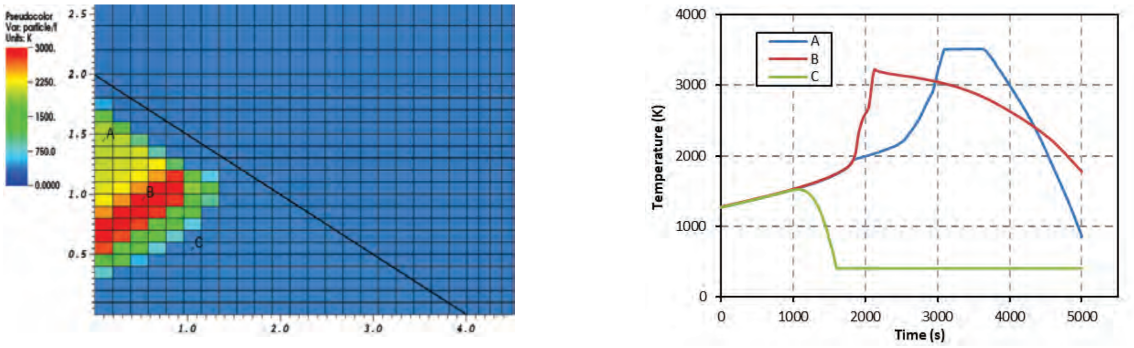

(a) (b)

Figure 3.18: Quenching of the 75% UO_2+15% ZrO_2+10% Zr debris bed by top-flooding: (a) temperature profile at 2090s; (b) temperature evolution of three locations.

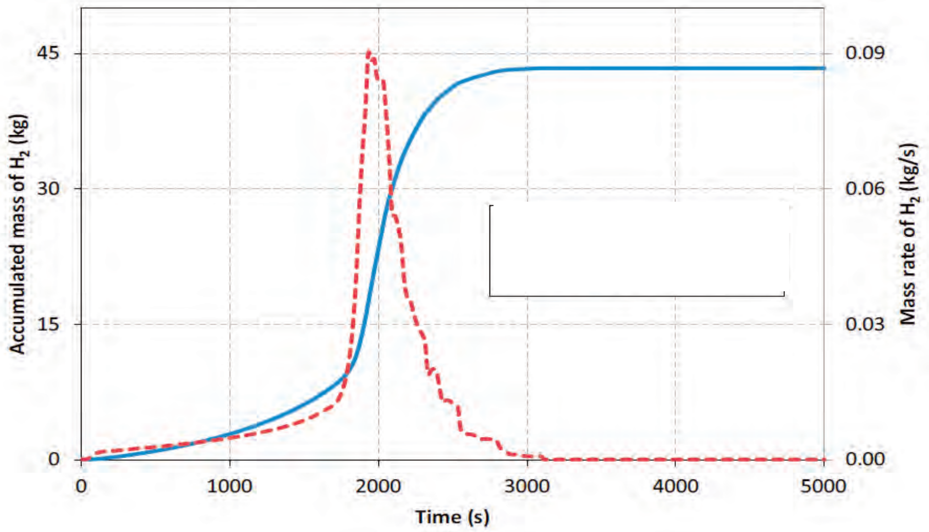

Figure 3.19: Accumulated mass and production rate of hydrogen during the quenching of the 75% UO_2+15% ZrO_2+10% Zr debris bed by top-flooding.

The accumulated amount and production rate of hydrogen are plotted in Figure 3.19, which shows an obvious peak of H_2 generation rate when the oxidation reaction culminates. The Zr oxidation is almost terminated after about 3000 s because:

- The major part of the debris bed has been successfully quenched and remains at a low temperature.
- The Zr in the unquenched region (still at high temperature) has almost been oxidized.

In total around 980 kg of Zr is oxidized in the end, yielding about 43 kg of hydrogen and 5880 MJ of energy, which significantly contributes to the heat-up of the debris bed and eventually leads to the unquenched condition.

To reach a quenchable condition for the above debris bed Zr oxidation, two severe accident management (SAM) measures are conceived to implement into the debris bed: (i) introducing a forced injection of water at velocity of 0.01m/ from the bottom of the debris bed; and (ii) adding a downcomer with 0.6m diameter in the middle of the debris bed.

The first SAM measure with water injection from the bed's bottom is predicted to be an effective strategy to quench the bed and mitigate the oxidation, since the water inflow is not hindered by the upward flow of steam and therefore could infiltrate whole bed quickly. Given a specific flowrate of bottom injection, the partial coverage of the cavity floor with the injection inlet near the center appeared to be more effective than the full coverage, as the water is targeted to the originally least quenchable region of the bed. The second suggested SAM measure has a downcomer embedded in the center of the debris bed, and the simulation indicated that it is also a practical alternative that can lead to a coolable state, although its efficiency is relatively lower compared to the bottom injection.

In summary, the MEWA code has been employed to investigate the quenching of an ex-vessel debris bed with/without oxidation, which is the precursory stage of long-term coolability. The next step ought to advance and validate the models involved in oxidation where we have poor knowledge. An experimental study to combine quench with oxidation of a debris bed should be realized in future to meet the needs for first-of-its-kind data.

3.4 Mechanisms of ex-vessel fuel-coolant interactions

Previously, the DEFOR experiment using melt of binary oxides [37] was carried out at KTH/NPS to identify the characteristics of debris bed forming from fuel coolant interactions (FCI), which are of importance to debris bed coolability. It was found the well-fragmented debris beds had the porosity of 40%~60%, and the debris particles had a broad size distribution from micrometer to centimeter. The debris beds were likely to be heap-like, with possible formation of agglomerates or cake (unbroken melt jet) if the melt jet was large compared to the depth of water pool.

More and more evidence indicated that that the first pour of corium upon vessel failure is most likely to be a metal rich jet. Therefore, experimental studies on metallic melt-coolant interactions have been initiated at KTH/NPS in APRI-10. The DEFOR facility has been adopted to investigate fuel coolant interactions (FCI) using metallic tin melt with the objectives to (i) look into the characteristics of metallic debris beds formed from FCI as well as jet fragmentation; and (ii) exploit engineered features for enhancing melt fragmentation and suppressing steam explosion.

The picture and schematic of the new test facility (named DEFOR-M) is as shown in Figure 3.20, mainly composed of an induction furnace, a melt delivery funnel, water supply system and a rectangle water tank. Tin is selected as the simulant of metallic phase of corium and melted in a SiC crucible of 15L by heating of a 45-kW medium frequency inductor. The heating power of the induction furnace can be adjusted in the preparation of molten Tin. The water tank has the height of 2 m and cross section of 0.45×0.45 m. The height of water pool is 1.5 m in the tank with transparent glass windows around for visualization.

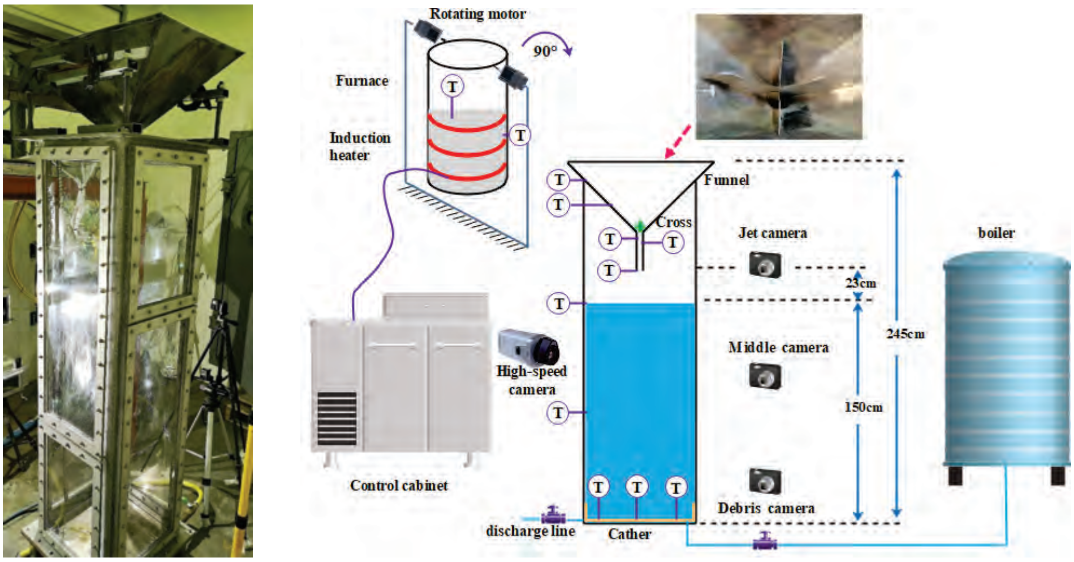

Figure 3.20: Picture and schematic of DEFOR-M test facility.

During each run of experiment, manual mixing of the melt in the crucible is executed by applying a stirring rod to ensure a uniform temperature. After the melt reaches a prescribed temperature in the crucible, it is poured into the delivery funnel by tilting the crucible through a remote controller. A specially designed cross is located at the bottom of funnel to eliminate the revolving velocity of melt, so as to obtain a coherent jet at the outlet of the 20-mm-ID nozzle attached to the conical funnel underneath. A catcher is located at the bottom of the water tank to collect the debris bed. K-type thermocouples are employed to measure temperatures: two for melt temperatures in the funnel and at the outlet of the nozzle, two for coolant temperatures in the water tank, and five for debris temperatures at different radial and axial positions of the catcher (tracking the quenching process of debris bed). A data acquisition system (DAS) of National Instrumentation is adopted to read the temperatures. Three GoPro cameras at the shooting rate of with 240 fps are employed to record the information of jet penetration, jet breakup and debris bed formation at different elevations. A high-speed camera (Phantom-V311) is applied at shooting rate of 400 fps and resolution of 600×800 pixels to record the detailed dynamics of jet fragmentation. For operational safety, most parts of the DEFOR-M facility are located inside the containment at KTH/NPS laboratory, a bunker with 0.5-m-thick reinforced concrete wall.

After each test, the water tank is drained to obtain a dry debris bed on which quantitative measurements will be conducted. The measurements determine the shape of debris bed by a 3D laser scanning system, the debris particle size and morphology, and the porosity of the debris bed including close porosity and open porosity. The close porosity is related to the hollow particles in which the coolant cannot penetrate, while the open porosity is resulting from the pores where the coolant is accessible. Particle morphology is recorded by a Canon camera, while the particles are sieved by different sizes of sifters with an electronic oscillator.

Table 3.4 lists the five tests that have been conducted so far using the metallic melt Tin, where the test identifier “H-L” means high melt superheat and low water subcooling, and so on. In all five tests, 30 kg (4.1 liters) of Tin melt is poured into the water tank. The range of Weber number[4] during these tests are between 750~1050.

Table 3.4: Test matrix or DEFOR-M

Parameter	H-L	M-L	L-L	M-H	M-M
Simulant material	Sn				
Melt density [kg/l]	7.31				
Melting temperature [℃]	231.93				
Melt temperature in the funnel [℃]	346	314	282	309	307
Melt superheat in the funnel [℃]	114	82	50	77	75
Melt jet initial diameter [mm]	20				
Elevation of nozzle outlet [m]	1.7				
Jet free fall height [m]	0.23				
Duration of melt release [s]	8.3	7.45	7.32	7.3	7.16
Melt volume [l]	4.1				
Average flow rate [l/s]	0.494	0.55	0.56	0.56	0.57
Water pool depth [m]	1.5				
Water initial temperature [℃]	97.5	90	90	50	70.5
Water subcooling [℃]	2	10	10	50	30
Debris collection [kg]	29.706	29.138	29.356	29.45	29.76
Agglomeration[kg]	25.7	-	-	-	-

There was no steam explosion observed under the experimental conditions of all the five tests. Generally, it was observed that the melt superheat and water subcooling have significant effects on melt jet fragmentation phenomena [14] and debris bed characteristics [15].

---

[4] Weber number, *We*, is a dimensionless group that occurs in the analysis of bubble formation and other interfacial phenomena. It is equal to fluid density times square of velocity times characteristic dimension divided by interfacial surface tension. It represents the ratio of inertial force to surface tension force.

3.4.1. Melt jet fragmentation

From the overall view of GoPro camera as shown in Figure 3.21, it is hard to clearly identify the melt coolant interactions due to presence of large vapor cloud around the melt jet, although an outer shape including melt jet and the vapor pocket can be recognized. Moreover, a closer look through the high-speed camera, as shown in Figure 3.22a, provides the information of the fragments being stripped from the melt jet and forming a cloud of fragments around the jet. A similar observation was made in our previous work using CFD simulation as shown in Figure 3.22b [40]. The observations indicate that the jet breakup is dominated by hydrodynamic fragmentation, due to shear stripping mechanism (Kelvin-Helmholtz instability). In the present tests, the velocity of jet entering in the water pool is between 2-3 m/s which causes significant shear forces acting between jet and water. The CFD simulation [40] also confirmed that shear stripping was mainly responsible for the breakup.

The jet breakup length estimation is considered an important parameter while studying the melt jet fragmentation. When the melt jet enters the water pool, it undergoes break up and resulting fragments detach from the melt jet. The coherent part of the jet inside the water pool, measuring from the water pool surface is determined as the jet breakup length.

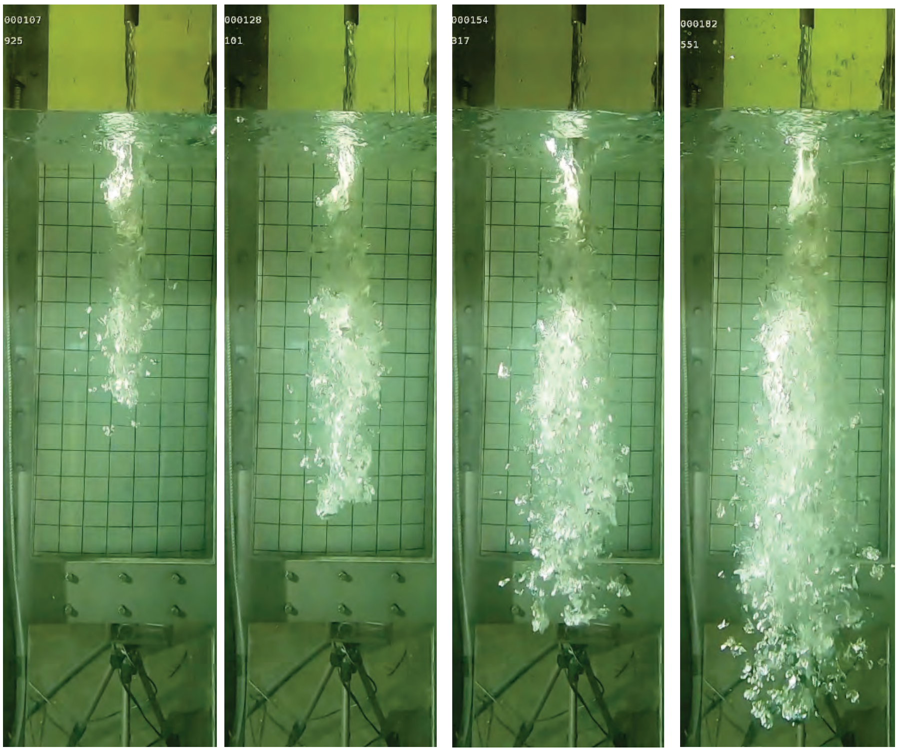

Figure 3.21: Snapshots of jet fragmentation process during the test M-L.

It is a challenging task to identify the jet breakup length through direct visualization, due to the presence of a large cloud of fragments and bubbles around the jet. Instead, two indirect methods were used to estimate the melt jet breakup length in a water pool.

In the first method, an intersection point of the extended cone of the jet spread with the extension of jet diameter is considered as the jet breakup location (Figure 3.23a). Whereas in the second method, a jet breakup is interpreted as the location where the velocity of the jet front start to decrease (Figure 3.23b). These two methods are applied to the sequence of images recorded by the high-speed camera.

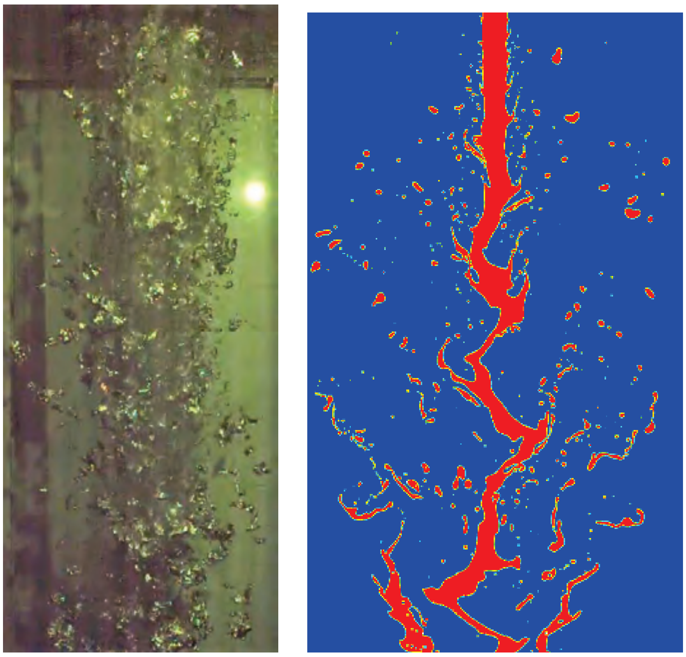

(a) (b)

Figure 3.22: Fragmentation due to stripping mechanism: (a) from the test M-L; (b) CFD simulation [40].

The estimated breakup lengths for the three respective tests of H-L, M-L and L-L using the above-mentioned two methods are provided in Figure 3.23a. In the tests M-H and M-M, partially frozen jets are observed due to medium melt superheat and high/medium water subcooling, and thus they are discarded in the estimate of jet breakup length. The jet breakup length data is containing ± 15% uncertainty in both the methods.

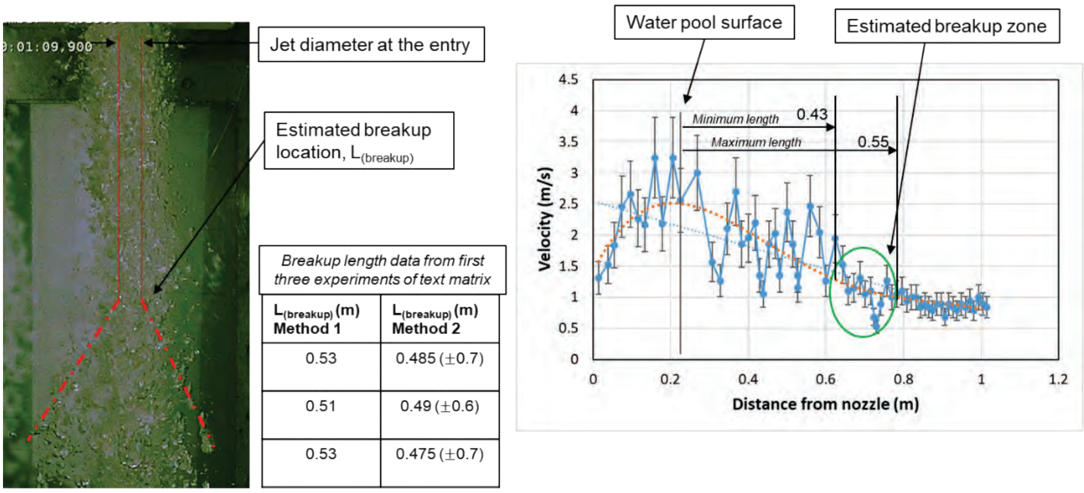

Breakup length data from first three experiments of text matrix

$L_{(breakup)}$ (m) Method 1	$L_{(breakup)}$ (m) Method 2
0.53	0.485 (±0.7)
0.51	0.49 (±0.6)
0.53	0.475 (±0.7)

(a) Method 1 (b) Method 2

Figure 3.23: Jet breakup estimation using two methods.

A generalized comparison of the present data with the existing experimental data were made in Figure 3.24 where the cloud of points represents various experimental data. It is seen from the literature that different melt materials and superheat as well as water subcooling were used by previous researchers. The different experimental conditions and measurement methods used in various experimental programs may be the causes of the diversity in jet breakup length.

Figure 3.24 also shows the comparisons with some widely used correlations [14]. The jet breakup length data from the present study is closely estimated by the Saito's correlation [41] and the Epstein & Fauske' correlation [42] with entrainment coefficient E_0=0.05, as follows:

Saito's correlation: $$\frac{L_{brk}}{D_j} = 2.1\left(\frac{\rho_j}{\rho_c}\right)^{0.5} Fr^{0.5}, \quad Fr = \frac{v_j^2}{gD_j} \tag{4}$$

Epstein & Fauske's correlation: $$\frac{L_{brk}}{D_j} = \frac{1}{2E_0}\left(\frac{\rho_j}{\rho_c}\right)^{0.5} \tag{5}$$

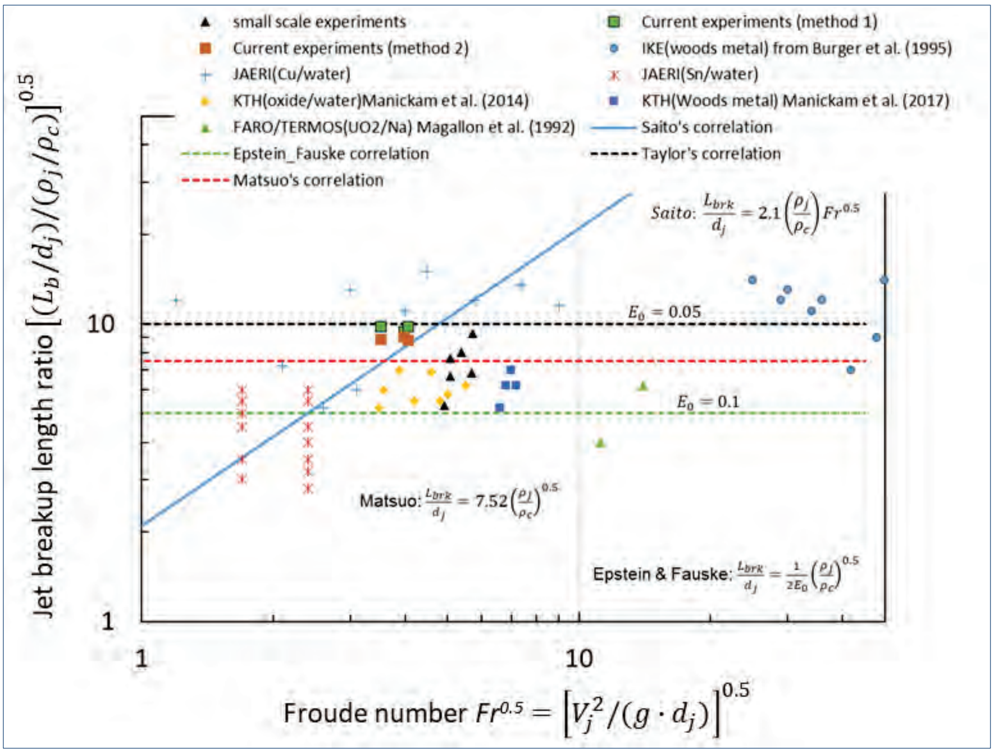

Figure 3.24: Comparisons of jet breakup lengths from experiments and correlations.

Due to the diversity in both experimental data and correlations' predictions as well as the limited data points in the present study, it is obvious and necessary that more investigations need to be done in this regard, including more test runs and using other simulants of metallic corium.

3.4.2. Debris bed characteristics

After the fragmentation of the melt jet in the water pool, the resulting debris particles will be quenched and settle on the floor of the water tank, forming a debris bed. The characteristics of the debris bed are analyzed in the present study [15].

Figure 3.25 shows the evolution of a debris bed forming from the melt-coolant interaction test L-L (low superheat of melt and low subcooling of coolant), where time zero is set as the point when the melt is discharged from the nozzle outlet. The travelling period of the jet leading edge from the nozzle outlet to the water tank bottom is 1.88s, which means that the average velocity of the initial phase is about 0.92m/s.

Solid Tin particles are found as it arrived at the bottom without further generation of steam bubbles, indicating the debris particles were fully quenched and cooled down for the first pour. Scattered particles were located on the bottom and spreading out to the periphery. Resulting from fine fragmentation and intense mixing, debris particles show a variety in size distribution and reached the side walls at 2.28s. As the coherent melt jet is penetrating through the water pool, steam bubbles are generated around the central line, forming a cloud of mixture of melt droplets and steam bubbles (see the snapshot at 2.76s). Steam bubbles are also generated and rise at the sides, leading to a clear recirculation pattern at 3.56s. This is because some debris particles of the later discharged melt remain at high temperature (over the saturation temperature of water) at their arrival at the bottom due to insufficient cooling.

Later, a conical debris bed is formed at the bottom and covered with a thick layer of steam bubbles. Following the generation of large amount of steam bubbles, the clear recirculation disappears, and the bubbles flow upward to fill in the water tank at 4.45s. Strong evaporation continues until the end of the melt discharge. The final debris bed was formed at 9.75s, which has almost the same conical angle of that at 3.56s.

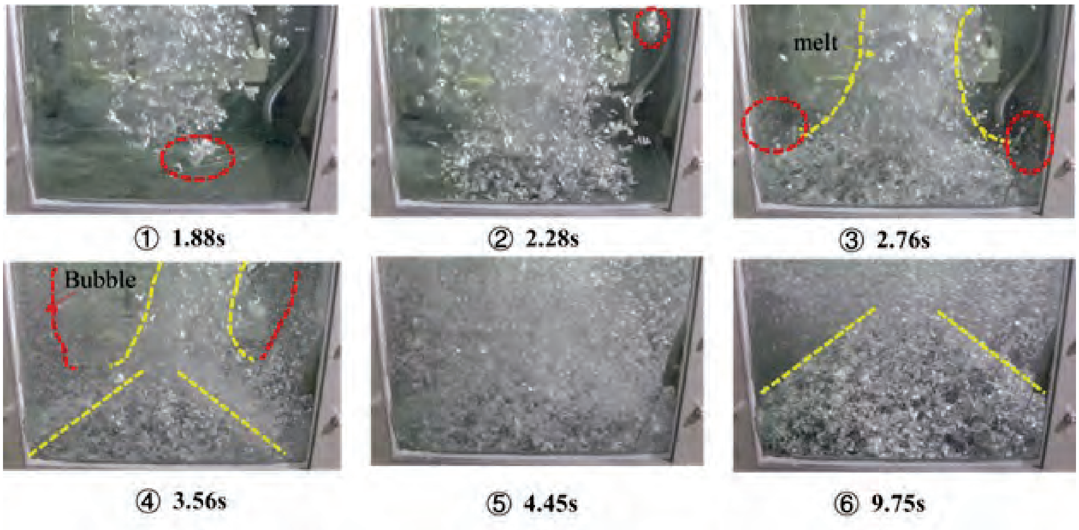

① 1.88s ② 2.28s ③ 2.76s

④ 3.56s ⑤ 4.45s ⑥ 9.75s

Figure 3.25: Snapshots of the debris bed formation process.

The temperature history of the thermocouple at the center of the debris catcher is shown in Figure 3.26. The debris temperature for the H-L test) is significantly higher than the those of the M-L and L-L tests. It took a considerable period of time for the debris bed of the H-L test) to be quenched, while the debris particles of the M-L and L-L tests were completely cooled during the sedimentation.

The debris beds of the three tests H-L, M-L and L-L are shown in Table 3.5. They are all conically shaped, and the agglomeration of debris particles is observed in the H-L case, which was also found in the DEFOR-E tests using oxidic melt [37]. The agglomeration causes the difficulty in quench. The debris beds in the M-L and L-L cases show inhomogeneity and stratification in particle sizes, with smaller particles tending to settle at the bottom while the larger ones settle at the top, as seen in the DEFOR-E tests using oxides [20]. The porosity of the debris bed from the H-L test is low due to agglomeration, but the porosity values of M-L and L-L are around 71% and 79%, respectively, which are all higher than the corresponding values of oxidic debris beds [37].

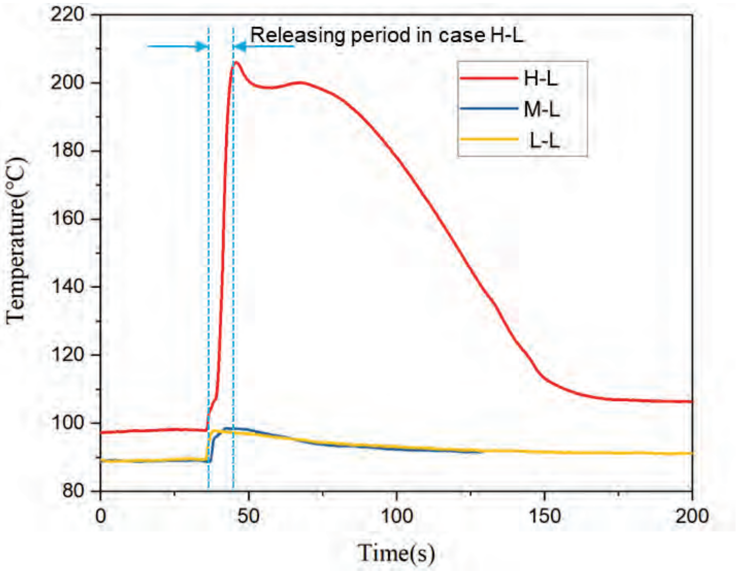

Figure 3.26: Temperature history at the center of debris beds.

Table 3.5: Comparison of debris beds

Case	Debris bed	Cross section	Particle morphology
H-L $\Delta T_m = 114$℃			
M-L $\Delta T_m = 82$℃			
L-L $\Delta T_m = 50$℃			

The movement of the particles to the peripheral region as well as fine fragmentation were driven by the coolant flow. The melt superheat has a significant influence on the morphology of debris particles. Smooth and round particles are found at high superheat while porous and flat particles are formed at low superheat. This is because in the high superheat case, the fragmented particles remain liquid droplets with surrounding film boiling for a relatively longer time during their falling in the water pool, which provides a favorable condition and time scale for surface tension to play an important role in solidification, resulting in the smooth and round particles. On the contrary, for the low melt superheat case, since the debris particles are rapidly solidified and quenched during their travelling in the water pool, the thermal stress and impact of vapor film collapse may all contribute to fragmentation of debris. The wire-like particles are observed due to ductility of metallic melt, which are quite different from the morphology of particles of oxidic melt.

Figure 3.27 shows the particle size distributions for different tests. It can be found that lower melt superheat gives rise to larger debris particles by average.

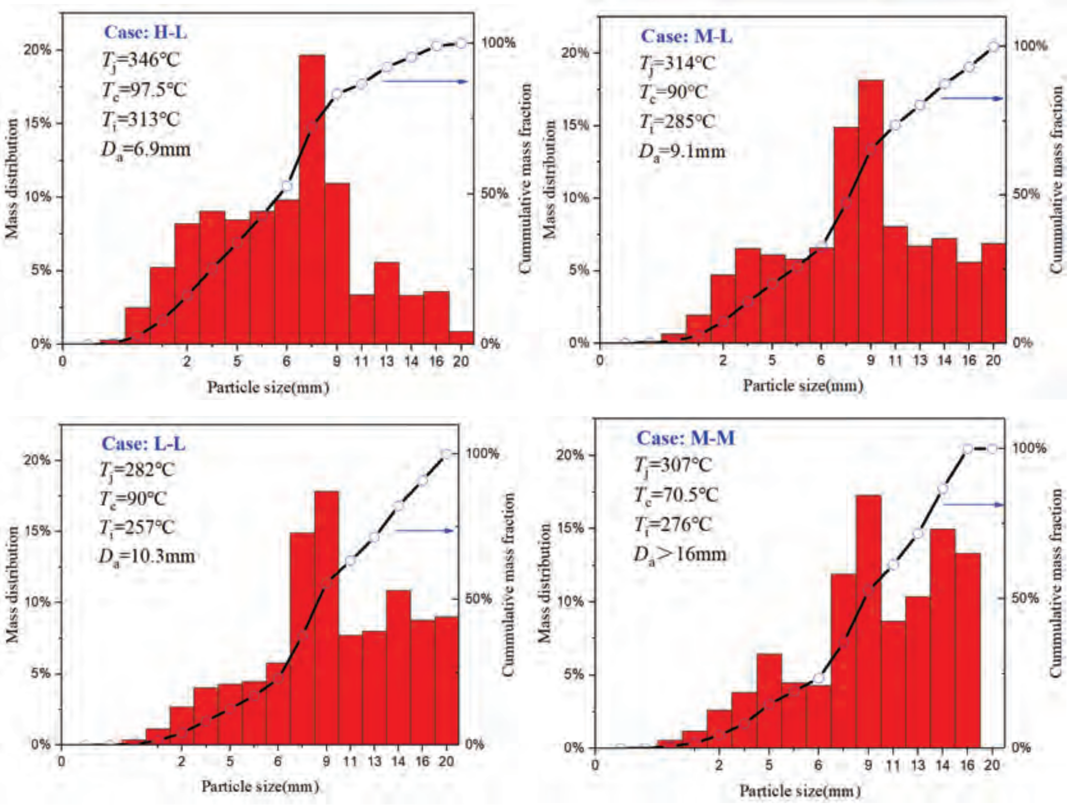

Figure 3.27: Particle size distributions.

In summary, motivated by the interest in the slump of metal-rich corium upon vessel failure during a hypothetical severe accident, five tests have been carried out to investigate the phenomena of molten Tin jets falling into a water tank, with the objective to address jet fragmentation and resulting debris bed characteristics. The preliminary finding is that the debris morphology and porosity are different from those of oxidic melt, and the metallic melt is prone to agglomerate at high melt superheat. This implies that at the same temperature, the metallic melt may help form cake which is unfavorable to melt coolability. For a concluding comprehensive understanding, more systematic tests are required with the current simulant and higher melting-point simulant of Zr/Fe, so as to build a database with a good coverage of key physics.

3.5 Development of models for deterministic analyses

Modelling and simulation are always among the cornerstones of the research at KTH/NPS, since they are the vehicles which can transfer our own understanding and developments elsewhere to reactor safety analysis. In APRI-10, new developments in modeling and simulation capabilities are as follows

- Modeling and simulation on the effect of internal radiation on natural convective heat transfer in a volumetrically heated molten pool [3].
- Advanced structural modeling of reactor pressure vessel behavior under thermal influence of corium – a work which is done in close collaboration with Solid Mechanic Department at KTH [7].
- Advanced turbulence modelling of melt pool heat transfer using Algebraic turbulent Heat Flux Model (AHFM) [16], which bears an international collaboration with NRG, Netherlands.

- Direct numerical simulation (DNS) of turbulent melt pool convection and heat transfer [17].
- Development of the lumped-parameter code transIVR for efficient assessment of in-vessel melt retention strategy of LWRs [18].
- A surrogate model is developed to predict dryout of two-dimensional debris beds, which can be employed for quick estimate of debris bed coolability, and suitable for PSA study and generation of coolability maps [19].
- The coupling of COCOMO-MEWA with RELAP5 was accomplished, and the coupled approach was employed to simulate the quenching process of the debris bed in the lower head of a BWR [20].

In total six doctoral students are contributing to the above modeling and simulation works, among which only the modeling of turbulent melt pool heat transfer are presented below. Other accomplishments have been well documented and can be found in the references.

3.5.1. Advanced turbulence modelling of melt pool heat transfer

Since the knowledge of debris bed/melt pool heat transfer in the lower head of a LWR is important information for the assessment of in-vessel accident progression as well as melt coolability and retention strategies, a large amount of research work has been conducted in this area both experimentally and numerically. For numerical simulations, the PECM and classical RANS turbulence models (e.g. k-ε and k-ω) have been applied at KTH/NPS.

This study is intended to improve the turbulence modelling of melt pool heat transfer by adding the Algebraic turbulent Heat Flux Model (AHFM) to the classical RANS equations, since the AHFM showed some advantages in the modelling of complex natural convections [43]. The goal is to implement the AHFM to the ANSYS Fluent solver through its User-defined functions (UDF), to be able to perform model validation activities.

In the classical RANS treatments, new terms occur in the equation due to the Reynolds decomposition which are Reynolds stress term $\overline{u_i'u_j'}$, and turbulent heat flux term $\overline{u_i'\theta'}$. More equations are required to close the equation set. Eddy-Viscosity Model (EVM) is generally used for the closure of Reynolds stress $\overline{u_i'\theta'}$ which uses the Boussinesq hypothesis and has following expression.

$$\overline{u_i'u_j'} = -\upsilon_t(\frac{dU_i}{dx_j} + \frac{dU_j}{dx_i}) + 2/3k\delta_{i,j} \tag{4}$$

This method is widely applied with various EVM models such as *k-ε*, *k-ω*, etc. One alternative to the EVM is the Reynolds Stress Model which will introduce more PDEs to describe $\overline{u_i'u_j'}$.

Analogy is taken to the description above to close the turbulent heat flux term which is then called Eddy Diffusivity Model (EDM) and has following expression.

$$\overline{u_i'\theta'} = -\frac{\upsilon_t}{\mathrm{Pr}_t}\frac{d\theta}{dx_i} \tag{7}$$

The Algebraic Heat Flux Model (AHFM) is chosen as an alternative to the EDM with the aim to improve the turbulence model performance in molten pool natural convection.

In the AHFM, turbulent heat flux terms are explicitly expressed as follows,

$$\overline{\theta' u_i'} = -C_{t0}\frac{k}{\varepsilon}\left(C_{t1}\overline{u_i'u_j'}\frac{\partial T}{\partial x_j} + C_{t2}\overline{\theta' u_j'}\frac{\partial U_i}{\partial x_j} + C_{t3}\beta g_i\overline{\theta'^2}\right) + C_{t4}a_{ij}\overline{\theta' u_j'} \tag{8}$$

where the new term $\overline{\theta'^2}$ in the above equation can be determined from following equations.

$$\frac{\partial(\rho\overline{\theta'^2})}{\partial t} + \frac{\partial(\rho\overline{\theta'^2}U_i)}{\partial x_i} = 2P_t - 2\rho\varepsilon_\theta + \frac{\partial}{\partial x_i}\left[\left(\frac{k_{con}}{C_P} + \frac{\mu_t}{\sigma_t}\right)\frac{\partial\overline{\theta'^2}}{\partial x_i}\right] \tag{9}$$

$$P_t = -\rho\overline{\theta' u_i'}\frac{\partial T}{\partial x_i} \tag{10}$$

$$R = \tau_\theta/\tau_m\,, \tau_\theta = \overline{\theta'^2}/2\,\varepsilon_\theta,\ \tau_m = k/\varepsilon \tag{11}$$

As mentioned above, the goal of this, the goal of this study is to implement the AHFM into the solver ANSYS Fluent through its User-defined functions (UDF), and then perform model validation against three flow problems: Rayleigh-Bernard convection [44], an internally-heated layer, and the BALI experiment [45].

Rayleigh-Bernard Convection (RBC): This refers to natural convection that is heated from the bottom surface and cooled from the top surface. A 2D 1×8 channel flow was considered. Periodic boundary was applied to the side boundaries by setting to zero mass flow rate with $Ra = 10^5$ and $Pr = 0.025$ at average bulk temperature $(T_{top} + T_{bottom})/2$. Calculations are executed for the steady-state case. Figures 3.29a and 3.28b show the velocity fields from the AHFM and the original k-ε model, respectively. The Rayleigh-Bernard convection cells are observed in both models. Figure 3.29 shows the vertical temperature profiles of the AHFM and the original k-ε models, together with DNS result [46]. Generally, the results from both models agree well with that of DNS.

Internally Heated Layer (IHL): This refers to flows that contain volumetric heat sources. Natural convection could form due to the heat source and cooling boundaries. An 1×8 computational domain was considered, with $Ra = 5 \times 10^6$ and $Pr = 7$ for which DNS data are available [47]. Figure 3.30 show the velocity fields from the AHFM and the original k-ε model, respectively. Cold plumes are observed in both models which is a reasonable expectation in such a internally heated natural convection: the fluid is heated by the internal heat source, arising to the top where it is cooled by the top surface, and then the cooled fluid would fall down. In the AHFM three cold plumes are observed, while in the original k-ε model there are four cold plumes. This indicates that the convection cells in the AHFM are wider than those in the original k-ε model. The maximum velocity in AHFM is 0.05344 m/s, which is higher than 0.0479 m/s in the original k-ε model. Figure 3.31 shows the vertical temperature profiles of the AHFM, the original k-ε model as well as the DNS result [47]. The temperature distributions of the AHFM, the original k-ε model and DNS generally agree with each other, except that DNS data shows slightly larger bulk region.

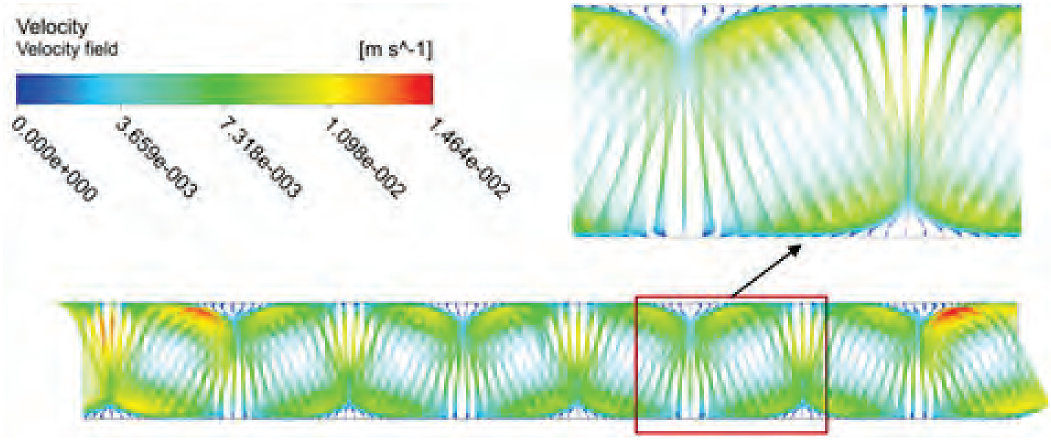

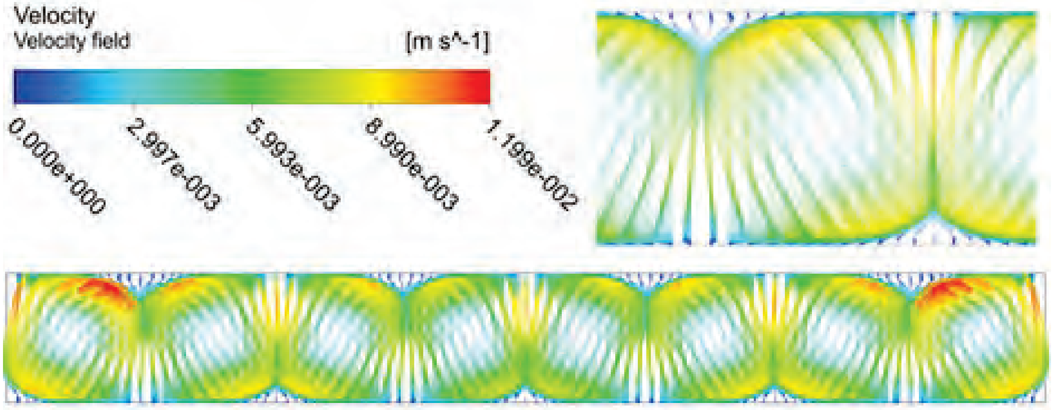

Figure 3.28: Velocity fields of the RBC: (a) AHFM, (b) k- ε model.

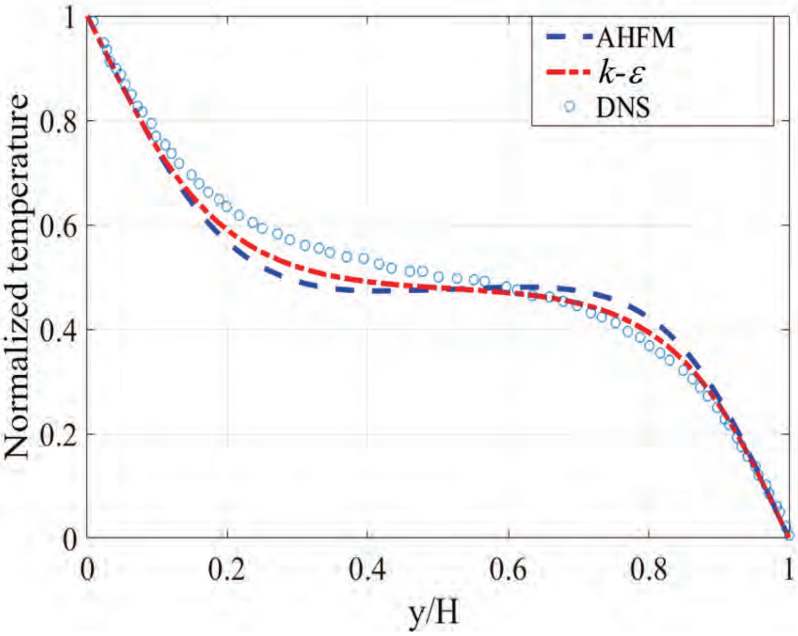

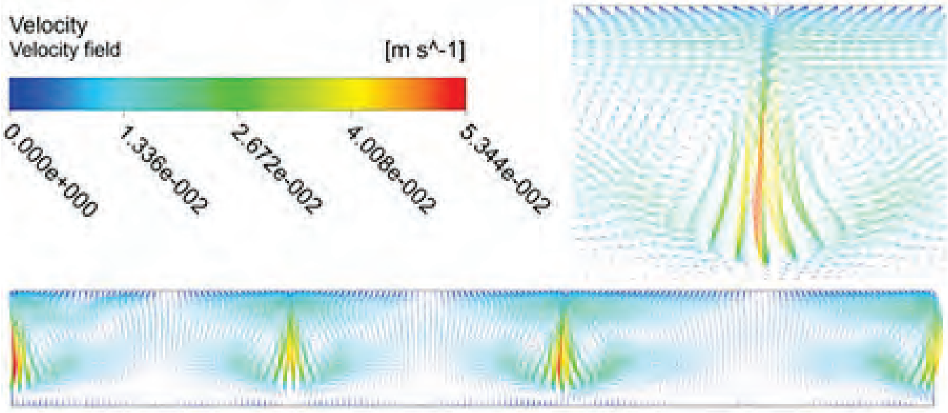

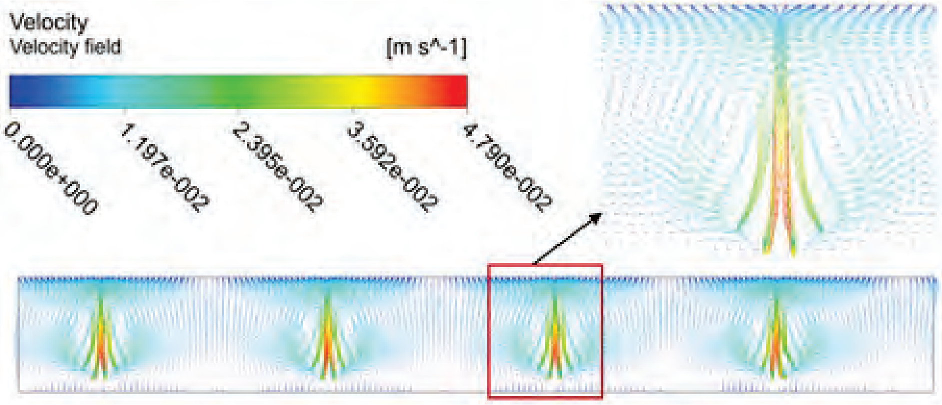

Figure 3.30: Velocity fields of the IHL: (a) AHFM, (b) k-ε model.

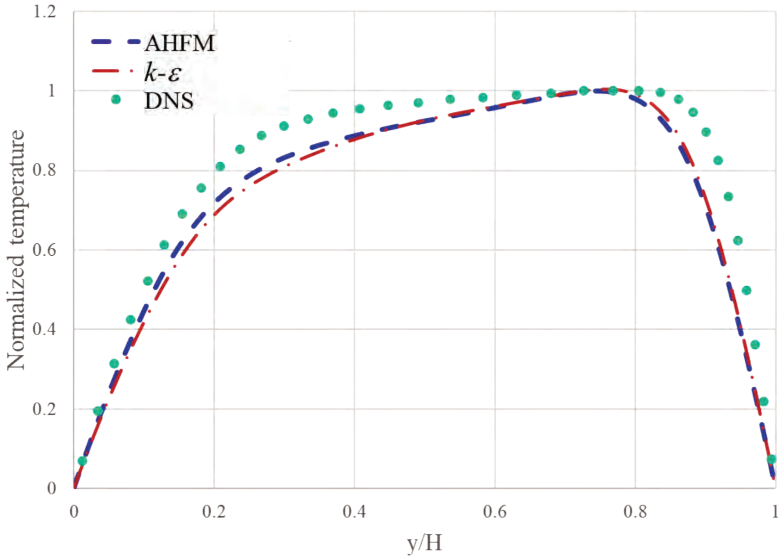

BALI Experiment: This experiment [45] was designed to investigate the internally heated natural convection of a pool in a slice geometry of an RPV lower head with a Rayleigh number up to 10^{16-17}employing water as melt simulant. The pool had a width of 2 m and a thickness of 0.15 m. The mesh of simulation was generated in hexahedron cells with well-resolved near wall region (Y+<1). Considering the liquid nitrogen cooling on both top and curved walls, constant temperature of 263 K was applied as boundary conditions to both walls in simulation. A volumetric heat source of 48.9 kW/m^3 was assumed for the simulation. Figure 3.32 compares the temperature fields of the results using the $k - \omega\ SST$ model and the AHFM. Both results show thermal stratification which is an expected phenomenon for such a natural convection study. Figure 3.33 compares the velocity fields between the $k - \omega\ SST$ model and the AHFM. In the upper region, convection cells are observed in both models while no significant convection cell is shown in the lower region. This is also consistent with the observation in experiment [45]. Figure 3.34 shows the heat flux distribution along the vessel. The results from an additional simulation using standard k-ε is also included as a classical RANS model for comparison purpose. Generally the results predicted by all models have a similar agreement with experimental data.

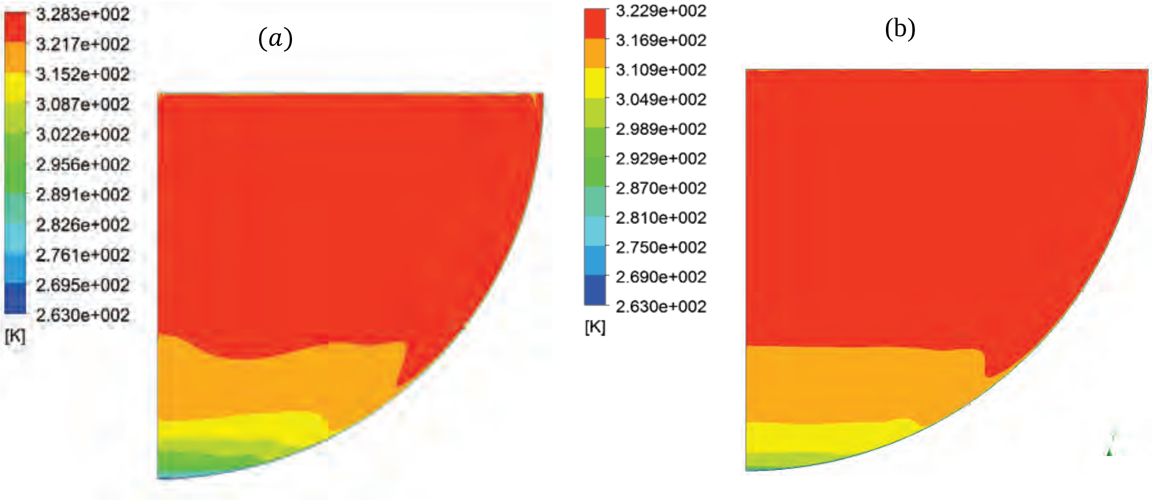

Figure 3.32: Temperature fields of BALI: (a) SST, (b) AHFM.

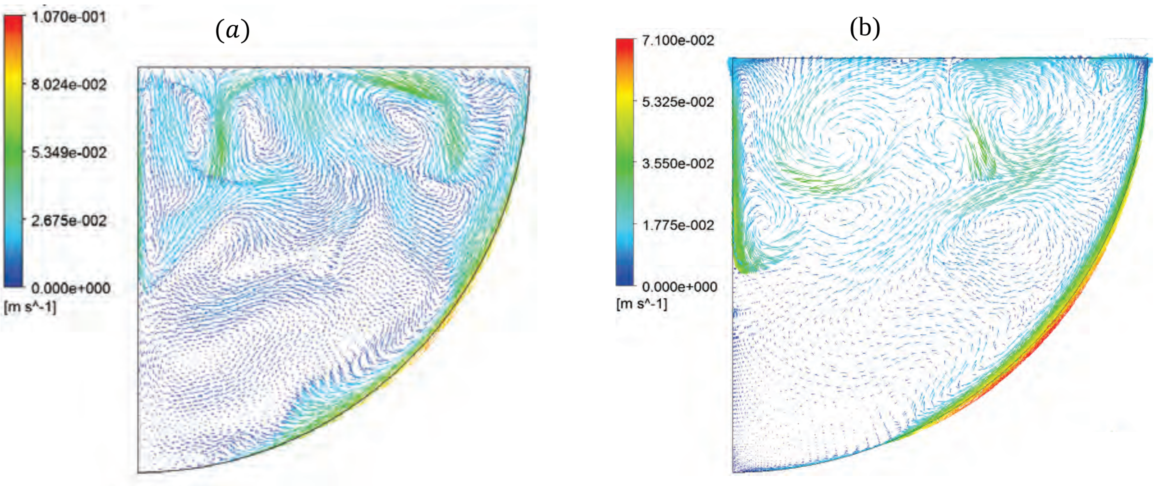

Figure 3.33: Velocity fields of BALI: (a) SST, (b) AHFM.

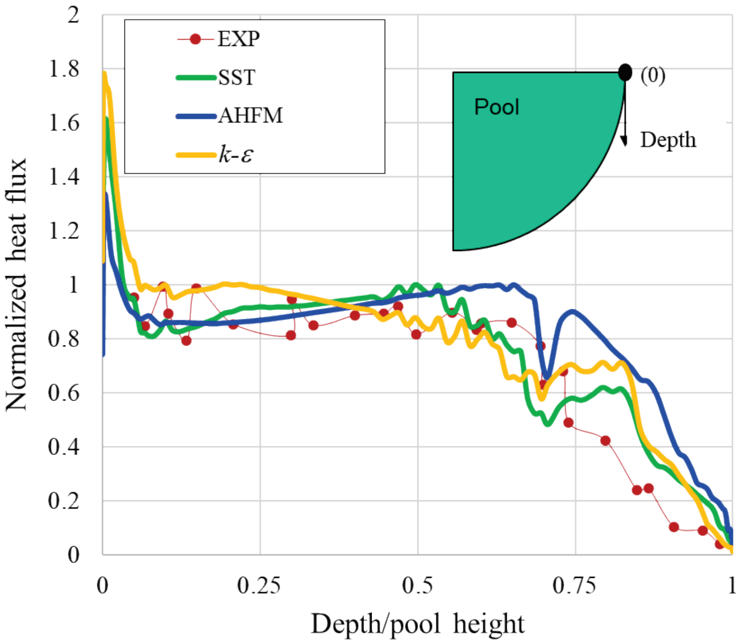

3.5.2. DNS simulation of molten pool convection

One of the remaining challenges in numerical simulations, , such as PECM and various turbulence models including Reynolds Averaged Navier-Stokes (RANS) and Large Eddy Simulation (LES), is rooted in the approximations of governing equations for the internally heated melt pool convection at very high Rayleigh number (Ra) up to 10^{16}~10^{-17} in a prototypical case.

To avoid such limitation of numerical simulations, Direct Numerical Simulation (DNS) is applied on a homogeneous oxidic molten pool in a scaled-down geometry of the SIMECO-2 facility using Nek5000. Nek5000 is a fast and scalable high-order solver for CFD with spatial discretization based on the spectral element method and massively-parallel high-performance computing.

To verify the nondimensional governing equations and the numerical implementation, the known calculation of an internally heated 3D box [48] is reproduced. As shown in Figure 3.35, a Dirichlet thermal boundary ($T = 0$) is specified on the top and bottom walls and periodic boundaries are set on the sides. Table 3.6 summarizes the comparison of the results. Two important quantities are compared: $\langle T \rangle$ – the time and volume averaged temperature, indicating the reduction of temperature by convection; $\langle wT \rangle$ – the time and volume averaged convective transport, quantifying the asymmetry of the heat transport due to buoyancy force. An excellent agreement is obtained for both quantities.

After the verification work, a ¼-scaled SIMECO-2 test was simulated by DNS. The original SIMECO-2 has $Ra \approx 10^{15}$, which is unaffordable with our current computational resources. Hence, a ¼-scale of the test section is assumed in the present study, leading to a reduced $Ra = 6.54 \times 10^{11}$. The Prandtl number remains the same, i.e. 3.11. In the modelling, a uniform heat source is applied with fixed thermal boundaries specified on the top and curved walls while an adiabatic condition is set on the front and back walls. The density variation is based on Oberbeck-Boussinesq approximation [44].

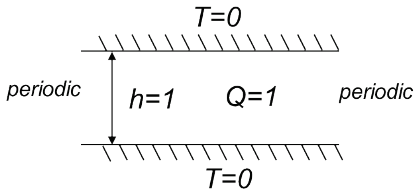

Figure 3.35: Schematic of the domain in the verification cases.

Table 3.6: Comparison results of the verification cases

	Parameter	Present study	Goluskin & van der Poel [48]
$Ra = 1 \cdot 10^6$ $Pr = 1$	<T>	0.0548	0.0547
	<wT>	0.114	0.117
$Ra = 2 \cdot 10^6$ $Pr = 1$	<T>	0.0490	0.0490
	<wT>	0.125	0.135
$Ra = 1 \cdot 10^8$ $Pr = 1$	<T>	0.0260	0.0258
	<wT>	0.205	0.208
$Ra = 2 \cdot 10^8$ $Pr = 1$	<T>	0.0225	0.0225
	<wT>	0.217	0.0222

Table 3.7 provides some simulation parameters. Near the top wall of the computational domain, the thermal and kinetic boundary layer thicknesses are estimated using the Grossman & Lohse's Rayleigh-Bénard Convection (RBC) regime map [49]. The mesh size in the bulk also satisfies the Kolmogorov length-scale requirement.

Table 3.7: Simulation parameters for the scaled-down SIMECO-2

Rayleigh number	6.54×10^{11}
Prandtl number	3.11
Total number of elements	45500
Polynomial order	9
Total number of grid points	45.5 Million
Target CFL	3.6
Maximum timestep [-]	1×10^{-6}

Figures 3.36 and 3.37 show a quasi-steady solution of temperature and velocity distributions on a XZ-plane, respectively. The qualitative thermo-fluid behavior of the molten pool shows similarities with the general flow observations from the BALI experiment [37]. In particular, there is a clear separation between the upper and lower parts of the fluid domain. In the upper part, turbulent Rayleigh-Bénard Convection (RBC) cells are observed where fluid is heated and goes up, and then cooled by the top and descends. In the lower part, flow is mainly propelled by weak shear forces and temperature field is characterized by thermally stratified layers. In addition, flow descends along the curved wall which is known as the ν-phenomenon [50] and this can be clearly seen in Figure 3.38 (blue spots on the sides that ends at z=0.25).

In summary, motivated to improve the fidelity of models and simulations, a DNS and a modified RANS modeling with AHFM have been developed at KTH/NPS to simulate turbulent natural convection of internally heated melt pools. The AHFM approach did not show much too much advantage over the classical k-ε and SST, probably due to the usage of water instead of melt in the pool. In this regard, further validation can be done against melt pool experiments (e.g. COPRA or LIVE) which employed binary nitrate salts as corium simulant. A scrutiny is also needed for the constants of the AHFM. The preliminary results of the DNS are promising, but a lot of work is still needed to reach such an extent that either reveals key physics or resolve issues in melt pool convection. Hence, the development of both AHFM and DNS at KTH/NPS is still at the premature stage and calls for more research efforts in future.

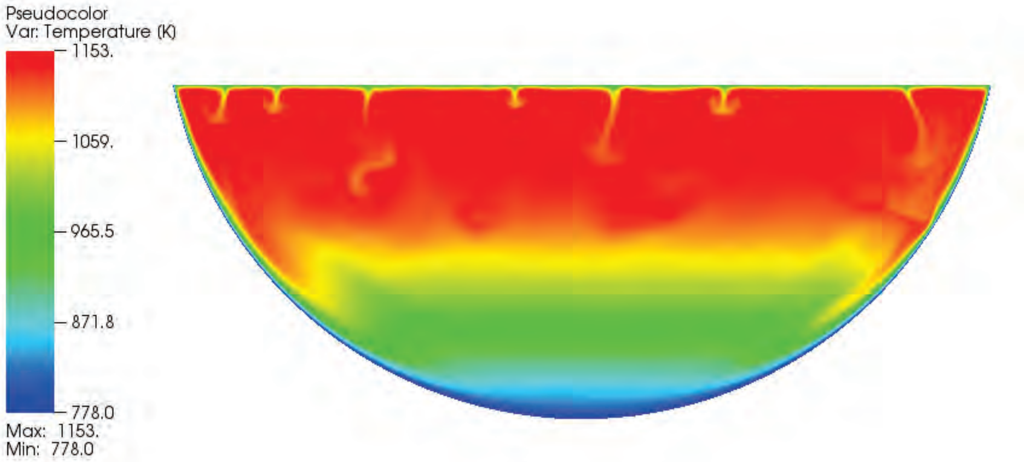

Figure 3.36. Temperature distribution in melt pool (front middle plane - ZX).

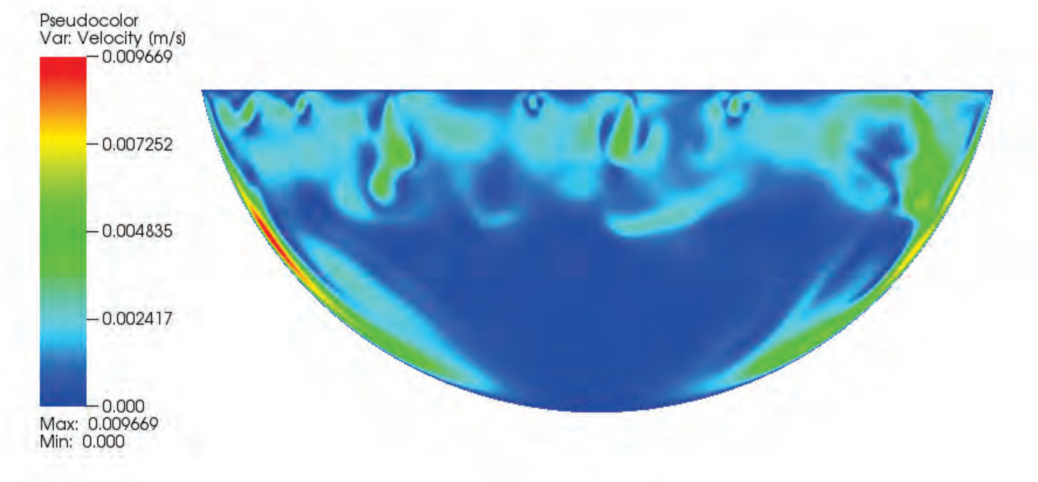

Figure 3.37: Velocity distribution in melt pool (front middle plane - ZX)

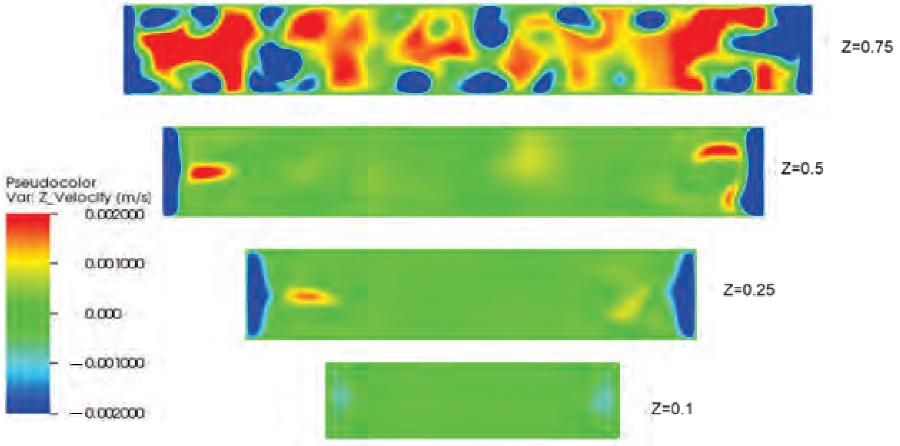

Figure 3.38: z-component velocity distribution on different XY planes.

3.6 MISTEE experiment toward prototypical materials

MISTEE (Micro-Interactions in Steam Explosion Experiments) platform was developed to pursue a basic understanding of micro-interactions in steam explosion phenomena, with the goal of identifying mechanisms which may limit the explosivity of molten corium in a severe accident scenario with fuel-coolant interactions (FCI). The MISTEE platform [21] features up-to-date instrumentation well-controlled test conditions.

The recent emphasis in the MISTEE study is upgrading the test platform toward applying prototypical compositions of corium in the experiment, to reduce the knowledge gap in material properties. Due to the restriction of handling UO_2 in the KTH/NPS laboratory, only the metallic compositions Zr and Fe of corium are considered at this stage. Different from oxidic melt, oxidation reaction of the metallic Zr/Fe melt with coolant may occur during FCI, leading to the release of reaction heat and hydrogen which affect the accident progression and severity (e.g., the reaction heat may prolong the liquid state of corium, while the non-condensable hydrogen could reduce the explosivity of corium but instead create a combustible atmosphere and increase the static pressure in the containment). Motivated by this circumstance, the investigation of the oxidation of a molten zirconium droplet in water has been carried out since APRI-9.

Based on the previous experience with Zr oxidation experiment, a significant effort is to advance the Zr/Fe oxidation experimentation in APRI-10 has been performed:

- More tests of Zr oxidation and data analysis [22], and
- New developments of the facility, including a hydrogen collector [23], Zr-Fe alloy preparation and a new furnace suitable for melting Zr-Fe [24].

Other efforts that are devoted to separate-effect studies are as follows

- Effect of materials on steam explosion [25]
- Quenching of high-temperature spheres in seawater [26]
- Effect of salinity on film boiling heat transfer [27]
- Steam explosion in seawater [28].

For the Zr oxidation study [22], a pattern of "cyclic oxidation" was observed in the high-speed images, without occurrence of any steam explosions indicating that the oxidation (and hydrogen generation) may suppress the potential for a spontaneous steam explosion, and water subcooling has a substantial effect on the oxidation process. For the study of material effects [25], the binary mixtures of oxides WO_3-CaO and WO_3-ZrO_2 which have the comparable melting point were employed in single droplet steam explosion experiments, and the results have shown qualitative similarities in steam explosion progress of the two different melt materials. It was also identified that spontaneous steam explosions were not been observed even with experimental conditions involving a high melt superheat up to 350 K and a high subcooling up to 85 K. Since these two pieces of work have been well documented and published in [22] and [25], the description below is given to other three activities: (i) oxidation of Zr-Fe alloy; (ii) quenching of spheres in seawater; and (iii) steam explosion in seawater.

3.6.1. Oxidation of Zr-Fe droplets

The test facility for Zr-Fe alloy oxidation is as shown in Figure 3.39. A 3-way valve is used to direct inert gas flow through the crucible nozzle and to isolate the furnace from the water pool. When the alloy droplet is heated to a desired melt temperature in the induction furnace, the fast-acting 3-way valve is switched to the release position to discharge the molten droplet into the water pool. The droplet temperature before entering the water pool is monitored by a fast-responding two-color pyrometer. The water pool has a transparent wall for visual recording with a high-speed camera.

In the Zr oxidation experiment [22], the amount of hydrogen generated during the quenching of a droplet was estimated by image processing of non-condensable bubbles (Figure 3.40a) and SEM analysis of the resulting debris particle. To improve the measurement accuracy, a subsystem is added to collect the hydrogen produced from Zr-Fe alloy oxidation. The hydrogen collecting system is composed of a dual nozzle quartz cover, a graduated cylinder and connecting pipes, as shown in Figure 3.40b. The cover was designed to match the tank opening size (150mm×100mm) and the location of the side nozzle was aligned under melt discharging tube. The graduated cylinder (100*ml* with graduation of 1*ml*) fully filled with water prior to experiment is used as a final storage container for rising hydrogen bubbles.

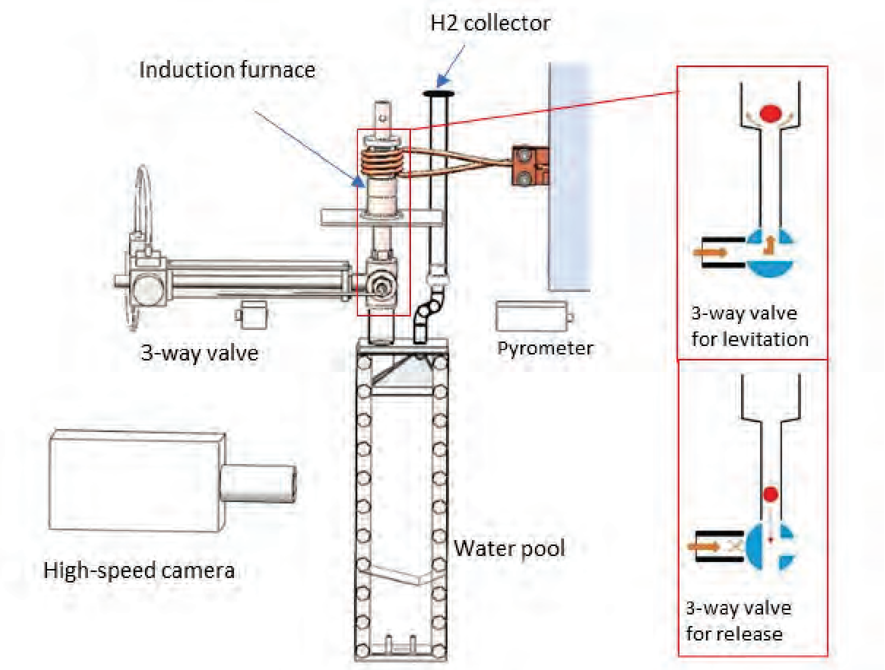

Figure 3.39: Schematic of the MISTEE facility for Zr-Fe oxidation tests.

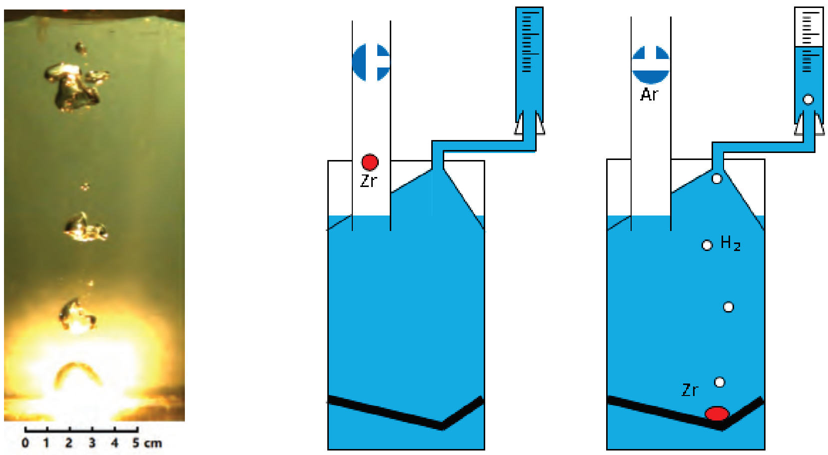

(a) (b)

Figure 3.40: Hydrogen production and collecting system.

A new furnace with double crucibles (Figure 3.41) was developed to replace the old furnace which had a single crucible that was previously employed in the MISTEE for molten oxide or Zr droplet tests. The new furnace was motivated by the fact that contamination of carbon was observed when the old furnace with graphite crucible was used to melt Zr-Fe mixture sample, as shown in Figure 3.42, while it was well-functioning for pure Zr droplet tests. In the double-crucible furnace, the outer crucible is made of graphite to generate heat by induction and the inner crucible is made of refractory materials to minimize sample contamination from the crucible.

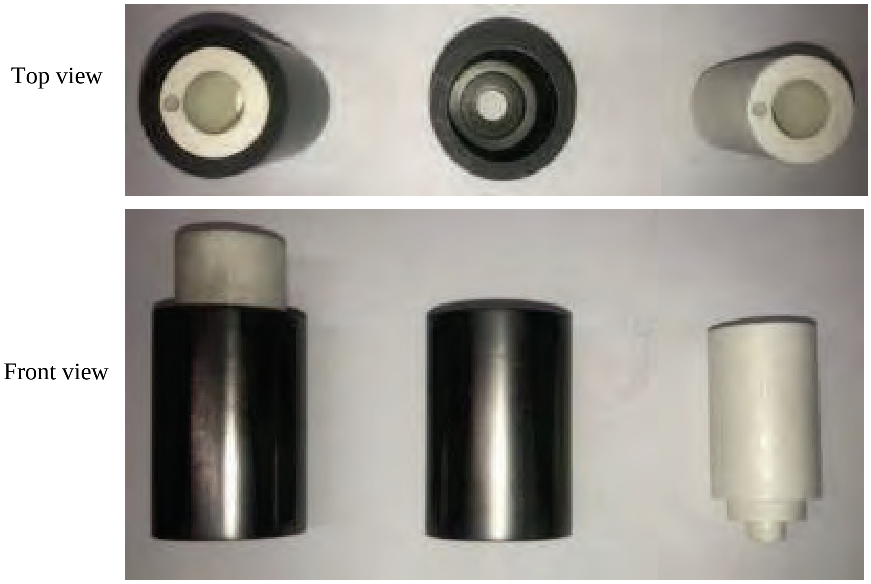

Figure 3.41: Pictures of arrangement of double crucibles for the new furnace.

For the inner crucible, several high-temperature resistant materials including BN, SiC, Al_2O_3 and MgO, have been tested, and MgO was finally selected due to its low material interaction between molten Zr-Fe alloy and the crucible. In Figure 3.43, the SEM results indicated that the elements O and Mg were rarely dissolved in the alloy and the influenced layer of the crucible was within ~10um.

It should be noted that the proper preparation of Zr-Fe mixture to be loaded in the furnace plays an important role in forming a well-mixed droplet. Three methods had been tested to prepare Zr-Fe mixture melt with the desired composition, as shown in Table 3.8. It was found that (a) the first method to make tablets from Zr and Fe powder is complicated, since the powder has a high risk to be partially oxidized during mixing, processing and storage, (b) the second method to melt the Zr and Fe pellets tends to form inhomogeneous mixture, and (c) the third method to order the customized alloy with a proper composition of Zr and Fe is proven to be the best to meet the requirement, i.e. forming a droplet of uniform composition.

Table 3.8 also shows the photos of refrozen samples prepared using the different methods. A composition examination of the customized alloy by SEM confirmed that the measured percentage of Zr and Fe in the alloy ($Zr_{0.72}$-$Fe_{0.28}$) is close to the expected composition ($Zr_{0.75}$-$Fe_{0.25}$), and no other impurity elements were detected except for O and Hf (~0.5%) which also exist as trace in the Zr pellets). All the elements were uniformly distributed in the alloy.

Due to the remaining difficulty of melt delivery, so far only 10 successful tests have been carried out under the experimental conditions as shown in Table 3.9.

Table 3.8: Effects of Zr-Fe alloy preparation on melting

Methods for preparation of Zr-Fe alloy	*Frozen sample of Zr-Fe alloy after melting*
(a) Pressing mixed Zr/Fe powder for tablet 	partially oxidized melt (remains in crucible) 

(b) Melting of mixed Zr and Fe pellets Zr 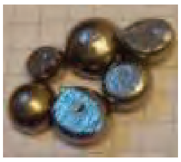 Fe 	not well mixed (remains in crucible) 
(c) Ordering of customized Zr-Fe alloy 	well-mixed Zr-Fe alloy (desired droplet) 

Table 3.9: Test matrix for oxidation of molten Zr-Fe droplets

Composition	Coolant temperature/°C	Subcooling of coolant (°C)	Melt temperature (°C)	Superheat of melt (°C)	Runs of tests
$Zr_{0.72}Fe_{0.28}$	20, 50	80,50	1200	150	7
$Zr_{0.07}Fe_{0.93}$	20	80	2000	660	3

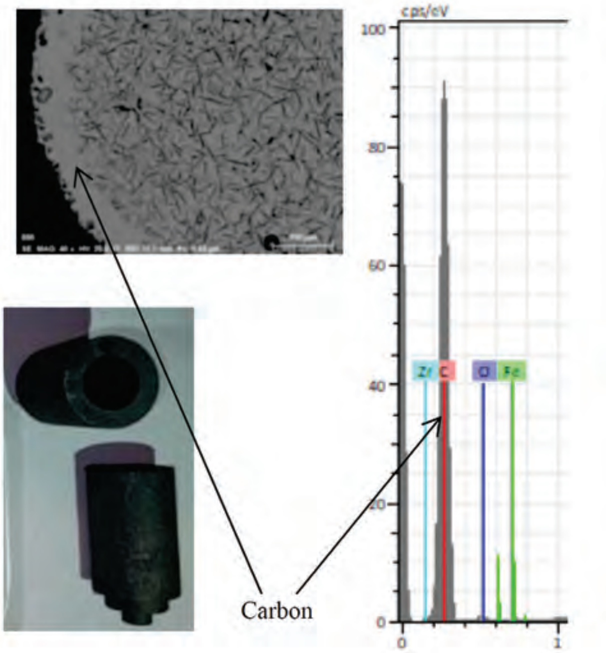

Figure 3.42: Composition of a refrozen Zr-Fe sample prepared by the old furnace.

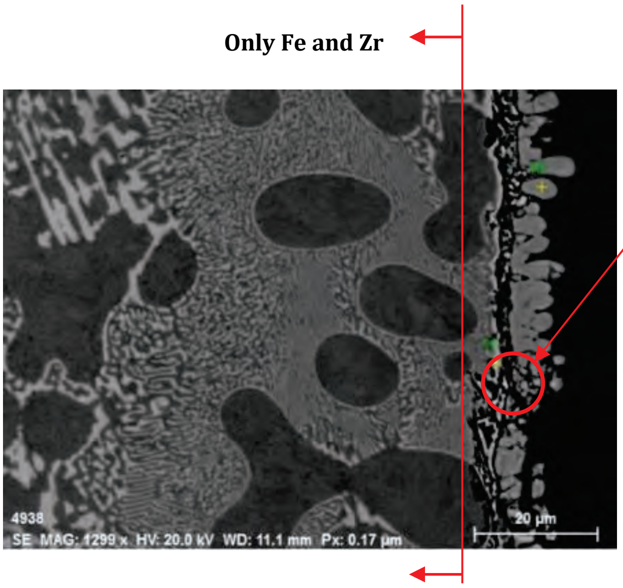

```
Element    Atom. C
             [at.%]
---------------------
Iron          77.09
Zirconium     17.91
Oxygen         4.94
Magnesium      0.06
----------------------
    Total:   100.00
```

Figure 3.43: Composition of a refrozen Zr-Fe sample prepared by the new furnace.

Figure 3.44 illustrates the snapshots of a test recorded by the high-speed camera. The hydrogen bubbles are collected by the newly added collector as expected, so that the total volume of hydrogen production during the quenching of a Zr-Fe droplet can be quantified with more certain accuracy. Theoretically, the bubbles reaching the collector are likely to be composed of hydrogen, steam and argon trapped by the droplet. However, the collector was cooled to room temperature, so the steam can be excluded. Compared with the total gas volume in the collector, the trapped argon should be negligible – to verify this hypothesis in future, tests with a chemically inert material should be performed to assess the amount of argon that is trapped in the vapor film.

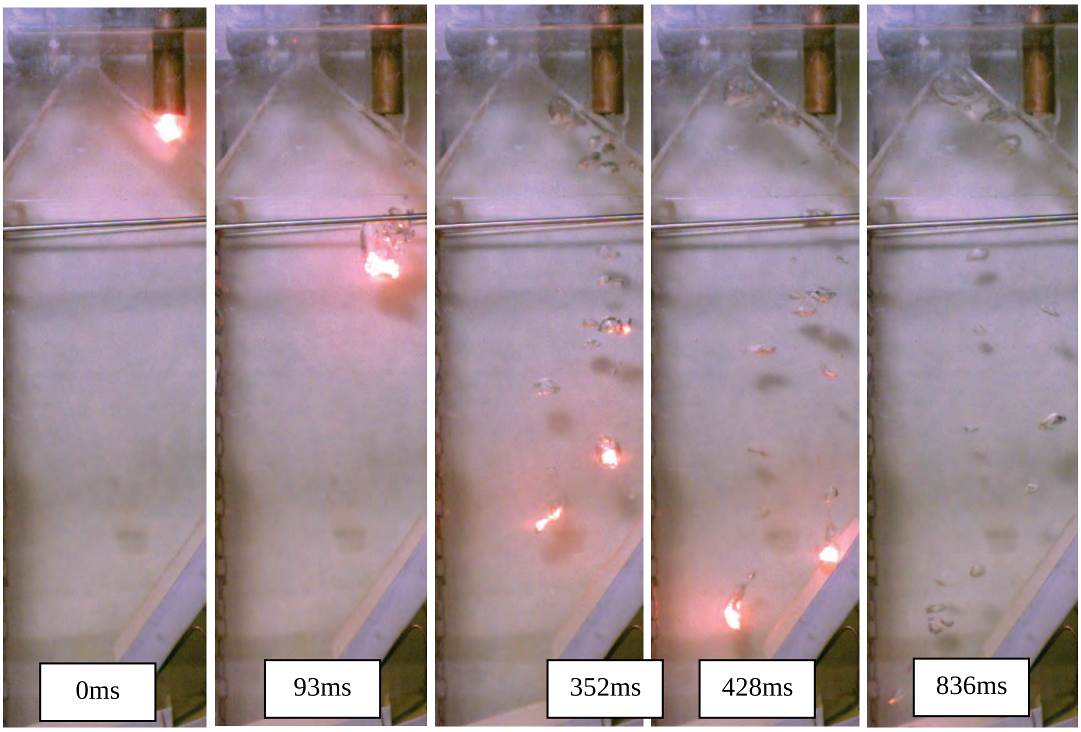

Figure 3-44: Snapshots of the process of $Zr_{0.72}Fe_{0.28}$ *droplet* ($\Delta Tsup \approx 150K$) *quenched in water* ($\Delta Tsub \approx 80K$).

A calibration of the hydrogen collector using air bubbles [23] indicated that the measurement error can be limited to 5%, which is significantly reduced from errors in the previous approach – image processing of bubbles. Nevertheless, the image processing approach is still employed to provide transient information of hydrogen generation rate which is important to further reveal kinetics of reaction between metallic phase and surrounding vapor.

Figure 3.45 shows the hydrogen volume per gram of melt generated from repeating tests using $Zr_{0.72}Fe_{0.28}$ alloy droplets at 1230 °C. Similar to the previous tests using pure Zr droplets [22], the water subcooling has an effect on the oxidation of the melt during the quenching of the droplets at the same temperature (1230°C), and the lower subcooling brings a higher oxidation ratio to the melt.

Figure 3.46 shows the hydrogen volume per gram of melt generated from repeating tests using $Zr_{0.07}Fe_{0.93}$ alloy droplets at 2000 °C. A comparison with the Zr oxidation shows that the hydrogen production is much less in the alloy.

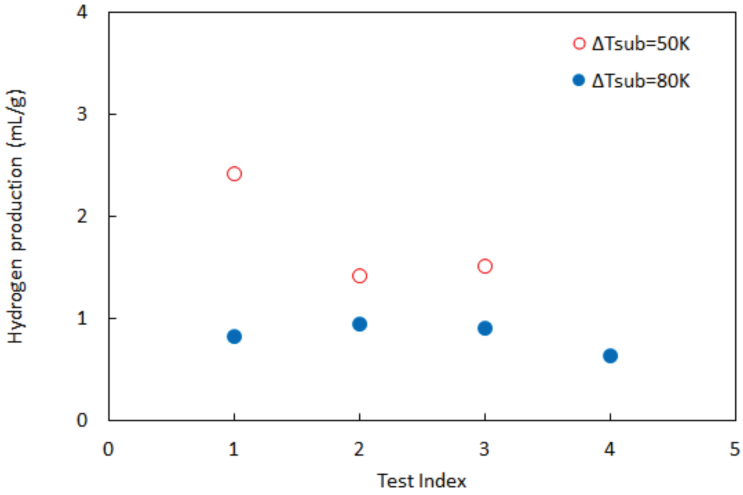

Figure 3.45: Effect of water subcooling on H_2 production ($Zr_{0.72}Fe_{0.28}$, T_{melt} =1230℃).

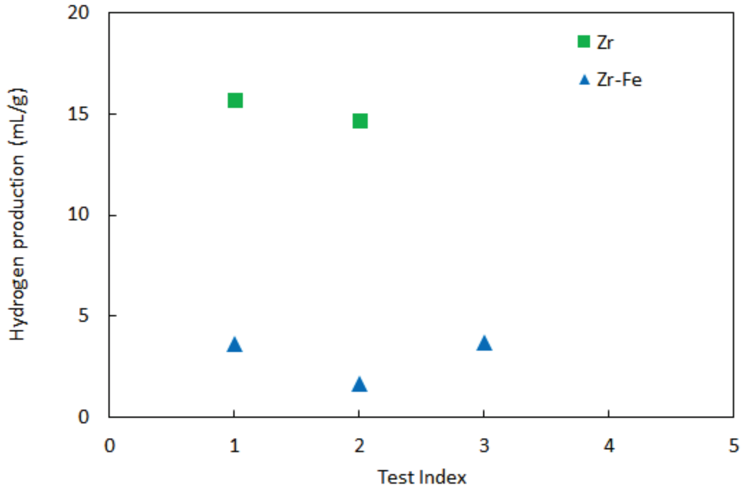

Figure 3.46: H_2 production of Zr and $Zr_{0.07}Fe_{0.93}$ oxidation (T_{melt}=2000℃, ΔT_{sub}=80℃).

In summary, the MISTEE facility has been updated to perform single droplet steam explosion experiment using the Zr-Fe alloy as corium composition. Some interesting data have been obtained, but more tests (including verification of repeatability) are needed in the future (i.e. in APRI-11) to make a solid conclusion.

3.6.2. Quenching of spheres in seawater

Motivated by quenching of melt droplets and debris particles in seawater during a hypothetical severe accident of light water reactors (LWRs), the quenching process of stainless-steel spheres in a seawater pool was investigated in the present study. The polished spheres were pre-heated up to 1000℃ in an induction furnace with inerted atmosphere (flushed with argon gas), and then immersed into a subcooled water pool in a chamber made of transparent quartz. A thermocouple was embedded in the center of the sphere to measure the history of the sphere's temperature, while a high-speed camera was employed to record the quenching process and vapor film dynamics. Quantitative data (e.g. film thickness and oscillation) of the vapor film evolution during the quenching process were obtained through image processing program developed in MATLAB.

Figure 3.47 shows the schematic of the experimental setup (aka MISTEE-SQ) employed to investigate the quenching phenomenon. The experimental setup consists of six parts: (1) the induction furnace where a stainless-steel sphere was heated in inerted atmosphere (flushed with argon gas) to a prescribed temperature; (2) the linear motion slide rail which held the sphere in desired positions through a sheathed thermocouple whose tip was fixed in the center of the sphere; (3) the transparent quartz cubic chamber which was placed under the furnace and filled with water for quenching the sphere; (4) the visualization system equipped with a high-speed camera; (5) the lighting system; and (6) the data acquisition system (DAS) for the temperature measurement. A thermocouple was inserted into the center of the sphere to hold the sphere and monitor its temperature. All spheres in the present study were made of stainless steel with the diameter of 15 mm; moreover, they were all polished using the same protocol to ensure consistent surface conditions. During the experiment, the sphere was heated to 1000 ^{o}C in the furnace at the location of 30 mm above the water level, and then inserted in the water pool at the velocity of 1.0 m/s until the location of 30 mm under the water level. Table 3.10 is the test matrix.

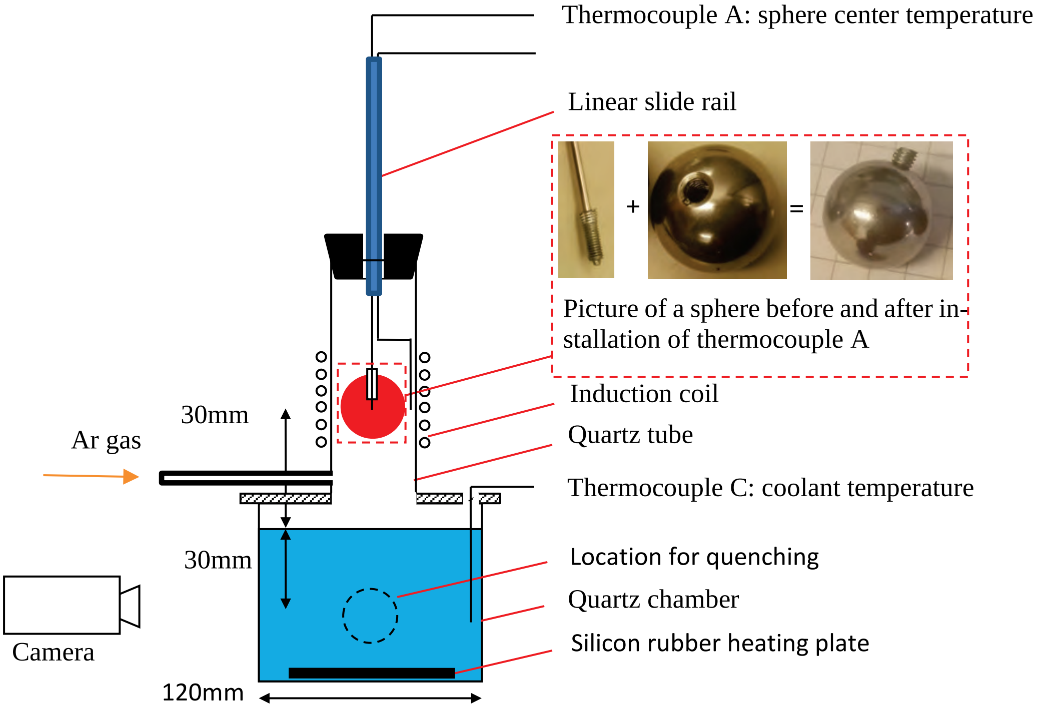

Figure 3.47: Schematic of MISTEE-Q experimental setup.

Table 3.10: Test matrix for quenching of spheres in seawater vs. DI water

Coolant	Salinity (g/kg)	Coolant temperature (°C)	Initial temperature of sphere (°C)	Number of tests
DI water	0	30-90 (±1.5)	1000 (±5)	150
Seawater	35.2±0.3	35-85 (±1.5)	1000 (±5)	148

Figure 3.48a and 3.48b show the snapshots of visualization at different phases of the quenching process, and the temperature history of a sphere-quenching test in seawater at temperature of 55 °C, respectively. The data of a corresponding test in DI water are also shown for comparison. Based on the observations, the quenching process can be divided in to six phases with distinct heat transfer characteristics: (1) immersing phase of sphere delivery; (2) vapor film formation phase at the sphere's final location in the quartz chamber; (3) film boiling phase; (4) transition boiling phase; (5) nucleate boiling phase; and (6) convection phase below the boiling point. An important observation is that the transition from film boiling to nucleate boiling was completed much earlier at higher sphere's temperature in seawater than in DI water, which means the sphere could be quenched much earlier at a higher temperature of the sphere in seawater than in DI water. In other words, one can say the Leidenfrost temperature was higher in seawater than in DI water – 106 °C higher in this case.

(a) Snapshots of visualization

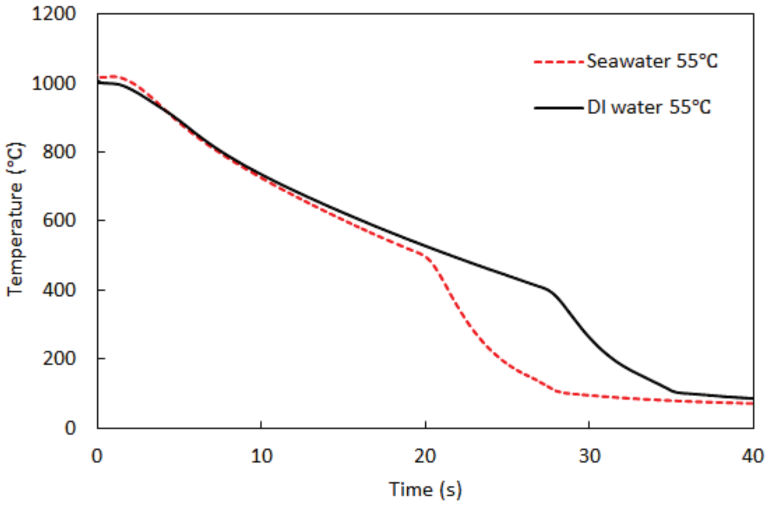

(b) Temperature at the center of sphere

Figure 3.48: Typical quenching process of high-temperature spheres in seawater and DI water.

Figure 3.49 shows the influences of coolant temperature on the quenching characteristics, based on which some important observations are as follows: (1) quenching was accelerated with decreasing coolant temperature for both seawater and DI water, but it appeared that the rate was higher in seawater; (2) both Leidenfrost temperature and minimum heat flux were higher in seawater than in DI water, and elevated by increasing coolant subcooling; (3) at low coolant temperature of 35 °C, the Leidenfrost temperature in DI water was 571 °C, corresponding to the minimum film heat flux of 240 kW/m^2, while interestingly in seawater no stable film boiling was established (see Figure 3.50), and therefore there was no Leidenfrost temperature and minimum film boiling heat flux.

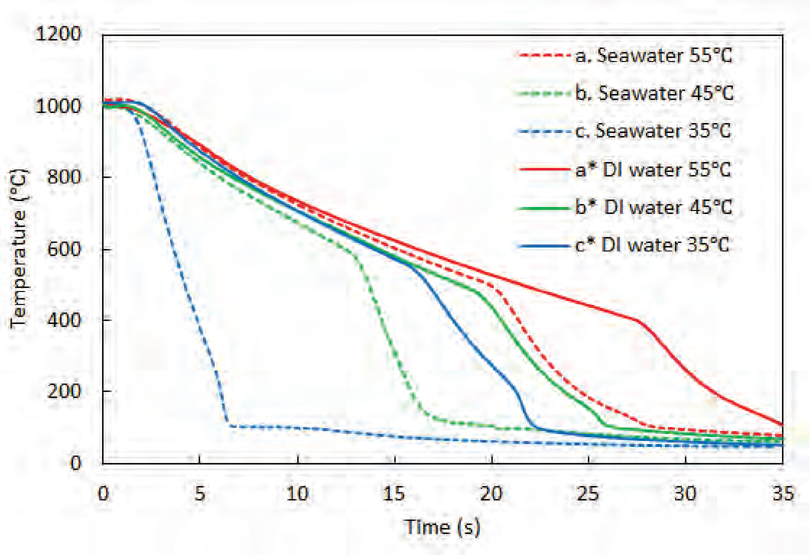

Figure 3.49: Boiling curves at different coolant temperatures.

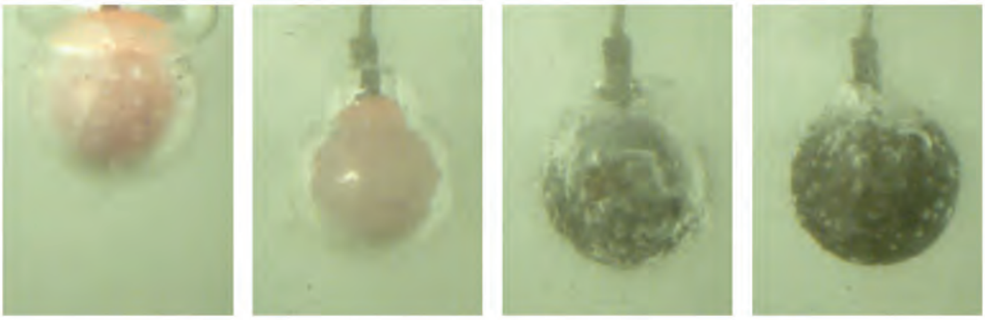

t=30 ms | t=1000 ms | t=2000 ms | t= 3000ms

Imersing phase | Transition boiling | Intensive and moderated nucleate boiling

Figure 3.50: Quenching characteristics of a sphere in seawater at high subcooling.

The influence of coolant temperature on Leidenfrost temperature was illustrated in Figure 3.51, where other relevant results were also plotted for comparison. The trends of the Leidenfrost temperatures from both seawater and DI water linearly decrease with increasing coolant temperature, and hence the empirical correlations can be respectively expressed by Eqs. (10) and (11):

$$T_{MHF} = -5.76T_l + 854.89 \;\; (seawater, 35℃ \le T_{liq} \le 85℃) \tag{12}$$

$$T_{MHF} = -3.57T_l + 602.12 \;\; (DI\ water, 32℃ \le T_{liq} \le 89℃) \tag{13}$$

The Leidenfrost temperature was significantly higher in seawater than in DI water, which means vapor film in seawater was prone to collapse and rewetting of the spherical surface was easier.

Another observation from Figure 3.51 is the scattering nature of the measured sphere temperatures at the Leidenfrost point: the standard deviations were ±65 °C and ±55 °C for respective seawater and DI water at high subcooling, and ±31 °C and ±22 °C at low and medium subcooling. Thus, the related standard deviations are within ±10%. The seemingly random behavior of the quenching process was mainly due to the involvement of multi-scale thermohydraulic mechanisms in the multifaceted boiling transition problem, which was further complicated by deposition and electrochemical reaction in seawater. A mechanistic modeling of vapor film instability under the influence of water chemistry may provide insights to understand the underlying mechanisms.

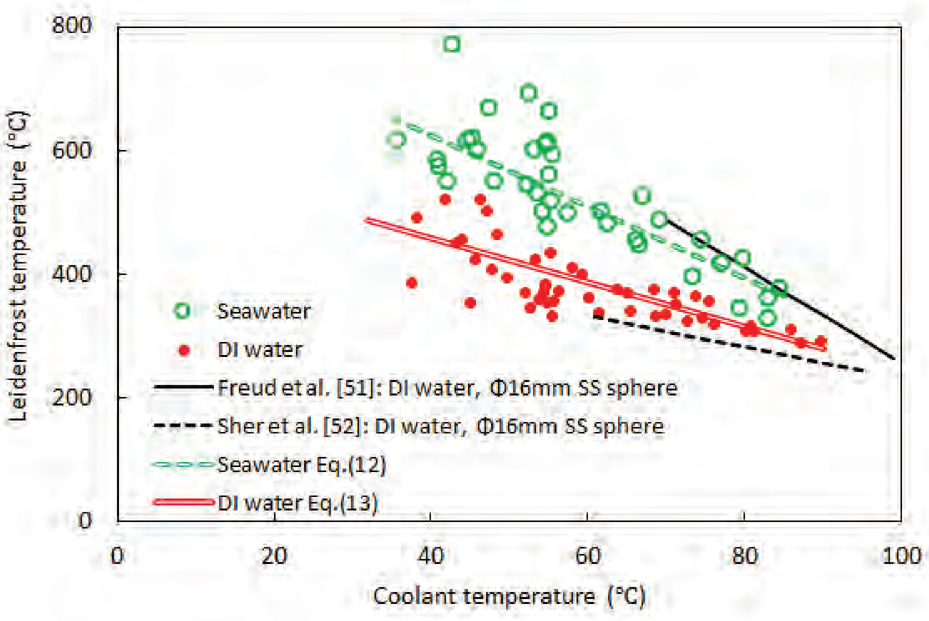

Figure 3.51: Leidenfrost temperature in seawater and DI water.

The data of vapor film thickness were extracted by the image-processing method of the high-speed photography. Since a thick vapor trail always appeared around the connecting point of the thermocouple A with the sphere, its thickness was out of the interest of the present study. Hence, the thickness of vapor film surrounding the sphere was estimated and analyzed only in the angular range of -160° ~ 160° from the bottom. Figure 3.52 shows the evolution of averaged vapor film thickness during vapor film formation phase and the stable film boiling phase, respectively. It was noticed that the vapor film thickness in seawater was remarkable thinner than that in DI water, which may be caused by the higher vapor condensation rate on the interface between vapor film and salt solution. It also showed that the film thickness was reduced with increasing coolant subcooling, obviously due to the increase of condensation rate by higher coolant subcooling. It was noticed the averaged film thickness was linearly decreasing with time during film boiling. In addition, from the evolution curves of vapor film thickness, it is also possible to conclude that high subcooling and salt additives of coolant would reduce both the minimum film thickness and the duration of film boiling.

Figure 3.53 shows that the profiles of vapor film thickness around the sphere at a sphere temperature of 850°C. The thickness was not uniform around the sphere, and it was generally thinner on the downward-facing surface (in the angular range of -90° ~ 90°) than on the upward-facing surface. The vapor film thickness was growing with raising angular location mainly due to vapor accumulation. In addition, it appeared that in the early stage of film boiling (temperature of sphere at 850°C) the salt additives and high subcooling resulted in a thinner vapor film, however in the late stage (close to the Leidenfrost temperature) the impact of coolant conditions on film thickness was diminishing.

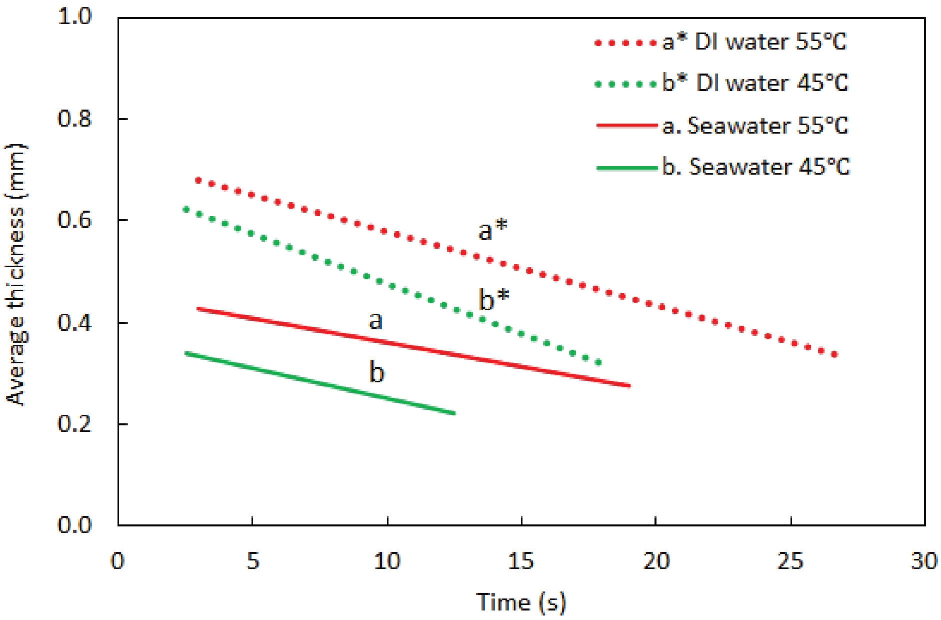

Figure 3.52: Evolution of averaged vapor film thickness.

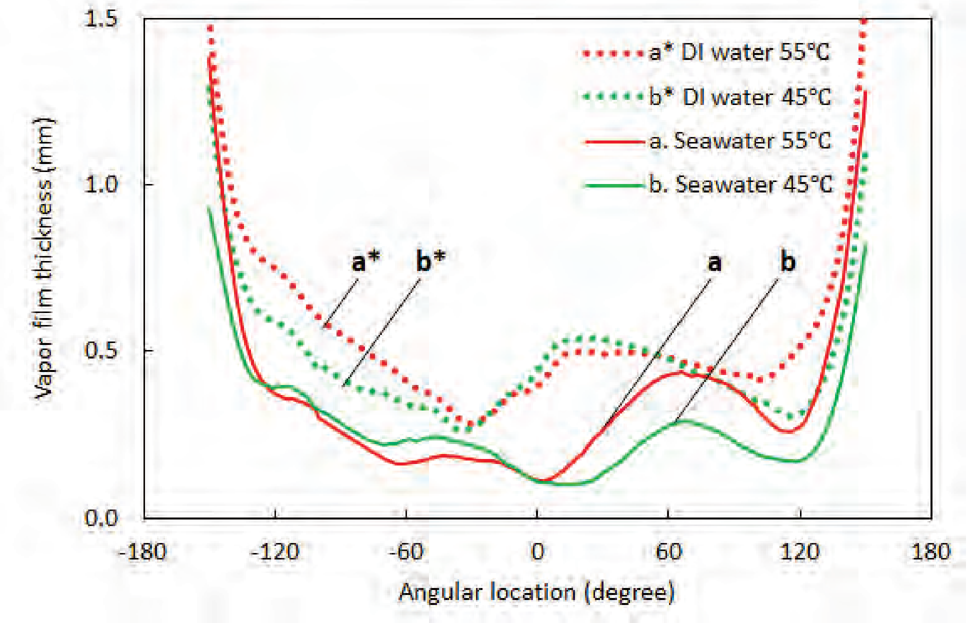

Figure 3.53: Vapor film thickness profile around the sphere during film boiling phase.

In the visual observation it was found that the vapor film was oscillating even during the stable film boiling phase. The vapor film instability was the precursory indicator of film collapse. It is therefore important to have the information on film stability. Figure 3.54 shows the evolution of film thickness in the late stage of film boiling at the angular location 90°.

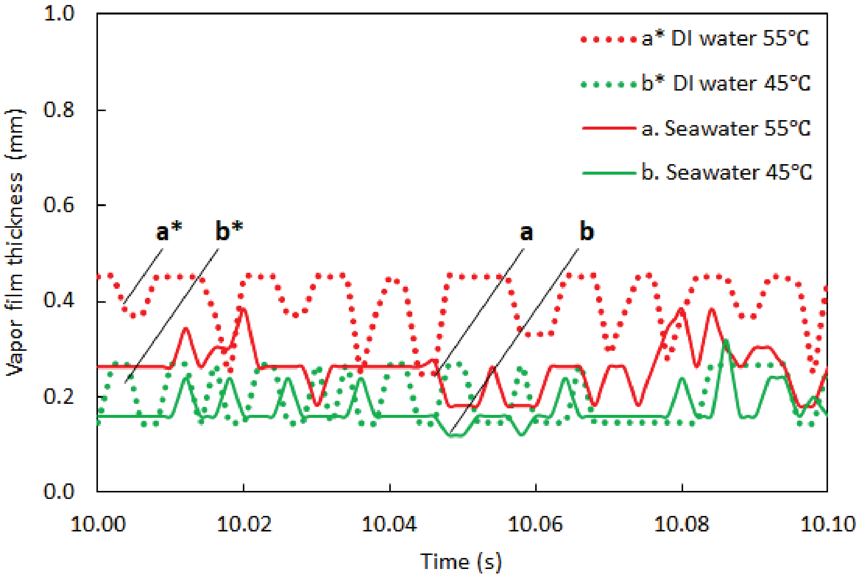

Fig. 3.54: Vapor film fluctuation in the late stage of film boiling at angular location 90°.

3.6.3. Steam explosion in seawater

The interest in seawater effect on steam explosion was raised by the Fukushima accident where seawater was employed to cool the reactors under a desperate condition.

A series of tests of single droplet steam explosion in seawater has been carried out on the MISTEE facility. Table 3.11 shows the test matrix using 0.8-1.2 g molten Tin. To obtain the probability of spontaneous steam explosion, 20-30 repeated tests under each condition were conducted. In the experiment, a single droplet of molten Tin was heated up to prescribed temperature and then delivered into the water tank, in which the interactions between the droplet and water were recorded by the high-speed camera, and the fragments after the steam explosions were collected by a debris catcher.

Table 3.11: Experimental conditions for steam explosions in seawater

Coolant	Salinity (g/kg)	Coolant temperature (°C)	Melt material	Melt temperature (°C)
Deionized water	0	22	Tin	600, 800
Diluted seawater	17.5			
Seawater	35.2			

In order to describe the influences of coolant salinity on steam explosion, in the present study two terms are defined as below:

- Frequency of spontaneous steam explosion: the number of tests with occurrence of spontaneous steam explosion, divided by the total number of tests under the same condition.
- Depth of spontaneous steam explosion: the distance from the surface of the water pool, where a spontaneous steam explosion takes place.

Based on the experimental results, the important observations are as follows.

- The frequency of spontaneous steam explosion increases with the salinity of water and given the same salinity the frequency of spontaneous steam explosion is reduced for droplets with high melt superheat (see Figure 3.55 and Table 3.12).

- The depth of water pool where a spontaneous steam explosion occurs is significantly reduced in seawater with high salinity (see Figure 3.56), indicating the explosions in seawater occur at the elevations closer to the pool surface. On the other hand, an increased superheat of the melt tends to increase the depth of a spontaneous steam explosion.
- The seawater promotes the fine fragmentation of debris, as shown in Figure 3.57 where a debris size distribution is the average of all debris particles under the same test condition, i.e., the data under a given condition concern all tests that underwent spontaneous steam explosion and no energetic interactions.

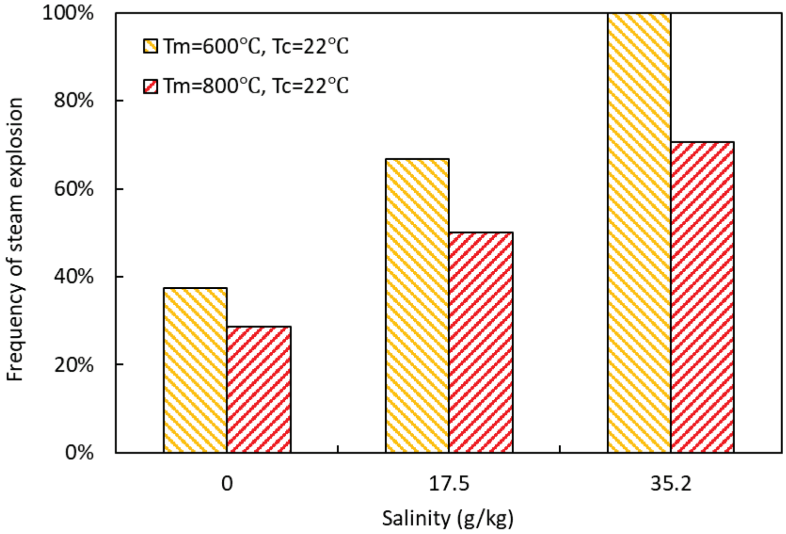

Figure 3.55: Salinity effect on the frequency of spontaneous steam explosion.

Table 3.12: Frequency of spontaneous steam explosion

Melt temperature (℃)	FSE[+] in deionized water	FSE in diluted seawater	FSE in standard seawater	FSE increase[++] in diluted seawater	FSE increase in standard seawater
600	38%	67%	100%	78%	167%
800	29%	50%	71%	75%	147%

[+] FSE: Frequency of spontaneous steam explosion

[++] FSE increase = FSE in seawater / FSE in deionized water - 100%

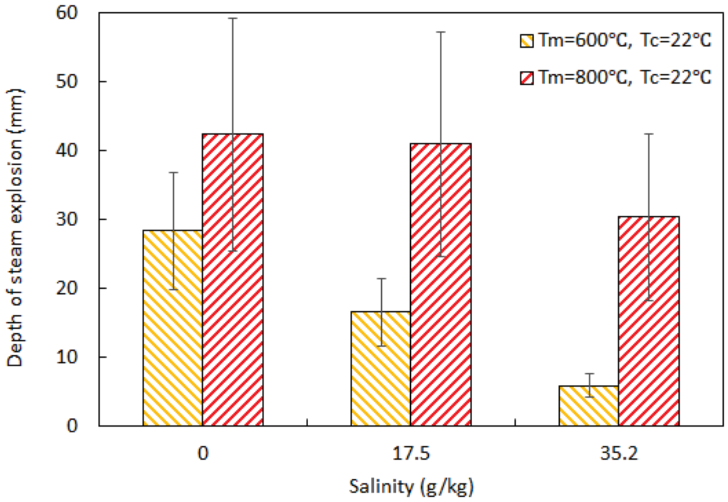

Figure 3.56: Salinity effect on the depth of spontaneous steam explosion.

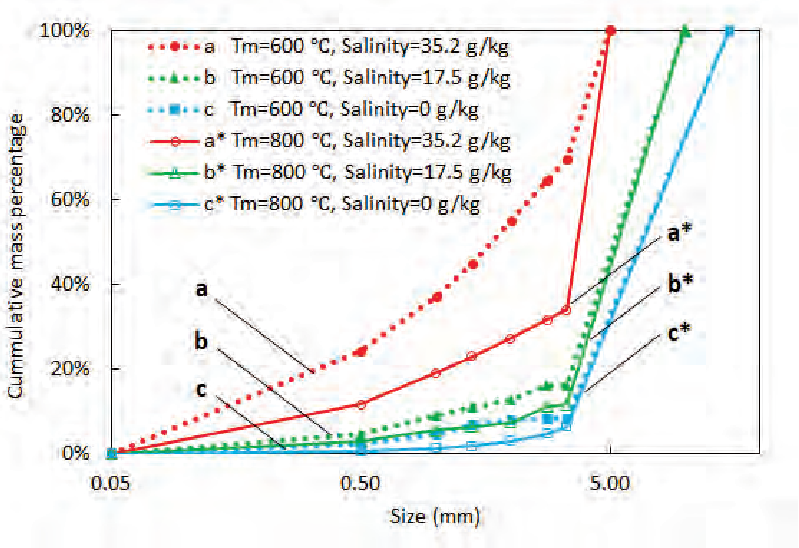

Figure 3.57: Salinity effect on size distribution of fragments.

3.7 Summary and outlook

The severe accident research at KTH/NPS is to assess the ex-vessel corium risks under severe accident management (SAM) measures adopted in Swedish nuclear power plants. Before APRI-10 extensive studies have been carried out on ex-vessel debris bed coolability and steam explosion, and the conclusion is that uncoolable debris bed and steam explosion cannot be excluded if a large jet of molten corium is discharged upon the vessel failure from the lower head to the water pool in the reactor cavity, even for the deep water pool of an BWR, let alone the shallow water pool of an PWR. This indicates the importance of the corium discharge characteristics following the vessel failure.

Therefore, the focus of APRI-10 research at KTH/NPS is placed on the late phase of in-vessel core melt progression which imposes thermal load on the lower head of a reactor pressure vessel (RPV), with the goal to quantify the high likelihood of the dripping mode of gradual melt discharge from the RPV to the cavity, so that the risks of ex-vessel steam explosion and forming non-coolable debris bed are diminishing.

Specifically, the research is emphasized on the behavior of multi-composition corium in the lower head of RPV, including debris remelting and resulting molten composition infiltration in debris beds, melt-vessel interactions, lower head failure due to vessel wall creep or penetration melt-through, and finally the corium discharge characteristics which provides the initial and boundary conditions for the assessment of ex-vessel corium risks. Notably, the study on the late phase of in-vessel core melt progression is also paramount to assessment of in-vessel melt coolability and retention.

In addition to the late phase, the research efforts at KTH/NPS are extended to other areas which were not or less touched in the previous APRI phases, including metallic melt coolant interactions, quenching of debris bed and oxidation of metallic melt, as well as development of advanced modeling capabilities. Some issues from Fukushima accident are also considered, e.g., the effect of seawater injection on accident phenomena.

As a result, the specific tasks of APRI-10 research at KTH/NPS are concerned with (i) debris/molten pool behavior in the lower head and RPV failure which are important to identify the boundary conditions for assessment of ex-vessel corium behavior, (ii) quenching and oxidation of ex-vessel debris bed which are important to corium coolability; (iii) ex-vessel molten metal-coolant interactions and suppression of steam explosion; (iv) development of modeling and simulation capabilities; and (v) MISTEE investigations on Zr/Fe droplet oxidation and sea-water effects.

Below are a summary of achievements in each area during APRI-10 and an outlook of next steps toward resolution of remaining issues.

3.7.1. Summary

Debris/molten pool behavior in the lower head

The study is concerned with the evolution of multi-composition corium in the lower head (e.g., debris remelting, melt infiltration, crust dynamics, physicochemical interactions). In this regard experimental investigations are conceived to be carried out on the SIMECO-2 and REMCOD/MRSPOD facilities, respectively. The main achievements are the development of the experimental approaches:

- The SIMECO-2 test facility [1] was supposed to be developed in the EU project IVMR finished in 2019 with the original objective to study heat transfer of stratified melt pools, and it was planned to use the facility for APRI-10 study on debris behavior (e.g., dryout of debris bed, debris remelting) in the lower head. However, the construction of the facility was delayed by system complexity and technical difficulties. Therefore, a significant extra effort of APRI-10 is allocated to make the SIMECO-2 facility to be ready by the end of APRI-10.
- Per the primary support of the Nuclear Regulation Authority (NRA) in Japan, the REMCOD/MRSPOD test facilities have been developed to study the thermal-hydraulic characteristics of molten metal penetration into debris beds [4-5]. Melt infiltration through porous debris and effect of solidification were studied in detail, with an improved understanding of competition mechanisms between hydrodynamics and solidification. Wettability and temperature profile of a debris bed had very strong effects on the melt infiltration. The database is needed for model development and validation.

RPV failure analysis

The study is concerned with prediction of reactor pressure vessel (RPV) failure mode (e.g., lower head breach vs penetration failure; creep vs melt-through; ablation vs plug), which together with the debris/molten pool evolution in the lower head will determine the corium discharge characteristics following the vessel failure.

The main achievements are the development of coupling approaches for thermo-mechanical simulations and models for physical phenomena related to RPV failure analysis during severe accidents:

- The initial state of corium in the lower head can be determined by simulations of the MELCOR code [6], and using the thermal loads from the MELCOR simulations the behavior of an ablated lower head was simulated by the ANSYS Mechanical code [7].
- A new creep model for the RPV steel 16MND5 was developed to have the capability to cover all three creep stages [8].
- A coupling approach for RPV failure analysis was developed based on the latest multi-physics platform of ANSYS Workbench, with a validation against FOREVER-EC2 experiment [9]. The new approach facilitates transient simulation of complex geometries, addition of advanced models as well as reduction of user effect.
- A comparative study [10] indicated that the new coupling approach using volume loads mapping (VLM) between thermal and mechanical data is computationally efficient than that using surface loads mapping (SLM).

Quenching and oxidation of ex-vessel debris bed

The study is concerned with quenching and oxidation of ex-vessel debris bed which are important to corium coolability but were not considered in the previous APRI studies. The main achievements in APRI-10 include

- The MEWA code was further validated against experiments and applied to coolability analysis for ex-vessel debris beds formed in postulated severe accident of a reference BWR [11].
- Moreover, the code was employed to simulate the quench of a large debris bed in the PEARL facility, and after the validation a reactor case was analyzed for quenching process of an ex-vessel debris bed with consideration of oxidation of metallic debris [12].
- A doctoral dissertation was issued in the field of debris bed coolability [13].

Ex-vessel molten metal-coolant interactions

The study is concerned with characterization of a debris bed forming from breakup of molten metallic corium jet and settlement of debris particles in a water pool, in contrast to previous studies which were focused on molten oxidic corium jet. Due to limitation of resources, only five tests were carried out APRI-10. No steam explosion observed were under the experimental conditions of all the five tests, and the preliminary results show that the melt superheat and water subcooling have significant effects on melt jet fragmentation phenomena [14] and debris bed characteristics [15].

Development of modeling and simulation capabilities

The study is concerned with the development of models and simulation capabilities which can help understanding of physics in severe accident phenomena and transfer the knowledge to reactor safety analysis.

In addition to the modeling of internal radiation in a melt pool [3], other achievements in APRI-10 are as follows

- Advanced turbulence modelling of melt pool heat transfer using Algebraic turbulent Heat Flux Model (AHFM) [16], which bears an international collaboration with NRG, Netherland.
- Direct numerical simulation (DNS) of turbulent melt pool convection and heat transfer [17].
- Development of a lumped-parameter code for efficient assessment of in-vessel melt retention strategy of LWRs, as a part of doctoral dissertation [18].
- Development of a surrogate model for quick estimate of debris bed coolability [19].
- The coupling of COCOMO-MEWA with RELAP5 to simulate the quenching process of the debris bed in the lower head of a BWR [20].

MISTEE investigations on Zr/Fe droplet oxidation and seawater effects

The study is concerned with basic understanding of physical mechanisms in fuel coolant interactions using the MISTEE platform, with the recent emphasis to upgrade the test platform toward applying prototypical compositions of corium in the experiment [21]. In addition, separate-effect studies are also performed using particles and simulant droplets of low melting points. Specific achievements in APRI-10 are made in the following aspects:

- Advance of Zr oxidation experiment and data analysis [22].
- Developments of a hydrogen collector [23], Zr-Fe alloy and a furnace suitable for melting the Zr-Fe alloy [24].
- Effect of materials on steam explosion [25]

- Effect of seawater on quenching of high-temperature particles [26]
- Effect of salinity on film boiling heat transfer [27]
- Effect of seawater on steam explosion [28].

More detailed results of KTH/NPS research in APRI-10 can be found the references [1]~[28], including publications by the end of APRI-10 and some technical presentations. Notably, three doctoral students [13][18][21] have been graduated in APRI-10.

3.7.2. Outlook

In-vessel debris behavior

As a first-of-its-kind infrastructure featuring high operational temperature, transparent visualization and novel instrumentation, the SIMECO-2 facility commissioned in the end of APRI-10 will be a unique platform for KTH/NPS to start the investigation on the evolution and heat transfer of multi-composition debris bed in the lower head. The behavior of a stratified melt pool at high temperature where we have little data will also be investigated on the facility.

After the completion of the NRA tasks by early 2021, the approaches and expertise of the REMCOD/MRSPOD experiments are fully available to future APRI research which should be focused on interpreting the previous results and performing more tests to reduce the gap between prototypical materials and simulants in the experiment, for a better understanding of molten metal (Zr/Fe) infiltration in an oxidic (UO_2/ZrO_2) debris bed.

In parallel with the experimental investigations, development of models and simulation capabilities (tools) will be introduced or enhanced, since they are the effective vehicles by which the understanding from experiment can be applied to reactor safety analysis, and the knowledge can be retained and transferred from generation to generation. Notably, mechanistic models have not been available yet in the field of corium debris evolution in the lower head, though they are important for the prediction of the corium’s state and dynamic loads (both thermal and mechanical) on the vessel.

Vessel failure modes

Given the thermal and mechanical loads from the corium in the lower head, the coupled thermo-mechanical analysis approaches developed in APRI-10 will be applied to predict the vessel failure modes in various severe accident scenarios, e.g., to study penetration failures in the RPV of an BWR with a detailed representation of penetrations (IGTs and CRGTs), as well as RPV integrity study under SAM measures of an PWR. The previous estimate of thermal load on the lower head is limited to melt pool, but the precursory debris bed and post-RPV-failure melt discharge characteristics are equally important to assessment of corium risk, especially for Swedish NPPs where the melt release conditions and history are crucial to the success of their SAM actions. In addition to vessel failure mode and corium state upon vessel failure, the failure hole ablation and plug are also important to corium discharge characteristics, and therefore should be addressed in the future study.

Melt-coolant interactions

For the slump of metal-rich corium upon vessel failure during a hypothetical severe accident, only five scoping tests were carried out in APRI-10 using molten Tin. For a concluding comprehensive understanding, more systematic tests are required with the current simulant (Tin) and higher melting-point simulant of Zr/Fe, so as to build a database with a good coverage of key physics during molten metal-coolant interactions, with a particular interest in jet fragmentation and resulting debris bed characteristics.

MISTEE experiment

A lot of efforts have been spent on the development of a new technique to melt Zr and the mixture of Zr/Fe which are among the prototypical compositions of corium. The mixture of molten Zr/Fe were proven to be aggressive to most of crucible materials tested in the MISTEE platform. The MgO crucible with a proper treatment appeared compatible with molten Zr/Fe and able to form a deliverable droplet. However, the successful rate of droplet delivery is still so low that the available data are insufficient to make any conclusions. Technical difficulties were also encountered in quantifying oxidization kinetics of Zr/Fe. Therefore, it is still on the way to optimize the MISTEE platform capable of performing tests using prototypical compositions of corium (Zr, Zr/Fe or Zr/Fe/ZrO_2).

Ex-vessel corium-structure interactions

Previously, all studies on ex-vessel steam explosion and debris coolability were based on such an assumption that a coherent melt jet falls from the lower head of the RPV into a water pool in a severe accident scenario of BWRs. However, it is well known that an BWR has a forest of structures (e.g., control rod driving mechanisms) and supporting plates below the lower head. The corium must pass through these structures before it reaches the water pool in the pedestal. It is still an open question on how the structures below the RPV of an BWR will affect ex-vessel corium risks.

Reactor applications and safety analyses

While considerable knowledge bases (e.g., data, models, codes) on severe accident have been developed from APRI projects and international projects (e.g., EU and OECD/NEA), a systematic application of the research results to the Swedish nuclear power safety context should be considered in the future, so as to boost confidence in the safety of nuclear power plants.

3.8 References

[1] A. Komlev, W. Villanueva, A. Konovalenko, M. Khan, P. Sköld, W. Ma, S. Bechta, Future experimental facility for IVR study: SIMECO-2. International Seminar IVMR-2020, Juan-les-Pins, France, January 21-23, 2020.

[2] D.B. Lopukh, I.N. Skrigan, A.V. Vavilov, A.P. Martynov, S.V. Bechta, A.A. Komlev. Numerical simulation of induction heating for molten pool heat transfer experiments in slice geometry, International Multi-Conference on Industrial Engineering and Modern Technologies (FarEastCon), pp.1-6, 2018.

[3] M. Khan, A. Komlev, W. Villanueva, P. Yu, S. Bechta, Effect of internal radiation on natural convective heat transfer in a volumetrically heated molten pool, Proceeding of the 48th MSWI Meeting, Stockholm, June 4, 2019.

[4] S.M. Hoseyni, W. Villanueva, S. Thakre, A. Konovalenko, and S. Bechta, Melt infiltration through porous debris at temperatures above solidification: Validation of analytical model, *Annuals of Nuclear Energy*, submitted.

[5] S.M. Hoseyni, A. Konovalenko, S. Thakre, W. Villanueva, A. Komlev, S. Bechta, P. Sköld, M. Akiba, A. Hotta, Metallic melt infiltration in preheated debris bed and the effect of solidification, *Nuclear Engineering and Design*, submitted.

[6] Y. Chen, H. Zhang, W. Villanueva, W. Ma, S. Bechta, A sensitivity study of MELCOR nodalization for simulation of in-vessel severe accident progression in a boiling water reactor, *Nuclear Engineering and Design* 343: 22–37, 2019.

[7] H. Wang, W. Villanueva, Y. Chen, A. Kulachenko, S. Bechta, Thermo-mechanical behavior of an ablated reactor pressure vessel wall in a Nordic BWR under in-vessel core melt retention, *Nuclear Engineering and Design*, to be submitted.

[8] P. Yu, W. Ma, A modified theta projection model for creep behavior of RPV steel 16MND5, *Journal of Materials Science & Technology* 47: 231–242, 2020.

[9] P. Yu, W. Ma, W. Villanueva, A. Karbojian, S. Bechta, Validation of a thermo-fluid-structure coupling approach for RPV creep failure analysis against FOREVER-EC2 experiment, *Annuals of Nuclear Energy* 133: 637–648, 2019.

[10] P. Yu, W. Ma, Comparative analysis of reactor pressure vessel failure using two thermo-fluid-structure coupling approaches, *Nuclear Engineering and Design* 368: 10819, 2020.

[11] Z. Huang, W. Ma, Validation and application of the MEWA code to analysis of debris bed coolability, *Nuclear Engineering and Design* 327: 22–37, 2018.

[12] Z. Huang, W. Ma, Numerical investigation on quench of an ex-vessel debris bed at prototypical scale, *Annals of Nuclear Energy* 122: 47–61, 2018.

[13] Z. Huang, Numerical Investigations on debris bed coolability and mitigation measures in Nordic boiling water reactors. Doctoral Dissertation, Royal Institute of Technology, Stockholm, 2019.

[14] S. Thakre, Y. Xiang, W. Ma, W. Villanueva, A. Komlev, S. Bechta, Study on metallic melt jet fragmentation in a water pool: Experiments and numerical simulations, *to be submitted to a journal*.

[15] Y. Xiang, S. Thakre, W. Ma, W. Villanueva, A. Komlev, S. Bechta, An experimental study on the characteristics of metallic debris beds, *to be submitted to a journal*.

[16] P. Yu, W. Villanueva, A. Shams, W. Ma, S. Bechta, Turbulent heat transfer in molten pool: Modelling, implementation and validation, Proceedings of MSWI-47, MSWI-48 and MSWI-49 Meetings, Stockholm, December 2018, June and December 2019.

[17] B. Bian, W. Villanueva, S. Bechta, Direct numerical simulation of molten pool convection, Proceedings of MSWI-49 and MSWI-50 Meetings, Stockholm, December 2019, June 2020.

[18] P. Yu, Modelling and Simulation of Reactor Pressure Vessel Failure during Severe Accidents, Doctoral Dissertation, Royal Institute of Technology, Stockholm, 2020.

[19] Y. Chen, W. Ma, Development and application of a surrogate model for quick estimation of ex-vessel debris bed coolability, *Nuclear Engineering and Design 370*: 110898, 2020.

[20] Z. Huang, W. Ma, On the quench of a debris bed in the lower head of a Nordic BWR by coolant injection through control rod guide tubes, *Nuclear Engineering and Design* 351: 189–202, 2019.

[21] L. Manickam, An Experimental Study on Melt Fragmentation, Oxidation and Steam Explosion during Fuel Coolant Interactions, Doctoral Dissertation, Royal Institute of Technology, Stockholm, 2018.

[22] L. Manickam, Q. Guo, A. Komlev, W. Ma, S. Bechta, Oxidation of molten zirconium droplets in water, *Nuclear Engineering and Design* 354: 110225, 2019.

[23] Q. Guo, L. Manickam, A. Komlev, W. Ma, S. Bechta, On oxidation of a zirconium droplet falling in subcooled water. Proceedings of SWINTH-2019, Paper number 039, Livorno, Italy, October 22-25, 2019.

[24] Q. Guo, Y. Deng, A. Komlev, W. Ma, S. Bechta, MISTEE experiment on oxidation of Zr-Fe alloy quenching in subcooled water, Proceedings of MSWI-49 and MSWI-50 Meetings, Stockholm, December 2019, June 2020.

[25] L. Manickam, Q. Guo, W. Ma, S. Bechta, An experimental study on the intense heat transfer and phase change during melt and water interactions, *Experimental Heat Transfer* 32: 251–266, 2019.

[26] Q. Guo, Y. Deng, W. Ma, S. Bechta, An experimental study on quenching of metallic spheres in seawater, *International Journal of Heat and Mass Transfer*, submitted.

[27] Q. Guo, Y. Deng, W. Ma, S. Bechta, Effects of salinity in coolant on film boiling heat transfer, *to be submitted to a journal*.

[28] Q. Guo, L. Manickam, W. Ma, S. Bechta, Effects of salinity in coolant on steam explosion, Proc. of the 18th International Topical Meeting on Nuclear Reactor Thermal Hydraulics (NURETH-18), pp. 4556–4567, Portland, Oregon, USA, August 18-23, 2019. *Being revised for submission to a journal*.

[29] A. Komlev, W. Villanueva, A. Konovalenko, P. Yu, M. Khan, P. Sköld, M. Harti, T. Laato, W. Ma, S. Bechta, Final Report on Top Cooling, Deliverable D3.11 of the EU project IVMR, 2019.

[30] B.G. Korshunov, V.V. Safonov, D.V. Drobot, Phase Equilibria in Halide Systems, Moscow, 1979.

[31] H. Okamoto, Al-Mg (Aluminum-Magnesium), Journal of Phase Equilibria, 19 (6): 598, 1998.

[32] Y. Li, CFD Pre-test Analysis of SIMECO-2 Experiment. Master Thesis, Royal Institute of Technology, Stockholm, 2016.

[33] C.T. Tran and T.N. Dinh, The effective convectivity model for simulation of melt pool heat transfer in a light water reactor pressure vessel lower head, *Progress in Nuclear Energy* 51: 849-871, 2009.

[34] A. Hotta, M. Akiba, A. Morita, A. Konovalenko, W. Villanueva, S. Bechta, et al, Experimental and analytical investigation of formation and cooling phenomena in high temperature debris bed, *Journal of Nuclear Science and Technology* 57(4): 353–369, 2020.

[35] W. Villanueva, S.M. Hoseyni, A. Komlev, S. Thakre, A. Konovalenko, S. Bechta, Investigation of Cooling Phenomena of High Temperature Molten Core – Phase-6: Post-test Analysis of PULiMS and DEFOR Tests and Test Series of REMCOD, Research Report for Nuclear Regulation Authority of Japan, 271 pages, Royal Institute of Technology, March 2020.

[36] A. Theerthan, A. Karbojian, B. R. Sehgal, EC-FOREVER experiments on thermal and mechanical behavior of a reactor pressure vessel during a severe accident Technical report-1: EC-FOREVER-2 test, Research Report SAM-ARVI-D008, March 2001.

[37] A. Karbojian, W. Ma, P. Kudinov, T.N. Dinh, A scoping study of debris bed formation in the DEFOR test facility, *Nuclear Engineering and Design* 239: 1653–1659, 2009.

[38] M. Bürger, M. Buck, W. Schmidt, Validation and application of the WABE code: investigations of constitutive laws and 2D effects on debris coolability, *Nuclear Engineering and Design* 236: 2164–2188, 2006.

[39] N. Chikhi, F. Fichot, Experimental and theoretical study of large-scale debris bed reflood in the PEARL facility, *Nuclear Engineering and Design* 312: 48–58, 2017.

[40] S. Thakre, L. Manickam, W. Ma, A numerical simulation of jet breakup in melt coolant interactions, *Annals of Nuclear Energy* 80: 467-475, 2015.

[41] M. Saito, Experimental study on penetration behaviors of water jet into freon-11 and liquid nitrogen, ANS-Proc. 25th Natl. Heat Transfer Conf. (pp. 173-183), 1988.

[42] M. Epstein, H.K. Fauske, Applications of the turbulent entrainment assumption to immiscible gas-liquid and liquid-liquid systems, *Chemical Engineering Research and Design* 79(4): 453-462, 2001.

[43] A. Shams, Towards the accurate numerical prediction of thermal hydraulic phenomena in corium pools, *Annals of Nuclear Energy* 117: 234–246, 2018.

[44] D. Goluskin, Internally Heated Convection and Rayleigh-Bénard Convection, Springer, 2016.

[45] M. Bonnet, J.M. Seiler, Thermal hydraulic phenomena in corium pools: the BALI experiment. Proc. of the 7th International Conference on Nuclear Engineering (ICONE-7), Tokyo, Japan, April 19-23, 1999.

[46] I. Otić, G. Grötzbach, M. Wörner, Analysis and modelling of the temperature variance equation in turbulent natural convection for low-Prandtl-number fluids, *Journal of Fluid Mechanics* 525: 237–261, 2005.

[47] M. Schmidt, M. Woerner, DNS database of turbulent natural convection in horizontal fluid layers: https://www.iket.kit.edu/iket_ordner/ihl_5e6.pdf.

[48] D. Goluskin, E.P. Van der Poel, Penetrative internally heated convection in two and three dimensions, *Journal Fluid Mechanics* 791: 1–12, 2016.

[49] S. Grossmann, D. Lohse, Scaling in thermal convection: a unifying theory, *Journal Fluid Mechanics* 407: 27–56, 2000.

[50] R.R. Nourgaliev, T.N. Dinh, B.R. Sehgal, Effect of fluid Prandtl number on heat transfer characteristics in internally heated liquid pools with Rayleigh numbers up to 10^{12}, *Nuclear Engineering and Design* 169: 165-184, 1997.

[51] R. Freud, R. Harari, E. Sher, Collapsing criteria for vapor film around solid spheres as a fundamental stage leading to vapor explosion, *Nuclear engineering and Design*: 239(4): 722-727, 2009.

[52] I. Sher, R. Harari, R. Reshef, E. Sher, Film boiling collapse in solid spheres immersed in a sub-cooled liquid, *Applied Thermal Engineering* 36: 219-226, 2012.

4. KTH – DEP. OF NUCLEAR ENGINEERING – DEVELOPMENT OF ROAAM+ FRAMEWORK

4.1 Background: Severe Accident Management in Nordic BWR.

Severe accident management (SAM) strategy in Nordic boiling water reactors (BWRs) employs ex-vessel debris coolability. Molten core materials are released from the vessel into a deep pool of water under the reactor (see Figure 4.1.***1***) and expected to fragment, quench, and form a debris bed that is coolable by natural circulation of water. An energetic steam explosion and formation of non-coolable debris bed pose credible threats to containment integrity.

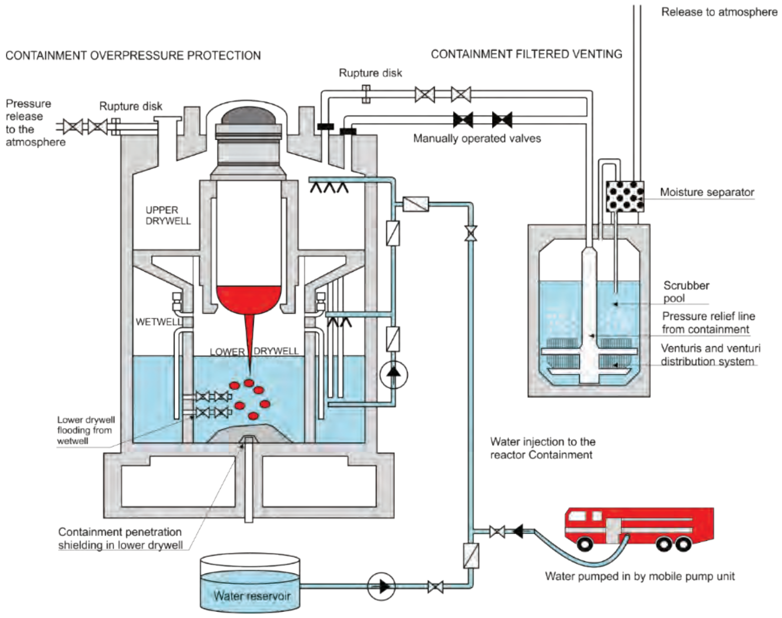

Figure 4.1.1 Severe Accident Management in Nordic BWR [15]

Conditions of melt release from the vessel determine (i) debris bed properties and thus coolability, and (ii) steam explosion energetics. The strategy involves complex phenomena affected by the transient accident scenarios and thus intractable [68], [69] for carried out separately probabilistic or deterministic analysis.

4.2 ROAAM+ Framework for Nordic BWR

The Risk Oriented Accident Analysis Methodology (ROAAM) that marries probabilistic and deterministic approaches was proposed to address problems where both stochastic phenomena (aleatory) and phenomenological (epistemic) uncertainties are significant. The ROAAM was developed and successfully applied by Professor Theofanous and co-workers for assessment and management of severe accident risks [114], [115]. After Fukushima accident, the Risk Management Task Force provided recommendation that NRC should implement a consistent process that includes both deterministic and probabilistic methods in risk assessments that can inform decisions about appropriate defense-in-depth measures [2].

This section provides an overview of ROAAM+ Framework for Nordic BWR [69], including probabilistic framework and its implementation ([15], [16], [65]). ROAAM has been successful in resolving several severe accident issues (e.g. [116], [118], [91], [117]). However, the tight coupling between severe accident threats, sensitivity to timing and characteristics of the events (e.g., vessel failure and melt release conditions) present new challenges in problem decomposition. Furthermore, in classical ROAAM applications the safety margins are (or were made by design modifications) sufficiently large, thus making possible conservative treatment of uncertainties in risk assessment. In case of SAM of Nordic BWR it is not possible to demonstrate effectiveness of the SAM with conservative assumptions. There is a question though if assumptions in the analysis are too conservative and the SAM can achieve its goal while state-of-the-art knowledge is insufficient to demonstrate that yet. An extension of ROAAM (called ROAAM+) was developed [16] and is based on an iterative process of knowledge refinement in risk analysis. The process is guided by identification of the major sources of uncertainty. The goal of ROAAM+ is to support decision making regarding the effectiveness of SAM strategy. ROAAM+ framework provides an extended treatment of safety goals in support for both possible decisions:

(i) current SAM strategy is sufficiently reliable ("possibility" of the containment failure is low);

(ii) SAM strategy is not sufficiently reliable ("necessity" of the containment failure is high) and thus changes in the SAM design are necessary.

4.2.1. ROAAM+ Probabilistic Framework

Quantification of Risk and Approach to Decision Making

It was emphasized by Kaplan and Garrick [43] that "the purpose of risk analysis and risk quantification is always to provide input to an underlying decision problem, which involves not just risks but also other forms of costs and benefits. Risk must thus be considered always within a decision theory context" [43]. The analysis of complex systems usually involves answering to the three following questions [43]: (i) what can happen? (ii) how likely? (iii) if it happens, what are the consequences? Which leads to the "risk triplet idea" presented in Kaplan and Garrick's paper "On the quantitative definition of risk" (see [43]), which has become a cornerstone of modern risk analysis. The risk R_i associated with a specific scenario s_i can be characterized by its frequency f_i and consequencesc_i.Consequences are obtained from assessments which are subject to uncertainty due to incomplete knowledge (epistemic uncertainty, degree of confidence), which can be quantified as probability P_i (likelihood) of c_i

$$\boldsymbol{R_i = \{s_i, pdf(f_i, P_i(c_i))\}} \tag{1}$$

Consequences c_i of scenario s_i can be presented as joint probability density function $\mathrm{pdf}_{C_i L_i}(L_i, C_i)$ of loads (L_i) on the system and its capacity (C_i) to withstand such loads. Thus, failure probability P_{Fi} for scenario s_i can be evaluated as

$$P_{Fi} = P(L_i \geq C_i) = \iint_{L_i \geq C_i} \mathrm{pdf}_{C_i L_i}(c, l) dc dl \tag{2}$$

Residual risk is judged in ROAAM with screening frequency for aleatory, and with screening probability for epistemic. I.e. plant damage states (D_j) selected for the analysis include those that have frequency higher than selected screening frequency f_s and lower than target frequency f_t achieved as the prevention goal, that is, $f_s < f_j(D_j) < f_t$ (severe accident mitigation window [114]. Demonstration of reaching the safety goal is successful if P_{Fi} is below respective screening probability level P_s. An arbitrary scale for probability is introduced in ROAAM to define the process likelihood [114]: 1/10 - Behavior is within known trends but obtainable only at the edge-of-spectrum parameters; 1/100 - Behavior cannot be positively excluded, but it is outside the spectrum of reason; 1/1000 - Behavior is physically unreasonable and violates well-known reality. Its occurrence can be argued against positively.

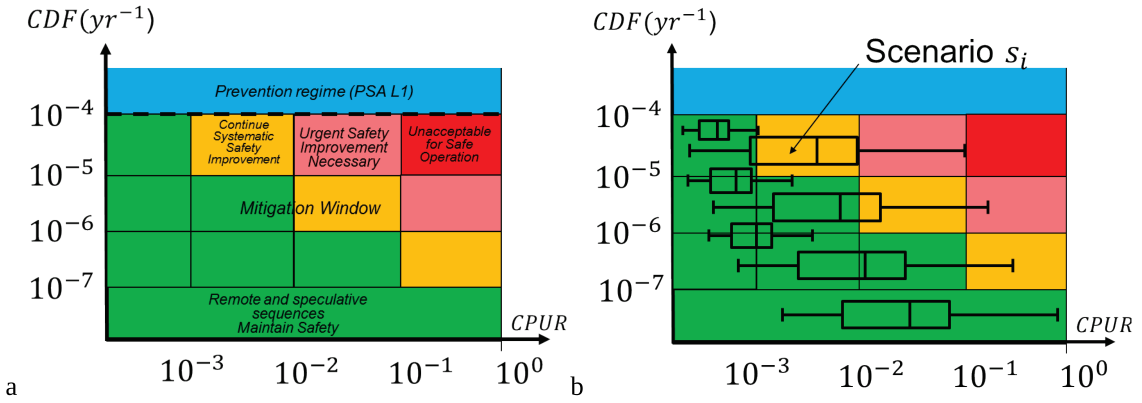

Figure 4.2.1. Conditional Probability of Unacceptable Release, (a) Decision Support in Classical ROAAM; (b) Decision support in ROAAM+.

The aim of the ROAAM+ framework is to provide an assessment in support of the decision whether the risk associated with current SAM strategy is acceptable. Scenario frequencies are the inputs to ROAAM+ framework provided from PSA L1 analysis results, i.e. frequencies of correspondent plant damage states (PDSs). Conditional containment failure probability (or probability distribution of conditional containment failure probability) for each scenario is a main outcome of ROAAM+ framework analysis. It is instructive to note that different modes of failure can potentially lead to quite different consequences in terms of fission products release. At this point we consider any failure mode as unacceptable for the sake of conservatism. Figure 4.2.***1***a presents decision criterion as a function of accident scenario frequency (CDF – Core Damage Frequency) and Conditional Containment Failure Probability (CCFP) or Conditional Probability of Unacceptable Release (CPUR) which is used in classical ROAAM. If there is no uncertainty in CCFP, then the decision can be made directly using the correspondent values of CDF and CCFP as it demonstrated in the Figure 4.2.***1***a. In case of CCFP values being uncertain and represented by $pdf(P_{Fi})$ – as in Figure 4.2.***1***b where ROAAM+ results - $pdf(P_{Fi})$ are presented as box and whiskers plots for scenarios s_i, with respective frequencies f_i; the abovementioned approach can be used to support decision making.

ROAAM+ Framework for Nordic BWR

ROAAM is based on decomposition of severe accident processes into key physical phenomena that can be described by well-posed mathematical problems. Figure 4.2.***2*** illustrates the top layer of the ROAAM+ framework for Nordic BWR which decomposes severe accident progression into a set of causal relationships (CR) represented by respective surrogate models (SM) connected through initial and boundary conditions such that the uncertainty can be propagated from the initial plant damage state $\{D_i\}$ to the ex-vessel containment phenomena. Computational efficiency of the top layer of the framework is achieved through application of surrogate models (SMs), and is a must for extensive sensitivity and uncertainty analysis in the forward and reverse analyses: “Forward” analysis defines conditional containment failure probability for each scenario $\{s_i\}$; “Reverse” analysis identifies failure domains in the space of scenarios $\{s_i\}$, and model input parameters $\{p_i\}$.

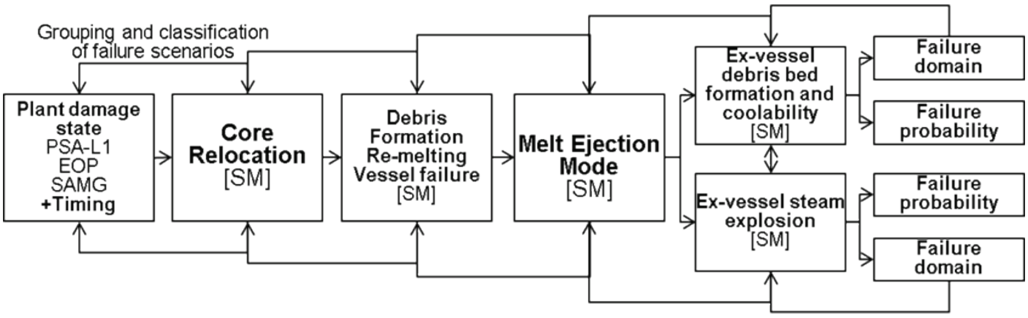

Figure 4.2.2. ROAAM+ framework for Nordic BWR [69].

For each plant damage state $\{D_j\}$ defined in PSA Level 1 there is a set of respective scenarios $\{s_{ji}\}$ ($\{s_i\}$ – for brevity) characterized by their frequencies $\{f_i\}$. Scenarios introduce specific combinations of initial and boundary conditions for the models used in the framework and the structure of the probabilistic framework.

We distinguish four different kinds of parameters in the framework. For example, a causal relation - CR_k have: (i) scenario $\{s_i\}$ parameters (determined by initial plant damage states, possible operator actions and random success/failures of activation of different systems), (ii) model input/output parameters $\{p_{ki}\}$ (predicted/used by the models at earlier/later stages of the framework respectively). The epistemic (modeling) parameters are treated differently depending on the degree of knowledge [115], **[**28]: deterministic $\{d_{ki}\}$ modeling parameters (internal model parameters) have complete probabilistic knowledge (i.e. probability distribution), intangible $\{i_{ki}\}$ modeling parameters (internal model parameters), have incomplete or no probabilistic knowledge, i.e. one can only argue regarding possible ranges of such parameters.

ROAAM+ framework employs a two-level coarse-fine analysis and iterative process of framework refinement in the development of the SMs. Detailed discussion of the FM and SM development are presented in a series of publications (see Table 4.1). Four techniques were used for implementation of the SMs: (i) mapping (based on mapping of the FM solution to a grid in the space of the input parameters); (ii) polynomial (scaling analysis and data fitting); (iii) physics based uses simplified modelling of the phenomena; (iv) Artificial Neural Networks (ANN).

Table 4.1. Summary of full and surrogate models developed for the ROAAM+ framework

SM	**FM, experiments and SM purpose**	**References**
CORE	FM: MELCOR model of the Nordic BWR containment. SM Type: Mapping. Given timing of ADS and ECCS activation provides time, composition and mass of core relocation and conditions in the lower drywall: pressure, pool temperature and depth.	[18] [19] [20] [21] [22] [23] [24] [25] [26] [27] [31] [32] [33] [63] [70]
Vessel failure	FM: coupled thermo-mechanical analysis (PECM/ANSYS, DECOSIM code) of the vessel lover head and debris. SM Type: Polynomial. Given mass and composition of the debris SM computes timings of the IGT, CRGT and vessel wall failure and corresponding mass and composition of liquid melt available for release.	[40], [41], [73], [105], [106], [107], [119], [120], [121], [122], [123], [124], [125], [126], [127], [128], [129], [130], [131], [132], [133], [144], [142], [141], [152]

Melt release	FM: MELCOR and parametric models of the melt release rate and vessel wall ablation. Experiment: remelting of multi-component debris and interaction with the vessel. SM Types: Regression tree learning applies so called recursive partitioning. Physics based. Given timings and mode of lower head failure SM computes conditions of melt release, i.e. ablation of the breach, rate and duration of the release, thermal properties of the melt.	[15] [16] [17] [77], [76], [64], [66], [74], [63]
SEIM	Steam Explosion Impact Map. FM: TEXAS-V code. SM Type: ANN. Given conditions of melt release and LDW characteristics SM returns a distribution of possible explosion impulses.	[18] [34] [35] [36] [37] [38] [39] [72] [75] [71] [96]
DECO	Debris Coolability. FMs: DECOSIM code for coolability of the debris, debris bed spreading model, debris agglomeration models. Series of experiments on debris bed formation, agglomeration and particulate debris spreading are carried out. SMs Type: Physics based. Given conditions of melt release and pool, respective SMs return dryout heat flux and max debris bed heat flux, the effect of debris spreading and agglomerated debris are taken into account.	[3] [4] [5] [6] [7] [8] [13] [14] [44] [45] [46] [47] [48] [53] [54] [55] [56] [57] [58] [59] [60] [61] [62] [74] [78] [79] [80] [81] [82] [83] [84] [85] [86] [87] [88] [89] [90] [92] [108] [134] [135] [136] [137] [138] [139] [140] [142] [143] [144] [145] [146] [147] [148] [149] [150] [151] [154]

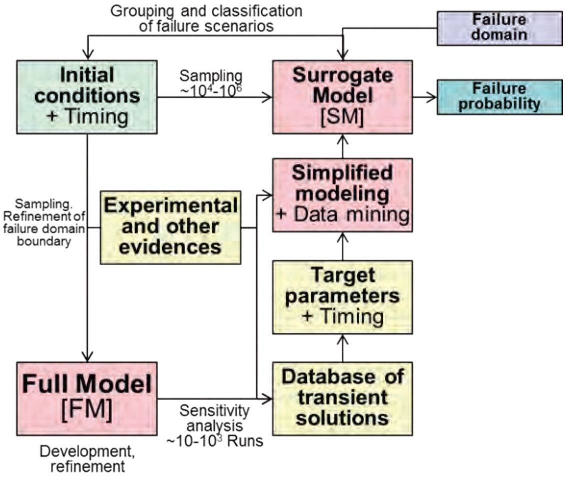

Figure 4.2.3. Full and Surrogate model development, integration with evidences, refinement, prediction of failure probability and failure domain identification [69]

Initial conditions for FM and SM development and analysis come from the respective stages of the analysis at the previous stages of the framework (Figure 4.2.*2*). The process are illustrated in Figure 4.2.3. Experimental and other evidences provide a knowledge base for validation of the FMs and calibration of SMs. Full Model (FM) is implemented as detailed fine resolution (computationally expensive) simulation approach. FMs are used assuming wider possible ranges of the input parameters to generate a database of the FM transient solutions. Surrogate model (SM) is developed as an approximation of the FM model prediction of the target parameters which employ simplified (coarse resolution) physical modeling, calibratable closures, or approximations of the response surface of FM (e.g. using machine learning, such as artificial neural networks (ANNs) [97]). This process is iterative in nature and is guided by failure domain analysis, which is used to identify the needs for further refinement of Full and Surrogate models and overall structure of the framework.

Failure Domain and Treatment of Model Intangible Parameters

ROAAM+ framework employs an extended treatment of safety goals and support for both possible decisions, either to maintain current SAM strategy as sufficiently reliable ("possibility" of the containment failure is low) or SAM strategy is not sufficiently reliable ("necessity" of the containment failure is high) and thus changes are necessary. This is achieved through application of two definitions of screening probability levels P_S for

- "Possibility" of failure: P_s=1.e-3. According to [114] P_s=1.e-3 defines the process likelihood as *physically unreasonable* and violates well-known reality. Its occurrence can be argued against positively.
- "Necessity" of failure: P_s=0.999. Is equivalent to statement that possibility that containment doesn't fail is low (P_s=1.e-3).

In classical ROAAM uncertainty in the intangibles can only be qualitatively approached, but it can always be bounded [114]. Such bounding approach is, in fact, similar to the interval analysis [42]. In case of large inherent safety margins, the bounding approach will not affect conclusions from the risk analysis. However, if failure probability P_f is sensitive not only to the ranges but also to the distributions, then the uncertainty in prediction of P_f with "conservative" or "optimistic" bounding assumptions might be too large (e.g. probability of failure can range from 0 to 1 in both cases), and results would not be suitable for decision making.

While ranges of the intangible parameters can be always (conservatively) bounded, the knowledge about distributions within the ranges is missing (i.e. no probabilistic knowledge **[28]**). In order to assess the importance of the missing information about the distributions we consider distributions as uncertain (i.e. parameters that characterize probability distributions are considered as uncertain parameters). We randomly select a set of distributions of model intangible parameters $pdf_k(i_{N,i})$ and calculate the value of P_{Fk} for selected combination of model input ($p_{N-1,i}$) and scenario parameters (s_i). Repeating this process for every possible set of distributions of $i_{N,i}$ would yield a probability distribution of P_F, which can be expressed as complimentary cumulative distribution (tail distribution) of probability of failure – $CCDF\left(P_F(s_i, p_{N-1,i})\right)$. Repeating the same process for each stage of the framework in the reverse analysis provides distributions of the failure probability for all possible combination of model input p_{ki} and scenario parameters s_i.

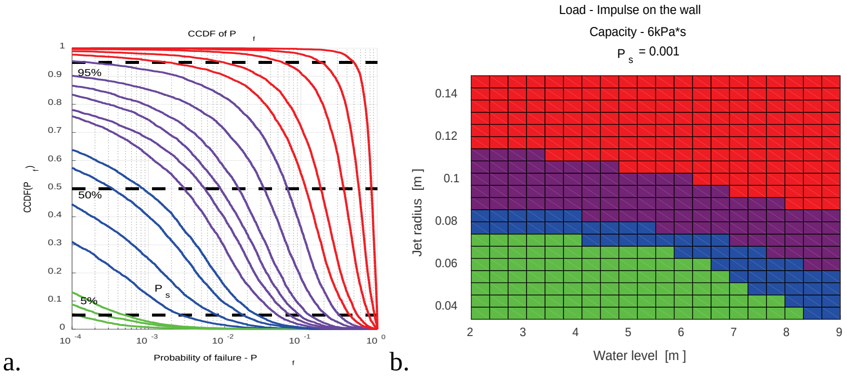

Figure 4.2.4. Complimentary cumulative distribution function of probability of failure $\boldsymbol{CCDF(P_F)}$ *(a) and an example of the failure domain map (b) [16]*

Failure domain is defined as the domain of model input and scenario parameters where the values of P_f exceed respective screening probability level P_S. In the analysis we obtain not a single value of failure probability but a distribution of possible values of P_F. Figure 4.2.***4*** shows an example of possible CCDFs of P_F that can be obtained in ROAAM+ failure domain analysis. These resultant CCDFs can be color-coded as follows: **Green**: at most in 5% of the cases $P_f > P_s$, i.e. with 95% confidence the probability of failure P_F will not exceed selected screening probability P_s. If selected P_s is sufficiently small, then green domain indicates a combination of parameters where “failure is physically unreasonable” regardless of the modeling uncertainties. **Red**: at least in 95% of the cases $P_f > P_s$, i.e. with 95% confidence the probability of failure P_F will exceed selected screening probability P_s. If selected P_s is sufficiently large, then red domain indicates a combination of parameters where “failure is imminent” regardless of the modeling uncertainties. **Blue**: P_F exceeds P_s in 5-50% of the cases. **Purple**: P_F exceeds P_s in 50-95% of the cases.

Probabilistic Framework Implementation

The top layer of the ROAAM+ framework is implemented as a set of modules (ROAAM Driver, FoRevAn and SMS), implemented in MATLAB, with respective methods and properties to perform forward and reverse analysis for the whole sequence of casual relationship represented by respective surrogate models (SM). The schematic diagram of probabilistic framework implementation is illustrated in Figure 4.2.***5***. The main functions of ROAAM+ drivers are: User input processing (list of SMs, framework settings for sampling, type of analysis, etc.); Generation of the jobs for sensitivity analysis and uncertainty quantification in FoRevAn (Forward and Reverse Analysis) based on the user input (e.g. SM execution order and structure, etc.).

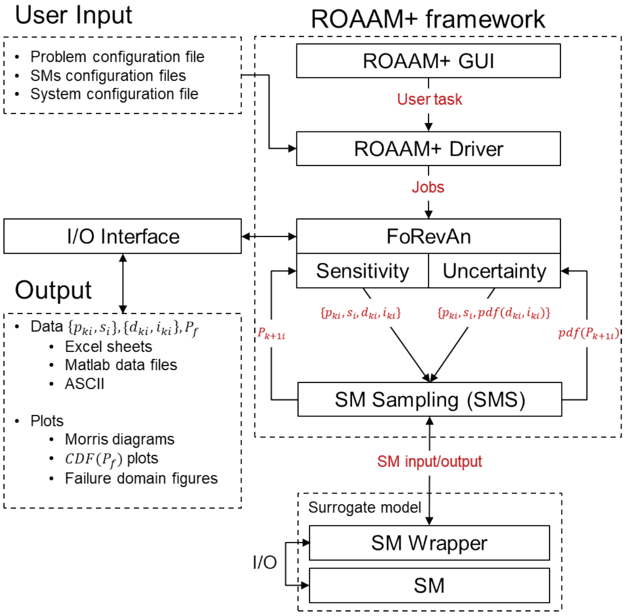

Figure 4.2.5. Schematic Diagram of Probabilistic Framework [16]

FoRevAn module is responsible for carrying out forward (calculation of failure probability - P_f) and reverse (failure domain) analyses. The main functions of FoRevAn are: Execution of the jobs received from the ROAAM+ Driver; Coupling between SMs and generation of the general input/output structure for the whole set of SMs to be used in the analysis; Generation of the sampling set in the space of model input - p_{ki} and scenario s_i parameters with static/adaptive grid; Random generation of the set of the parameters characterizing probability density functions of model intangible parameters $\{pdf(i_{ki})\}$; Generation of the set of multidimensional $pdf(d_{ki}, i_{ki})$, given the information provided by the user; Calculation of the probability of failure P_F; Failure Domain Analysis; Model (SM) sensitivity analysis for individual and coupled SMs. The execution of individual surrogate models is performed in SMS (Surrogate Model Sampling) Module, where the main functions are: Iterative generation of the sampling sets in the domains of model deterministic and intangible parameters according to $pdf(d_{ki}, i_{ki})$ specified by FoRevAn module; Execution of the Surrogate model (generating SM input, running the SM, and collecting SM output, checking output ranges); Preliminary analysis of the results for each iteration to check statistical convergence of the SM output; Reporting of the SM outputs to FoRevAn module.

Sampling

For model input and scenario parameters $\{p_{ki}, s_i\}$, the grid-based sampling is used in order to provide coverage of the uncertainty space and knowledge about failure domain location. Note that grid-based approach is most adequate when the size of the failure domain is relatively large (as in the specific application to Nordic BWR case). If size of the failure domain is small and its location is a-priori unknown, adaptive sampling (e.g. based on global optimum search) would be more adequate. We use sampling in the space of model input and scenario parameters $\{p_{ki}, s_i\}$ on the regular (static) grid, with optional Adaptive Mesh Refinement of the boundary of the failure domain [93],[22]. Application of the grid-based sampling techniques, in general, is computationally expensive, thus, in order to make failure domain analysis more efficient, it is necessary to identify a few most influential parameters. This is done by performing model sensitivity analysis (e.g. using Morris method [109]) with respect to a) individual models; b) coupled models. Model sensitivity analysis allows to improve our understanding of the impact of each step in multi-stage analysis process on the final outcome and on the probability of failure (e.g. Jet diameter – is the most influential parameter for steam explosion, on the other hand Jet diameter is predicted by Melt-Ejection SM [17] and defined by the properties of relocated debris in LP, which in turn depends on the accident scenario and recovery time of safety systems [23].

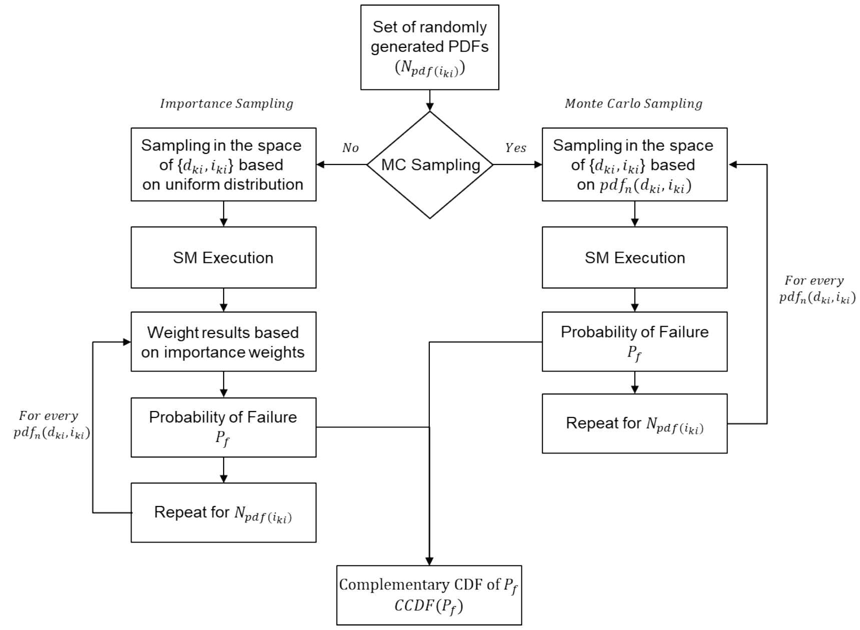

Figure 4.2.6. Schematic representation of approach for quantification of the uncertainty in $\boldsymbol{P_f}$ [16]

In probabilistic framework the probability space of model intangible parameters is represented by the joined probability density function that characterize the uncertain parameters. Currently, two distribution families are implemented in the framework: (i) Truncated normal distribution [10]; (ii) Scaled beta distribution [99]. Sampling in the space of model deterministic and intangible parameters $\{d_i, i_i\}$ is performed using Halton [100], [101], [102] sequence based on respective probability distributions. The number of samples in space of $\{d_i, i_i\}$ parameters depends on the convergence of the SM output. Currently there are two approaches for sampling in the space of model deterministic and intangible parameters $\{d_i, i_i\}$ implemented in the framework. These approaches are schematically represented in Figure 4.2.***6*** and briefly discussed below:

Monte Carlo sampling. In case of Monte Carlo sampling, the sampling in the space of $\{d_i, i_i\}$ is performed based on the joint PDF, which include randomly generated PDFs for model intangible parameters. The sampling is performed for every set of randomly generated PDFs until either convergence of the resultant distribution is achieved or maximum number of samplings is reached, defined for both – amount of randomly generated PDFs and SM samplings. The probability of failure is approximated as the fraction of samples resulted in failure (load exceeding capacity) for every set of randomly generated PDFs.

Importance Sampling. In case of Importance sampling, the sampling in the space of $\{d_i, i_i\}$ is performed using uniform distribution. The sampling is performed until convergence of the resultant SM output distribution is reached or the max. amount of SM samplings is reached. The probability of failure is approximated as the fraction of samples resulted in failure (load exceeding capacity), where every sample is weighted by the importance weights derived from the target PDF and sampling PDF (uniform) [103][104]. The sampling of target PDFs is performed until either convergence of the distribution of probability of failure or the max. number of samples is reached.

ROAAM+ GUI

The graphical user interphase (Figure 4.2.7) has been developed based on the main modules of the ROAAM+ probabilistic framework, described in the previous sections. The software implementation is designed to facilitate the usage of the main features of the probabilistic framework, such as model (SM) sensitivity analysis, forward and reverse analysis, post-processing of the results and results visualization. Furthermore, it provides a quick access to the major part of the framework execution settings, problem configuration and surrogate model input files. The user can perform: Model sensitivity analysis (using Morris method) for individual and coupled surrogate models. Probabilistic framework execution, which include forward analysis and reverse analysis. Generation and visualization of failure domains. Data and analysis results export (probability of failure and all relevant data) to Excel.

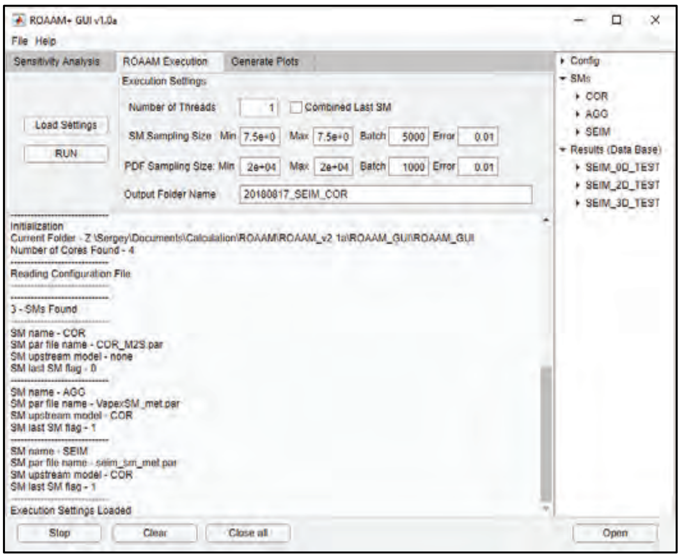

Execution Settings

Number of Threads: 1 ☐ Combined Last SM

SM Sampling Size: Min 7.5e+0 Max 7.5e+0 Batch 5000 Error 0.01

PDF Sampling Size: Min 2e+04 Max 2e+04 Batch 1000 Error 0.01

Output Folder Name: 20180817_SEIM_COR

```
------------------------------
Initialization
Current Folder - Z:\Sergey\Documents\Calculation\ROAAM\ROAAM_v2 1a\ROAAM_GUI\ROAAM_GUI
Number of Cores Found - 4
------------------------------
Reading Configuration File
------------------------------
------------------------------
3 - SMs Found
------------------------------
SM name - COR
SM par file name - COR_M2S.par
SM upstream model - none
SM last SM flag - 0
------------------------------
SM name - AGG
SM par file name - VapexSM_met.par
SM upstream model - COR
SM last SM flag - 1
------------------------------
SM name - SEIM
SM par file name - seim_sm_met.par
SM upstream model - COR
SM last SM flag - 1
------------------------------
Execution Settings Loaded
```

Figure 4.2.7. ROAAM+ GUI Interface

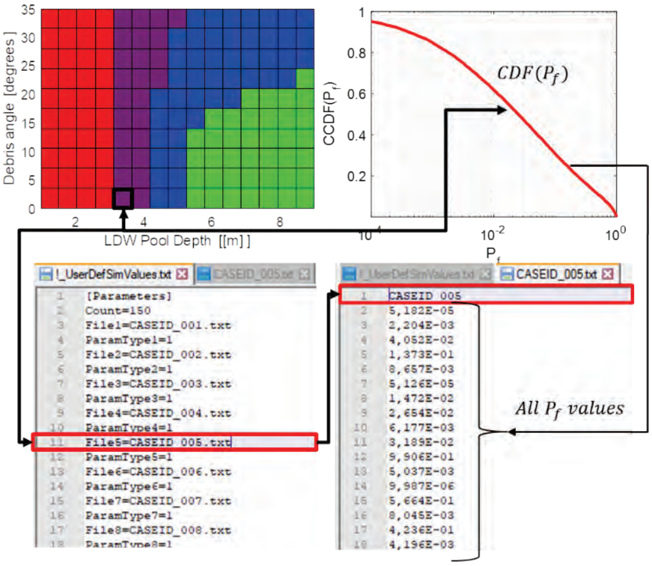

```
[Parameters]
Count=150
File1=CASEID_001.txt
ParamType1=1
File2=CASEID_002.txt
ParamType2=1
File3=CASEID_003.txt
ParamType3=1
File4=CASEID_004.txt
ParamType4=1
File5=CASEID_005.txt
ParamType5=1
File6=CASEID_006.txt
ParamType6=1
File7=CASEID_007.txt
ParamType7=1
File8=CASEID_008.txt
ParamType8=1
```

```
CASEID_005
5,182E-05
2,204E-03
4,052E-02
1,373E-01
8,657E-03
5,126E-05
1,472E-02
2,654E-02
6,177E-03
3,189E-02
9,906E-01
5,037E-03
9,987E-06
5,664E-01
8,045E-03
4,236E-01
4,196E-03
```

Figure 4.2.8. ROAAM+ Results Export to RiskSpectrum PSA

An extension to ROAAM+ GUI has been developed to export analysis results into specific format that can be used directly in the RiskSpectrum PSA, in form of “user defined simulation values”. In RiskSpectrum PSA these values can be used as probabilities, failure rates, frequencies, etc., for uncertainty analysis in PSA models [155]. In current implementation ROAAM+ results are exported into RS PSA user defined simulation parameters as probabilities

(“ParamType<Number>=1”), that can be used as basic events probabilities (e.g. probability of failure due to ex-vessel steam explosion, ex-vessel debris coolability). This functionality is accessible through the following menu in ROAAM+ GUI (File->Export->Export results to RS PSA), and schematically illustrated in Figure 4.2.***8***. Furthermore, basic information regarding each case can be found in the file “!_CaseData.txt” generated automatically during ROAAM+ results export. This information includes: Names of scenario parameters, (record I.Names followed by parameter names (e.g. [XPW], [SLPA] – the same names are used in SM\FM parameter definitions presented in 4.3, 4.5, 4.6 and 4.7); ROAAM data base scenario number; Respective output file number (CASEID_NNN) with the values of probability of failure; Failure mode number (FM-N) and the record O.Names followed by output parameter names (e.g. [TEMPMAX]>[TEMPMAXLIMIT2] – the same names are used in SM\FM output parameter definitions presented e.g. in 4.4)); Descriptive statistics, such as: 0.05,0.25,0.5,0.75,0.95 quantiles of distributions; Expected value and standard deviation.

4.3 ROAAM+ Deterministic Models

This chapter provides an overview of full and surrogate models used in the ROAAM+ framework for Nordic BWR, that connect plant damage states with respective threats to containment integrity. This models include (i) Melt ejection surrogate model (MEM SM), based on MELCOR code; (ii) Steam explosion surrogate model (SEIM SM), based on TEXAS V code; (ii) Ex-vessel debris agglomeration (AGG SM) – based on VAPEX SD code; (iv) ex-vessel debris coolability (DECO SM), based on DECOSIM code.

4.3.1. Melt Ejection Surrogate Model

The goal of Melt Ejection Framework (MEM) in ROAAM+ for Nordic BWR is to develop deterministic and surrogate models to establish connection between plant damage states and respective characteristics of (i) core relocation; (ii) vessel failure (timing and mode); and (iii) melt ejection (vessel breach size, melt superheat, composition, flow rate and total amount of ejected melt).

Sensitivity and Uncertainty Analysis using MELCOR code.

In ROAAM+ Framework for Nordic BWR Melt Ejection Surrogate Model (MEM SM) is used to predict melt release conditions from the vessel. Melt ejection mode surrogate model (MEM SM) [17] is based on the uncertainty analysis results of vessel failure mode and melt release conditions in Nordic BWR **[26]** predicted by MELCOR code [29][30] (Figure 4.3.***1***).

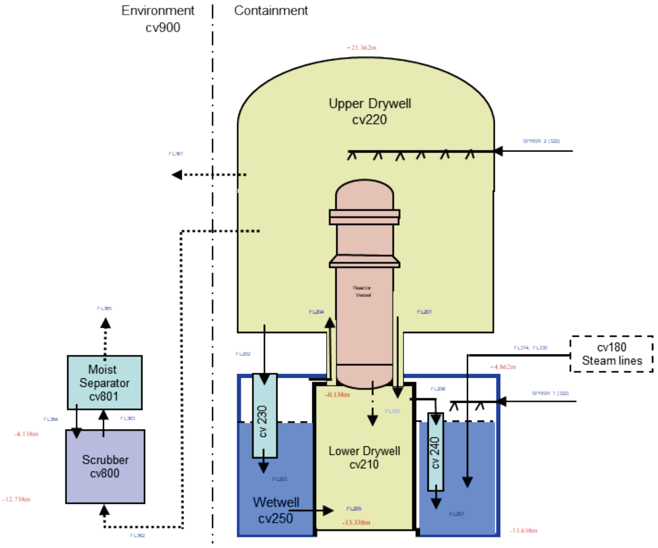

Figure 4.3.1. Nordic BWR Containment MELCOR Nodalization

The MEM SM is built for the unmitigated station blackout (SBO) scenario with depressurization, denoted as (SBO LP). In considered scenario the accident is initiated by the station blackout that results in complete loss of safety systems that require AC power. That is, the systems such as Emergency Core Cooling System (ECCS, both high and low pressure), Residual Heat Removal System (RHR) are considered unavailable during the whole transient. Reactor shutdown, safety relief valves and automatic depressurization systems are activated according to the control logic. Flooding of the lower dry well (LDW) from the wet well for ex-vessel debris coolability is initiated according to the standard control logic, i.e. (water level below TAF for 10min.). Containment venting system (CVS) includes filtered (through CVS MVVS – multi-venturi scrubbing system) and non-filtered containment venting, which are activated when correspondent pressure set-points are reached (5.5Bar and 6.5Bar in the upper drywell).

MELCOR Code Parameters for Sensitivity and Uncertainty Analysis

Vessel failure mode and melt release conditions are affected by the in-vessel phase of accident progression and resultant properties of relocated debris in the lower plenum, which depend on several phenomena, such as thermal hydraulic behavior in RPV, degradation and relocation of core materials, formation of a debris bed and its interactions with in-vessel structures, etc. Based on previous analysis [23] [25] we consider for sensitivity study several modelling parameters in MELCOR listed in Table 4.2.

Table 4.2. Selected MELCOR parameters and their ranges

	Parameter name	**Range**	**Units**
Debris Properties	Particulate Debris Porosity (PDPor)	[0.3-0.5]	[-]
	LP Particulate debris equivalent diameter (DHYPDLP)	[0.002-0.005]	m
Radial and Axial Debris Relocation	Time Constant for radial (solid) debris relocation (SC10201)	[180-720]	sec
	Time Constant for radial (liquid) debris relocation (SC10202)	[30-120]	sec
	Velocity of falling debris (VFALL)	[0.01-1.0]	m/s
Candling Model	Molten Zircaloy Melt Break Through Temperature (SC1131-2)	[2100-2540]	K
	Molten cladding/pool drainage rate (SC1141-2)	[0.1-2.0]	kg/(m·s)

	Refreezing heat transfer coefficient for Zircaloy (HFRZZR)	[1000-7500]	W/(m^2·K)
	Refreezing heat transfer coefficient for stainless steel, control rod poison material (HFRZSS)	[1000-2500]	W/(m^2·K)
Vessel Failure Modelling	Heat transfer coefficient from debris to penetration structures (HDBPN)	[100-1000]	W/(m^2·K)
	Penetration Failure Temperature (TPFAIL)	[1273-1600]	K
	Fraction of strain at which lower head failure occurs (SC1601-4)	[0.16 - 0.20]	[-]

Melt Release Modelling in MELCOR: After a failure has occurred, the mass of each material in the bottom axial level that is available for ejection (but not necessarily ejected) is calculated. There are two options available provided by so called solid debris ejection switch (Figure 4.3.***2***). In the default option (ON, IDEJ = 0), the masses of each material available for ejection are the total debris and molten pool material masses, regardless of whether or how much they are molten. In the second option (OFF, IDEJ = 1), the masses of steel, Zircaloy, and UO_2 available for ejection are simply the masses of these materials that are molten; the masses of steel oxide and control poison materials available for ejection are the masses of each of these materials multiplied by the steel melt fraction, based on an assumption of proportional mixing; the mass of ZrO_2 available for ejection is the ZrO_2 mass multiplied by the Zircaloy melt fraction. Additionally, the mass of solid UO_2 available for ejection is the Zircaloy melt fraction times the mass of UO_2 that could be relocated with the Zircaloy as calculated in the candling model using the secondary material transport model [29][30]. Furthermore, MELCOR puts additional constraints on the mass that can be ejected at vessel failure: (i) to initiate melt ejection the mass of molten material should be greater than SC1610(2) (5000kg – default value), or a melt fraction should be larger than SC1610(1) (0.1 – default value). In this analysis the values of sensitivity coefficients SC1610(1,2) were set to zero, so any amount of melt available for ejection would be ejected. In case of gross failure of vessel wall, it is assumed that all debris in the bottom axial level of the corresponding ring, regardless its state, is discharged linearly over 1s time step without taking into account failure opening diameter. The maximum mass of all materials that can be ejected during a single COR package time step is calculated as [29][30]:

$$M_{ej} = \rho_m A_f v_{ej} \Delta t$$

(1)

where ρ_m – is density of material being ejected, A_f- failure area, v_{ej} – velocity of debris being ejected, Δt – COR package time step. The fraction of the ejected material mass M_{ej} to the total mass available for ejection has a maximum value of 1.0. This fraction is applied to each material available for ejection. The velocity of material being ejected is calculated by [29][30]:

$$v_{ej} = C_d (2\Delta P / \rho_m + 2g\Delta z_d)$$

(2)

where C_d – is flow discharge coefficient ($C_d = 1$ (default value) was used in the analysis presented in this paper), ΔP – pressure difference between LP and reactor cavity control volumes, g – gravitational acceleration constant, and Δz_d – debris and molten pool height (see references [29][30] for more details).

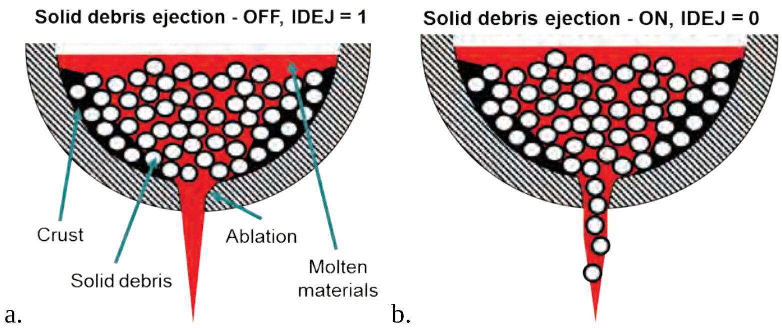

Figure 4.3.2. MELCOR modelling of debris ejection in case of penetration failure: (i) IDEJ1 – Solid debris ejection – OFF; (ii) IDEJ0 – Solid debris ejection – ON

Sensitivity Analysis Results

Figure 4.3.***3*** suggest that in case of (IDEJ0) the major part of the in-vessel debris is ejected from the vessel and the mass remaining at the time of vessel creep rupture is in the range from 0 to 50 tons for high pressure scenario and up to 100tons for low pressure scenario with respective median values equal to ~15 and 20 tons. In case of solid debris ejection off (IDEJ1) the ejected mass is limited to the molten materials and the mass that remains in-vessel is significantly higher, ranging from ~175 tons to almost 300 tons, with median values equal to ~250 and 225 tons for high and low pressure scenarios respectively.

Figure 4.3.***4*** shows the mass averaged temperature of the debris in the lower plenum at the time of vessel lower head wall failure. The temperature of the LP debris is significantly lower in scenarios simulated with solid debris ejection – on (IDEJ0) compared to (IDEJ1), e.g. in case of IDEJ0 the median value is ~1500 K while in case of IDEJ1 the median value is ~2200 K, which means that the major part of stainless steel and metallic zirconium will be molten at the time of vessel wall failure. On the other hand, the temperature is below 2500 K in most of the cases, which means that the mass of molten oxides will be small and mostly represented by stainless steel oxide. The results presented in 4.3.***3*** and 4.3.***4*** show that there is significant difference in melt release conditions between scenarios simulated with solid debris ejection – on (IDEJ0) compared to scenarios simulated with solid debris ejection – off (IDEJ1). Characteristics of individual releases can be the mass averaged debris ejection rate (kg/s), presented in Figure 4.3.***5***.

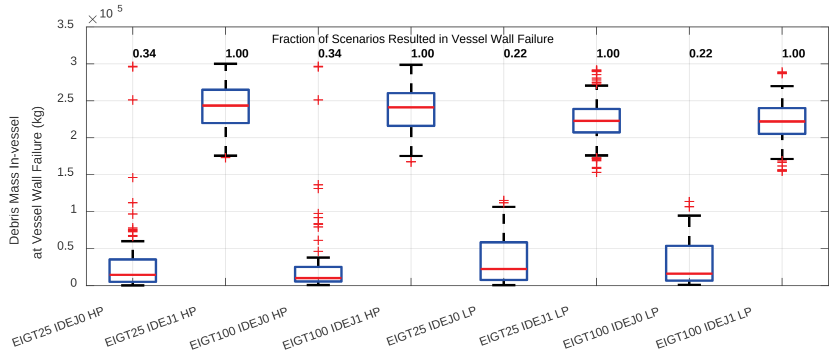

Figure 4.3.3. Debris mass in the LP at $\boldsymbol{T_{VF}}$ *(kg)*

The solid debris ejection mode (IDEJ) in MELCOR code has the dominant effect on the mode of failure and melt release from the vessel. In case of solid debris ejection – off (IDEJ 1, i.e. only molten materials can be released), 100% of the cases simulated with MELCOR code resulted in eventual failure of the vessel lower head wall, on average ~7000sec after initial vessel breach due to penetration failure, while in case of solid debris ejection – on (IDEJ 0) only 22-

34% (in low and high pressure scenarios respectively) of the cases resulted in the vessel LH wall failure. The median value of the in-vessel debris mass at the time of vessel lower head wall failure (in case of IDEJ 1) is ~250 tons, which means that only small amount of the debris has been released through the failed penetrations before the vessel LH wall failure; on the other hand, there are significant amounts of molten metallic debris remaining in-vessel at the time of vessel LH wall failure. This can be explained by the assumption that particulate debris will sink into a molten pool, displacing the molten pool volume upwards.

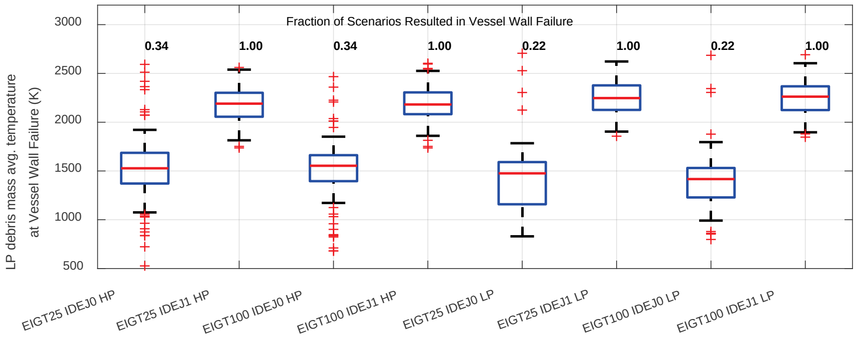

Figure 4.3.4. Mass averaged temperature of the debris in the LP at the time of vessel LH wall failure (K)

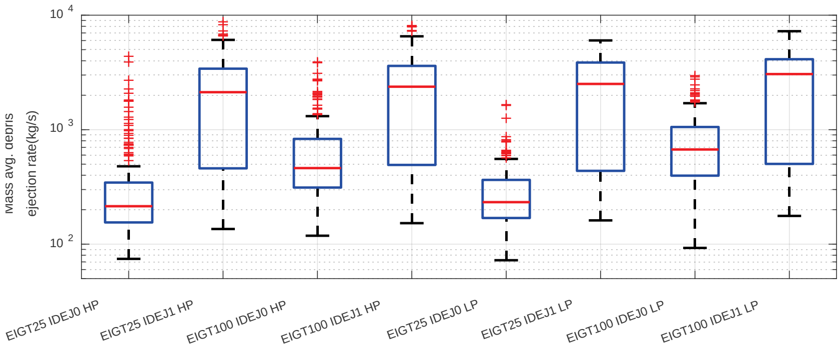

Figure 4.3.5. Mass averaged debris ejection rate (kg/s)

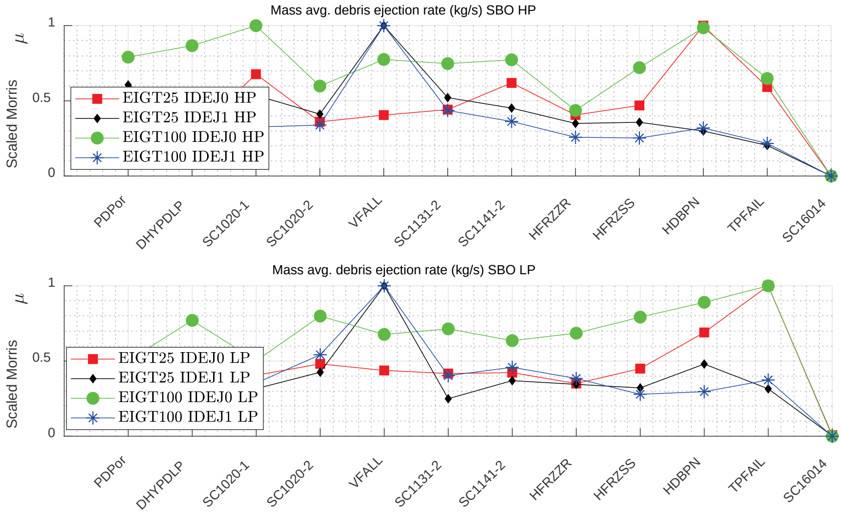

Figure 4.3.6. Sensitivity of the mass averaged debris ejection rate (kg/s)

The effect of the opening area of the vessel breach (EIGT25 and EIGT100) is noticeable, but only in case of solid debris ejection – on (IDEJ 0), where the larger opening area results in larger values of mass and energy release rates. The effect of severe accident scenario has also noticeable effect only in case of solid debris ejection – on (IDEJ 0), where the high pressure scenario results in slightly smaller median values of the mass and energy release rates compared to the low pressure scenario. Other MELCOR modelling parameters also have noticeable effect on the results. Figure 4.3.***6*** shows the sensitivity indices of the mass averaged debris ejection rate. In case of solid debris ejection – on (IDEJ 0) – the most influential parameters are TPFAIL and HDBPN in low pressure scenario, and HDBPN and SC1020-1 (only in EIGT100) in high pressure scenario. In case of solid debris ejection – off (IDEJ 1) the most influential parameter is VFALL in both accident scenarios and both penetration modelling options considered in the analysis. The dominating effect of VFALL in case of IDEJ1 can be explained by the modelling of vessel lower head wall failure in MELCOR code. As it was demonstrated in Figure 4.3.***3*** – in case of IDEJ1 100% of scenarios simulated result in eventual vessel lower head wall failure, and the mass of the in-vessel debris is in the range from ~200 to 300 tons. Note, that the debris ejection rate is limited only by (i) the amount of the debris in the cell with failed vessel LH segment and (ii) debris supply to the failure location – which is majorly controlled by VFALL [29][30]. In case of solid debris ejection – on, the release of both solid and liquid debris can start once there is a small fraction of molten material in a cell adjacent to a failed penetration. The release frees a volume in the cell making it available for debris relocation from the axial levels located above. This mechanism results in continuous supply of hot solid debris + melt mixture that can be gradually released from the vessel, and it is limited by the failure opening area and debris supply to the failure location.

Effect of Delayed Water Injection

Sensitivity and uncertainty analysis has been performed to assess the effect of eventual recovery of low pressure ECCS (LPCI) [24], which was initially unavailable due to power outage. It was assumed in the analysis that the water injection, can be recovered with full injection capacity (4x366kg/s) after 2h after initiating event (SBO)). The results obtained in the mitigated SBO scenario are compared to the previously obtained results for the unmitigated SBO scenario with depressurization (SBO LP), presented in [26].

Figure 4.3.***7*** show the distribution of the mass averaged debris ejection rate. In case of IDEJ=1 (solid debris ejection off) the mass averaged debris ejection rate can range from several hundred to several thousand kg/s with median value equal to ~2000-3000kg/s. In case of IDEJ=0 (solid and liquid (molten) debris can be ejected) the rate of debris ejection ranges from ~100kg/s to 1000kg/s, with median values equal to 230 and 670kg/s. In mitigated scenario the effect of solid debris ejection mode in MELCOR code is smaller, compared to unmitigated scenario, with median values equal to ~500-700kg/s regardless the solid debris ejection mode option being used.

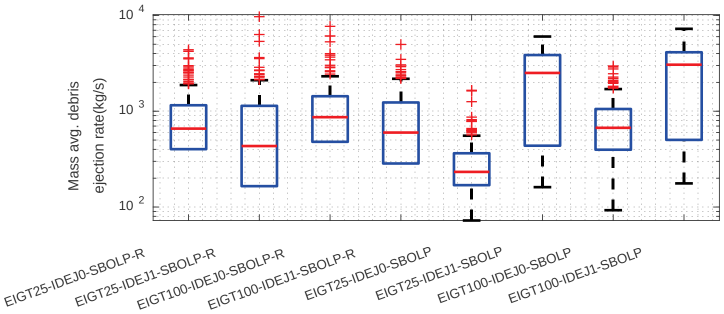

Figure 4.3.7. Mass averaged debris ejection rate (kg/s)

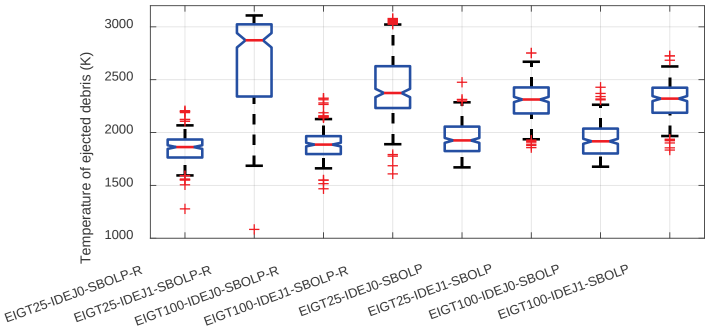

Figure 4.3.8. Mass averaged temperature of ejected debris (K)

Figure 4.3.***8*** show the mass averaged temperature of ejected debris, which is calculated as *the maximum debris temperature in the cells adjacent to the vessel lower head*. The results show that the ejected debris temperature is mostly affected by the solid debris ejection mode (IDEJ1 vs IDEJ0). In case of IDEJ=0 (solid and liquid debris can be ejected) – the temperature of ejected debris is slightly lower in the mitigated scenario, compared to the unmitigated scenario. It ranges from ~1700K to 2150K, and ~1700 to 2250K, with the median values equal to ~1850 and 1900K in mitigated and unmitigated scenarios respectively. In case of solid debris ejection – off (IDEJ=1, mostly molten materials can be ejected) – the temperature of ejected debris can reach very large values e.g. in the mitigated scenario with EIGT25 (~1700-3100K). In the unmitigated scenario with IDEJ=1, the temperature of ejected debris ranges from ~1850 to 2700K with median values equal to ~1900K in both EIGT100 and EIGT25. Further analysis is necessary to identify causes for such significant temperature differences of ejected debris (see Figure 4.3.***8***) between these scenarios with solid debris ejection – off (IDEJ1).

Uncertainty Analysis Results

Based on the results of sensitivity analysis a large-scale uncertainty analysis has been performed for low pressure scenario (SBO LP). The analysis has been performed for 4 scenarios (phenomenological splinters), given by combinations of solid debris ejection mode (IDEJ) and the fraction of ejected instrumentation guide tubes (EIGT):

- Solid debris ejection – on (IDEJ0) with 100% of IGTs failure in a radial ring (EIGT100-IDEJ0).
- Solid debris ejection – off (IDEJ1) with 100% of IGTs failure in a radial ring (EIGT100-IDEJ1).
- Solid debris ejection – on (IDEJ0) with 25% of IGTs failure in a radial ring (EIGT25-IDEJ0).
- Solid debris ejection – off (IDEJ1) with 25% of IGTs failure in a radial ring (EIGT25-IDEJ1).

Sampling is performed using scrambled Halton sequence [101][102]. In total 2997 uniformly distributed samples that represent different parameter combinations presented in Table 4.3 were generated for the analysis for every splinter scenario (i.e. total amount of code runs equals 2997x4). The results of the analysis are presented in from of box-and-whisker plots[5] [99]. Ad-

---

[5] Box values are quartiles of the distribution (q_1, q_3), whiskers lengths are calculated according to $q_1 - (q_3 - q_1)$ and $q_3 + (q_3 - q_1)$. Red crosses indicate individual "outliers" that lie outside the $[q_1 - (q_3 - q_1), q_3 + (q_3 - q_1)]$ interval.

ditionally, we use moving average and moving quantiles of the resultant distributions of different system response quantities (SRQs) to illustrate the trend in behavior and interdependencies of different parameters and quantities, as well as uncertainty in the results.

Figure 4.3.***9***a,b show the effect of MELCOR modelling parameters (penetration failure temperature – TPFAIL, heat transfer coefficient from debris to penetration(s) – HDBPN) on the time of vessel breach due to penetration failure T_{BRCH}. The results show that the larger values of TPFAIL and smaller values of HDBPN, on average, results in the larger values of vessel breach (Figure 4.3.***9***a,b). The behavior is very consistent for all splinter scenarios. Thus the effect of penetration failure modelling (EIGT) and debris ejection from the vessel (IDEJ) can be considered as negligible for the timing of vessel breach (T_{BRCH}) and the onset of debris ejection from the vessel (T_{REL}). The MELCOR code modelling parameters (especially TPFAIL and HDBPN) are the major contributors to the uncertainty in these system response quantities (SRQs).

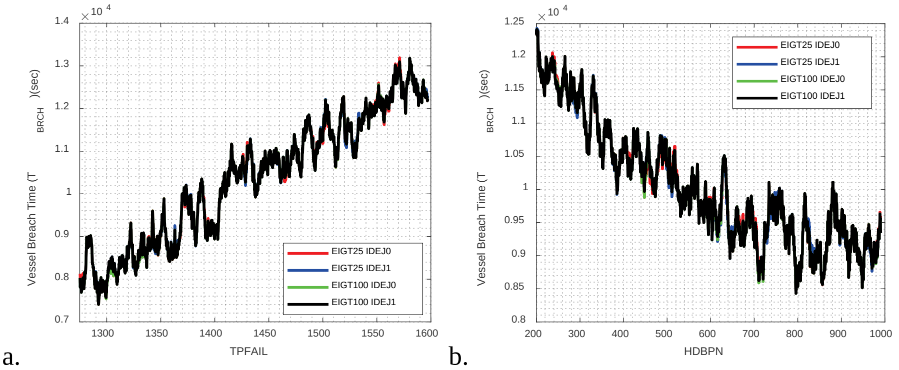

a. b.

Figure 4.3.9. (a) Moving average of $\boldsymbol{T_{BRCH}}$ *(sec) as a function of (a) TPFAIL (K); (b) HDBPN (W/(m^2·K))*

The mass averaged temperature of the debris in the lower plenum increases with the time delay between initial vessel breach and the onset of melt release from the vessel (Figure 4.3.***10***). The post-processing of the results using regression trees [97] has been performed. The regression trees were built for two scenario splinters (EIGT25-IDEJ0, EIGT100-IDEJ0) with solid debris ejection – on (IDEJ0), in order to identify what parameter combinations can lead to vessel LH wall failure, and for what parameter combinations this mode of failure can be avoided. The results [97] suggest that if penetration failure temperature is set above ~1545K then, the probability of the vessel LH wall failure is ~12-13%, however if it is below 1545K then it is ~27-30%. Furthermore, the moving average of the fraction of scenarios that result in vessel LH wall failure as a function of TPFAIL (Figure 4.3.***11***) suggest that the probability of this mode of failure gradually decreases with increase of TPFAIL, reaching ~7% at 1600K (upper range of the respective distribution).

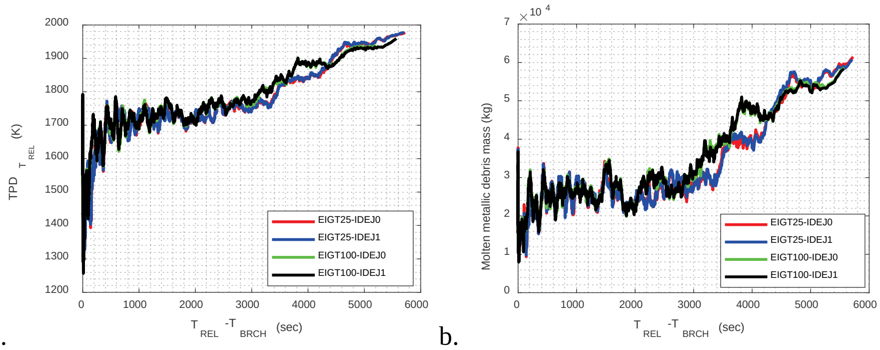

a. b.

Figure 4.3.10. Moving average of (a) mass averaged temperature of particulate debris in the LP (K) (b) molten metallic debris mass in the LP (kg); at $\boldsymbol{T_{REL}}$ *as a function of time delay between* $(\boldsymbol{T_{REL}} - \boldsymbol{T_{BRCH}})$ *(sec)*

The mass averaged debris ejection rate (kg/s) and mass averaged temperature of ejected debris was calculated using equation (3). Note that the MELCOR code does not calculate directly the temperature of ejected debris, therefore the temperature of ejected debris is assumed as the maximum particulate debris temperature in the COR cells adjacent to the vessel lower head. The results are presented in Figure 4.3.***12***a and Figure 4.3.***12***b.

$$\bar{f} = \sum_{i=1}^{N} f(t_i) * \Delta M_{ej}(t_i\ ) / M_{ej_{TOT}}$$
(3)

where $f(t_i)$ – system response quantity value as a function of time $\Delta M_{ej}(t_i)$ – fraction of mass ejected during t_i and t_{i-1} and $M_{ej_{TOT}}$ – total ejected mass. The results suggest that the mode of debris ejection from the vessel (IDEJ) has dominant effect on debris ejection rate from the vessel. The effect of penetration failure modelling (EIGT) has also quite significant impact on the results, especially in case of solid debris ejection – on (IDEJ0).

In case of EIGT25-IDEJ0 the mass averaged debris ejection rate is distributed between very small values (dripping mode) up to ~2000kg/s, however the major part of the distribution lies between 117-590 kg/s (0.05,0.95 quantiles respectively). In case of EIGT100-IDEJ0 the mass averaged debris ejection rate is distributed between very small values (dripping mode) up to ~4000kg/s, however the major part of the distribution lies between 250 and 1500 kg/s. In case of solid debris ejection – off (IDEJ1) the mass averaged debris ejection rate is distributed between ~300 and 7000-8000 kg/s, with median value equal to 3000 and 3250 kg/s for EIGT25 and EIGT100 respectively. Furthermore, post-processing of the results suggests that velocity of falling debris (VFALL) is one of the major contributors to the uncertainty in debris ejection rate in case of (IDEJ1). Smaller values of VFALL result in smaller values of mass averaged debris ejection rate, as illustrated in Figure 4.3.***13***. VFALL has no apparent effect on debris ejection rate in case of (IDEJ0), with exception to very small values of VFALL in EIGT100-IDEJ0 scenario splinter.

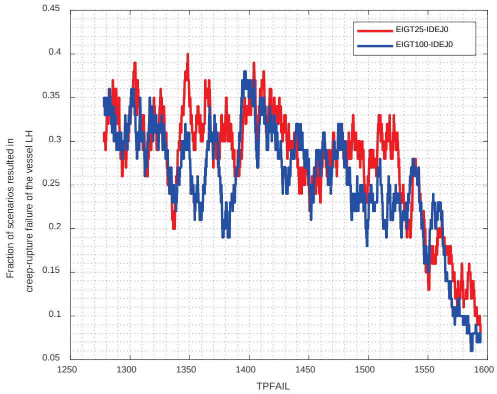

Figure 4.3.11. Fraction of scenarios resulted in creep-rupture failure of the vessel LH as a function of TPFAIL (K) in case of IDEJ0

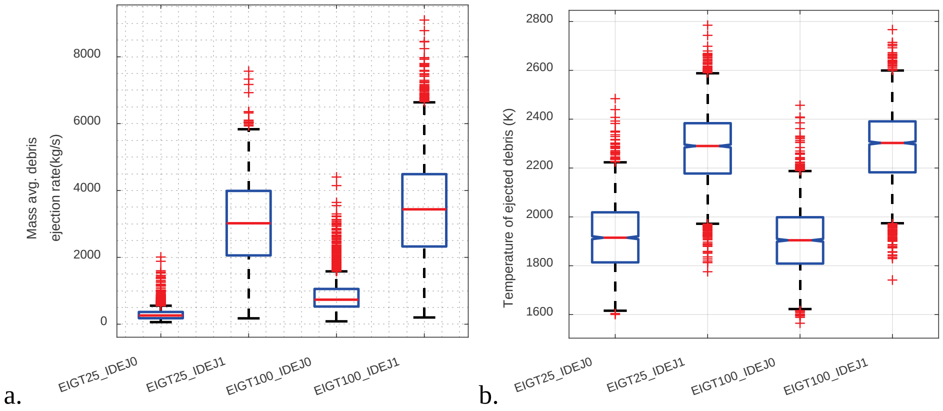

Figure 4.3.12. (a) Mass averaged debris ejection rate (kg/s); (b) Mass averaged temperature of ejected debris (K)

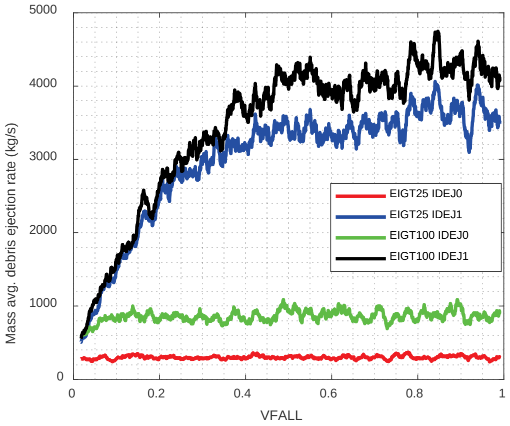

Figure 4.3.13. Moving average of mass averaged debris ejection rate (kg/s) as a function of VFALL (m/s)[26]

The resultant temperature of ejected debris (Figure 4.3.***12***b) is also affected by the debris ejection mode (IDEJ). In case of (IDEJ0) the temperature is distributed between 1600 and 2500K, with median value equal to ~1760K. In case of (IDEJ1) the temperature is distributed between ~1700 and 2800K, with median value equal to ~2300K. This means that the debris ejected from the vessel in case of (IDEJ1) will be (i) SS, ZR, SSOX will be molten, (ii) molten materials can have quite significant superheat; in case of (IDEJ0) the molten fraction of ejected debris will mostly limited to SS and SSOX, with significantly smaller melt superheat.

1.1.1 Development of Melt Ejection Surrogate Model

Post-processing of MELCOR analysis results of vessel failure mode and melt release conditions is carried out, in order to provide initial database of full model solutions for the development of the MEM SM. The MELCOR code does not predict directly such parameters as jet radius and jet speed used as initial conditions in the model for assessment of ex-vessel steam explosion loads on the containment (called SEIM SM) in Nordic BWR. The complete list of the input parameters in the SEIM SM can be found in [38].

Melt jet radius and speed. It is important to note that the current SEIM SM can predict steam explosion loads on the containment per single melt jet, defined in terms of jet radius (mm), with minimum size $\mathrm{R_{MIN}}$=35mm (that corresponds to a single IGT size break) and $\mathrm{R_{MAX}}$=300mm, without taking into account possible interactions between jets during premixing and explosion phases [38]. The jet radius and jet speed determine the size of the break in the vessel and initial velocity of the debris ejected from the vessel. These parameters can be derived using MELCOR predicted quantities, such as total debris mass ejected from the vessel (kg), total breach area (m^2), number of failed penetrations (-) and respective accident progression time. Thus, based on the MELCOR results, the debris ejection rate (kg/s) can be derived as follows:

$$\dot{M}_{deb}\left(\frac{kg}{s}\right) = \frac{\Delta M_{ejected}(kg)}{\Delta T_P(s)} \tag{4}$$

where $\Delta M_{ejected}$ is the mass of ejected debris during ΔT_P time interval (MELCOR plotting time step).

The jet radius can be derived through the total breach area (A_{breach}) and the number of failed IGTs ($nIGT_{failed}$) as follows:

$$RPARN = \sqrt{\frac{A_{breach}(m^2)}{\pi * nIGT_{failed}}} \tag{5}$$

The jet speed can be derived through the debris mass flow rate ($\dot{M}_{deb}$), total breach area (A_{breach}) and melt density (ρ) – which is currently assumed to take value equal to 8000kg/m^3 (average corium density, based on [95], [38]):

$$UPIN = \frac{\dot{M}_{deb}\left(\frac{kg}{s}\right)}{\rho\left(\frac{kg}{m^3}\right) * A_{breach}(m^2)} \tag{6}$$

Note that if gross failure of the vessel lower head is declared (due to vessel lower head creep-rupture) then it is assumed that in-vessel debris will be ejected through a single opening (jet) with the maximum jet radius size permitted by SEIM SM ($\mathrm{R_{MAX}} = 300mm$). Then the jet speed is calculated as:

$$UPIN = \frac{\sqrt{2gh} * R_{ring}{}^2 \mathrm{U}_{MELC}}{\sqrt{2gh\mathrm{R_{MAX}}^4 + (\mathrm{R_{MAX}}^4 - R_{ring}{}^4)\mathrm{U}_{MELC}{}^2}} \tag{7}$$

where $g\left(\frac{m}{s^2}\right)$ – gravitational acceleration constant, $h(m)$ - free fall height (derived from water pool depth), $\mathrm{U}_{MELC}\left(\frac{m}{s}\right)$ – initial jet velocity calculated by equation (6) and R_{ring}(m) – is the radius derived from the cross section area of the ring with failed segment of vessel lower head.

Temperature of ejected debris. The temperature of ejected debris (TPIN) is calculated as the maximum debris temperature in the cells adjacent to the vessel lower head.

Pool Conditions. The pool conditions, such as water pool depth (XPW), lower drywell pressure (PO) and water pool temperature (TLO) – can be directly imported from the MELCOR analysis results.

Post-Processing of the Results, Assumptions and Limitations. To summarize, when performing post-processing of the MELCOR results the following assumptions have been made. Uniform distribution of ejected debris flow between all failed IGTs, without taking into account failed IGTs locations (e.g. in the center or periphery). Ejected debris density is assumed to be equal to $\rho = 8000\left(\frac{kg}{m^3}\right)$. This vale was assumed based on SERENA-II BWR benchmark exercise [95], [38]. Debris ejection rate $\dot{M}_{deb}$ is uniform during MELCOR plotting time step $\Delta T_P(s)$. Debris ejection temperature is calculated as the maximum particulate debris temperature in the COR cells adjacent to the vessel lower head. No correction is made for the fraction of solid debris during debris ejection from the vessel. If gross failure is declared (due to vessel lower head creep-rupture) the ejection is calculated as a single jet with jet radius defined as $\mathrm{R_{MAX}} = 300mm$ (max. permitted value of SEIM SM) and respective jet velocity is recalculated based on equation (7). The last assumption is particularly necessary, since MELCOR code does not consider neither debris state nor breach area when calculating debris ejection in case of gross failure of vessel lower head wall (e.g. due to creep-rupture). Currently, it is assumed in MELCOR code that all debris in the bottom axial level of the corresponding ring, regardless its state, is discharged linearly over 1s time step without taking into account failure opening diameter [29], [30]. Current state-of-knowledge in the field of vessel failure mode and multi-component debris ejection from the vessel is quite limited. In reality, the process of vessel failure and debris ejection involve several interacting phenomena, which include formation and accumulation of liquid melt, gravity driven drainage of molten materials through the porous debris bed, melt resolidification and crusts formation in colder regions of the debris bed, that prevent further material drainage, which can result either in slow dripping of the melt from the vessel or in accumulation of significant amounts of superheated metallic melt above the crust, which will be released upon crust remelting/failure. The crust formation can result in interaction of significant amounts of debris at high temperature with the vessel lower head wall, and significant mechanical loads on the structures which can lead to creep-rupture failure of the vessel lower head and massive ejection of the debris from the vessel. It is difficult to assess the fraction of failed (ejected) penetrations. Thus the fraction of failed penetrations and debris ejection mode (solid debris ejection switch) are treated as splinters in ROAAM+ considering the (i) high sensitivity of MELCOR results to the selection of these parameters and (ii) lack of knowledge about them. Splinter scenario in ROAAM [114] is defined as a scenario where relevant epistemic uncertainties are *beyond the reach of any reasonably verifiable quantification*. Thus, in total 4 different splinter scenarios, with respective surrogate models are considered in the analysis: EIGT100 IDEJ0 LP; EIGT100 IDEJ1 LP; EIGT25 IDEJ0 LP; EIGT25 IDEJ1 LP. Based on the post-processing of the MELCOR analysis results, respective mass averaged values were calculated using eq.(8).

$$\bar{f} = \sum_{i=1}^{N} f(t_i) * \Delta M_{ej}(t_i)/M_{ej_{TOT}} \tag{8}$$

where $f(t_i)$ – system response quantity value as a function of time $\Delta M_{ej}(t_i)$ – fraction of mass ejected during t_i and t_{i-1} and $M_{ej_{TOT}}$ – total ejected mass. The motivation for the use of mass averaged values in SM development is twofold, first – the current implementation of SEIM SM does not calculate explosion impulses during time dependent melt release, and consequences of ex-vessel steam explosion, based on the sensitivity study presented in [34], are determined by the mass (enthalpy) released from the vessel.

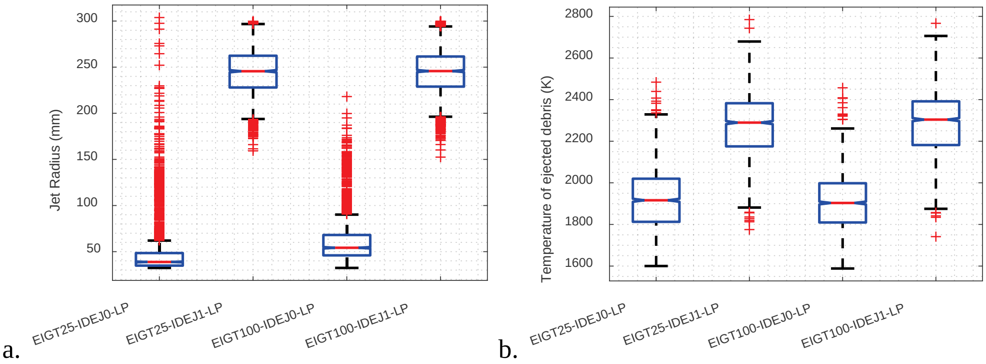

Figure 4.3.14. a) Mass averaged Jet Radius (mm); b) Mass averaged temperature of ejected debris (K)

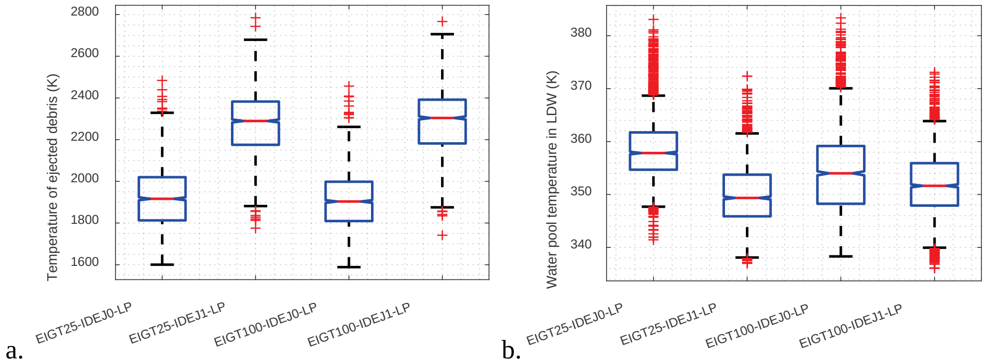

Fig 4.3.15. a) Mass averaged temperature of ejected debris (K); b) Mass averaged temperature of LDW Pool (K)

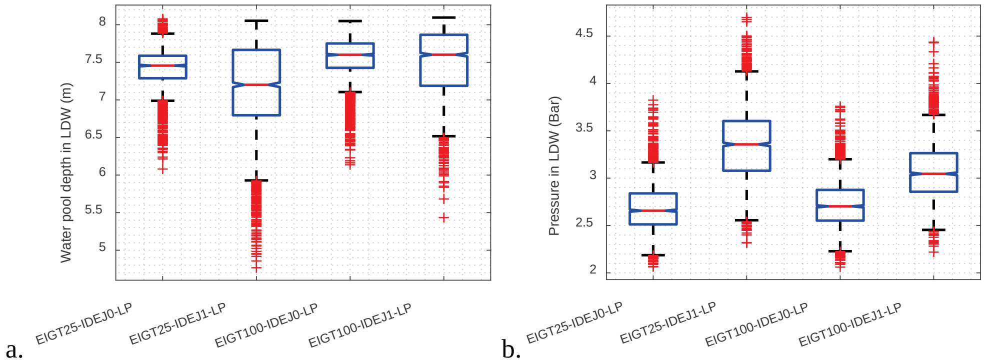

Fig 4.3.16. a) Mass averaged LDW Pool Depth (m); b) Mass averaged Pressure in the LDW (Bar)

The results of post-processing are presented in 4.3.14. -4.3.***16*** in form of box-and-whisker plots with a total amount of samples for each splinter scenario considered, equals to $n_{MELCOR} = 2997$. The list of input parameters and respective ranges used to generate the data base of MELCOR solutions is presented in Table 4.3, detailed discussion on parameters selection, and sensitivity of the MELCOR code response to the variability of these parameters can be found in Section 0. The same parameters will be used to develop the MEM SM. The list of MEM SM outputs and their ranges is presented in Table 4.4. Note that the ranges, presented in the Table 4.4 can be considered as conservative than the actual MEM SM predicted quantities.

Melt Ejection Surrogate Model

Regression tree learning applies so called *recursive partitioning* of the global input space into smaller sub-domains, where simple models can be applied. The global predictive model has two parts: (i) the recursive partitioning, and (ii) a model for each final cell (leaf node) of the partition (regression tree). In this work the regression trees were trained on the post-processed results of MELCOR code analysis of vessel failure mode and melt release conditions in unmitigated station blackout scenario with depressurization (SBO LP). This scenario corresponds to HS2-TL4 plant damage state in PSA L1. Fraction of failed penetrations and debris ejection mode (solid debris ejection switch) are treated as splinters [114] in ROAAM+ considering the (i) high sensitivity of MELCOR results to the selection of these parameters and (ii) lack of knowledge about them. In total 4 splinter scenarios, with respective surrogate models are considered in the analysis: EIGT100 IDEJ0 LP; EIGT100 IDEJ1 LP; EIGT25 IDEJ0 LP; EIGT25 IDEJ1 LP. The list of the MEM SM input parameters and their ranges is presented in Table 4.3. The list of MEM SM outputs and their ranges is presented in Table 4.4.

Table 4.3. MEM SM epistemic modeling parameters and ranges

Parameter name	Range	Units
Particulate Debris Porosity (PDPor)	[0.3-0.5]	[-]
LP Particulate debris equivalent diameter (DHYPDLP)	[0.002-0.005]	M
Time Constant for radial (solid) debris relocation (SC10201)	[180-720]	Sec
Time Constant for radial (liquid) debris relocation (SC10202)	[30-120]	Sec
Velocity of falling debris (VFALL)	[0.01-1.0]	m/s
Molten Zircaloy Melt Break Through Temperature (SC1131-2)	[2100-2540]	K
Molten cladding/pool drainage rate (SC1141-2)	[0.1-2.0]	kg/m-s
Refreezing heat transfer coefficient for Zircaloy (HFRZZR)	[1000-7500]	W/m^2-K
Refreezing heat transfer coefficient for stainless steel, control rod poison material (HFRZSS)	[1000-2500]	W/m^2-K
Heat transfer coefficient from debris to penetration structures (HDBPN)	[100-1000]	W/m^2-K
Penetration Failure Temperature (TPFAIL)	[1273-1600]	K

Table 4.4. MEM SM output parameters and their ranges

Parameter name	Range	Units
Lower drywell pool depth	[2-9]	M
Lower drywell pressure	[1.e5-5.5e5]	Pa
Lower drywell pool temperature	[293-393]	K
Jet radius	[0.035-0.3]	M
Melt inlet temperature	[1700-3200]	K
Initial jet velocity	[0-8]	m/s
Time after SCRAM	[10000-50000]	sec
Melt release duration	[1000-10000]	sec
Ejected debris mass	[150000-300000]	Kg

In 4.3.***17***-4.3.***20*** we show the results in form of respective cumulative distribution functions (CDFs) of different MEM SM response quantities generated with random sampling of MEM SM in ROAAM+ Framework. The results are compared to the original MELCOR data distribution, obtained with random sampling of the MELCOR code. The results show that the MEM SM reproduces the distributions of the different characteristics of melt release from the vessel (e.g. Jet radius - RPARN (mm) and Jet velocity – UPIN (m/s)) in Nordic BWR in different

splinter scenarios. This feature of the SM is crucial for the risk analysis. The results show that in some cases the MEM SM slightly underestimates the tails of the distribution, however these discrepancies can be taken into account by application of the approaches for quantification of the uncertainty due to SM approximation of FM[36]. One of the disadvantages of application of the regression trees is a non-smooth response, which is observable on the plots – blue lines on Figures 4.3.***17***-4.3.***20***. However, it does not affect significantly the statistical result. Smoothness can be achieved by increasing a number of leaf nodes in the tree. However, it might lead to overfitting, and overall reduction of predictive capability of the model.

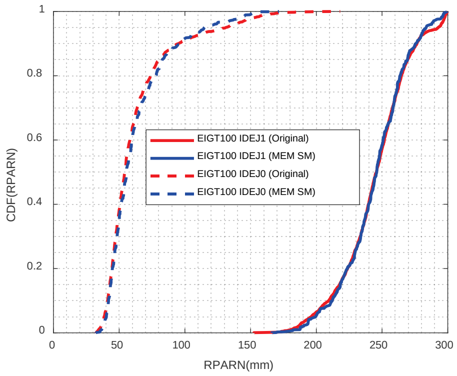

Figure 4.3.17. Distribution of jet radius for EIGT100, comparison MEM SM (red) to original data (blue)

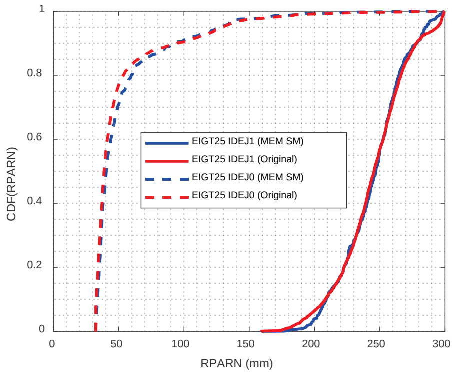

Figure 4.3.18. Distribution of jet radius for EIGT25, comparison MEM SM (red) to original data (blue)

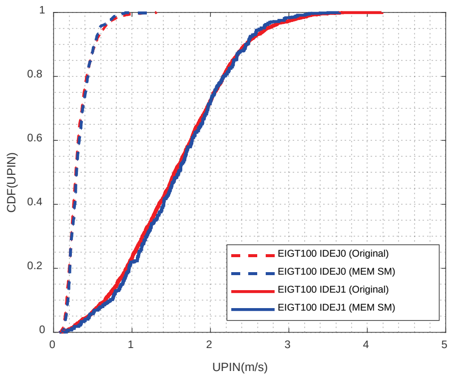

Figure 4.3.19. Distribution of jet speed for EIGT100, comparison MEM SM (red) to original data (blue)

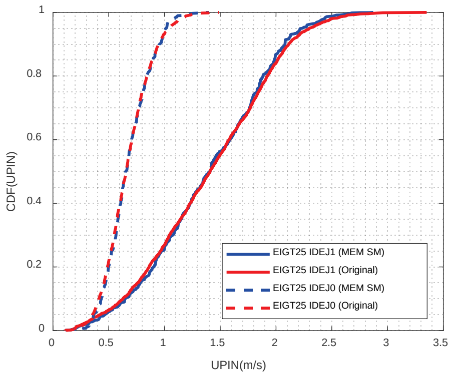

Figure 4.3.20. Distribution of jet speed for EIGT25, comparison MEM SM (red) to original data (blue)

4.3.2. Ex-vessel Steam Explosion Surrogate Model

Steam Explosion Surrogate Model (SEIM SM) has been developed [38], [34] for the assessment of the risk of containment failure due to steam explosion in Nordic BWR [36] using a database of solutions generated by an FCI code TEXAS-V. The problem setting in TEXAS-V for assessment of the effect of melt release conditions in Nordic BWR on the containment loads is shown in Figure 4.3.***21***. Texas-V is has two modules for calculation of premixing and steam explosion [11]. The surrogate model uses Multilayer Perceptron Artificial Neural Network (ANN) [38], [34]. The ANN predicts impulses which correspond to certain percentiles of the impulse distribution for given melt release characteristics (Table 4.5) and arbitrary triggering time. The motivation for the parameters selection and respective ranges can be found in [38]. Note that since MELCOR code in most of the cases predicts melt release temperatures below 2500-2700K [26][27], we assume mostly “metallic release”, thus melt properties (such as, CP, RHOP, KFUEL, etc.) were adjusted accordingly.

Table 4.5. SEIM SM input and epistemic modelling parameters and ranges

Parameter name	Range	Units
Water level (XPW)	[2-9]	m
System pressure (PO)	[1.e5-5.5e5]	Pa
Water temperature (TLO)	[288-368]	K
Initial Jet radius (RPARN)	[0.035-0.3]	m
Fuel heat capacity (CP)	[350-650]	J/kg*K
Fuel density (RHOP)	[7500-8000]	kg/m^3
Fuel latent heat (PHEAT)	[2.6e5-3.0e5]	J/kg
Fuel melting temperature (TMELT)	1700	K
Fuel inlet temperature (TPIN)	[1710-3200]	K
Melt release velocity (UPIN)	[1-8]	m/s
Fuel thermal conductivity (KFUEL)	[6-32]	W/m*K
Proportionality constant for the rate of fuel fragmentation (CFR)	[2.e-3-2.7e-3]	-
Fragmentation time (TFRAGLIMIT)	[0.5e3-2.5e-3]	s

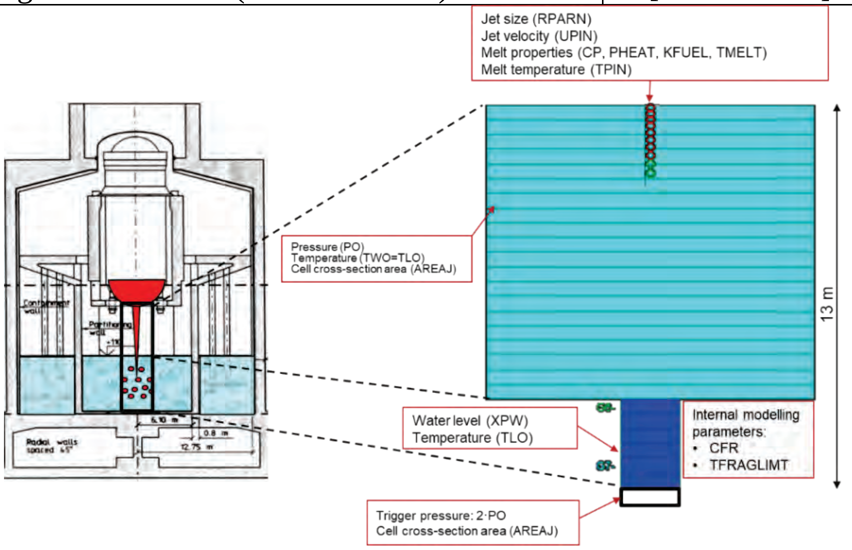

Figure 4.3.21. Nordic BWR TEXAS-V model setup [39]

4.3.3. Ex-vessel Debris Coolability

Non-coolable debris bed in the lower drywell presents a credible threat to containment integrity. Phenomenology of ex-vessel debris formation and coolability includes (i) jet breakup; (ii) melt droplets cooling and solidification; (iii) agglomeration of melt droplets; (iv) particulate debris spreading in the pool; (v) debris self-levelling; (vi) debris coolability; (vii) post-dryout debris behavior (e.g. remelting).

The debris bed is cooled by evaporation water that is pushed inside the debris bed by hydrostatic pressure. Steam generated inside the debris bed is escaping predominantly upwards, generating convection flows in the pool and changing conditions for melt-coolant interactions. This changes particle properties (size distribution and morphology), packing, agglomeration, and bed formation phenomena. The large-scale circulation in the pool can spread effectively the falling corium particles over the basemat floor, distributing the sedimentation flux beyond the projection area of particle source (e.g., size of reactor vessel). Debris is gradually spread under the influence of steam production in the bed, resulting in self-leveling of the settled portion of the debris and changing the shape of debris bed with time.

The ex-vessel debris coolability framework is currently subdivided into sub-frameworks: (i) analysis of the effect of melt release conditions on jet breakup, droplets cooling and solidification and agglomeration of melt droplets – treated in Debris Agglomeration analysis (VAPEX SM and Agglomeration mode [55][54]) and Agglomeration SM (AGG SM [62]) ; (ii) ex-vessel debris spreading and coolability – treated in DECOSIM code (DECO SM)[139][135].

Ex-vessel Debris Agglomeration

Hydraulic resistance is a limiting factor that determines maximum decay heat that can be removed from the bed. If decay heat exceeds this maximum value, it will lead to the bed dryout, reheating and remelting of the debris. If melt is not completely solidified prior to settlement on top of the debris bed, agglomeration of the debris and even “cake” formation is possible [112]. Formation of agglomerated debris can significantly increase hydraulic resistance and reduce maximum decay heat which can be removed without reaching dryout of the debris bed. Thus, agglomeration is important factor which can inhibit effectiveness of ex-vessel debris coolability [112]. Phenomena of agglomeration of the debris and “cake” formation have been observed in fuel-coolant interaction (FCI) experiments with prototypic corium mixtures (e.g. in FARO [94], CWTI and CCM [110] tests) and with corium simulant materials (e.g. in DEFOR-E [45] and DEFOR-S [80] tests), the first systematic experimental data was provided in DEFOR-A [81], [83], [84] tests that was used for development and validation of modeling approaches for prediction of agglomerated debris in various scenarios of melt ejection. The data obtained in DEFOR-A tests was used for development and validation of modelling approaches for prediction of agglomerated debris in various scenarios of melt ejection (e.g. [55], [54]). Proposed model for agglomeration is implemented in deterministic code VAPEX [12] that simulates Fuel-Coolant-Interaction (FCI) phenomena including melt jet breakup, formation of liquid droplets, heat transfer between melt and coolant, sedimentation and solidification of the particles.

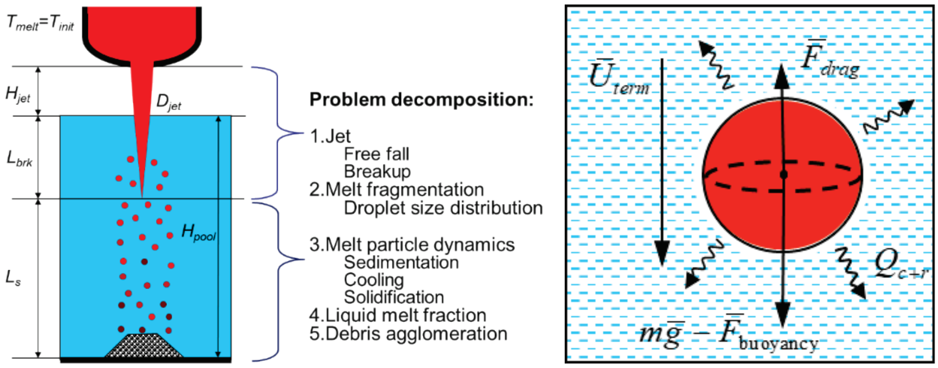

Figure 4.3.22. Problem decomposition for debris agglomeration surrogate model [62]

Based on VEPEX code a physics based surrogate modelling approach was employed where computational efficiency and numerical stability are achieved by (i) considering only most important physical phenomena, and by (ii) decomposing tightly coupled problem into a set of loosely coupled ones with information exchange through initial and boundary conditions. The merits of physics-based SM are (i) reduced number of the full model runs which are necessary for the calibration process; (ii) application of the SM beyond the domain covered with the original model. Physical phenomena and parameters important for assessment of agglomeration fraction are presented in Figure 4.3.*22*. The most important physical phenomena are modelled in the SM explicitly. Mutual feedbacks between such parameters as jet breakup length, coolant void fraction and velocity are considered as closures. Details of model implementation, calibration and verification are provided in [55], [54].

An ANN based surrogate model (AGG SM) was developed for analysis of the fraction of agglomerated debris [62]. The AGG SM predicts the fraction of agglomerated debris depending on melt release and pool conditions, provided by MEM SM. The list of input parameters of AGG SM is presented in Table 4.6. More details on full and surrogate models, experimental data and parameters used for SM development can be found in [55], [54], [62] and [112].

Table 4.6: AGG SM input parameters

Variable Name	Description	Units	Range
RHOP	Fuel density	kg/m3	[7500 ; 8500]
PHEAT	Fuel latent heat	J/kg	[2.6e5 ; 4.0e5]
CP	Fuel heat capacity	J/kg*K	[350 ; 650]
KFUEL	Fuel thermal conductivity	W/m*K	[2 ; 42]
EM	Emissivity	-	[0.1 ; 1.0]
TMELT	Fuel Melting Temperature	K	[1600 ; 2800]
TSH	Melt superheat	K	[10 ; 1000]
RPARN	Jet radius	m	[0.07 ; 0.6]
UPIN	Melt release velocity(initial)	m/s	[1 ; 8]
TLO	Water pool temperature	K	[288 ; 368]
XPW	Pool depth	m	[5 ; 9]
PO	Containment pressure	Pa	[1e5 ; 4e5]

Ex-vessel Debris Coolability

Ex-vessel debris coolability surrogate model (DECO SM) is based on DECOSIM code. The mathematical models implemented in DECOSIM code are based on multifluid formulation, they include several submodules describing two-phase pool flows, disperse particle sedimentation, as well as flows in heat-releasing porous media related to debris bed coolability in in-vessel and ex-vessel configurations. In this work, we concentrate on validation of the models relevant to modeling natural convection flows in the pool, spreading of particles and their fallout onto the bottom surface of the pool [135]. Air-water flow in the pool is described by the mass and momentum, and energy conservation equations for liquid water and gas; turbulence is taken into account only in continuous liquid and described by the $k - \varepsilon$ model with additional terms for turbulence generation due to relative motion of liquid and gas phases. Validity of $k - \varepsilon$ turbulence model in the context of two-fluid model has been addressed previously [52]. Flow-particle interaction due to drag depends on the diameter of the particle, relative velocity and phase composition of the ambient two-phase mixture. To account for turbulent dispersion of particles, the random walk model is applied. The effects of turbulence on particle dispersion are modelled by adding a fluctuating component to the liquid phase velocity.

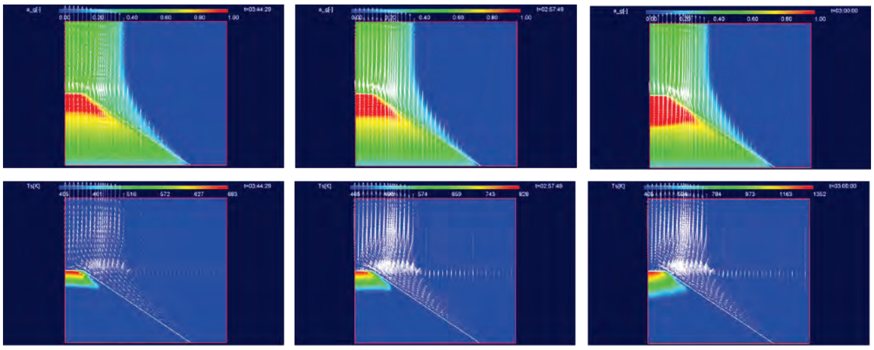

χ_{top}= 0%　　　20%　　　50%

Figure 4.3.23. Void fraction (top row), particle temperature (bottom row) for particle size ($\boldsymbol{d_p}$=2mm), decay heat power W=250W/kg [140]

A set of improvements to full and surrogate models has been implemented recently in order to account for low permeability zones in the bulk of debris bed, which can happen due to incomplete fragmentation of corium jet due to e.g. jet penetration depth is larger than pool depth; agglomeration of debris fragments due to incomplete solidification of melt droplets, etc. Furthermore, formation of low permeability zones can be enhanced by effective pool depth decrease with time due to debris bed growth and increase in jet size due ablation of the opening in the vessel.

Table 4.7: DECO SM input parameters

Variable Name	Description	Units	Range
RHOP	Fuel density	kg/m3	[7500 ; 8500]
PHEAT	Fuel latent heat	J/kg	[2.6e5 ; 4.0e5]
CP	Fuel heat capacity	J/kg*K	[350 ; 650]
KFUEL	Fuel thermal conductivity	W/m*K	[2 ; 42]
TMELT	Fuel Melting Temperature	K	[1600 ; 2800]
TSH	Melt superheat	K	[10 ; 1000]
TSCRAM	Time after SCRAM	s	[10000-50000]
TREL	Release duration	s	[1000 ; 10000]
MAGG	Mass fraction of agglomerates	[-]	[0 ; 1]
POR	Debris bed porosity	[-]	[0.3 ; 0.45]
SLPA	Slope angle	degrees	[0 ; 30]
DPAR	Effective particle diameter	mm	[1.5 ; 3]
TLO	Water pool temperature	K	[288 ; 368]
XPW	Pool depth	m	[5 ; 9]
PO	Containment pressure	Pa	[1e5 ; 4e5]

Based on a set of full model simulations it has been shown that agglomerates (χ_{top}) increase drag and promote development of a larger and hotter dry zone on top of the debris bed (Figure 4.3.*23*). Physics based DECO SM has been updated to consider the effect of melt agglomerated on debris bed coolability [139], [140]. Table 4.7 presents the list of DECO SM input parameters and respective ranges. More details on full and surrogate models for ex-vessel debris coolability can be found in [139], [135], [112], [140].

Currently, in assessment of the risk of formation of non-coolable debris bed two types of failure criteria were implemented. The first criterion assumes that debris bed is “coolable” if there is “no dryout”. However, it might be too conservative. After dryout, particle temperature rises above the saturation temperature, however, a small dry zone can be coolable by steam flow and high temperatures are reached only in case of large dryout zones. Therefore, in updated DECO SM [140] a set of less conservative criteria was introduced - debris bed is non-coolable if debris remelting or oxidation occurs, and it is coolable if debris temperature is stabilized below certain temperature limit. In current implementation we consider three temperature limits: (i) 1200K - for debris oxidation [9], (ii) 1700K - melting temperature of stainless steel as assumed in MELCOR code MP package [29][30], and 2800K - melting temperature of oxidic debris [29][30].

4.4 Uncertainty Quantification and Risk Analysis Results

This section presents the results of application of the ROAAM+ framework for Nordic BWR for analysis of ex-vessel debris coolability (addressed in the section 4.4.2) and ex-vessel steam explosion (addressed in section 4.4.1). Synthesis of the result obtained with ROAAM+ for treatment within enhanced PSA model is presented in section 0.

4.4.1. Ex-vessel Steam Explosion

Risk Analysis using standalone SEIM SM

The analysis of the risk of containment failure due to ex-vessel steam explosion has been performed using surrogate model for ex-vessel steam explosion in Nordic BWR [34]. In the analysis two fragility limits for containment hatch door in the lower drywell of Nordic BWR were considered: (i) original design “non-reinforced hatch door” – 6kPa*s; and (ii) modified design “reinforced hatch door” – 50kPa*s.

The ROAAM+ treatment for Nordic BWR SAM is iterative in nature and aims to reduce the uncertainty to the level where a robust decision can be made (i.e. decision becomes insensitive to the remaining uncertainty). Therefore, as the first step of the analysis we treat all parameters in steam explosion surrogate model (Table 4.5) as model intangible parameters, i.e. with incomplete probabilistic knowledge.

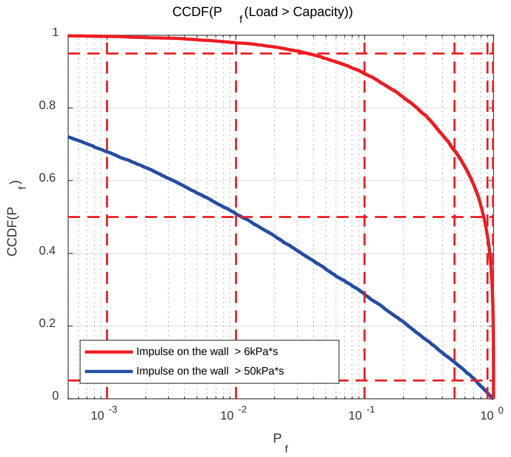

*Figure 4.4.1. CCDF of conditional containment failure due to ex-vessel steam explosion: (red) 6kPa*s fragility limit (non-reinforced hatch door), (blue) 50kPa*s fragility limit (reinforced hatch door) using SEIM SM[16]*

Using ROAAM+ probabilistic framework the complementary cumulative distribution of probability of failure $CCDF(P_F)$ can be obtained using SEIM SM. Figure 4.4.***1*** illustrate $CCDF(P_F)$ obtained for non-reinforced and reinforced hatch door. The results show that the screening probability P_S =1.e-3 which corresponds to “physically unreasonable” limit (see [114] for details) is exceeded in approximately 99% of the cases with non-reinforced hatch door and in ~70% of the cases with reinforced hatch door. Thus, it is not possible to demonstrate that failure is physically impossible (i.e. “possibility” of containment failure is low) even with reinforced door.

If consider “necessity” of containment failure, i.e. the possibility that containment doesn’t fail. For that we set the screening probability to $P_S = 0.999$. The fraction of scenarios where $P_F > P_S = 0.999$, is approximately 0.06 and 0.003 for the original and modified designs respectively. The “necessity” of the containment failure due to ex-vessel steam explosion is not sufficiently high to claim that the failure is unavoidable. Analysis based on the total failure probability distribution is useful for an overall assessment of system reliability and can be used for decision making in cases when both the possibility and necessity of failure are either low or high simultaneously. However, in cases such as shown in Figure 4.4.***1***, where possibility of failure can be large but necessity is relatively small, further understanding of the system might be useful in order to make a decision. Note that risk assessments are based on available knowledge. Thus, there can be two possible decisions:

(i) Collect more knowledge, if it is likely that reduced uncertainty in the analysis can help to demonstrate effectiveness of the strategy (focus on the improvement of the risk assessment).

(ii) Modify current SAM strategy, if it is unlikely that more knowledge will change conclusion (focus on the risk management).

By considering the failure probability distribution, it might be hard to choose between those decisions. In this example further clarification of the importance of different input parameters for steam explosion analysis will be helpful in order to converge to a decision with respect to (i) effectiveness of SAM, or (ii) need for more information, or (iii) the need to modify the design. In order to tell which parameters' uncertainty should be addressed first, we perform global sensitivity analysis using Morris method (see [98][109] for details). In the analysis we considered the effect of SEIM SM input parameters, presented in Table 4.5 on the magnitude of explosion impulse, predicted by the SEIM SM. The results of sensitivity analysis are presented in Figure 4.4.*2* in the form of Morris diagram, where the parameters in the legend are ordered according to their influence on the SEIM SM response, characterized by the Morris μ values (see [109] for details). The most influential parameters are RPARN (initial jet radius), TPIN (fuel inlet temperature) and XPW (water pool depth).

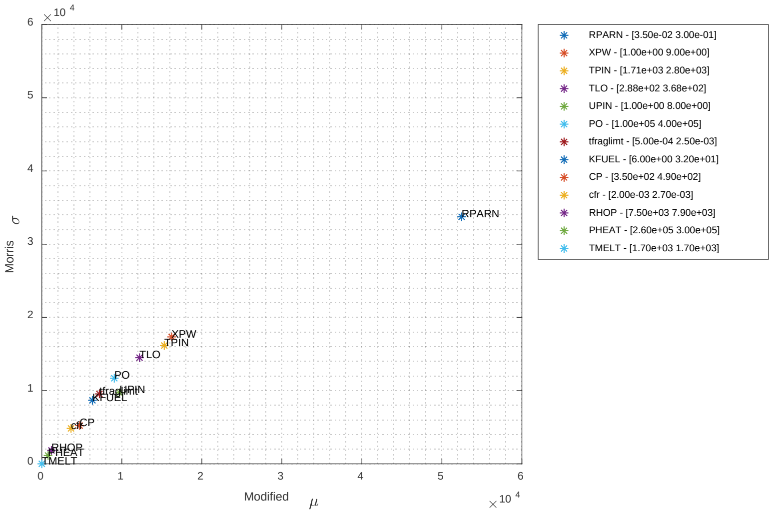

Figure 4.4.2. SEIM SM Morris Sensitivity Analysis Results

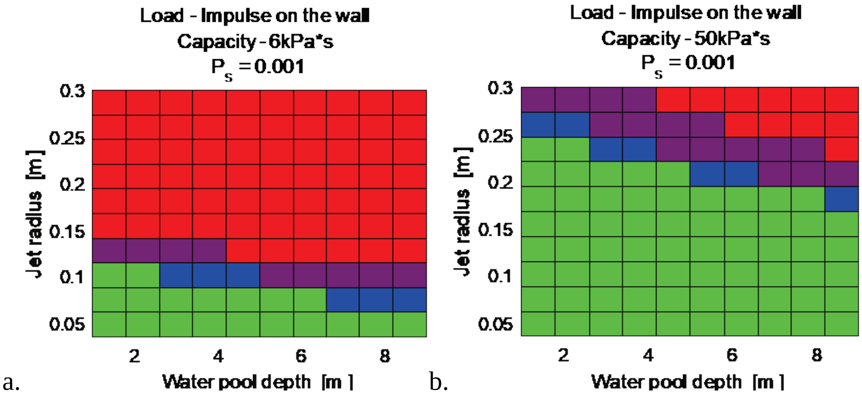

a. b.

Figure 4.4.3. SEIM Failure domains (possibility of failure $\boldsymbol{P_s = 10^{-3}}$) for (a) non-reinforced hatch door; (b) reinforced hatch door

The next step in ROAAM+ is failure domain analysis, performed to identify combinations of the most influential parameters that lead to failure (or success). Failure domain analysis is performed using probabilistic framework, where respective complementary cumulative distributions of probability of failure $CCDF(P_F)$ are obtained in the space of the influential parameters. In failure domains every $CCDF(P_F)$ is color coded with respect to the exceedance frequency of screening probability level P_s, as shown in Figure 4.2.***4***. Figure 4.4.***3*** illustrate the failure domain maps for SEIM SM in the space of XPW (water pool depth) and RPARN (jet radius) considering different fragility limits that correspond to non-reinforced (6kPa*s) and reinforced hatch door (50kPa*s). Failure can be considered as physically unreasonable even with original design (non-reinforced hatch door), regardless of modeling uncertainty if one can demonstrate that the jet radius (RPARN) will be limited to 0.05m (corresponds to vessel lower head opening with only slightly ablated failure of the penetration for instrumentation guide tube (IGT)). If the temperature of ejected debris is below 2400K then the jet radiuses up to 0.09 m (slightly ablated failure of the control rod guide tube (CRGT) penetration) can be considered as safe for ex-vessel steam explosion.

In case of modified design, i.e. reinforced hatch door, containment failure due to ex-vessel stream explosion can be considered as physically unreasonable regardless of the modeling uncertainty if one can demonstrate that the jet radius (RPARN) will be limited to ~0.15 m (corresponds to the vessel LH opening with significantly ablated CRGT penetration failure).

Neither original nor modified design can ensure that containment failure due to steam explosion is physically unreasonable, unless one can demonstrate that the size of the melt jet diameter and initial melt temperature can be limited. Such reduction of uncertainty in the input parameters for steam explosion analysis would require consideration of the effect of phenomena and scenarios at the previous stages of the accident progression. However, analysis of the failure domains suggest that it is quite unlikely that such a demonstration (that jet size is sufficiently small) can be provided for the original design because the maximum "safe" size of the jet is smaller than the size of the CRGT penetrations. On the other hand, reduction of uncertainty in the initial jet diameter and melt temperature might be fruitful for the modified design where "safe" jet size is much larger than the size of CRGT penetration. E.g. one can investigate if the vessel ablation after initial failure of a penetration can be limited, considering prototypic accident scenario conditions.

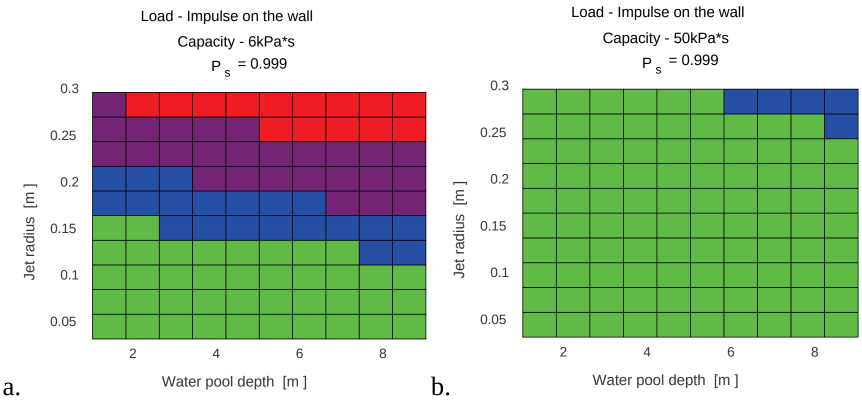

Figure 4.4.4. SEIM Failure domains (necessity of failure $\boldsymbol{P_s = 1 - 10^{-3}}$*) for (a) non-reinforced hatch door; (b) reinforced hatch door*

The lack of clear demonstration of effectiveness of SAM strategy sometimes might be insufficient for rejection of the SAM design by the decision makers. An argument can be that the analysis of the possibility of failure was done too conservative. In order to address the argument, let's consider the question about "what is the possibility that containment doesn't fail". Figure

4.4.***4*** illustrates the results of failure domain analysis with screening probability $P_S = 0.999$. The original design (Figure 4.4.***4***a) has a relatively large domain of input parameters with jet radiuses RPARN > ~0.25 m, where $P_F > P_S = 0.999$ in more than 95% cases (i.e. necessity of containment failure is high). In the modified design with reinforced hatch door (see Figure 4.4.***4***b) the size of the domain with high necessity of failure is significantly reduced ($P_F > P_S = 0.999$ in more than 5% cases when RPARN > ~0.25 m and water pool depth is above 6m (XPW > 6m)).

The failure domain analysis suggests that it is unlikely that the design with non-reinforced hatch door can be demonstrated as an effective SAM strategy because (i) the maximum “safe” size of the jet is quite small and (ii) the size of the failure domain where necessity of failure is large. Modified design with reinforced door also cannot be proven as an effective strategy, given the current state of knowledge. However, the sizes of the failure domain for both possibility and especially necessity of failure are fairly small. Thus there is much better chance that obtaining more knowledge about vessel failure and melt release phenomena can reduce the uncertainty in the results.

Risk Analysis of Ex-Vessel Steam Explosion Using Complete Framework.

The results of sensitivity analysis (see Figure 4.4.***2***) and failure domain analysis (see Figure 4.4.***3***) for ex-vessel steam explosion surrogate model show that the radius of the jet, water pool depth and the temperature of the melt – are the most influential parameters on the magnitude of loads on the containment produced by ex-vessel steam explosion in Nordic BWR. These parameters depend on the in-vessel phase of accident progression, vessel failure mode and melt release conditions predicted by the melt ejection surrogate model in ROAAM+ framework for Nordic BWR.

The ROAAM+ analysis of probability of failure has been performed using complete framework (MEM SM and SEIM SM) for unmitigated SBO scenario with depressurization (see for details). In the analysis using complete framework, SEIM SM predicts steam explosion loads on the containment depending on MEM SM predictions of melt release conditions for 4 splinter scenarios (see Chapter 4.3.1). The results are presented in Figures 4.4.***5*** and 4.4.***6***.

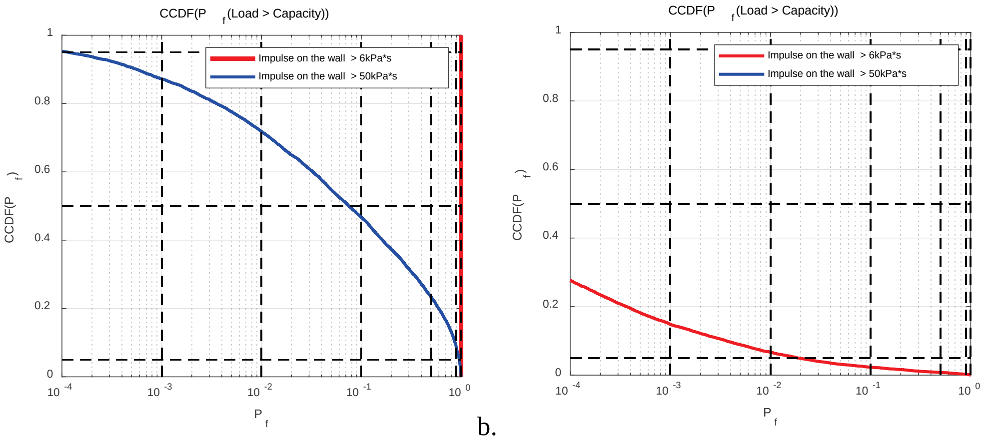

a. b.

*Figure 4.4.5. Complimentary CDF of conditional containment failure due to ex-vessel steam explosion: (red) given 6kPa*s fragility limit (non-reinforced hatch door), (blue) given 50kPa*s fragility limit (reinforced hatch door) using complete framework for (a) EIGT100IDEJ, (b) EIGT100IDEJ0 Scenario[18]*

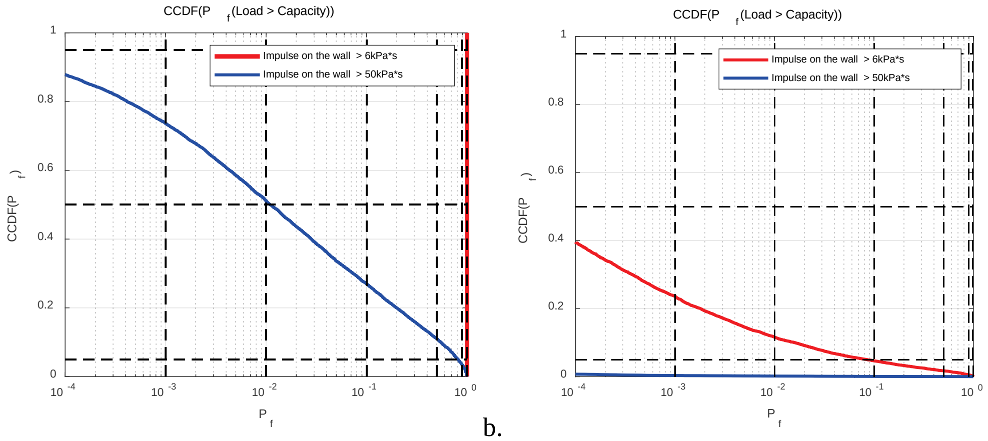

a. b.

*Figure 4.4.6. Complimentary CDF of conditional containment failure due to ex-vessel steam explosion: (red) given 6kPa*s fragility limit (non-reinforced hatch door), (blue) given 50kPa*s fragility limit (reinforced hatch door) using complete framework for (a) EIGT25IDEJ1, (b) EIGT25IDEJ0 Scenario[18]*

The results show the dominant effect of solid debris ejection mode (IDEJ0 and 1) on melt release conditions from the vessel and resultant loads on the containment due to ex-vessel steam explosion. In case of IDEJ0 (solid debris ejection – on) – the melt and debris mixture is released in a dripping mode, resulting in relatively small values of jet radius (RPARN), melt release velocity (UPIN) and melt temperature (TPIN) compared to IDEJ1 (solid debris ejection – off) – where the major part of in-vessel debris is ejected in form of massive release (due to vessel lower head wall failure). Initial breach area due to failed penetrations (EIGT25 vs EIGT100) also has quite significant effect on the results, however it does not change the conclusions in case of a single jet SEIM model. The effects of the number of failed penetrations on melt release conditions and ex-vessel steam explosion are subject to future research and are beyond the scope of the present work.

In case of solid debris ejection – off (IDEJ1) containment failure due to ex-vessel steam explosion cannot be considered as physically unreasonable, even in modified design with reinforced hatch door (50kPa*s, see Figures 4.4.***5***a and 4.4.***6***a). Furthermore, in the original design the necessity of failure is high (e.g. all values of $P_f > P_s = 0.999$ [1]). In case of solid debris ejection –on (IDEJ0) – containment failure due to ex-vessel steam explosion can be considered as physically unreasonable only in case of modified design (with reinforced hatch door); in the original design – physically unreasonable level is exceeded in ~15-25% of the cases, however the necessity of failure is small, therefore further reduction of uncertainty can yield positive results. Figure 4.4.*7* and 4.4.***8*** show the results of sensitivity analysis for coupled melt ejection and ex-vessel steam explosion surrogate models (MEM-SEIM SMs) for EIGT100IDEJ1 and EIGT100IDEJ0 splinter scenarios. Note that water pool depth is considered as scenario parameter in these calculations.

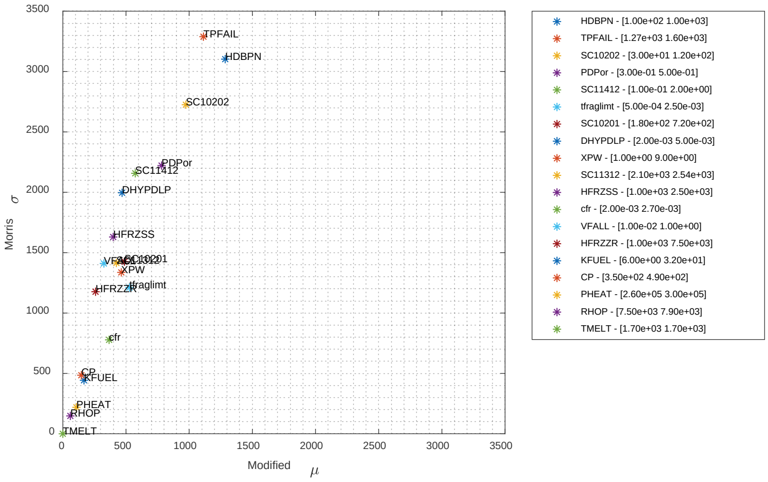

*Figure 4.4.7. Sensitivity of steam explosion impulse on pedestal wall (kPa*s) in EIGT100IDEJ0 scenario*

The results of sensitivity analysis indicate that the uncertainty in the results in coupled MEM-SEIM analysis in case of IDEJ0 is majorly driven by parameters that control failure of penetrations (HDBPN and TPFAIL – heat transfer coefficient from debris bed to penetrations and penetrations failure temperature respectively) in MELCOR code (see section 4.3.1, and references [17][29][30] for details). It can be explained by overall small values of jet radiuses and ejected debris temperatures predicted by MELCOR code in case of IDEJ0 (see Figure 4.3.***14***a and b), and the uncertainty is mostly dominated by TPFAIL and HDBPN, as demonstrated in [27].

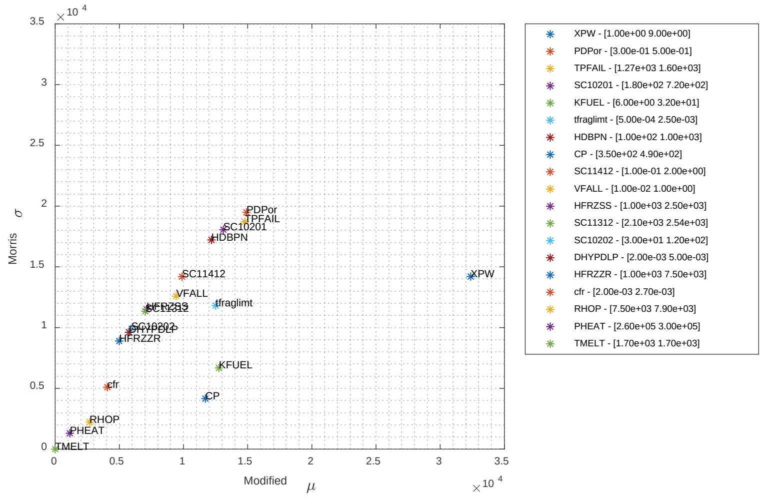

*Figure 4.4.8. Sensitivity of steam explosion impulse on pedestal wall (kPa*s) in EIGT100IDEJ1 scenario*

In case of IDEJ1 the results of coupled MEM-SEIM analysis are mostly affected by the pool depth (XPW), in-vessel particulate debris porosity (PDPor) and penetrations failure temperature (TPFAIL); which can be explained by the distributions of the jet radiuses (RPARN) and ejected debris temperatures (TPIN) predicted by MELCOR code in case of IDEJ1 (see Figure 4.3.***14***a and b). In case of large jet radiuses, the uncertainty in the results is mostly driven by the water pool depth, i.e. water pool depth defines system confinement and availability of volatile liquid available for interaction; thus, with reduction of pool depth steam explosion energetics diminishes.

Figure 4.4.***9***a-d show the results of failure domain analysis in case of EIGT100-IDEJ1 in the domain of the most influential parameters identified in Figure 4.4.***8***. The results show that in the original design both possibility ($P_s = 1.e - 3$) and necessity ($P_s = 0.999$) of failure is high,

i.e. no matter the uncertainty in modelling parameters, the non-reinforced door can fail in case of EIGT100-IDEJ1 scenario (solid debris ejection – OFF).

In case of EIGT100-IDEJ0 (Figure 4.4.9e-h) containment failure due to ex-vessel steam explosion can be considered as physically unreasonable in the original design (non-reinforced hatch door) in case of early failure of penetrations (IGTs), provided by large values of heat transfer coefficient between debris and penetration structures (HDBPN) and small values of penetrations failure temperature (TPFAIL). This effect can be explained by the amount of melt and melt superheat available at the time of penetrations failure, i.e. later time of penetrations failure can lead to increased amount of liquid melt and larger values of melt superheat that can affect ablation of the opening, and, thus, steam explosion energetics. In case modified design with reinforced hatch door, containment failure due to ex-vessel steam explosion can be considered as physically unreasonable for all combinations of the most influential parameters.

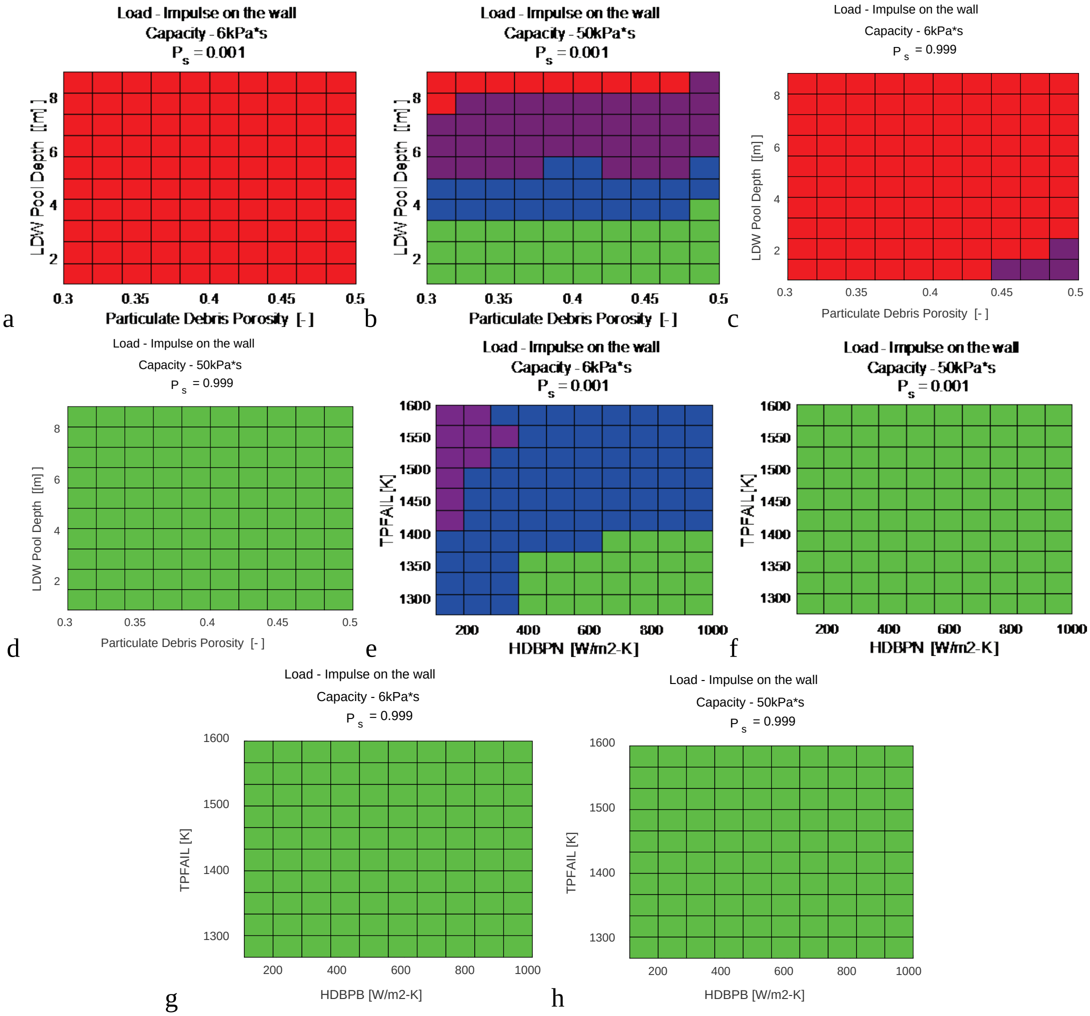

Figure 4.4.9. MEM-SEIM Failure domain (a) EIGT100-IDEJ1, $\boldsymbol{P_s = 1 - 10^{-3}}$ *non-reinforced; (b) EIGT100-IDEJ1,* $\boldsymbol{P_s = 1 - 10^{-3}}$ *reinforced; (c) EIGT100-IDEJ1* $\boldsymbol{P_s = 0.999}$ *non-reinforced; (d) EIGT100-IDEJ1* $\boldsymbol{P_s = 0.999}$ *reinforced; (e) EIGT100-IDEJ0* $\boldsymbol{P_s = 1 - 10^{-3}}$ *non-reinforced; (f) EIGT100-IDEJ0* $\boldsymbol{P_s = 1 - 10^{-3}}$ *reinforced; (g) EIGT100-IDEJ0* $\boldsymbol{P_s = 0.999}$ *non-reinforced; (h) EIGT100-IDEJ0* $\boldsymbol{P_s = 0.999}$ *reinforced*

4.4.2. Ex-vessel Debris Coolability

Risk Analysis Using Surrogate Model for Debris Coolability.

The analysis of the risk of containment failure due to ex-vessel debris coolability (formation of non-coolable debris configuration) has been performed using surrogate models for debris agglomeration (section 0) and coolability (section 0) in Nordic BWR. In the analysis four groups of parameters were considered for the load and capacity listed below:

(i) Heat flux (HF) vs. dryout heat flux (DHF) (MW/m2), failure is declared when HF>DHF.

(ii) Stabilized temperature of solid debris (TMAX) vs. debris oxidation temperature, failure is declared when TMAX>1200K.

(iii) Stabilized temperature of solid debris (TMAX) vs. melting temperature of metallic debris, failure is declared when TMAX>1700K.

(iv) Stabilized temperature of solid debris (TMAX) vs. melting temperature of oxidic debris, failure is declared when TMAX>2800K.

In the first step of the analysis we treat all parameters in debris agglomeration and coolability surrogate models (Table 4.6 and 4.7) as model intangible parameters, i.e. with incomplete probabilistic knowledge.

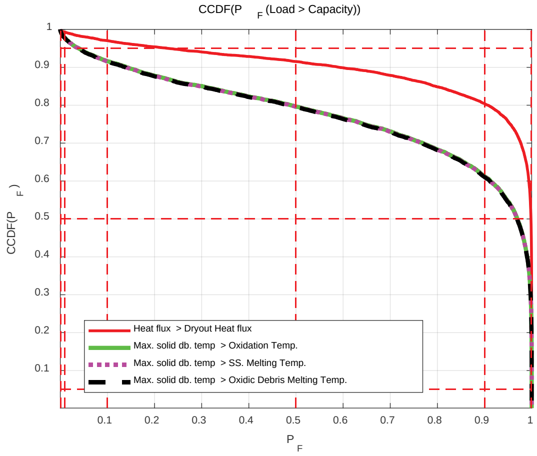

Figure 4.4.10. Complimentary CDF of conditional containment failure probability due to ex-vessel debris coolability: (red) HS>DHS (MW/m2); debris temperature > oxidation temperature (solid green); metallic debris remelting temperature (dashed purple); oxidic debris remelting temperature (dashed black)

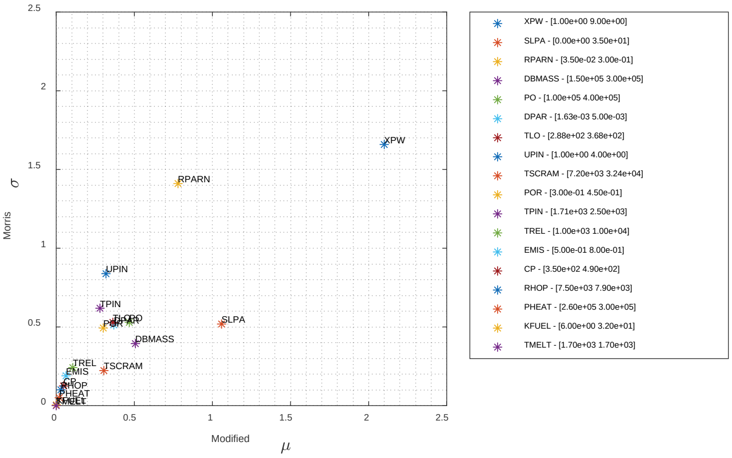

Figure 4.4.11. Sensitivity of the value of (HF-DHF) (MW/m^2)

Using ROAAM+ probabilistic framework the complementary cumulative distribution of probability of failure $CCDF(P_F)$ can be obtained. Figure 4.4.***10*** illustrate $CCDF(P_F)$ obtained for different loads and fragility limits. The results show that the screening probability P_s =1.e-3 which corresponds to “physically unreasonable” limit (see [114] for details) is exceeded in approximately 99% in all of the cases. If consider “necessity” of containment failure, i.e. the possibility that containment doesn’t fail. For that we set the screening probability to $P_s = 0.999$. The fraction of scenarios where $P_F > P_s = 0.999$, is approximately ~0.468 for HF>DHF and ~0.253/0.252/0.252 for TMAX>1200/1700/2800K. The “necessity” of the containment failure due to ex-vessel debris coolability is high, but not sufficiently high to claim that the failure is unavoidable.

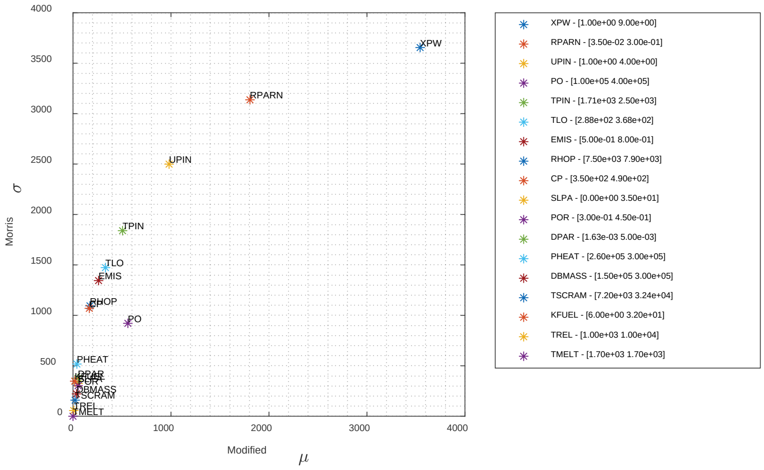

Figure 4.4.12. Sensitivity of the max. temperature of solid debris (K)

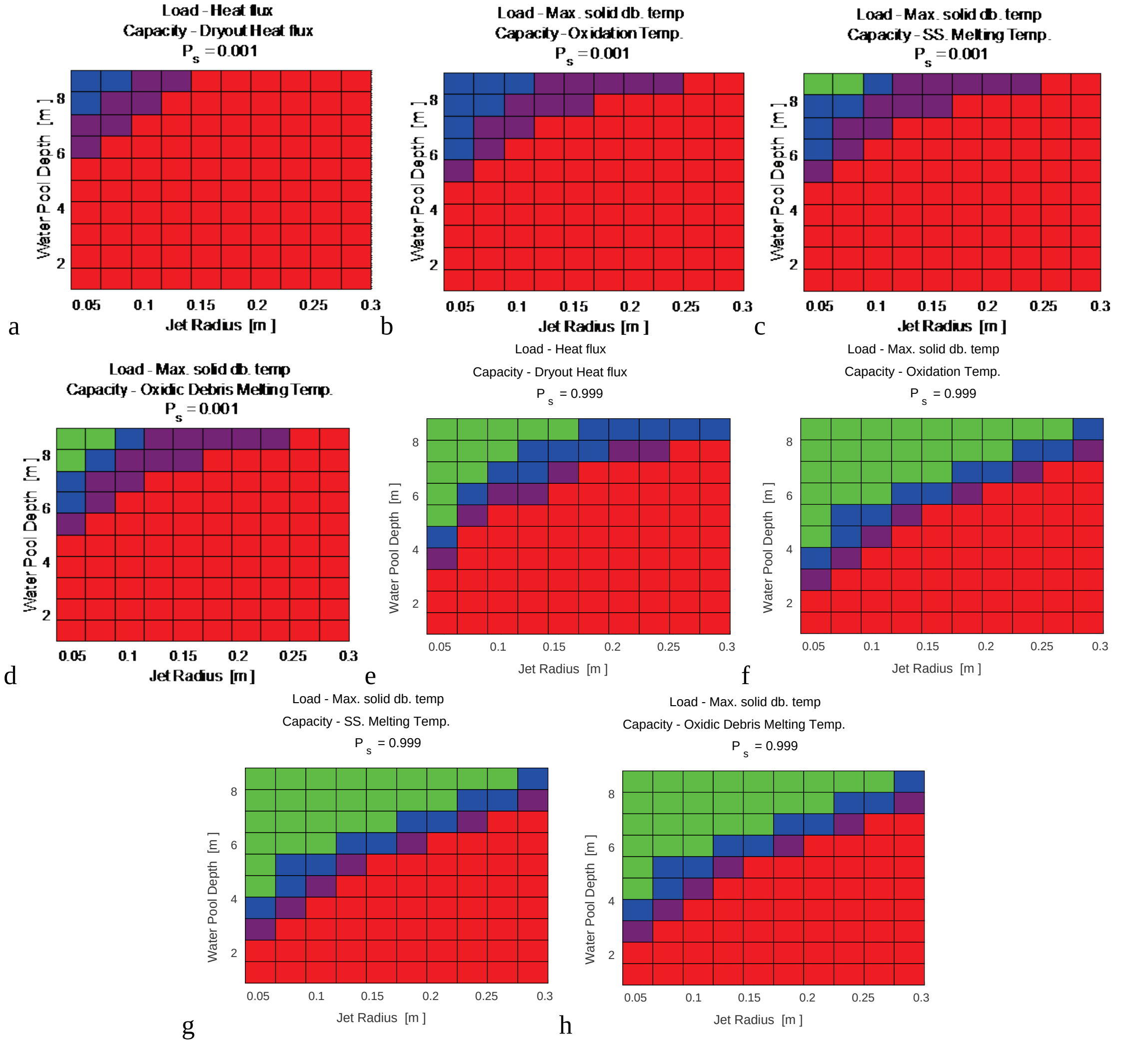

Figure 4.4.13. AGGDECO Failure domain analysis results for $\boldsymbol{P_s = 1.e - 3}$ *(a-d) and* $\boldsymbol{P_s = 0.999}$ *(e-h)(a,e)*
HF>DHF [W/m2-K]; (b,f) Debris temperature > Oxidation temperature (K);
(c,g) Debris temperature > melting temperature of metallic debris (K);
(d,h) Debris temperature> melting temperature of oxidic debris (K)

Further clarification can be achieved through sensitivity and failure domain analysis. Figure 4.4.***11*** and 4.4.***12*** show the results of Morris [109] sensitivity analysis for the difference between heat flux and dryout heat flux (HF-DHF), and max. stabilized temperature of solid debris (TMAX). Parameters that affect debris bed coolability are water pool depth (XPW), jet radius (RPARN), melt jet velocity (UPIN) and debris bed slope angle (SLPA).

Next, failure domain analysis (

Figure 4.***4.13***) is performed using probabilistic framework, where $CCDF(P_F)$ are obtained (and color coded Figure 4.2.***4***) in the space of the influential parameters. The probability of HF>DHF and TMAX>Debris oxidation temperature cannot be considered as physically unreasonable for all combinations of jet radiuses (RPARN) and water pool depths (XPW). The probability of containment failure due to formation of non-coolable debris configuration significantly decreases with increase of water pool depth (XPW) and decrease of jet radiuses (RPARN). If we consider melting temperature of metallic or oxidic debris (1700 and 2800K respectively) as a failure criterion, then failure can be considered as physically unreasonable for deep pools

(above 8.5m) and jet radiuses up to ~0.1m (slightly IGT size break). The results for “necessity” ($P_S = 0.999$) of failure suggest that containment failure can be considered as imminent (regardless uncertainty) in case of water pool depth below ~2-3.5m, and is strongly dependent on the size of the vessel breach, e.g. in case of CRGT size break – failure is imminent if the pool depth is below ~6-7m (which is a typical depth of LWD pool under SA conditions in Nordic BWR, as demonstrated in [17][26]).

Risk Analysis of Ex-vessel Debris Coolability Using Complete Framework.

The results of sensitivity (Figure 4.4.***11*** and 4.4.***12***) and failure domain analysis (Figure 4.4.***19*** and Figure 4.4.***20***) performed for ex-vessel debris coolability surrogate models (AGG-DECO) demonstrated that the success of SAM strategy strongly depends on melt release characteristics (e.g. jet radius) and pool conditions (e.g. water pool depth), which depend on in-vessel phase of SA progression, vessel failure mode and melt release – which is predicted by melt ejection surrogate model (MEM SM).

A coupled analysis has been performed using complete ROAAM+ framework for Nordic BWR (MEM-AGG-DECO SMs). The results for failure probability are illustrated in the Figure 4.4.***14***a,b for EIGT100-IDEJ0 and EIGT100-IDEJ1 scenarios respectively. The major contributor to the uncertainty in probability of containment failure is the mode of debris ejection from the vessel (IDEJ0 vs. IDEJ1) – which is represented by two phenomenological splinters. Sensitivity and failure domain analyses can help to identify the list of parameters that contribute the most to the uncertainty in these splinter scenarios and ranges of these parameters, where we can observe a transition from success failure.

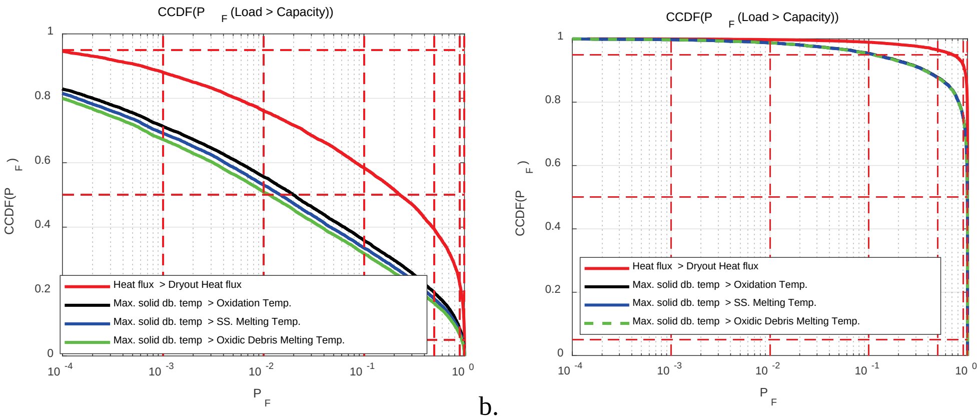

a. b.

Figure 4.4.14. Complimentary CDF of probability of failure due to ex-vessel debris coolability for (a) EIGT100-IDEJ0;(b) EIGT100-IDEJ1

The sensitivity analysis results of the relationship between heat flux and dry-out heat flux (HF vs. DHF, (see section 0 for details)) are presented in Figure 4.4.***15*** for EIGT100-IDEJ0 scenario, and in Figure 4.4.***16*** for EIGT100-IDEJ1 scenario. Based on the results, the most influential parameters are: water pool depth (XPW), debris bed slope angle (SLPA). Sensitivity of the maximum temperature (see section 0 for details) of solid debris is illustrated in Figure 4.4.***17*** for EIGT100-IDEJ0 scenario, and in Figure 4.4.***18*** for EIGT100-IDEJ1 scenario. Based on the results, the most influential parameter (by a large margin) is the depth of LDW pool (XPW) and parameters that contribute the most to the uncertainty in MEM SM, such as HDBPN and TPFAIL in case of IDEJ0, and VFALL and PDPor in case of IDEJ1. In case of IDEJ0 these results can be explained by the effect of these parameters (HDBPN and TPFAIL) on the size of the jet (RPARN) which was demonstrated in [26][27], which is among the most influential parameters in AGG-DECO SMs (Figure 4.4.***11*** and 4.4.***12***). The effect of VFALL (velocity of falling debris in MELCOR code) and PDPor (initial particulate debris porosity in MELCOR code) on the results is yet to be explained.

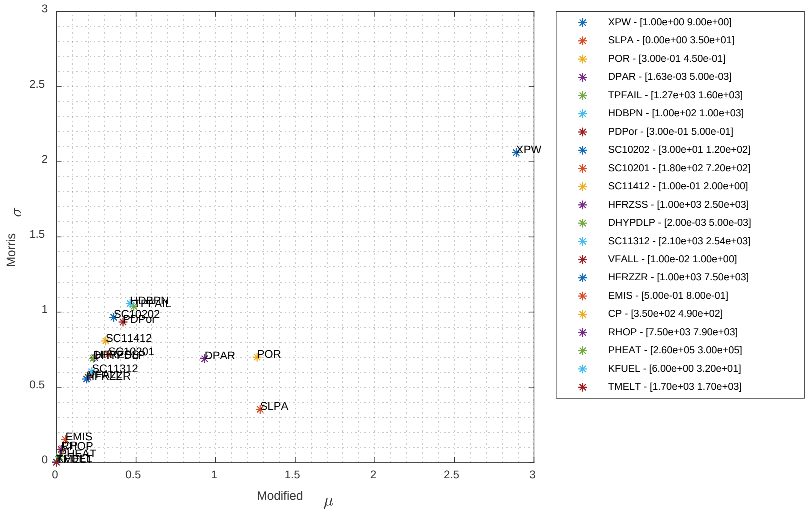

Figure 4.4.15. Sensitivity of the value of (HF-DHF) (MW/m^2) in EIGT100IDEJ0 scenario

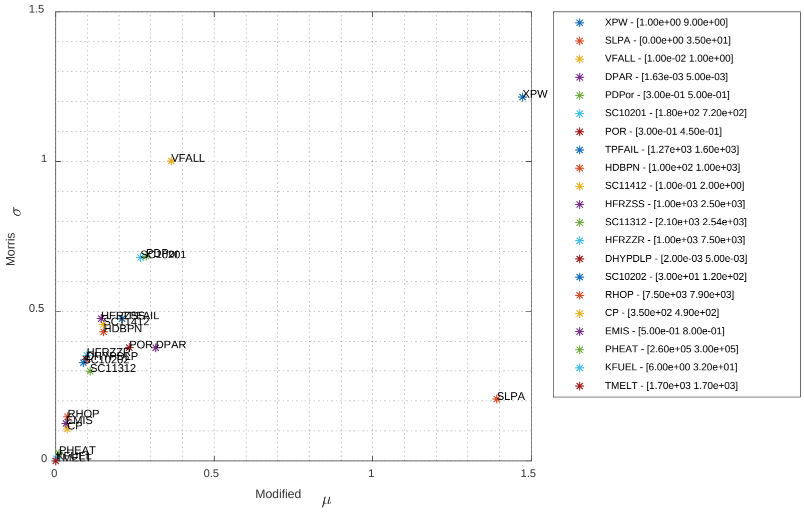

Figure 4.4.16. Sensitivity of the value of (HF-DHF) (MW/m^2) in EIGT100IDEJ1 scenario

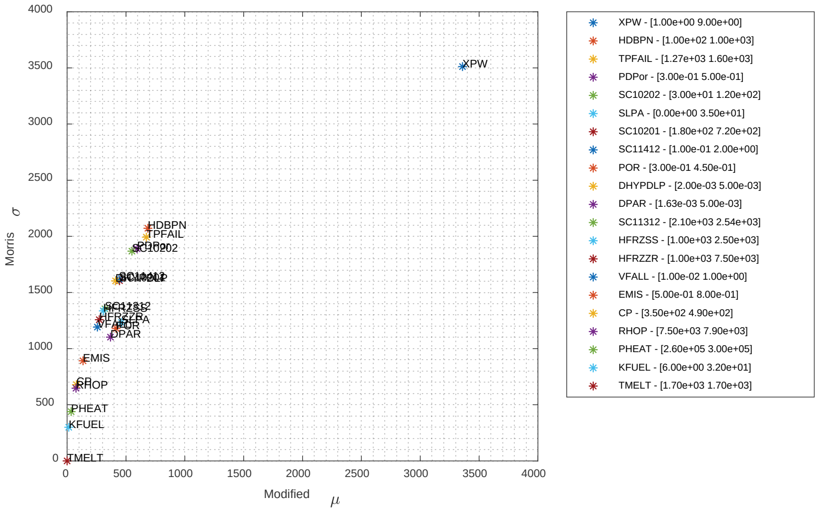

Figure 4.4.17. Sensitivity of the max. temperature of solid debris (K) in EIGT100IDEJ0 scenario

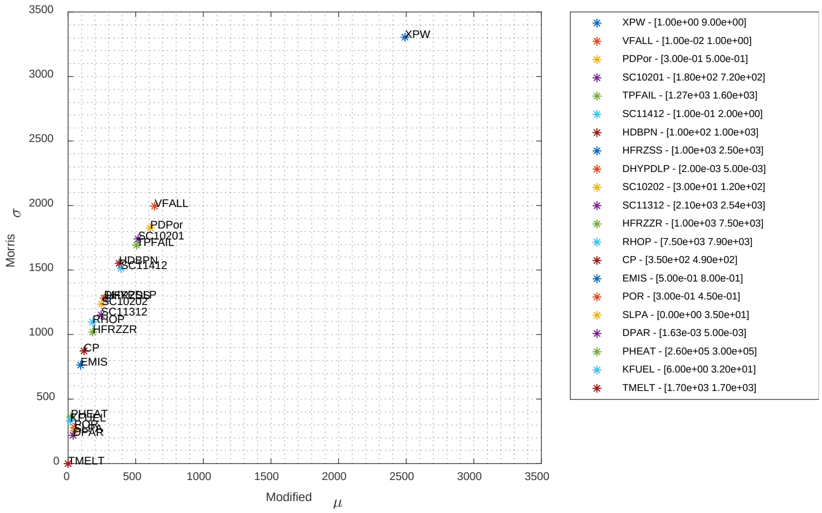

Figure 4.4.18. Sensitivity of the max. temperature of solid debris (K) in EIGT100IDEJ1 scenario

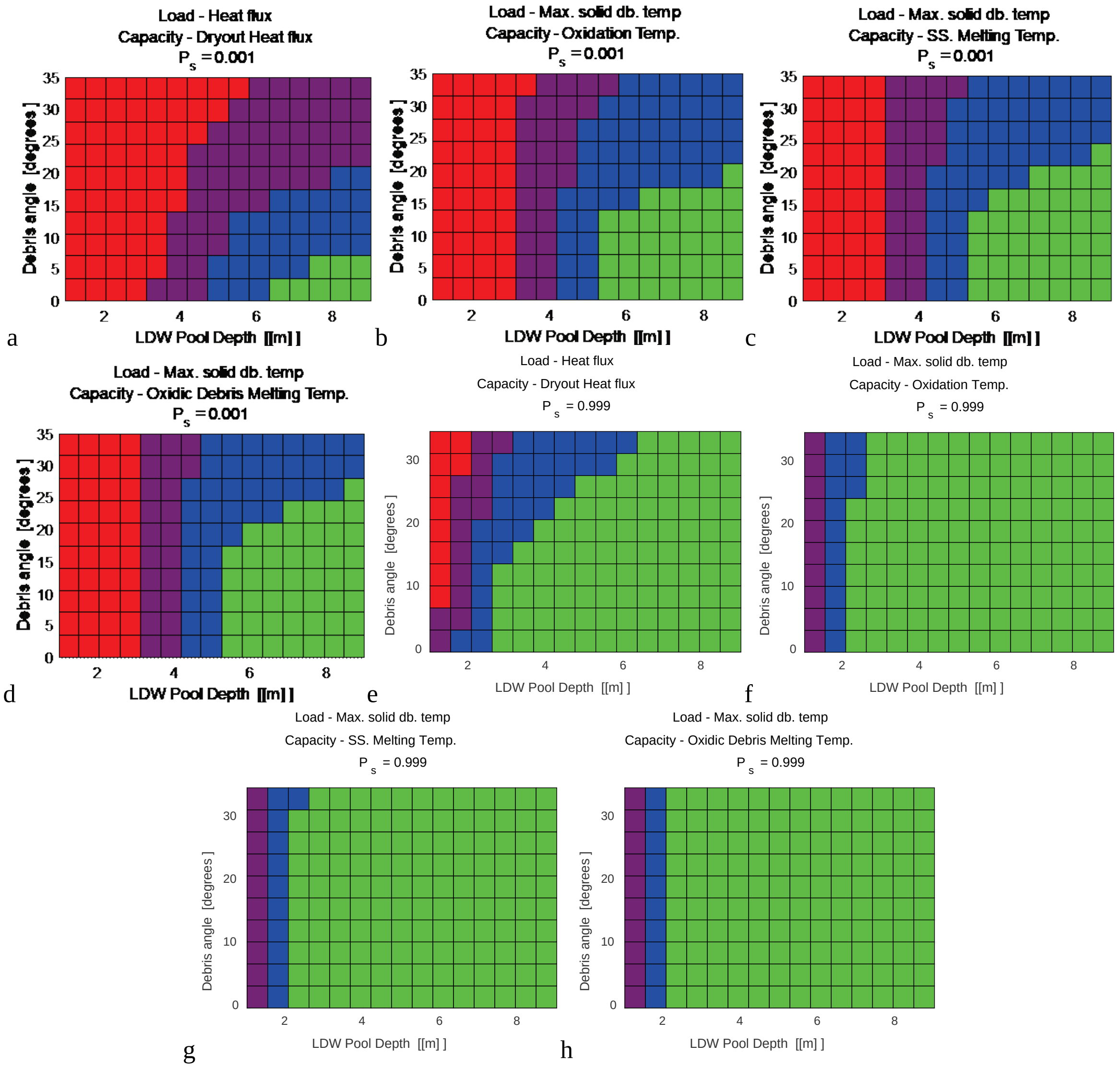

Figure 4.4.19. COR-AGGDECO Failure domain results EIGT100-IDEJ0

$\boldsymbol{P_s = 1.e - 3}$ *(a-d) and* $\boldsymbol{P_s = 0.999}$ *(e-h)*

(a,e) HF>DHF [W/m2-K]; (b,f) Debris temperature > Oxidation temperature (K);
(c,g) Debris temperature > melting temperature of metallic debris (K);
(d,h) Debris temperature> melting temperature of oxidic debris (K)

Failure domain analysis results are shown in Figure 4.4.***19*** for EIGT100-IDEJ0 scenario and in Figure 4.4.***20*** for EIGT100-IDEJ1. If we consider dry-out as a failure criterion, then failure can be considered as physically unreasonable only for deep pools (above 6m) and relatively flat debris bed shape, with slope angle below ~7.5 degrees. If we consider less conservative criteria, such as temperature of solid debris is below (i) debris oxidation temperature; (ii) metallic debris remelting temperature or (iii) oxidic debris remelting temperature, then domain of parameters where respective failure mode can be considered as physically unreasonable is considerably larger. E.g. the minimum depth of the pool should be above ~5m and the maximum allowed slope angle can be up to ~15 degrees (~up to 20-25 degrees for pool depths above 8m). Note that the difference between the failure domains obtained for oxidation temperature, melting temperature for metals and oxides are relatively small. If we consider necessity of failure ($P_S = 0.999$), i.e. “the possibility that containment doesn’t fail”. The results suggest that failure can be considered as unavoidable (i.e. over 95% of the cases exceed $P_S = 0.999$) only in case of “no dry-out” criterion and in case of very shallow pool (below 2m) and debris bed slope angle above 7.5 degrees, as illustrated in Figure 4.4.***19***f. For the other criteria, based on maximum debris bed temperature $P_f > P_S = 0.999$ in more than 5% of the cases only when the pool depth is below 2m.

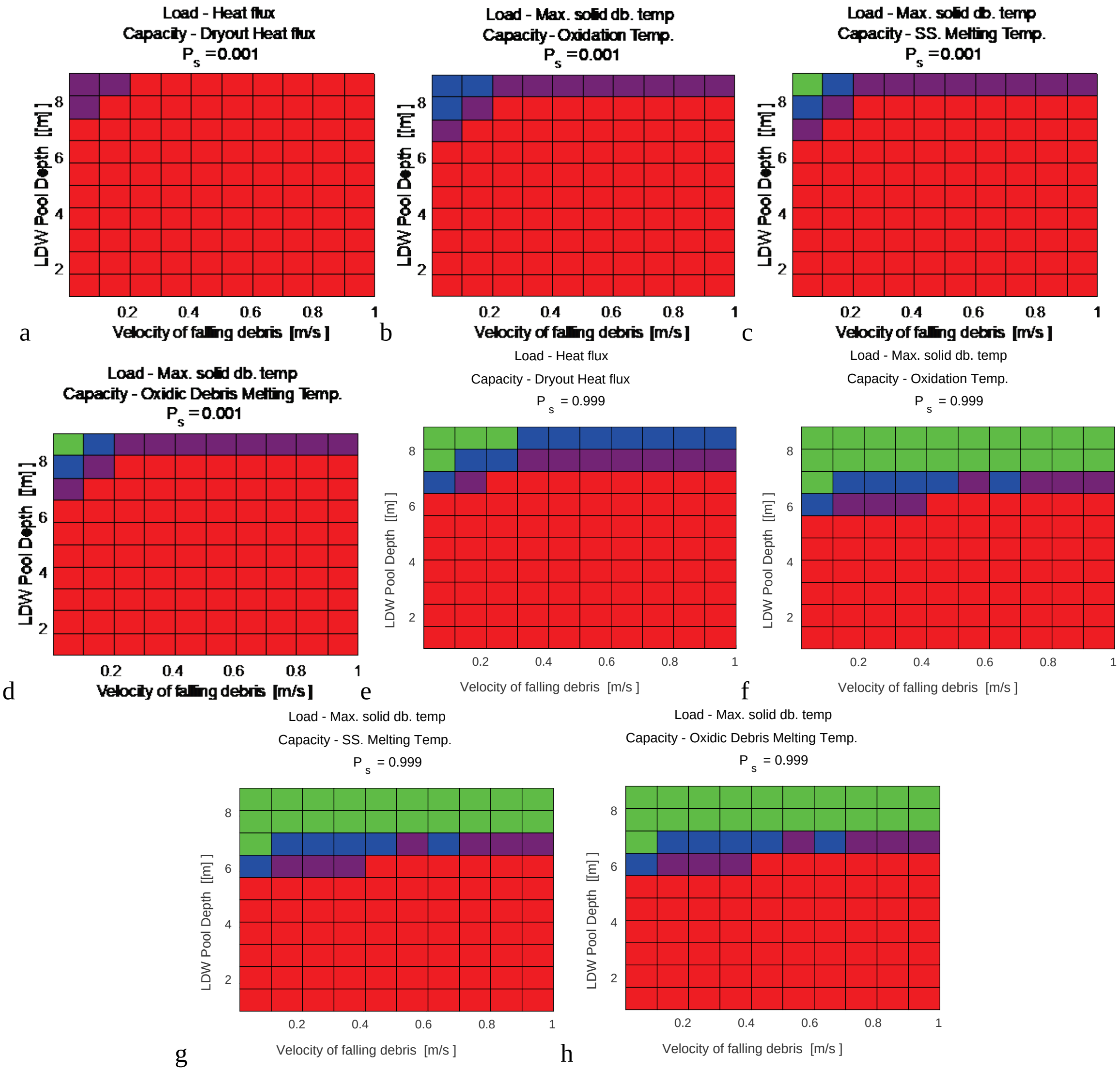

Figure 4.4.20. COR-AGGDECO Failure domain results EIGT100-IDEJ1

$\boldsymbol{P_s = 1.e-3}$ *(a-d) and* $\boldsymbol{P_s = 0.999}$ *(e-h)*

(a,e) HF>DHF [W/m2-K]; (b,f) Debris temperature > Oxidation temperature (K);

(c,g) Debris temperature > melting temperature of metallic debris (K);
(d,h) Debris temperature> melting temperature of oxidic debris (K)

Figure 4.4.***20*** presents failure domain analysis results for EIGT100-IDEJ1 scenario. A small domain where failure can be considered as physically unreasonable ($P_f < P_s = 10^{-3}$, in over 95% of the cases) exist only in case when melting temperature of metals (Figure 4.4.***20***c) or oxides (Figure 4.4.***20***d) was used in the failure criterion and with very deep pool depth (above 8m) and very small values of velocity of failing debris (VFALL<0.1m/s). It is important to note that the value of VFALL=0.01m/s is recommended by the MELCOR code best practices guidelines [153]. However, this value is recommended for falling debris quench model, which is triggered by a failure of core support plate in one of the radial rings. On the other hand, the same value is used for axial debris relocation in “stationary” debris mode, which, as a results, give quite significant contribution to debris ejection rate in case of gross failure of vessel LH wall, which was identified in [26], [27] and illustrated in Figure 4.3.***13***. Thus, the effect of this parameter and respective MELCOR modelling of phenomena of debris ejection form the vessel require further investigation. If we consider necessity of failure ($P_s = 0.999$), then the failure can be considered as unavoidable ($P_f > P_s$ with 95% confidence) for EIGT100-IDEJ1 scenario for all failure criteria, if the water pool depth is below ~6m. For the pool depths above ~8m, the necessity of failure is small only in cases where stabilized temperature of solid debris is considered as a failure criterion (Figure 4.4.***20***e,f,g,h).

4.5 PSA with ROAAM+ for Uncertainty Quantification.

This chapter provides an overview of the results of combined use of ROAAM+ tool (ROAAM GUI) and PSA software (RiskSpectrum) [156] taking into account both aleatory and epistemic sources of uncertainty. In a standard PSA, the output of PSA Level 1 is typically core damage (possibly separated in a few sub-categories). These core damage sequences are then divided into a number of sub-categories representing the important features for Level 2 progression. The link between PSA L1 and L2 is the plant damage states. The plant damage states describe not only the core damage state but also the conditions of the primary system and the containment. There are normally around 20-40 Plant Damage States (PDS) defined in the interface between Level 1 and 2.

For the generic Nordic BWR PSA model studied here, there are 27 PDSs for power operation and low power operating modes. The attributes that are considered relevant for modelling of the continued process are: Core damage state (failure of shutdown, core cooling or residual heat removal); Initiating event (transient or LOCA); Time of core melt (early, late); Reactor pressure (low, high); Containment atmosphere (inert, air); Containment spray system status; Containment pressure relief status (activated, not activated); Filtered containment venting status (activated, not yet activated, failed); Bypass of containment (bypass, intact); Suppression pool temperature (warm if pool cooling fails, else cool).

The events that are represented in a PSA Level 2 are those that may change the conditions for retaining of releases within the RPV or the containment. Hence, if the coolability in the RPV is different in different scenarios – then this is vital information. If the sequences are affecting the phenomena that can occur, then this is also vital information. For each of the PDS, a subsequent containment event tree (CET) is defined, modelling the continued accident progression.

The accident progression sequences are influenced by various physical phenomena. The types of phenomena that are usually accounted for in a PSA are: Re-criticality (in the core, in lower plenum, in containment); Hydrogen burn (deflagration and detonation); In-vessel steam explosion; Ex-vessel steam explosion; Direct containment heating; Rocket mode; Melt concrete interaction (basemat penetration); Steam generator tube rupture (only for PWR). The effect of the phenomena can be: Containment rupture; Different types of containment bypass; Activation of filtered containment venting.

The sequences in the CET end at the release categories (RC) and there are normally around 15-40 of such. The RCs can be defined in different ways, for example by release size or type of sequence. The normal approach is to use the sequence type, because then only a limited number of deterministic calculations are required. For the sequence type approach, the characterization is for example based on: Release path (containment bypass, containment rupture, filtered release, leakage); Timing of release (early, late); Initiator (pipe rupture, transient); Sprinkling of containment established (yes/no).

In a generic PSA model for Nordic BWR, which is used as reference case in this report, each phenomenon is modelled with one fixed probability per binning sequence (if relevant). The reference case provides information to the deterministic analysis about which phenomena and parameters that are currently analyzed and is used in the binning of sequences and consequences.

Two important phenomena occurring at or after reactor vessel melt-through are steam explosion and debris bed coolability. The parameters that may influence the phenomena are physical parameters such as pressure, temperature and water depth in different parts of the plant, which depend on accident scenario. Furthermore, assessment of the phenomena consequences is subject to epistemic uncertainty, which can significantly affect level 2 PSA analysis results.

4.5.1. Reference PSA model

The reference PSA model is a generic full-scale PSA for a Nordic BWR. In the reference PSA model, the accident progression for PSA level 2 is modelled in a containment event tree, CET. In the CET there is no explicit modelling of phenomena. Instead, there is a function event where all the phenomena are treated in a common fault tree.

The probabilities for steam explosion resulting in containment failure are: 1E-3 - for melt release at low pressure; 3E-3 - for melt release at high pressure. These values are always applied even if the lower drywell (LDW) flooding system fails. That is to give no positive credit for system failures. If LDW is flooded, there may be enough water for a steam explosion to occur but not enough to avoid melt through of the penetrations in the LDW floor. The probabilities for melt through of the penetrations in the LDW floor are: 1E-3 - for successful LDW flooding; 1.0 - for failure of the LDW flooding system.

The studied PDSs in this study are two plant damage states where the initiating event is a transient or a CCI, core cooling has failed and the reactor vessel pressure: (i) HS2-TH1 is high (the automatic depressurization system, ADS, has failed); (ii) HS2-TL4 is low.

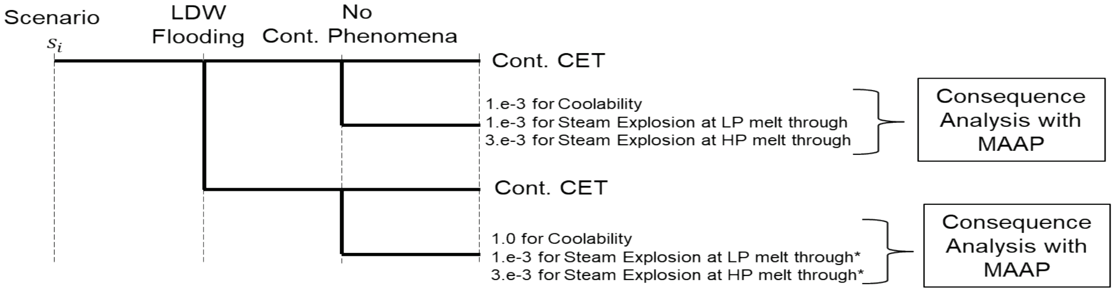

* These values are applied even if LDW fails, since no positive credit should be taken for systems failures.

Figure 4.5.1. Treatment of containment phenomena in reference PSA model of Nordic BWR

In current PSA-L2 approach, epistemic uncertainty in the outcomes of the phenomena is represented by a single probability that reflects the likelihood (a measure of confidence in prediction) that containment will be damaged in such scenario. The number can be based on expert judgment combined with some sort of uncertainty quantification. This number is sometimes (wrongly) perceived as frequency, e.g. of occurrence of explosion or formation of non-coolable debris. When failure is governed by deterministic phenomena, our confidence in the possibility of failure given all uncertainties in the analysis can be 1E-3, while failure frequency at the same melt release conditions can be 1. Furthermore, consequences of containment damage are often point estimates (e.g. using a few MAAP calculations) for given accident sequences, without quantification of modelling uncertainty in the magnitude of the release or other source term characteristics.

4.5.2. Enhanced PSA Model with Uncertainty Quantification

The reference PSA model containment event trees for the plant damage states HS2-TH1 and HS2-TL4 were modified to consider the depth of the water pool in lower drywell (LDW) and respective ex-vessel phenomena, such as ex-vessel debris coolability (COOL) and ex-vessel steam explosion (STEX). The water depth alternatives are (i) Deep water pool in LDW; (ii) Shallow water pool in LDW; (iii) No water in LDW.

Figure 4.5.*2* shows an example of the sequences with explicit modelling of ex-vessel steam explosion and debris coolability (dashed red). For each end state in the CET there is a specific probability distribution generated with ROAAM+ framework for Nordic BWR (see Chapter 0). In the complete CET there are also function events and sequences for isolation, stabilized residual heat removal etc. As seen in Figure 4.5.*2* there is one common function event for steam explosion and one common function event for coolability. For each sequence, however there is a unique basic event used for each phenomenon depending on the sequence (i.e. the combination of depth and melt flow).

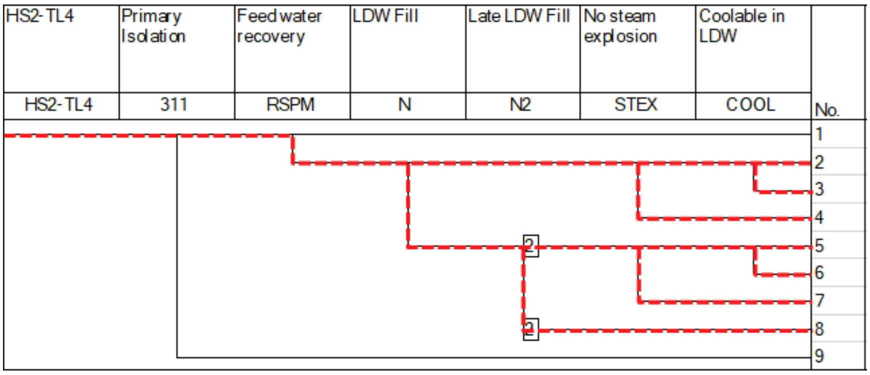

Figure 4.5.2. Containment event tree sequences in enhanced PSA model of Nordic BWR with explicit modelling of containment phenomena (dashed red)

4.5.3. Enhanced Model Results

ROAAM+ Input to Enhanced PSA model

All PSA Level 1 sequences that are leading to the same PDS are treated in the same manner in the continued sequence. If a failure in Level 1 should affect systems in Level 2, it will be a different scenario from a deterministic standpoint, e.g. if there is an initial loss of offsite power and no start of the diesels, compared to a scenario where the diesels would stop after some hours of initially successful operation. One of the purposes with the improved PSA is to be able to judge if these scenarios need to be treated differently in the PSA context.

Based on the ROAAM+ analysis results (chapter 4.4), the risk of containment failure due to ex-vessel steam explosion and ex-vessel debris coolability is affected by the uncertainty in the water pool depth, which can be reflected in enhanced PSA modelling. Other parameters that have high influence on the results (e.g. debris slope angle, velocity of falling debris, heat transfer coefficients between debris and IGTs, etc.) can be treated as epistemic modelling parameters that are not considered in ET/FT analysis. Such parameters as mode of debris ejection from the vessel (IDEJ1/IDEJ0) are considered as phenomenological splinters, i.e. phenomenological scenarios where relevant epistemic uncertainties are beyond the reach of any reasonably verifiable quantification. These splinters will be treated in PSA analysis in the same manner as in ROAAM+ framework. If the LDW flooding system works, there will always be about 7-8 m of water in LDW. Thus, for the "deep pool" analysis cases in ROAAM+ framework MELCOR code predictions of the pool depth were used **[26]**. The water depth for shallow pool conditions is much more sensitive to the accident sequence, therefore in current implementation it was considered as an intangible parameter with a specified range. The effect of possible design modification (reinforcement of the containment hatch door) on unacceptable release frequency estimated by RiskSpectrum PSA using the data generated by ROAAM+.

Figure 4.5.***3*** - 4.5.***6*** show the resulting distributions of probability of failure obtained from failure domain analysis for ex-vessel debris coolability and steam explosion, presented in sections 4.4.1 and 4.4.2. Here the analysis was performed for ex-vessel debris coolability and steam explosion simultaneously, i.e. the same set of respective input and deterministic/intangible parameters and probability distributions was used in risk assessment, and respective results are exported from ROAAM+ GUI (see section 0 and Figure 4.2.***8***) to RiskSpectrum PSA as user defined simulation values (i.e. the data is properly correlated between the two events).

Note that two fragility limits will be used for ex-vessel steam explosion, in order to evaluate the effect of design modification of PSA analysis results: Non-reinforced hatch door, that can withstand 6kPa*s explosion impulses (original design); Reinforced hatch door, that can withstand 50kPa*s explosion impulses (modified design). In case of ex-vessel debris coolability – remelting of metallic debris (debris bed temperature exceeding stainless steel melting temperature (1700K)) was considered as a failure criterion. Table 4.8 show the summary of the results presented in the Figure 4.5.***3***, 4.5.***4***, 4.5.***5*** and 4.5.***6*** and to be used in RiskSpectrum PSA analysis using enhanced model.

Table 4.8. RiskSpectrum PSA simulation matrix

Description	**Debris ejection mode (splinter)**	
	EIGT100-IDEJ1	**EIGT100-IDEJ0**
Deep pool (M)[6], Steam explosion load vs. fragility (Non-reinforced door).	CASEID_001D Mean: 1.0[7]	CASEID_001D: Mean: 1.236e-2
Deep pool (M)[6], Steam explosion load vs. fragility (Reinforced door).	CASEID_002D Mean: 2.697e-1	CASEID_002D Mean: 0.0
Deep pool (M)[6], Debris non-coolable if max. temperature exceed 1700K (SS melting temperature).	CASEID_003D Mean: 6.047e-1	CASEID_003D Mean: 8.547e-3

---

[6]. LDW water pool depth (XPW) for "Deep pool" was predicted by MELCOR code (MEM SM).

[7]. Mean values are obtained from respective distributions of probability of failure (P_F) illustrated in Figure 96-99.

Shallow pool (1-4m)[8], Steam explosion load vs. fragility (Non-reinforced door).	CASEID_001S Mean: 9.98e-1	CASEID_001S Mean: 1.647e-3
Shallow pool (1-4m)[8], Steam explosion load vs. fragility (Reinforced door).	CASEID_002S Mean: 7.144-e4	CASEID_002S Mean: 0.0
Shallow pool (1-4m)[8], Debris non-coolable if max. temperature exceed 1700K (SS melting temperature).	CASEID_003S Mean: 1.0	CASEID_003S Mean: 5.312e-1

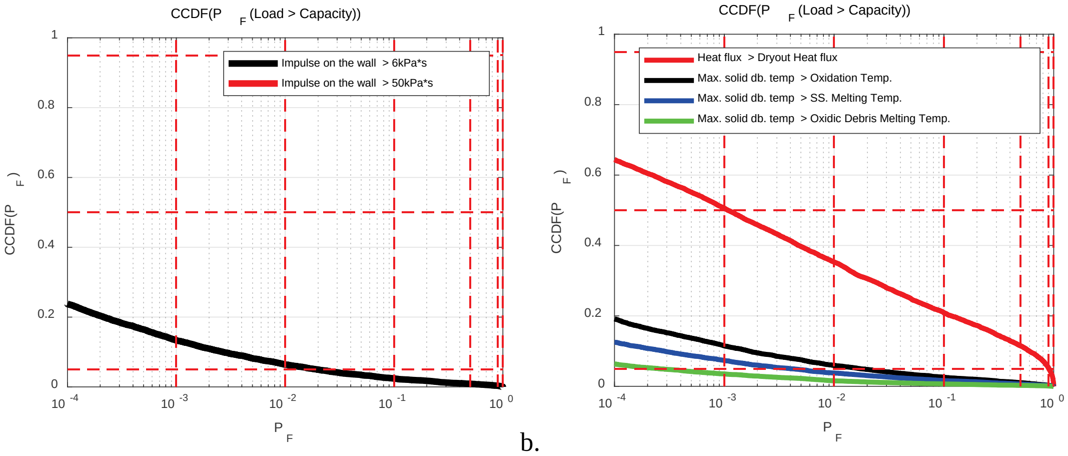

a. b.

Figure 4.5.3. CCDF of $\boldsymbol{P_F}$ *for EIGT100-IDEJ0 scenario a) MEM-SEIM b) MEM-AGGDECO in case of deep pool*

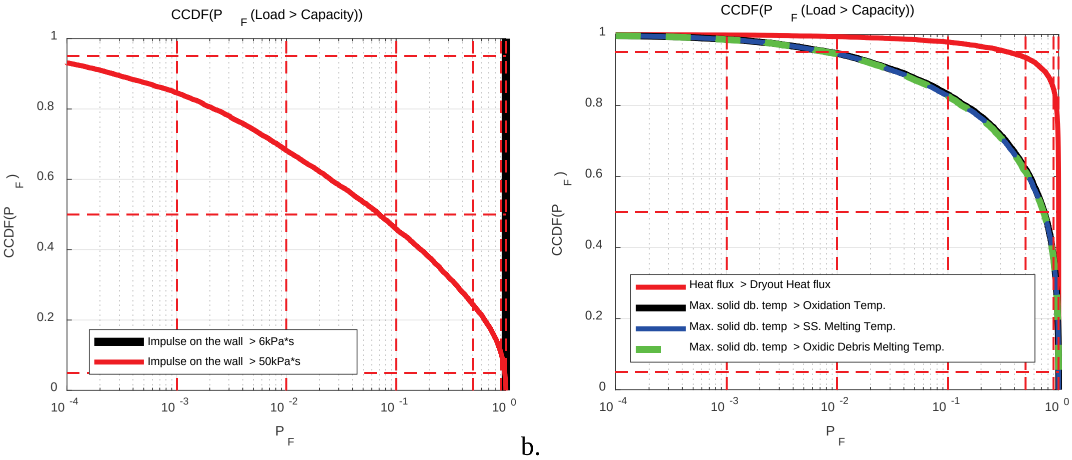

a. b.

Figure 4.5.4. CCDF of $\boldsymbol{P_F}$ *for EIGT100-IDEJ1 scenario a) MEM-SEIM b) MEM-AGGDECO in case of deep pool*

---

[8]. LDW water pool depth (XPW) for “Shallow pool” was considered as intangible parameter on the range from [1-4m].

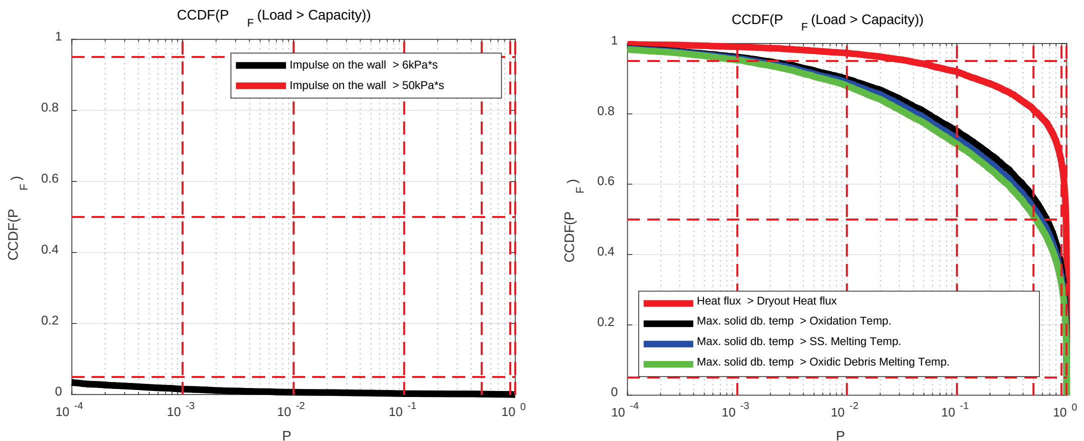

a. b.

Figure 4.5.5. CCDF of $\boldsymbol{P_F}$ *for EIGT100-IDEJ0 scenario a) MEM-SEIM b) MEM-AGGDECO shallow pool*

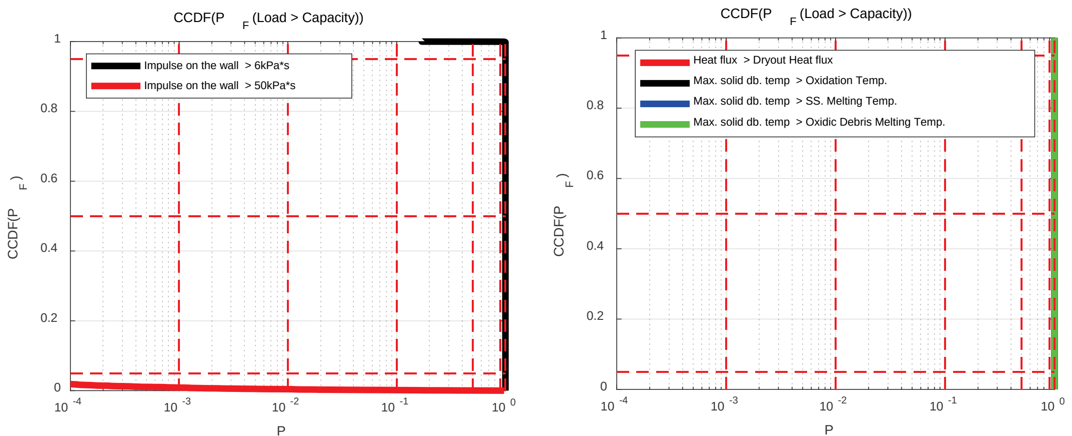

a. b.

Figure 4.5.6. CCDF of $\boldsymbol{P_F}$ *for EIGT100-IDEJ1 scenario a) MEM-SEIM b) MEM-AGGDECO shallow pool*

Analysis and Comparison between Reference Case Model and Enhanced Model

All transients and CCIs leading to the plant damage states HS2-TH1 and HS2-TL4 (core damage due to inadequate coolant inventory make-up) were analyzed for all level 2 release categories. Release categories leading to release frequencies over 0.1% of the core inventory of an 1800 MW BWR are grouped as non-acceptable. Furthermore, in the analyses presented in [67], the release category “basemat melt-through” was, according to industry standard, presented individually. Those results were excluded from the group of non-acceptable releases. It can, however, be argued that basemat melt-through cases could represent large releases e.g. after the standard analysis period of 72 h. To account for this possibility, the former non-acceptable release group is, in the current analysis, merged with the basemat melt-through group to form a group named “non-contained release”.

The normalized results for medium values of non-contained release frequency per type of initiating event are shown in Figure 4.5.*7* and Figure 4.5.***8***. The normalization is done with respect to the frequency for non-contained release due to Loss of offsite power. The results show that the non-contained release frequency in most of the cases are higher in the enhanced model with EIGT100-IDEJ1 leading to much larger increase compared to EIGT100-IDEJ0. It is clear from these results the high sensitivity of the non-contained release frequency to the mode of debris ejection from the vessel (IDEJ0 vs. IDEJ1) predicted by MELCOR code (MEM SM).

The initiating event group spurious M-isolation is much more affected by the enhanced modelling compared to the other initiating event types studied. To explain the reason for this, it can first be noted that the group of non-acceptable releases, for a BWR, to a relatively large extent contains so-called bypass sequences, in which closure (isolation) of the containment fails and the release path occurs through e.g. through open steam-lines. Such sequences will not be affected by the ROAAM+ approach since they are not affected by the studied containment rupture phenomena. M-isolation, or IM-isolation, refers to a specific function of the reactor protection system, which initiates closing of isolation valves in the feedwater lines. The effect of the initiating event is thereby at first sight similar to that of the loss of feedwater transient. However, in the generic Nordic BWR plant design represented by the PSA model used in this study, M-isolation automatically activates another isolation function that initiates closure of the steam lines. This implies that for sequences starting with spurious M-isolation, bypass sequences through open steam lines are directly excluded (apart from cases with mechanical errors in the MSIVs) and this category of initiating events becomes the only category where the ROAAM+ methodology will influence all the resulting accident sequences. In contrast, e.g. the loss of feedwater initiating event category has a relatively low frequency, which implies that together with the event probabilities prescribed by the ROAAM+ methodology, sequences affected by ROAAM+ to a large extent end up below the cut-off frequency of the PSA analysis, leaving almost only bypass sequences above it. In summary, loss of feedwater sequences will in this model be minimally affected by ROAAM+ while the inverse is true for spurious M-isolation sequences, thereby creating a large difference between these seemingly similar initiating event families [70].

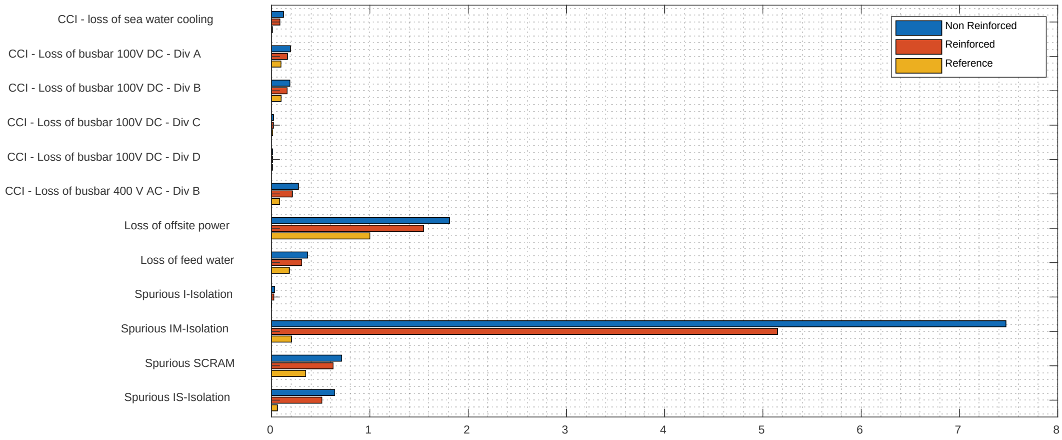

Figure 4.5.7: Comparison of normalized non-contained release frequencies (expected value) obtained with enhanced model for reinforced and non-reinforced hatch door in EIGT100-IDEJ1 scenario

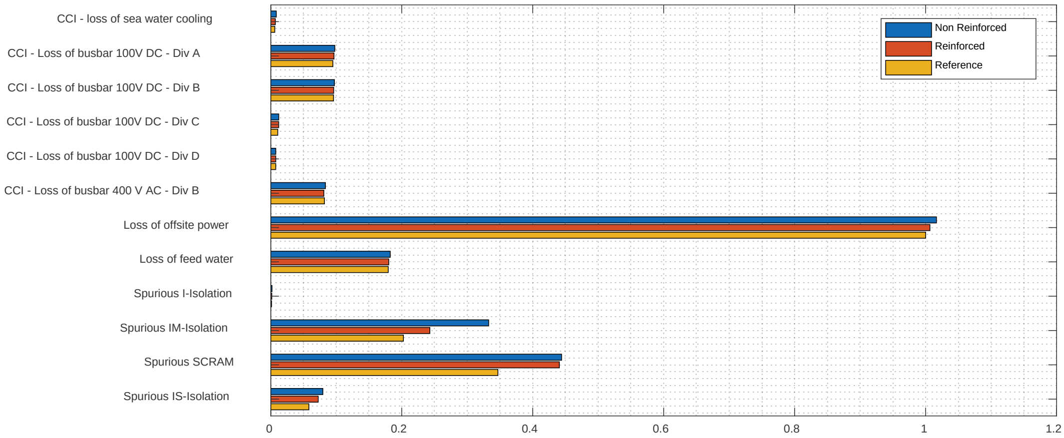

Figure 4.5.8: Comparison of normalized non-contained release frequencies (expected value) obtained with enhanced model for reinforced and non-reinforced hatch door in EIGT100-IDEJ0 scenario

Figure 4.5.***9*** and Figure 4.5.***10*** show the results of uncertainty analysis using ROAAM+ generated values of probability of containment failure due to ex-vessel debris coolability and steam explosion (see Figure 4.5.***3*** - 4.5.***6***). The results show that the uncertainty depends on the mode of debris ejection from the vessel. For example, in case of IDEJ1 (solid debris ejection – OFF) the resultant distributions are concentrated around its expected values, which can be explained by the probability distribution of conditional containment failure probability due to ex-vessel steam explosion with non-reinforced hatch door (Figure 4.5.***4***a (deep) and Figure 4.5.***6***a (shallow)), which mean that the results of PSA analysis will not be significantly affected by probability distributions for ex-vessel debris coolability, with exception to some scenarios with shallow pool conditions.

In case of IDEJ0 (Figure 4.5.***10***) the resultant distributions are very narrow; however, the right tails of the distributions can span over several orders of magnitude for some accident scenarios. Furthermore, Figure 4.5.***9*** and Figure 4.5.***10*** show the values of normalized non-contained release frequencies obtained with reference PSA model of Nordic BWR (marked with black "●"). The results indicate that in case of IDEJ1 (Figure 4.5.***9***), the reference values lie outside the range of respective distributions generated with enhanced model. In case of IDEJ0 (Figure 4.5.***10***) the reference values give very good estimates of non-contained release frequencies (e.g. judging by 0.25, 0.5, 0.75 quantiles of the distributions) in all initiating event groups.

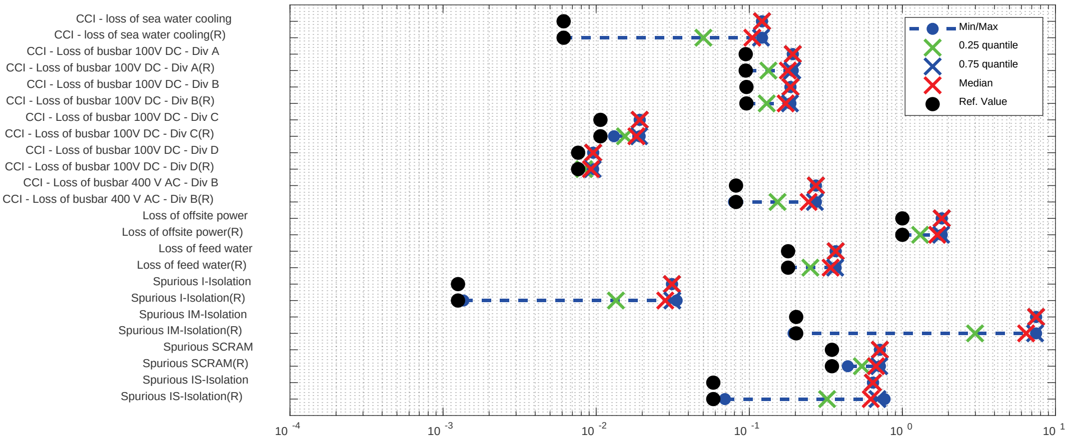

Figure 4.5.9: Comparison of distributions of normalized non-contained release frequencies obtained with enhanced model for reinforced (R) and non-reinforced hatch door in EIGT100-IDEJ1 scenario

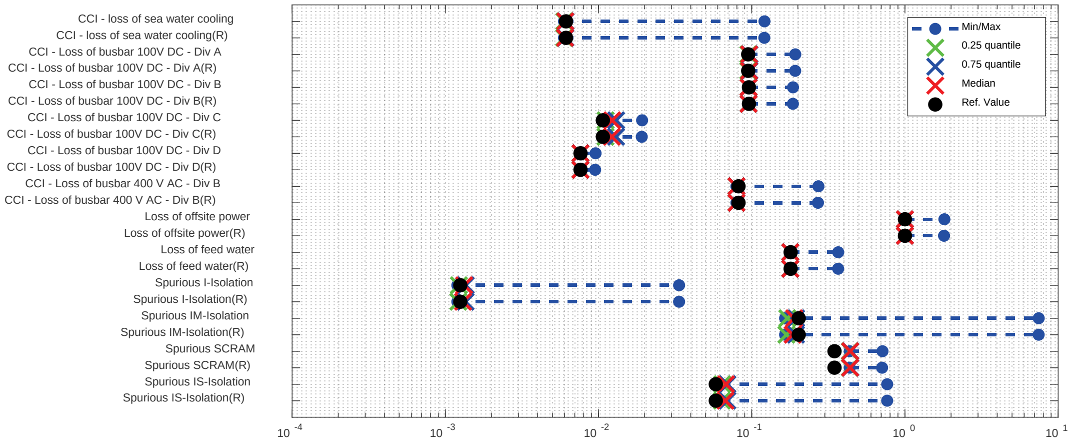

Figure 4.5.10: Comparison of distributions of normalized non-contained release frequencies obtained with enhanced model for reinforced (R) and non-reinforced hatch door in EIGT100-IDEJ0 scenario

The effect of design modification.

Analysis of the effect of possible design modification (reinforcement of hatch door) on PSA results using ROAAM+ generated data has been performed. Based on ROAAM+ analysis results, reinforcement of the containment hatch door, located in the LDW, can significantly reduce the risk of containment failure due to ex-vessel steam explosion, as demonstrated in the Chapter 4.4.1.

Figure 4.5.***7*** and 4.5.***8*** show the comparison of PSA analysis results for the original and modified designs (reinforced vs. non-reinforced hatch door) and reference cases (non-reinforced). Note that the results presented in Figure 4.5.***7*** - 4.5.***10*** – are normalized with respect to the frequency for non-contained release due to Loss of offsite power in the reference PSA model.

In case of IDEJ1 (that typically results in large melt release rates and jet sizes, and, hence significant ex-vessel consequences), the design modification results in reduction of non-contained release frequency, however the effect is not very significant. In case of IDEJ0 (that typically results in rather small jet sizes and release rates) the difference between non-reinforced, reinforced and reference cases is relatively small in all initiating event groups. The remaining difference can be explained by contribution from ex-vessel debris coolability, which is not affected by containment hatch door reinforcement and very sensitive to the pool depth (e.g. expected value of P_f in case of IDEJ0 and deep pool is 8.547e-3, while in case of shallow pool it is 5.312e-1).

Figure 4.5.***9*** and 4.5.***10*** show the results of uncertainty analysis, that give better perspective regarding the effect of design modification on ranges and distributions of the non-contained release frequencies. In case of IDEJ1 (Figure 4.5.***9***), reinforcement of the hatch door results in reduction of the non-contained release frequency in over 25% of the cases, however the major part of the distribution is concentrated around the values obtained with non-reinforced hatch door. It can be explained by the effect of the distribution of probability of failure due to ex-vessel debris coolability (Figure 4.5.***4***b, blue curve), which is not affected by design modification. If we compare the contribution from the sequences that lead to basemat melt-through in the reinforced and non-reinforced designs, the contribution from these sequences in case of the non-reinforced design is relatively small, compared to its contribution in the reinforced design, which is due to the large values of probability of failure (Pf = 1) due to ex-vessel steam explosion in the non-reinforced design (i.e. in case of very large values of probability of ex-vessel steam explosion, the frequency of the sequences that lead to ex-vessel debris coolability in the CET (Figure 4.5.***2***) will be affected by success probability of steam explosion (i.e. no steam

explosion), e.g. $(1 - Q_{SE})$, where Q_{SE} – is probability of failure due to ex-vessel steam explosion generated by ROAAM+ analysis, this value of success probability in turn is applied to all further events in the sequence [155]). In case of IDEJ0 (Figure 4.5.***10***) reinforcement of the hatch door does significantly affect the results, which can be explained by relatively small values of probability of failure due to both ex-vessel debris coolability (Figure 4.5.***3***b) and steam explosion (Figure 4.5.***3***a).

It should be noted however that different modes of containment failure can potentially lead to different paths and consequences in terms of fission products release. Therefore, current analysis implementation should be extended further, to take into account the effect of SA progression and containment phenomena on the magnitude, path and the timing of the release. Furthermore, proper consideration of different sources of uncertainty on the path and magnitude of potential releases is necessary (e.g. scrubbing, deposition on complex structures, mechanical resuspension, etc.)

Summary of the Results

Figure 4.5.***11*** and 4.5.***12*** summarize the results showed in the previous chapters as normalized non-contained release frequency for HS2-TL4/TH1 plant damage states for all previously mentioned initiating event groups (i.e. all transients and CCIs leading to these plant damage states). The obtained non-contained release frequencies were normalized against the values obtained with the reference PSA model of Nordic BWR. The results are presented for combinations of 2 phenomenological splinter scenarios (IDEJ1 vs. IDEJ0) and possible effect of design modification ($IDEJ1_R$ and $IDEJ0_R$).

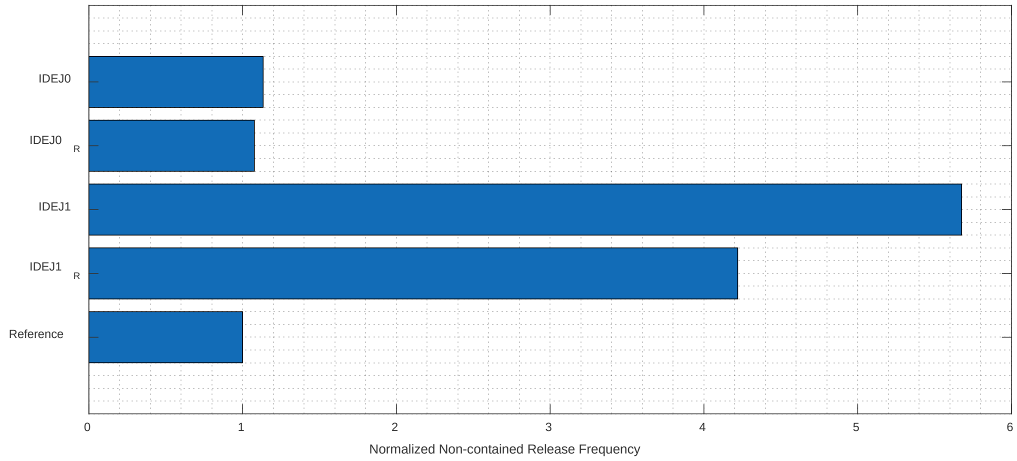

Figure 4.5.11: Expected value of Normalized Non-contained Release Frequency

The results show that in case of IDEJ0 (solid debris ejection – ON, typically results in gradual melt & debris ejection with relatively small sizes of the jet) the frequency of non-contained release increases by approximately 13% when compared with reference value. In case of IDEJ1 (solid debris ejection – OFF, typically leads to massive melt & debris ejection from the vessel with large sizes of the jet) the frequency on non-contained release is increased by a factor of ~5.6, when compared to the reference value. The effect of design reinforcement has relatively small impact on the results in case of IDEJ0 (see $IDEJ0$ vs. $IDEJ0_R$), since design modification does not affect ex-vessel debris coolability, however in case of IDEJ1 (see $IDEJ1$ vs. $IDEJ1_R$) it results in quite significant reduction of the frequency of non-contained release, from ~5.6 to 4.2, however these values are still above the values obtained with reference model.

Figure 4.5.***12*** show the results of uncertainty analysis. The resultant distributions of non-contained release frequency have quite significant spread in most of the cases, with exception to

IDE1. On the other hand, in case of IDEJ0 and IDEJ0$_R$ the major part of the distribution is concentrated very close to the minimum value, however there are parameter combinations in deterministic models that can lead significantly large sizes of the jet and large values of non-contained release frequency. In case of IDEJ1$_R$ the distribution of non-contained release frequency is skewed to the right, however in ~50% of the cases it is below 5 times the reference value, and in ~25% of the cases it is below ~2.85 times the reference value, and for some deterministic models parameters combinations it can be very close to the values obtained with reference model.

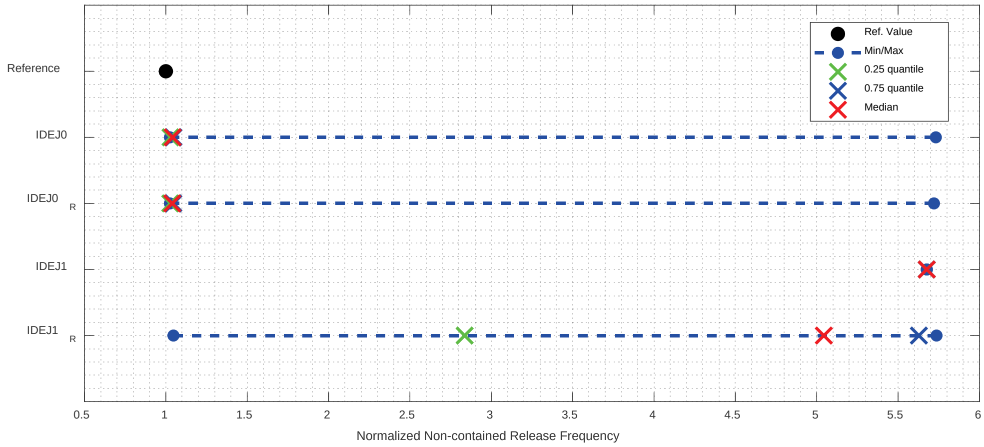

Figure 4.5.12: Uncertainty Analysis of Normalized Non-contained Release Frequency

4.6 Discussion and conclusions.

This report presents development of ROAAM+ methodology and an example of its application in PSA. PSA is used as a basis to select important initiating events and sequences in the severe accident progression. These scenarios are then analyzed with deterministic models, yielding information about which parameters that are of the highest importance for the development of the accident progression. The results from the deterministic analysis are used in the PSA to improve sequence definition as well as improve the estimation of phenomena depending on the sequence and the varied parameters. Furthermore, ROAAM+ framework provides an assessment of the effect of epistemic (knowledge) uncertainty on the results employing “knowledge-based treatment” of epistemic uncertain parameters, i.e. no probability distributions of epistemic uncertain parameters are assumed if there is no available knowledge about them.

In particular, probability of containment failure due to ex-vessel steam explosion and ex-vessel debris coolability strongly depends on modeling uncertainty in debris ejection mode from the vessel (Solid debris ejection option – IDEJ1 vs IDEJ0 in MELCOR). In case of solid debris ejection – off (IDEJ1) containment failure due to ex-vessel phenomena cannot be considered as physically unreasonable. In case of solid debris ejection – on (IDEJ0), containment failure due to ex-vessel steam explosion can be considered as physically unreasonable only in case of modified design (with reinforced hatch door)). On the other hand, containment hatch door reinforcement does not affect the probability of containment failure due to basemat melt-through and this threat cannot be considered as physically unreasonable in case of IDEJ0. ROAAM+ analysis results show that the probability of phenomena damaging the containment significantly depend on the depth of the pool in the lower drywell, e.g. coolability increases with the depth of the pool, however opposite is true for steam explosion (i.e. higher energetics in the deep pool), this information was used in enhanced PSA modelling.

The results obtained with the enhanced PSA model suggest that the non-contained release frequency depends on the mode of debris ejection from the vessel (IDEJ). In case of IDEJ1, it results in ~5.6 times larger value of non-contained release frequency when compared to the results obtained with reference model. Reinforcement of the hatch door in case of IDEJ1 results in reduction of the non-contained release frequency from ~5.6 to 4.2 times the value obtained with the reference PSA model. In case of IDEJ0 (both reinforced and non-reinforced design) enhanced PSA modelling results show relatively low increase of non-contained release frequency, from ~8 to 13% for non-reinforced and reinforced hatch door respectively.

Overall results show that the values of probabilities of phenomena damaging the containment used in the reference PSA model can be underestimated, judged by the respective values predicted by ROAAM+ framework. On the other hand, if it can be demonstrated that the vessel LH failure will be limited to IGTs failure and ablation of the opening will be limited, then the reference PSA model values of probabilities of phenomena damaging the containment can be considered as valid.

Present results show the dominant effect of the mode of debris ejection (IDEJ) on the results. However, given current state of knowledge about these phenomena, it should be treated as “phenomenological splinters” scenarios in PSA, that is, it should be demonstrated that non-contained release frequency is below regulatory requirements for all splinter scenarios considered.

It should be noted that current modelling approaches used in MELCOR code, for prediction of penetrations failure and melt and debris ejection, might be over-simplified in some aspects and lack necessary validation database. Furthermore, resent evidences from the Fukushima Daiichi Unit 2 and 3 primary containment vessel investigation [157], provided evidences that challenge ability of existing severe accident analysis tools to adequately predict transition of SA progression from in-vessel to ex-vessel phases in BWRs.

From a PSA stand point, the project has demonstrated that:

- It is both possible, achievable and desirable to increase the interaction between the deterministic and probabilistic assessment with regard to especially PSA level 2.
- Probabilities for phenomena can be estimated using the physical models in the thermo-hydraulic codes
- The uncertainty can be assessed, and correlation between phenomena can be managed.
- There is room for improvement in current modelling in PSA level 2 (sequence parameters).

The implementation made in a large scale PSA model shows that the integration of the ROAAM+ results in the PSA model is not only feasible, but could potentially lead to a considerable change of the frequency for non-acceptable release. The results show that the parameters indicated by the ROAAM+ approach as being of high importance to the quantitative results. It also emphasizes the need to distinguish between different probabilities of phenomena depending on different scenario, physical and intangible parameters (e.g. pool depth, that significantly affect coolability and steam explosion).

The approach has demonstrated that the vision, to develop the sequence from core melting, and to understand what are the important factors, is possible to meet. The integrated approach will have the ability to give a more comprehensive estimation of the uncertainty compared to the standard approach. The uncertainty related to phenomena will consider the interdependency between phenomena (all the way back to relevant deterministic and intangible, boundary conditions and scenario parameters.

The approach requires extensive work regarding building the deterministic model. Once built, this model can however be modified to evaluate different initiating events and sequences. The changes in the enhanced PSA-model on the other hand are limited and easy to implement.

The integrated approach requires improvement in especially scenario definition, which practically leads to more plant damage states. The PDS should consider all necessary scenario parameters, that may affect the calculation of phenomena and hence consider also the system availability normally represented within CETs.

4.7 Outlook

The work presented in this report can be extended further along several directions. Possible improvements can be subdivided into two main categories related to: (i) ROAAM+ probabilistic framework and deterministic modelling; (ii) related to aspects of application of ROAAM+ results in PSA.

Current ROAAM+ results show the dominant effect of the mode of multi-component debris ejection (IDEJ) on the results. The mode of debris ejection from the vessel is controlled through the user-defined switch (IDEJ=0 i.e. solid and liquid can be released vs. IDEJ=1 only liquid can be released). Development of a more mechanistic modeling approach would be needed in order to address this source of uncertainty.

ROAAM+ probabilistic framework employs sampling in the space of possible probability distributions of model intangible parameters (i.e. incomplete or partial probabilistic knowledge is available). In this work the sampling was performed using truncated normal distribution, where parameters that define the shape of distributions are selected by the user. An approach has been proposed [19] to overcome these limitations in risk analysis, and it is being implemented in ROAAM+.

Further reduction of the uncertainty can be achieved through refinement of existing melt ejection full and surrogate models. It can be achieved through refinement of the data base of MELCOR code solutions that account for the numerical effects of the maximum time step on the results. Currently the MEM SM does not predict material properties of the ejected debris from the vessel (e.g. density, thermal conductivity, etc.). These properties can be added to the MEM SM in the future, based on MELCOR analysis results. Furthermore, current treatment of debris ejection from the vessel implemented in MEM SM assumes uniform distribution of the ejected debris through the number of failed penetrations. An approach can be developed for non-uniform debris ejection from the vessel, depending on localized properties of the debris in the lower plenum and locations of failed penetrations.

Current implementations of melt ejection mode, ex-vessel steam explosion and ex-vessel debris coolability surrogate models are designed to predict respective melt release characteristics and containment loads per single jet, without taking into account interdependencies (e.g. interactions between several melt jets during melt fragmentation, etc.). More realistic approach is under development. It would affect both, steam explosion energetics as well as fraction of debris agglomerated and shape of the debris bed – which can affect significantly the risk of formation of non-coolable debris configuration.

With regards to the user-defined mode of melt release (IDEJ) one has to resolve a number of interacting relevant phenomena such as formation and accumulation of melt, gravity driven drainage of molten materials through the porous debris bed, resolidification of molten materials and formation of crusts in colder regions of the debris bed, that prevent further material drainage, which can result in either slow dripping of the melt from the vessel or accumulation of significant amounts of superheated metallic melt above the crust, which will be released upon crust remelting/failure. Crust formation can facilitate interaction of significant amounts of debris at high temperature with the vessel lower head wall, and significant mechanical load on the structure. This can lead to creep-rupture failure of the vessel lower head and massive ejection of debris from the vessel. Reduction of the uncertainty in the mode of ejection of multi-component mixture of solid and liquid debris, melt filtration through the porous debris, and crust formation is a necessary step for modelling of severe accident transition from in-vessel to ex-vessel phases, which is important for assessment of the loads on containment due to ex-vessel steam explosion and formation of non-coolable debris bed in the lower drywell of Nordic BWR design. Another important aspect of SA progression in BWRs is interaction of ejected debris and molten materials with the structures located under the vessel (such as CRD support, etc.) – which can significantly affect melt release conditions (e.g. vessel failure mode, or by jet breaking-up during interaction with the structures).

Current analysis has been performed only for one plant damage state. In the future other accident scenarios and possible recovery actions should be considered in the analysis. For example, analysis performed in [24] suggest that in case of mitigated SBO scenario in Nordic BWR, with recovery of ECCS after 2h after initiating event results in significant change in the mode of the vessel lower head failure (e.g. probability of the LH creep-to-failure increases from ~22% (in unmitigated case) to ~40% (in mitigated case) in case of IDEJ0, and decreases from 100% to ~80% in case of IDEJ=1 for unmitigated and mitigated scenarios respectively). This information can significantly affect risk analysis results in ROAAM+ framework and PSA. Furthermore, this information can provide more accurate and refined definition of available times for different operating actions and thus provide a better basis material for the HRA. It might also indicate that the current assumptions regarding available time for recovery needs to be updated.

Current ROAAM+ framework for Nordic BWR considers conditional containment failure probability as an indicator of SAM effectiveness. Conditional containment failure probability obtained in ROAAM+ was used to calculate the frequency of non-contained release (or unacceptable release frequency) in PSA, which include contributions from bypass sequences, containment rupture due to steam explosion and basemat melt-through. However, different modes of containment failure can potentially lead to different consequences in terms of fission products release and environmental impact. For example, fission product release due to e.g. containment bypass, containment rupture due to energetic phenomena or basemat melt-through are completely different from each other in terms of (i) time scale, (ii) phenomena that can affect the magnitude of the fission product release, such as deposition on different surfaces, gravitational settling, chemical interactions, etc.; and, ultimately, (iii) offsite consequences in terms of release path and magnitude, e.g. directly to the environment in case of containment rupture or through auxiliary building or reactor building in case of containment bypass; ground water contamination in case of basemat melt-through.

Further complications that needs to be addressed in both PSA and deterministic modelling are the potential occurrence of major secondary sources of aerosol materials due to containment phenomena, e.g. steam explosion can lead to aerosol resuspension or revaporization of the deposited materials, molten core–concrete interaction (MCCI) on the other hand, result in significant diversification of suspended aerosol composition due to the addition of a large amount of largely nonactive aerosol material in the size range of the existing aerosols, which would act to promote agglomeration and accelerate depletion of activity suspended in the containment atmosphere.

Therefore, current framework implementation should be extended further, to take into account the effect of SA progression and containment phenomena on the path and magnitude of the release, which in turn should be reflected in enhanced PSA modelling.

From a PSA perspective it is relevant to discuss how the information from the ROAAM+ analysis shall be used and especially considering how to improve sequence definitions and treatment of uncertainties. Of especial interest is to discuss how parameters like the phenomenological splinters shall be treated. This also affects the existing PSA level 2 analyses, where the project has demonstrated that the probabilities used are closer to the IDEJ0 parameter. Uncertainty analysis and the impact of it on the evaluation for PSA level 2 should also be discussed – considering that the uncertainty can be quantified to a higher degree of realism than before.

4.8 References

[1] Ang M. L., Buttery N. E., “An approach to the application of subjective probabilities in level 2 PSAs”, Reliability Engineering and System Safety, Vol 58, pp.145-156. (1997).

[2] Apostolakis G., Cunningham M., Lui C., Pangburn G., Reckley W., “A Proposed Risk Management Regulatory Framework,” U.S. Nuclear Regulatory Commission, NUREG-2150, Washington, DC, April 2012.

[3] Basso S., Konovalenko A. and Kudinov P., “Development of scalable empirical closures for self-leveling of particulate debris bed”, In Proceedings of ICAPP-2014, Charlotte NC, USA, April 6-9, Paper 14330, 2014.

[4] Basso S., Konovalenko A. and Kudinov P., “Sensitivity and Uncertainty Analysis for Predication of Particulate Debris Bed Self-Leveling in Prototypic SA conditions”, In Proceedings of ICAPP-2014, Charlotte NC, USA, April 6-9, paper 14329, 2014.

[5] Basso S., Konovalenko A. and Kudinov P., “Scaling Approaches to Experimental studies of Debris Bed Self-Leveling,” Nuclear Engineering and Design, Submitted, 2015.

[6] Basso, S., Konovalenko, A., Kudinov, P. “Empirical Closures for Particulate Debris Bed Spreading Induced by Gas-Liquid Flow”, Nuclear Engineering and Design, 297, 19-25, (2016).

[7] Basso S., Konovalenko A., Yakush S. E. and Kudinov P., “Effectiveness of the debris bed self-leveling under severe accident conditions,” Annals of Nuclear Energy, Volume 95, September 2016, Pages 75-85, 2016.

[8] Basso S., Konovalenko A., Yakush S. E. and Kudinov P., “The Effect of Self-Leveling on Debris Bed Coolability Under Severe Accident Conditions,” Nuclear Engineering and Design, Volume 305, 246-259, 2016.

[9] Billone, M.C., Chung H.M. and Yan Y., “Steam Oxidation Kinetics of Zirconium Alloys”, Argonne National Laboratory (ANL), 2002.

[10] Burkardt J., “The Truncated Normal Distribution”, Department of Scientific Computing, Florida State University, 2014.

[11] Corradini, M.L., et al., Users’ manual for Texas-V: One dimensional transient fluid model for fuel-coolant interaction analysis. 2002, University of Wisconsin-Madison: Madison WI 53706.

[12] Davydov, M.V., “Mathematical modeling of the process of interaction between high temperature melt and coolant in severe accident at NPP with water cooled reactor installation,” PhD thesis: 05.14.03. 2010. 197p. (in Russian)

[13] Dombrovsky, L.A., Davydov, M.V., Kudinov, P., “Thermal radiation modeling in numerical simulation of melt-coolant interaction,” Comp. Therm. Sci. 1 (1) 2009, pp. 1-35.

[14] Dombrovsky, L.A., Davydov, M.V., and Kudinov, P., Thermal radiation modeling in numerical simulation of melt-coolant interaction, Proc. Int. Symp. Adv. Comput. Heat Transfer (CHT-08), May 11–16, 2008, paper 155.

[15] S. Galushin, “Development of Risk Oriented Accident Analysis Methodology for Assessment of Effectiveness of Severe Accident Management Strategy in Nordic BWR”, PhD Thesis, TRITA-SCI-FOU 2019:08, ISBN: 978-91-7873-103-9, (2019).

[16] S. Galushin, D. Grishchenko, P. Kudinov, “Implementation of Probabilistic Framework of Risk Analysis Framework for Assessment of Severe Accident Management Effectiveness in Nordic BWR”, Reliability Engineering & System Safety, 203, November 2020, 107049.

[17] S. Galushin, D. Grishchenko, P. Kudinov, “Surrogate Model Development for Prediction of Vessel Failure Mode and Melt Release Conditions in Nordic BWR based on MELCOR

code", ICONE-27, 27th International Conference on Nuclear Engineering, Ibaraki, Japan, May 19-24, 2019.

[18] S. Galushin, D. Grishchenko, P. Kudinov, "The Effect of the Uncertainty in Prediction of Vessel Failure Mode and Melt Release Conditions on Risk of Containment Failure due to Ex-Vessel Steam Explosion in Nordic BWR", ICONE-27, 27th International Conference on Nuclear Engineering, Tsukuba, Ibaraki, Japan, May 19-24, 2019.

[19] Galushin S., Grishchenko D., Kudinov P., "Quantification of the Uncertainty Due to State-Of-Knowledge Using ROAAM+ Framework for Nordic BWRs", 16th International Topical Meeting on Probabilistic Safety Assessment and Analysis, Charleston, South Carolina USA, April 28-May 3, 2019.

[20] Galushin S., and Kudinov P., "An Approach to Grouping and Classification of Scenarios in Integrated Deterministic-Probabilistic Safety Analysis," Probabilistic Safety Assessment and Management PSAM 12, June 22-27, 2014, Honolulu, Hawaii, Paper 330, 2014.

[21] Galushin S. and Kudinov P., "Analysis of Core Degradation and Relocation Phenomena and Scenarios in a Nordic-type BWR," Nuclear Engineering and Design, Volume 310, 15 December 2016, Pages 125–141, 2016.

[22] Galushin S. and Kudinov P., "An Approach to Grouping and Classification of Scenarios in Integrated Deterministic-Probabilistic Safety Analysis," Science and Technology of Nuclear Installations, Article ID 278638, 13 pages, 2015.

[23] Sergey Galushin and Pavel Kudinov, "Analysis of the Effect of Severe Accident Scenario on Debris Properties in Lower Plenum of Nordic BWR Using Different Versions of MELCOR Code," Science and Technology of Nuclear Installations, vol. 2019, Article ID 5310808, 18 pages, 2019. https://doi.org/10.1155/2019/5310808, 2019.

[24] S. Galushin, P. Kudinov, "Comparison of Vessel Failure Model and Melt Release Conditions in Mitigated and Unmitigated Station Blackout Scenarios in Nordic BWR Using MELCOR code", ICONE-27, 27th International Conference on Nuclear Engineering, Tsukuba, Ibaraki, Japan, May 19-24, 2019.

[25] Sergey Galushin, Pavel Kudinov, Analysis of the effect of MELCOR modelling parameters on in-vessel accident progression in Nordic BWR, Nuclear Engineering and Design, Volume 350, 2019, Pages 243-258, ISSN 0029-5493, https://doi.org/10.1016/j.nucengdes.2019.04.040. 2019.

[26] Galushin, S, and P Kudinov. "Uncertainty Analysis of Vessel Failure Mode and Melt Release in Station Blackout Scenario in Nordic BWR Using MELCOR Code." 18th International Topical Meeting on Nuclear Reactor Thermal Hydraulics (NURETH-18), no. Portland, OR, USA, August 18-22, 2019.

[27] Galushin, S., and P. Kudinov. "Sensitivity and Uncertainty Analysis of the Vessel Lower Head Failure Mode and Melt Release Conditions in Nordic BWR Using MELCOR Code." Annals of Nuclear Energy Volume 135, 106976, 2020.

[28] S.O. Hansson, "An Overview of Decision Theory", SKN Report 41, (1990).

[29] Humphries, L. L., R. K. Cole, D. L. Louie, V.G. Figueroa, and M.F. Young. 2015a. "MELCOR Computer Code Manuals." Vol. 2: Reference Manuals Version 2.1.6840, no. SAND2015–6692 R.

[30] Humphries, L.L., R. K. Cole, D. L. Louie, V.G. Figueroa, and M.F. Young. 2015b. "MELCOR Computer Code Manuals." Vol. 1: Primer and User's Guide Version 2.1.6840, SAND2015-6691 R.

[31] Galushin S., Villanueva W., Grishchenko D., Kudinov P., "Development of core relocation surrogate model for prediction of debris properties in lower plenum of a Nordic

BWR", NUTHOS-11: The 11th International Topical Meeting on Nuclear Reactor Thermal Hydraulics, Operation and Safety, Gyeongju, Korea, October 9-13, (2016).

[32] Galushin S., Kudinov P., "Comparison of MELCOR code versions predictions of the properties of relocated debris in lower plenum of Nordic BWR" 17th International Topical Meeting on Nuclear Reactor Thermal Hydraulics, Xi'an, Shaanxi, China, Sept. 3-8, (2017)

[33] Galushin S., Kudinov P., "Effect of Severe Accident Scenario and Modeling Options in MELCOR on the Properties of Relocated Debris in Nordic BWR Lower Plenum" 17th International Topical Meeting on Nuclear Reactor Thermal Hydraulics, Xi'an, Shaanxi, China, Sept. 3-8, (2017).

[34] Grishchenko, D., Basso, S., Galushin, S., Kudinov P., "Development of TEXAS-V Code Surrogate Model for Assessment of Steam Explosion Impact in Nordic BWR," The 16th International Topical Meeting on Nuclear Reactor Thermal Hydraulics (NURETH-16), Chicago, IL, USA, August 30-September 4, paper 13937, 2015.

[35] Grishchenko D., Basso S., Kudinov P., and Bechta S. "Sensitivity Study of Steam Explosion Characteristics to Uncertain Input Parameters Using TEXAS-V Code," The 10th International Topical Meeting on Nuclear Thermal-Hydraulics, Operation and Safety (NUTHOS-10), Okinawa, Japan, December 14-18, 2014, Paper 1293, 2014.

[36] Grishchenko D., Galushin S., Kudinov P., "Failure domain analysis and uncertainty quantification using surrogate models for steam explosion in a Nordic type BWR", Nuclear Engineering and Design, Volume 343, 2019, Pages 63-75, ISSN 0029-5493, 2019.

[37] Grishchenko, D., Konovalenko, A., Karbojian, A., Kudinova, V., Bechta, S., and Kudinov, P., "Insight into steam explosion in stratified melt-coolant configuration," 15th International Topical Meeting on Nuclear Reactor Thermal Hydraulics, NURETH 15, May 12 to 17, 2013, Pisa, Italy, Paper 599. (Best paper award).

[38] Grishchenko D., Basso S., Kudinov P., "Development of a surrogate model for analysis of ex-vessel steam explosion in Nordic type BWRs," Nuclear Engineering and Design, Volume 310, 15 December 2016, Pages 311-327, 2016.

[39] Grishchenko D., Kudinov P., "Validation of a Full Model for the Analysis of Ex-Vessel Steam Explosion in LWRs", 18th International Topical Meeting on Nuclear Reactor Thermal Hydraulics (NURETH-18), Portland, OR. August 18-23, 2019.

[40] Goronovski A., Villanueva W., Kudinov P., Tran C.-T. "Effect of Corium Non-Homogeneity on Nordic BWR Vessel Failure Mode and Timing," Proceedings of ICAPP 2015, May 03-06, Nice, France, Paper 15160, 2015.

[41] Goronovski, A., Villanueva, W., Tran, C.-T., and Kudinov, P., "The Effect of Internal Pressure and Debris Bed Thermal Properties on BWR Vessel Lower Head Failure and Timing," 15th International Topical Meeting on Nuclear Reactor Thermal Hydraulics, NURETH 15, May 12 to 17, 2013, Pisa, Italy, Paper 500.

[42] Helton, J.C., Johnson, J.D., Oberkampf, W.L., Sallaberry, C.J., "Representation of analysis results involving aleatory and epistemic uncertainty," International Journal of General Systems, Vol.39(6),pp.605-646, (2010).

[43] Kaplan S. and Garrick, B. J., "On The Quantitative Definition of Risk," Risk Analysis, 1: pp.11–27, (1981).

[44] Karbojian, A., Ma, W.M., Kudinov, P., Davydov, M., Dinh, N., "A scoping study of debris formation in DEFOR experimental facility", 15th International Conference on Nuclear Engineering, Nagoya, Japan, April 22-26, 2007, Paper number ICON15-10620.

[45] Karbojian, A., Ma, W., Kudinov, P., and Dinh, T.-N., “A Scoping Study of Debris Bed Formation in the DEFOR Test Facility”, Nuclear Engineering and Design, 239, 2009, 1653-1659.

[46] Konovalenko, A., Basso, S., Karbojian, A., and Kudinov, P., “Experimental and Analytical Study of the Particulate Debris Bed Self-leveling,” Proceedings of The 9th International Topical Meeting on Nuclear Thermal-Hydraulics, Operation and Safety (NUTHOS-9), Kaohsiung, Taiwan, September 9-13, N9P0305, 2012.

[47] Konovalenko A., Basso S., and Kudinov P. “Experiments and Characterization of the Two-Phase Flow Driven Particulate Debris Spreading in the Pool,” The 10th International Topical Meeting on Nuclear Thermal-Hydraulics, Operation and Safety (NUTHOS-10), Okinawa, Japan, December 14-18, 2014, Paper 1257, 2014.

[48] Konovalenko A., Basso S., Kudinov P., Yakush S. E., “Experimental Investigation of Particulate Debris Spreading in a Pool”, Nuclear Engineering and Design, Volume 297, pp208-219, 2016.

[49] Konovalenko A., Basso S., Kudinov P., Yakush S. E., “Experiments and Modeling of Particulate Debris Spreading in a Pool,” The 16th International Topical Meeting on Nuclear Reactor Thermal Hydraulics (NURETH-16), Chicago, IL, USA, August 30-September 4, paper 14221, 2015.

[50] Konovalenko, A., Karbojian, A., and Kudinov, P., “Experimental Results on Pouring and Underwater Liquid Melt Spreading and Energetic Melt-coolant Interaction,” Proceedings of The 9th International Topical Meeting on Nuclear Thermal-Hydraulics, Operation and Safety (NUTHOS-9), Kaohsiung, Taiwan, September 9-13, N9P0303, 2012.

[51] Konovalenko, A. and Kudinov, P., “Development of Scaling Approach for Prediction of Terminal Spread Thickness of Melt Poured into a Pool of Water,” Proceedings of The 9th International Topical Meeting on Nuclear Thermal-Hydraulics, Operation and Safety (NUTHOS-9), Kaohsiung, Taiwan, September 9-13, N9P0302, 2012. (Best paper award).

[52] Kolev N., Multiphase Flow Dynamics, Vol. 2, Ch. 2, Springer, Berlin, Heidelberg, NY (2005).

[53] Kudinov, P. and Davydov M., “Development of Surrogate Model for Prediction of Corium Debris Agglomeration,” In Proceedings of ICAPP-2014, Charlotte, USA, April 6-9, Paper 14366, 2014.

[54] Kudinov, P. and Davydov, M., “Approach to Prediction of Melt Debris Agglomeration Modes in a LWR Severe Accident,” Proceedings of ISAMM-2009, Böttstein, Switzerland, October 26 - 28, 2009.

[55] Kudinov, P. and Davydov, M., “Development of Ex-Vessel Debris Agglomeration Mode Map for a LWR Severe Accident Conditions,” Proceedings of the 17th International Conference on Nuclear Engineering, July 12-16, 2009, Brussels, Belgium, Paper ICONE17-75080.

[56] Kudinov, P. and Davydov, M., “Development and Validation of the Approach to Prediction of Mass Fraction of Agglomerated Debris,” The 8th International Topical Meeting on Nuclear Thermal-Hydraulics, Operation and Safety (NUTHOS-8), Shanghai, China, October 10-14, N8P0298, 2010.

[57] Kudinov P., Davydov M.V., “Development and validation of conservative-mechanistic and best estimate approaches to quantifying mass fractions of agglomerated debris,” Nuclear Engineering and Design, 262, September 2013, pp. 452-461.

[58] Kudinov and Davydov M., “Prediction of Mass Fraction of Agglomerated Debris in a LWR Severe Accident,” The 14th International Topical Meeting on Nuclear Reactor Thermal Hydraulics (NURETH-14), Toronto, Ontario, Canada, September 25-29, 2011.

[59] Kudinov, P., Davydov, M., Pohlner G., Bürger M., Buck M., and Meignen R., "Validation of the FCI codes against DEFOR-A data on the mass fraction of agglomerated debris," 5th European Review Meeting on Severe Accident Research (ERMSAR-2012) Cologne (Germany), March 21-23, 2012.

[60] Kudinov, P. and Dinh, T.-N., "An analytical study of mechanisms that govern debris packing in a LWR severe accident", The 12th International Topical Meeting on Nuclear Reactor Thermal Hydraulics (NURETH-12), Sheraton Station Square, Pittsburgh, Pennsylvania, U.S.A. September 30-October 4, 2007. Paper 247.

[61] Kudinov, P. and Dinh, T.-N., "A Computational Study of Debris Bed Formation," ANS Transactions, 2008, paper 193463.

[62] Kudinov P., Galushin S., Davydov M., "Analysis of the Risk of Formation of Agglomerated Debris in Nordic BWRs," NUTHOS-11:The 11th International Topical Meeting on Nuclear Reactor Thermal Hydraulics, Operation and Safety, Gyeongju, Korea, October 9-13, N11P0592, 2016.

[63] Kudinov P., Galushin S., Goronovski A., and Villanueva W., "RES1: Definition of a Reference Nordic BWR Plant Design and Plant Damage States for Application of ROAAM to Resolution of Severe Accident Issues," Research Report, The Eighth Framework of Accident Phenomena of Risk Importance (APRI-8), Division of Nuclear Power Safety, Royal Institute of Technology (KTH), Stockholm, Sweden, April 04, 2014.

[64] Kudinov P, Galushin S., Grishchenko D., Yakush S., Adolfsson Y., Ranlöf L., Bäckström O., Enerholm A., Krcal P., Tuvelid A., "Deterministic-Probabilistic Safety Analysis Methodology for Analysis of Core Degradation, Ex-vessel Steam Explosion and Debris Coolability", NKS-345, ISBN 978-87-7893-427-7. Jul 2015.

[65] Kudinov P., Galushin S., Grishchenko D., Yakush S., Davydov M., "ROAAM+ Analysis Results for Nordic BWRs". Accident Phenomena of Risk Importance (APRI-10) Report, 2019.

[66] Kudinov P., Galushin S., Raub S., Phung V.-A., Kööp K., Karanta I., Silvonen T., Adolfsson Y., Bäckström O., Enerholm A., Krcal P., Sunnevik K., "Feasibility Study for Connection Between IDPSA and conventional PSA Approach to Analysis of Nordic type BWR's," NKS-DPSA Project, NKS-R, Report: NKS-315, 2014.

[67] Pavel Kudinov, Sergey Galushin, Dmitry Grishchenko, Sergey Yakush, Yvonne Adolfsson, Lisa Ranlöf, Ola Bäckström, Anders Enerholm, "Scenarios and Phenomena Affecting Risk of Containment Failure and Release Characteristics," SPARC Project, NKS-395 22 Aug 2017, 2017.

[68] Pavel Kudinov, Sergey Galushin, Dmitry Grishchenko, Sergey Yakush, Simone Basso, Alexander Konovalenko, Mikhail Davydov, "Application of Integrated Deterministic-Probabilistic Safety Analysis to Assessment of Severe Accident Management Effectiveness in Nordic BWRs," The 17th International Topical Meeting on Nuclear Reactor Thermal Hydraulics (NURETH-17) Paper: 21590, Qujiang Int'l Conference Center, Xi'an, China, September 3-8, 2017.

[69] Kudinov P., Galushin S., Yakush S., Villanueva W., Phung V.-A., Grishchenko D., Dinh N., "A Framework for Assessment of Severe Accident Management Effectiveness in Nordic BWR Plants," Probabilistic Safety Assessment and Management PSAM 12, June 22-27, 2014, Honolulu, Hawaii, Paper 154, 2014.

[70] Pavel Kudinov, Sergey Galushin, Dmitry Grishchenko, Sergey Yakush, Anders Riber Marklund, Ola Bäckström, "Scenarios and Phenomena Affecting Risk of Containment Failure and Release Characteristics", NKS-410, ISBN 978-87-7893-499-4, (2018).

[71] Kudinov, P., Grishchenko, D., Konovalenko, A., Karbojian, A., Bechta, S., “Investigation of Energetic Interactions in Stratified Melt-Coolant Configurations, Phase I: Pre-study,” MHI-TRDC Project Report, Division of Nuclear Power Safety, KTH, Stockholm, Sweden, February 23, 2012.

[72] Kudinov P., Grishchenko D., Konovalenko A., Karbojian A. “Premixing and Steam Explosion Phenomena in the Tests with Stratified Melt-Coolant Configuration and Binary Oxdic Melt Simulant Materials,” Nuclear Engineering and Design, Volume 314, Pages 1-338 (1 April 2017).

[73] Kudinov P., Grishchenko D., Karbojian A., Villanueva W., “Design and development of experiments for validation of debris remelting and interactions with structures,” Accident Phenomena of Risk Importance (APRI-8), Report MEM1, Rev.2, January 10, 2015.

[74] Kudinov P., Grishchenko D., Konovalenko A., Karbojian A., “Experimental Investigation of Debris Bed Agglomeration and Particle Size Distribution Using WO3-ZrO2 Melt,” The 16th International Topical Meeting on Nuclear Reactor Thermal Hydraulics (NURETH-16), Chicago, IL, USA, August 30-September 4, paper 14220, 2015.

[75] Kudinov P., Grishchenko D., Konovalenko A., Karbojian A., Bechta S. “Investigation of Steam Explosion in Stratified Melt-Coolant Configuration,” The 10th International Topical Meeting on Nuclear Thermal-Hydraulics, Operation and Safety (NUTHOS-10), Okinawa, Japan, December 14-18, 2014, Paper 1316, 2014.

[76] Kudinov P., Grishchenko D., Galushin S., Yakush S., Konovalenko A., Basso S., Davydov M., Thakre S., Villanueva W., Ma W., Yu P., Manickam L., “Integrated ROAAM+ Development and Analysis Results for Nordic BWRs”. Accident Phenomena of Risk Importance (APRI-9) Report, January 2017.

[77] Kudinov P., Grishchenko D., Galushin S., Yakush S., Konovalenko A., Basso S., Davydov M., Villanueva W., Goronovski A., “RES3: Preliminary Analysis of Conditional Containment Failure Probabilities Using ROAAM+ Frameworks.” Risk Oriented Framework for Safety Analysis of Severe Accident Issues in Nordic BWRs. Accident Phenomena of Risk Importance (APRI-8), January 2016.

[78] Kudinov, P., Karbojian, A., Ma, W.M., Davydov, M., and Dinh, T.-N., “A Study of Ex-Vessel Debris Formation in a LWR Severe Accident”, Proceedings of ICAPP 2007, Nice, France, May 13-18, 2007, Paper 7512.

[79] Kudinov, P., Karbojian, A., Ma, W.M., and Dinh, T.-N., “An experimental study on debris formation with corium simulant materials,” Proc. ICAPP’08, Anaheim, CA USA, June 8–12, 2008, paper 8390.

[80] Kudinov, P., Karbojian, A., Ma, W., and Dinh, T.-N. “The DEFOR-S Experimental Study of Debris Formation with Corium Simulant Materials,” Nuclear Technology, 170(1), April 2010, pp. 219-230, 2010.

[81] Kudinov, P., Karbojian, A., and Tran, C.-T., “Experimental Investigation of Melt Debris Agglomeration with High Melting Temperature Simulant Materials,” Proceedings of ISAMM-2009, Böttstein, Switzerland, October 26 - 28, 2009.

[82] Kudinov, P., Karbojian, A., Tran, C.-T., Li, L., Ma, W., “Improvement of the MHI US-APWR and possibly MHI EU-APWR Severe Accident Mitigation Strategy for Applications in Europe,” Phase I Report, Division of Nuclear Power Safety, KTH, Stockholm, Sweden, March 30, 2010.

[83] Kudinov, P., Karbojian, A., Tran, C.-T., and Villanueva, W., “The DEFOR-A Experiment on Fraction of Agglomerated Debris as a Function of Water Pool Depth,” The 8th International Topical Meeting on Nuclear Thermal-Hydraulics, Operation and Safety (NUTHOS-8), Shanghai, China, October 10-14, N8P0296, 2010.

[84] Kudinov, P., Karbojian, A., Tran, C.-T., Villanueva, W., "Experimental Data on Fraction of Agglomerated Debris Obtained in the DEFOR-A Melt-Coolant Interaction Tests with High Melting Temperature Simulant Materials," Nuclear Engineering and Design, 263, October 2013, Pages 284-295, 2013.

[85] Kudinov, P., Konovalenko, A., and Karbojian, A., "Assessment of the Melt Spreading Effectiveness in the MHI APWR Severe Accident Mitigation Strategy for Application in Europe," Report, Division of Nuclear Power Safety, KTH, Stockholm, Sweden, March 30, 2011.

[86] Kudinov, P., Konovalenko, A., Karbojian, A., "Assessment of the Melt Spreading Effectiveness in the MHI APWR Severe Accident Mitigation Strategy for Application in Europe," Phase-III, Part-I, Report, Division of Nuclear Power Safety, KTH, Stockholm, Sweden, November 7, 2011.

[87] Kudinov, P., Konovalenko, A., Grishchenko, D., Karbojian, A., and Bechta, S., "Assessment of the Melt Spreading Effectiveness in the MHI APWR Severe Accident Mitigation Strategy for Application in Europe, Phase III" Report, Division of Nuclear Power Safety, KTH, Stockholm, Sweden, March 30, 2012.

[88] Kudinov, P., Ma, W.M., Tran, C.-T., Hansson, R., Karbojian, A., and Dinh, T.-N. "Multiscale Phenomena of Severe Accident," NKS-R and NKS-B Joint Summary Seminar, Armémuseum, Stockholm, 26th - 27th March 2009.

[89] Kudinov, P. and Kudinova, V., "Influence of Water Subcooling on Fracture of Melt Debris Particle," ANS Transactions, 2009, paper 210646.

[90] Kudinov, P., Kudinova, V., and Dinh, T.-N., "Molten Oxidic Particle Fracture during Quenching in Water," 7th International Conference on Multiphase Flow ICMF 2010, Tampa, FL USA, May 30-June 4, 2010.

[91] Kymäläinen, O., Tuomisto, H., and Theofanous, T. G., "In-Vessel Retention of Corium at the Loviisa Plant," Nucl. Eng. Des. 169, 109–130, 1997.

[92] Li L., Karbojian A., Kudinov P., Ma W., "An Experimental Study on Dryout Heat Flux of Particulate Beds Packed with Irregular Particles," Proceedings of ICAPP 2011, Nice, France, May 2-5, 2011, Paper 11185. 2011.

[93] Liao, W.-K., Liu, Y., and Choudhary, A.. "A Grid-based Clustering Algorithm using Adaptive Mesh Refinement," In proceedings of the 7thWorkshop on Mining Scientific and Engineering Datasets, 2004.

[94] Magallon, D., Huhtiniemi, I., Hohmann, H., "Lessons Learnt from FARO/TERMOS Corium Melt Quenching Experiments," In: Proceedings of the OECD/CSNI Specialists Meeting on Fuel-Coolant Interactions, Tokai-Mura, Japan, NEA/CSNI/R(97)26, Part II, 1997, pp.431-446.

[95] Magallon, D., et al., OECD research programme on fuel-coolant interaction. Steam explosion resolution for nuclear applications - SERENA. 2007.

[96] Meignen R., Raverdy B., Buck M., Pohlner G., Kudinov P., Ma W., Brayer C., Piluso P., Hong S.-W., Leskovar M., Uršič M., Albrecht G., Lindholm I., Ivanov I., "Status of steam explosion understanding and modelling," Annals of Nuclear Energy, Article in Press, Available online 23 August 2014.

[97] Mitchell T. M., Machine Learning, Mcgraw-Hill Series in Computer Science, McGraw-Hill, New York, NY, USA, 1997.

[98] Morris M. D., "Factorial sampling plans for preliminary computational experiments", Technometrics, 33, (2), pp. 161–174, 1991.

[99] DeGroot Morris H., Schervish Mark J., "Probability and Statistics (4th Edition). Pearson Education. 2014.

[100] Niederreiter, H., Random number generation and quasi-Monte Carlo methods, SIAM, p. 29, ISBN 0-89871-295-5, (1992).

[101] Christoph Schlier, “On scrambled Halton sequences”, Applied Numerical Mathematics, Volume 58, Issue 10, 2008.

[102] G. Ökten, “Random Sampling from Low-Discrepancy Sequences: Applications to Option Pricing”, Mathematical and Computer Modelling 35 (2002).

[103] J. Shortle and P. L’Ecuyer, “Introduction to rare-event simulation,” in Wiley Encyclopedia of Operations Research and Management Science, Wiley, 2010.

[104] Eric C. Anderson, “Monte Carlo Methods and Importance Sampling”, Lecture Notes for Statistical Genetics, 1999.

[105] Palagin A., Miassoedov A., Gaus-Liu X., Muscher H., Buck M., Tran C.T., Kudinov P., Carenini L., Koellein C., Luther W., Chudanov V., “Analysis and interpretation of the LIVE-L6 experiment,” 5th European Review Meeting on Severe Accident Research (ERMSAR-2012), Cologne (Germany), March 21-23, 2012.

[106] Phung, V. -A., Grishchenko, D., Galushin, S., Kudinov, P., “Prediction of In-Vessel Debris Bed Properties in BWR Severe Accident Scenarios using MELCOR and Neural Networks,” Journal of Annals of Nuclear Energy, submitted January 2017.

[107] Phung, V.-A. Galushin, S. Raub, S. Goronovski, A., Villanueva, W., Kööp, K., Grishchenko, D., Kudinov, P., “Characteristics of debris in the lower head of a BWR in different severe accident scenarios,” NED, Volume 305, 15, August 2016, pages 359-370, 2016.

[108] Pohlner G., Buck M., Meignen R., Kudinov P., Ma W., Polidoro F., Takasuo E., “Analyses on ex-vessel debris formation and coolability in SARNET frame,” Annals of Nuclear Energy, Volume 74, December 2014, Pages 50-57, 2014.

[109] Saltelli A., Tarantola S., Campolongo F., Ratto M., Sensitivity Analysis in Practice, John Wiley & Sons Ltd, p. 94, 2004.

[110] Spencer, B.W., Wang K., Blomquist, C.A., McUmber, L.M., and Schneider, J.P., “Fragmentation and Quench Behaviour of Corium Melt Streams in Water,” NUREG/CR-6133 ANL-93/32, Argonne National Laboratory. 1994.

[111] Strålsäkerhetsmyndigheten, “APRI-7 Accident Phenomena of Risk Importance”, En lägesrapport om forskningen inom svåra havarier under åren 2009-2011, rapportnummer 2012:12, ISSN:2000-0456, 2012.

[112] Strålsäkerhetsmyndigheten (SSM). “APRI 9 – Accident Phenomena of Risk Importance, En lägesrapport om forskningen inom området svåra haverier under åren 2015-2017”, June 2018.

[113] Taylor, G.I., “The dispersion of jets of metals at low melting point in water.” In: Batchelor, G.K. (Ed.), The Scientific Paper of Sir Geoffrey Ingram Taylor, vol. 3., Cambridge University Press, 1963. 559 pp.

[114] Theofanous, T. G., “On Proper Formulation of Safety Goals and Assessment of Safety Margins for Rare and High-Consequence Hazards,” Reliability Engineering and System Safety, 54, pp.243-257, (1996).

[115] Theofanous, T. G. and Dinh, T.-N., “Integration of multiphase Science and Technology with Risk Management in Nuclear Power reactors: Application of the Risk-Oriented Accident Analysis Methodology to the Economic, Simplified Boiling Water Reactor Design,” Multiphase Science and Technology, V20(2), 2008, Pages 81-211.

[116] T. G. Theofanous, W. W. Yuen, “The probability of alpha-mode containment failure”, Nuclear Engineering and Design 155, 459-473, 1995.

[117] T. G. Theofanous, H. Yan, M. Z. Podowski, “The Probability of Mark-I Containment Failure by Meltattack of the Liner”, NUREG/CR-6025 Report, 1993.

[118] M. M. Pilch, H. Yan, T. G. Theofanous, “The probability of containment failure by direct containment heating in Zion”, Engineering and Design 164, 1-36, 1996.

[119] Torregrosa, C., Villanueva, W., Tran, C.-T., and Kudinov, P., “Coupled 3D Thermo-Mechanical Analysis of a Nordic BWR Vessel Failure and Timing,” 15th International Topical Meeting on Nuclear Reactor Thermal Hydraulics, NURETH 15, May 12 to 17, 2013, Pisa, Italy, Paper 495.

[120] Torregrosa, M.C., “Coupled 3D Thermo-Mechanical Analysis of Nordic BWR Lower Head Failure in case of Core Melt Severe Accident” MSc Thesis, Royal Institute of Technology (KTH), 2013.

[121] Tran, C.T., and Dinh, T. N., "The Effective Convectivity Model for Simulation of Melt Pool Heat Transfer in a Light Water Reactor Pressure Vessel Lower Head. Part I: Physical Processes, Modeling and Model Implementation", pp.849-859, 2009. “Part II: Model Assessment and Application", Progress in Nuclear Energy, Vol.51, N.8, pp.860-871, 2009.

[122] Tran, C.-T. and Kudinov P., “Local Heat Transfer From The Corium Melt Pool to the BWR Vessel Wall,” The 14th International Topical Meeting on Nuclear Reactor Thermal Hydraulics (NURETH-14), Toronto, Ontario, Canada, September 25-29, 2011.

[123] Tran, C.-T. and Kudinov P., “A Synergistic use of CFD, Experiments and Effective Convectivity Model to Reduce Uncertainty in BWR Severe Accident Analysis,” CFD4NRS-3 Workshop, Bethesda, MD, USA, September 14-16, 2010.

[124] Tran, C.-T. and Kudinov, P., “The effective convectivity model for simulation of molten metal layer heat transfer in a boiling water reactor lower head,” Proceedings of ICAPP ’09, Tokyo, Japan, May 10-14, 2009 Paper 9114.

[125] Tran, C. T., Kudinov P., and Dinh, T. N. “An approach to numerical simulation and analysis of molten corium coolability in a BWR lower head,” XCFD4NRS Workshop, Grenoble, France, September 10-12, 2008.

[126] Tran, C. T., Kudinov, P., and Dinh, T. N., “An approach to numerical simulation and analysis of molten corium coolability in a BWR lower head,” Nuclear Engineering and Design, 240, 2010, 2148–2159.

[127] Tran, C.-T., Villanueva, W., and Kudinov, P., “A Study on the Integral Effect of Corium Material Properties on Melt Pool Heat Transfer in a Boiling Water Reactor,” Proceedings of The 9th International Topical Meeting on Nuclear Thermal-Hydraulics, Operation and Safety (NUTHOS-9), Kaohsiung, Taiwan, September 9-13, , N9P0289, 2012.

[128] Villanueva, W., Tran, C.-T., Kudinov, P., “Coupled thermo-mechanical creep analysis for boiling water reactor pressure vessel lower head,” Nuclear Engineering and Design, 249, 2012, 146-153.

[129] Villanueva, W., Tran C.-T., and Kudinov P., “Analysis of Instrumentation Guide Tube Failure in a BWR Lower Head,” Proceedings of The 9th International Topical Meeting on Nuclear Thermal-Hydraulics, Operation and Safety (NUTHOS-9), Kaohsiung, Taiwan, September 9-13, , N9P0268, 2012.

[130] Villanueva, W., Tran, C.-T., and Kudinov, P., “Effect of CRGT Cooling on Modes of Global Vessel Failure of a BWR Lower Head,” Proceedings of the 20th International Conference on Nuclear Engineering (ICONE-20), Anaheim, CA, USA, July 30 - August 3, Paper 54955, 2012.

[131] Villanueva W., Tran C.-T., and Kudinov P., “A Computational Study On Instrumentation Guide Tube Failure During a Severe Accident in Boiling Water Reactors,” The 14th International Topical Meeting on Nuclear Reactor Thermal Hydraulics (NURETH-14), Toronto, Ontario, Canada, September 25-29, 2011.

[132] Villanueva W., Tran C.-T., and Kudinov P., “Assessment with Coupled Thermo-Mechanical Creep Analysis of Combined CRGT and External Vessel Cooling Efficiency for a BWR,” The 14th International Topical Meeting on Nuclear Reactor Thermal Hydraulics (NURETH-14), Toronto, Ontario, Canada, September 25-29, 2011.

[133] Villanueva W., Tran C.-T. and Kudinov P., “Coupled Thermo-Mechanical Creep Analysis for Boiling Water Reactor Pressure Vessel Lower Head” The 8th International Topical Meeting on Nuclear Thermal-Hydraulics, Operation and Safety (NUTHOS-8), Shanghai, China, October 10-14, N8P0248, 2010.

[134] Yakush S. E., Konovalenko A., Basso S. and Kudinov P., “Effect of Particle Spreading on Coolability of Ex-Vessel Debris Bed” The 16th International Topical Meeting on Nuclear Reactor Thermal Hydraulics (NURETH-16), Chicago, IL, USA, August 30-September 4, paper 14112, 13p, 2015.

[135] S. E. Yakush, A. Konovalenko, S. Basso, P. Kudinov, ” Validation of DECOSIM Code Against Experiments on Particle Spreading by Two-Phase Flows in Water Pool”, NUTHOS-11: The 11th International Topical Meeting on Nuclear Reactor Thermal Hydraulics, Operation and Safety, Gyeongju, Korea, October 9-13, 2016.

[136] Yakush, S, Kudinov, P. “Effects of Water Pool Subcooling on the Debris Bed Spreading by Coolant Flow,” Proceedings of the 11th International Conference on Advanced Nuclear Power Plants (ICAPP 2011), Nice, France, May 2011, paper 11416, 14 p. 2011.

[137] Yakush S. and Kudinov P., “A Model for Prediction of Maximum Post-Dryout Temperature in Decay-Heated Debris Bed,” Proceedings of the 2014 22nd International Conference on Nuclear Engineering, ICONE22, July 7-11, Prague, Czech Republic, ICONE22-31214. 2014.

[138] Yakush S. E., and Kudinov P., “Effect of Melt Agglomeration on Coolability of a Debris Bed”. NUTHOS-11:The 11th International Topical Meeting on Nuclear Reactor Thermal Hydraulics, Operation and Safety, Gyeongju, Korea, October 9-13, 2016. N11A0590.

[139] Yakush S. E., and Kudinov P., “Melt Agglomeration Influence on Ex-vessel Debris Bed Coolability” The 17th International Topical Meeting on Nuclear Reactor Thermal Hydraulics (NURETH-17), Paper: 21455, Qujiang Int’l Conference Center, Xi’an, China, September 3-8, 2017.

[140] Yakush S. E., and Kudinov P., “Coolablity and Post-dryout Behavior of a Porous Debris Bed with Distributed Agglomerates” NUTHOS-12:The 12th International Topical Meeting on Nuclear Reactor Thermal Hydraulics, Operation and Safety, Quingdao, China, October 8-14, 2018, Paper 1087.

[141] Yakush S., Kudinov P., “In-vessel debris bed coolability and implications for vessel failure mode” NUTHOS-11:The 11th International Topical Meeting on Nuclear Reactor Thermal Hydraulics, Operation and Safety, Gyeongju, Korea, October 9-13, N11P0532, 2016.

[142] Yakush, S. E., Kudinov, P., Villanueva, W., and Basso, S., “In-Vessel Debris Bed Coolability and its Influence on the Vessel Failure,” 15th International Topical Meeting on Nuclear Reactor Thermal Hydraulics, NURETH 15, May 12 to 17, 2013, Pisa, Italy, Paper 464.

[143] Yakush, S. and Kudinov, P., “Transient Phenomena of Ex-vessel Debris Bed Formation in a LWR Severe Accident,” ANS Transactions, 2009, paper 210830.

[144] Yakush, S. and Kudinov, P., “Simulation of Ex-Vessel Debris Bed Formation and Coolability in a LWR Severe Accident,” Proceedings of ISAMM-2009, Böttstein, Switzerland, October 26 - 28, 2009.

[145] Yakush, S., Kudinov, P., and Dinh, T.-N., “Multiscale Simulations of Self-organization Phenomena in the Formation and Coolability of Corium Debris Bed,” Proc. The 13th International Topical Meeting on Nuclear Reactor Thermal Hydraulics (NURETH-13), September 27-October 2, 2009. Kanazawa -City, Ishikawa Prefecture, Japan, Paper N13P1143.

[146] Yakush, S., Kudinov, P., and Dinh, T.-N., “Modeling of Two-Phase Natural Convection Flows in a Water Pool with a Decay-Heated Debris Bed,” Proc. ICAPP’08, Anaheim, CA USA, June 8–12, 2008, paper 8409.

[147] Yakush, S., Kudinov, P., and Lubchenko, N., “Coolability of heat-releasing debris bed. Part 1: Sensitivity analysis and model calibration,” Annals of Nuclear Energy, 52, February 2013, pp. 59-71, 2013

[148] Yakush, S., Kudinov, P., and Lubchenko, N., “Coolability of heat-releasing debris bed. Part 2: Uncertainty of dryout heat flux,” Annals of Nuclear Energy, 52, February 2013, pp. 72-79.

[149] Yakush, S., Lubchenko, N., and Kudinov, P., “Risk-Informed Approach to Debris Bed Coolability Issue,” Proceedings of the 20th International Conference on Nuclear Engineering (ICONE-20), Anaheim, CA, USA, July 30 - August 3, Paper 55186, 2012.

[150] Yakush S. E., Lubchenko, N.T., and Kudinov P., “Surrogate Models for Debris Bed Dryout,” 15th International Topical Meeting on Nuclear Reactor Thermal Hydraulics, NURETH 15, May 12 to 17, 2013, Pisa, Italy, Paper 278.

[151] Yakush, S. E., Lubchenko, N. T., and Kudinov, P., “Risk and Uncertainty Quantification in Debris Bed Coolability,” 15th International Topical Meeting on Nuclear Reactor Thermal Hydraulics, NURETH 15, May 12 to 17, 2013, Pisa, Italy, Paper 283.

[152] Yakush S. E., Villanueva W., Basso S. and Kudinov P., “Simulation of In-vessel Debris Bed Coolability and Remelting,” The 10th International Topical Meeting on Nuclear Thermal-Hydraulics, Operation and Safety (NUTHOS-10), Okinawa, Japan, December 14-18, 2014, Paper 1281, 2014.

[153] Kyle Ross, Jesse Phillips, Randall O. Gauntt, Kenneth C. Wagner, MELCOR Best Practices as Applied in the State-of-the-Art Reactor Consequence Analyses (SOARCA) Project, NUREG/CR-7008, (2014).

[154] Yakush S. E., and Kudinov P., “On the Evaluation of Dryout Conditions for a Heat-Releasing Porous Bed in a Water Pool,” International Journal of Heat and Mass Transfer, 134, pp. 895–905 (2019).

[155] “Theory Manual, RiskSpectrum Analysis Tools”, Lloyd’s Register Consulting – Energy AB, Version 3.3.0.

[156] S. Galushin, A.R. Marklund, O. Bäckström, P. Kudinov, D. Grishchenko, S. Yakush, M. Davydov, ”Developing uncertainty analysis for PSA from ROAAM+”, Report No PRJ11084933-R001, SPARC 2018, WP2, June 30, 2019.

[157] “3-D Rendering of Images obtained during the Fukushima Daiichi Nuclear Power Station Unit 3 Primary Containment Vessel (PCV) Internal Investigation”, TEPCO, April 26, 2018.

5. CHALMERS – DEP. OF NUCLEAR CHEMISTRY - RESEARCH ON SOURCE TERM RELATED ISSUES IN SEVERE ACCIDENTS

5.1 Svensk Inledning

Haverikemi är en vetenskaplig disciplin som bidrar med kunskap om fissionsprodukters beteende under ett svårt haveri. Denna kunskap är viktig för förståelsen av hur spridningen av dessa radioaktiva ämnen i anläggningen kan begränsas efter att de har frigjorts från härden. Kunskapen är även nödvändig för utvecklingen av realistiska modeller för beräkning av det radioaktiva innehållet i den mängd material som kan komma att lämna reaktorinneslutningen i samband med utsläpp som sker under ett haveri. Utsläpp föranleds av det övertryck av icke kondenserbara gaser som utvecklas i inneslutningen där det radioaktiva innehållet i utsläppet, den s.k. källtermen (*source term*), har en direkt påverkan på haveriets omgivningskonsekvenser.

En fortsatt utmaning inom området haverikemi är att förbättra förståelsen för vad som sker med de radioaktiva ämnen som frigörs från härden då den överhettas i brist på kylning. Den kemiska sammansättningen hos ett ämne bestämmer ämnets förutsättningar att frigöras och spridas, däribland dess flyktighet. Gasformiga ämnen, såsom ädelgaserna xenon och krypton, frigörs redan då bränslekapslingen brister i haveriets inledning. Andra flyktiga ämnen, såsom olika former av jod och cesium, frigörs vartefter härden smälter. Det är sedan viktigt att förstå dessa och andra ämnens fortsatta transport i primärsystemet och vidare spridning ut i reaktorinneslutningen.

En kemisk reaktion påverkar den kemiska sammansättningen hos de kemiska föreningar som deltar i reaktionen. Omvandlingen leder till reaktionsprodukter med nya egenskaper som ofta skiljer sig från det ursprungliga materialet, bl.a. kan flyktigheten förändras. I haverimiljö medför detta att radioaktiva fissionsprodukter kan få förändrade förutsättningar att spridas som följd av de kemiska reaktioner som sker under de speciella betingelser som råder under haveriet. Kemiska reaktioner påskyndas normalt genom uppvärmning, genom s.k. termiska reaktionsprocesser. Inom haverikemi spelar även förekomsten av s.k. radiolytiska reaktionsprocesser en särskild roll. Denna typ av reaktioner uppstår vid gammabestrålning av ämnen eller kemiska föreningar och bidrar till ytterligare reaktionsprocesser, utöver den omvandling som uppstår genom de termiska reaktionsprocesserna. Båda reaktionstyperna kan förekomma i gasfas och i vattenfas, t.ex. i det vatten som samlas i botten av inneslutningen under haveriförhållanden. Den kemiska omvandlingen påverkas således både av temperatur och av strålningsnivåer. I vattenlösning påverkas kemin i vissa fall även av vattnets surhetsgrad, det s.k. pH-värdet. Interaktion mellan olika ämnen i vatten, kan också förändra löslighetsegenskaperna, så att fällningar bildas. Utfällning medför att den fortsatta spridningen i inneslutningen begränsas. Kemisk omvandling i vattenlösning kan även leda till flyktiga produkter som frigörs till gasfas. I gasfas finns processer som omvandlar gasformiga ämnen till små luftburna partiklar, s.k. aerosoler, som har ett annat transportbeteende än fria gaser, exempelvis kan deponering av dessa ske på olika ytor i inneslutningen. På ytan kan kemisk interaktion sedan ske, både termiskt och radiolytiskt, vilket kan ge nya kemiska föreningar med nya transportegenskaper som kan frigöras på nytt. Radioaktivt sönderfall av fissionsprodukter komplicerar bilden ytterligare, när det gäller att bestämma källtermen i det utsläpp som till sist lämnar inneslutningen. Kemiska processer och radioaktivt sönderfall fortsätter dessutom även sedan ämnena har lämnat inneslutningen och under den fortsatta spridningen i omgivningen.

Filtrerad tryckavlastning via haverifilter är en planerad åtgärd som utförs för att reducera det övertryck som uppstår under ett haveri. Filtreringen av jod sker på kemisk väg och gör att utsläppet av radioaktiv jod kan reduceras. Radioaktiva ämnen som inte påverkas av filtreringen leder till utsläpp som kan ge konsekvenser för omgivningen, men åtgärden att tryckavlasta är ändå nödvändig för att minska påfrestningar på reaktorinneslutningen som kan medföra större ofiltrerade utsläpp med allvarligare konsekvenser för omgivningen. Radioaktivt utsläpp förväntas även från det diffusa läckage som kan förväntas i viss omfattning då det råder övertryck, även om alla ventiler är stängda och reaktorinneslutningen är isolerad. För att kunna göra en realistisk bedömning av konsekvenserna av dessa utsläpp, så är det viktigt att skaffa sig kunskap om de radioaktiva ämnen som finns frigörs från härden. Lika viktigt är det att förstå de processer som möjliggör transport av dessa ämnen i reaktorinneslutningen och som leder fram till att de blir tillgängliga att följa med utsläppen.

Ädelgaser, som t.ex. xenon och krypton, dominerar i tidiga utsläpp vid ett svårt haveri. Detta är en grupp ämnen som är kemiskt inerta, dvs. de reagerar inte med andra ämnen eller med ytor. Därigenom kan de inte filtreras vid en tryckavlastning. De är inte heller kondenserbara vid de temperaturer som råder vid ett haveri. Ädelgasinventariet påverkas således i stort sett endast genom det radioaktiva sönderfall som de olika ädelgasnukliderna genomgår med varierande halveringstid.

Jod är ett ämne som har betydligt mer komplexa egenskaper än ädelgaserna. Jod har en synnerligen rik kemi och förekommer i ett stort antal kemiska föreningar med vitt skilda egenskaper. Jod förekommer både i gasform, i aerosoler, som deponerad på ytor och i vattenfasen, antingen i lösning eller som utfällning. Vissa former är stabila medan andra är reaktiva. Kemiska reaktioner gör att jod lätt bildar produkter med andra ämnen som får nya egenskaper, bl.a. vad gäller flyktighet. Fortsatta kemiska reaktioner kan göra att flyktigheten förändras genom att gasformig jod deponerar på olika ytor, eller att deponerat material frigörs på nytt. Jod bidrar liksom ädelgaser också till en betydande del av källtermen i tidiga utsläpp under ett haveri. Fördelen är emellertid att de flesta formerna av jod låter sig filtreras vid passagen genom den skrubberlösning som används i de haverifilter som finns installerade vid de svenska reaktorerna. Ett viktigt undantag utgörs av s.k. organisk jod som har egenskaper som liknar ädelgasernas. Förståelsen för hur denna bildas är därför viktig för att begränsa osäkerheterna i bedömningen av jodkälltermen i ett utsläpp.

Jodkemin har varit föremål för forskning i flera årtionden där syftet har varit att förstå alla de processer där jod ingår, samt att samla data för att bygga beräkningsmodeller som kan förutsäga hur jod beter sig under ett haveri. Jod ingår också i de studier som alltjämt pågår inom OECD/NEA-projekten BIP, STEM och THAI, samt de nystartade projekten ESTER och THEMIS, som har ett fortsatt fokus på organisk jod. (se avsnitt …).

Efter olyckan i Fukushima Dai-ichi upptäckte man vid mätningar i de närliggande samhällena, att markstrålningen den första tiden till stor del kom från radioaktiv tellur som hade deponerat. Radionukliden tellur-132 bidrog med nära 70 % av den totalamarkdosen i det inledande skedet. Tellur-132 har en halveringstid på ca 3 dagar och omvandlas successivt till jod-132, som har en halveringstid på ett par timmar. Det dröjde dock bortåt tre veckor innan bidraget från dessa båda nuklider hade klingat av.

5.2 Tellurium chemistry

Prior to Chalmers, tellurium has been part of several severe nuclear accident research programs, which have provided knowledge on the behavior of tellurium in accident scenarios. However, the research performed at Chalmers has aimed to add on to that knowledge in order to provide further information for tellurium source term assessment. In the following chapters, the relevance of tellurium, short descriptions of what species can be expected in accident conditions, and some potential chemical reactions are presented.

Some of the main concerns related to tellurium are the volatility (as seen during the VERCORS experiments [PON10]), the decay into radioactive iodine isotopes ([MAG15]), the suggested reactiveness of tellurium [ALO91] (e.g., as seen with zirconium cladding interaction [BOE97, BOE95, COL87, LOR83]), and potential dose contribution to humans during an accident ([DÖR10, TAY96]) .

5.2.1. Tellurium transport during a severe accident

From the fuel, tellurium will be released as Te/Te_2, TeO_2 and Cs_2Te [ALO91, IMO88, MCF96a]. However, it is known that tellurium will react with the zircaloy cladding by the formation of zirconium-tellurium complexes [BOE97, JOH88, BOE95, COL87]. This interaction requires either highly oxidized cladding material [JON15, SAN15] or sufficiently high temperature (2620 K) and results in a delay in the release of tellurium since the cladding acts as a trap for tellurium [PON10]. In addition to the delayed release of tellurium, the formation of SnTe can occur at the surface boundary of the cladding as well [JOH88, MAT94]. Depending if the oxygen potential remains sufficiently low, this species may remain stable and further affect the tellurium source term.

Inside the reactor coolant system (RCS), the tellurium species will be subjected to the conditions and surfaces found therein. For example, should reducing conditions exist, H_2Te may form which is more volatile than other tellurium species. However, the tellurium-hydrogen compounds are relatively unstable and decompose fast. Another tellurium species is $TeO(OH)_2$, which is formed between TeO_2 and steam at high temperature. As mentioned, the formed SnTe may also enter the RCS and travel through it. Aside from these specific tellurium species, both metallic (Te, Te_2) and oxidic (TeO and TeO_2) tellurium exist depending on the ambient conditions (oxidizing, inert and reducing) [POT85, DUT66, JOH88]. Additionally, metallic surfaces inside the RCS have also been found to react with tellurium forming iron and nickel tellurides [SAL84].

Tellurium will eventually be released from the RCS to the containment. The containment chemistry of tellurium is less explored. However, expected tellurium species to enter the containment from the RCS would depend on the preceeding conditions and candidate species would be Te/Te_2, H_2Te, Cs_2Te and SnTe [ALO91, BEA86]. These species would then be exposed to a range of different conditions, such as other fission products, aerosols consisting of structural and control rod material, air, steam, liquid water, organic material, concrete and metal surfaces. In addition, different engineered safety features, such as the containment spray system (CSS), affect the source term of fission products by mitigating the potential releases. The chemistry related to the CSS and its effect on tellurium has not been considered prior to Chalmers research. However, the CSS chemistry has been found to have an effect on the removal efficiency of other fission products, such as iodine [Hilliard&Postma1970]. Finally, the species removed by either the CSS or natural processes, enter the sump on the bottom of the containment. Due to the relatively complex tellurium chemistry as well as the complexity of the sump, tellurium can undergo chemical reactions which are important to consider not only for source term assessment of tellurium but also in relation to other fission products. Previously, the tellurium chemistry data related to severe nuclear accident research has been taken from geological research which does not take into consideration all of the potential factors important for the tellurium speciation. One of the key parameters neglected prior to Chalmers research is the radiation chemistry of tellurium. Although some aspects of irradiation of tellurium have been described in the literature [McFarlane, Moreyama, Beahm], a severe accident focused research has not been considered.

5.3 Seawater Experiment

During the Fukushima accident, seawater was used to maintain cooling of the core. Such an action may have resulted in the enhanced volatilization of different fission products. This by the formation of halides, which generally have lower melting and boiling point than the corresponding metallic or oxide parts. One such example was the observed change in release behavior of ^{95}Nb, which was suggested being due to halide formation of the Nb [KAN15]. One such halide could be chloride, which is one of the main constituting parts of seawater [RUM20]. Hence, it was decided to investigated if chloride containing seawater affects other fission products, in this case tellurium.

5.3.1. Experiment

The investigation was performed using two furnaces, one being a thermogravimetric analyzer (TGA) and the other a tubular furnace. See Figure 5.3.***1***.

Thermogravimetric analysis is an analytical technique used to determine a material's thermal stability and its fraction of volatile components by monitoring the weight change that occurs as a sample is heated at a constant rate. For the TGA experiments, triplicates of three different types of tellurium and sodium chloride mixtures (1:1, 1:4 and 4:1) were used. These were heated under either oxidizing (synthetic air) or inert (nitrogen gas) conditions. The procedure for the TGA was as follows: 1 mg of the mixture was added to an alumina pan, which was placed inside the TGA. Heating (10 K/min) was performed up to isothermal temperature (1173 K) and maintained for 20 min. Following this, the system was left to cool until ambient temperature was reached.

The second furnace was only used for experiments under oxidizing conditions. For this part, only the 1:1 mixture of tellurium and sodium chloride was investigated, the aim was to achieve a visualization of what occurred at different temperatures. 2 g of the mixture was added to the crucible. This was then placed inside the furnace, within an aluminum tube. Heating (10 K/min) was then performed to a specific isothermal temperature (either 473 K, 573 K, 623 K, 673 K, 723 K, 773 K, 823 K, 873 K, 923 K, 973 K, 1023 K or 1073 K.) and maintained for 20 min.

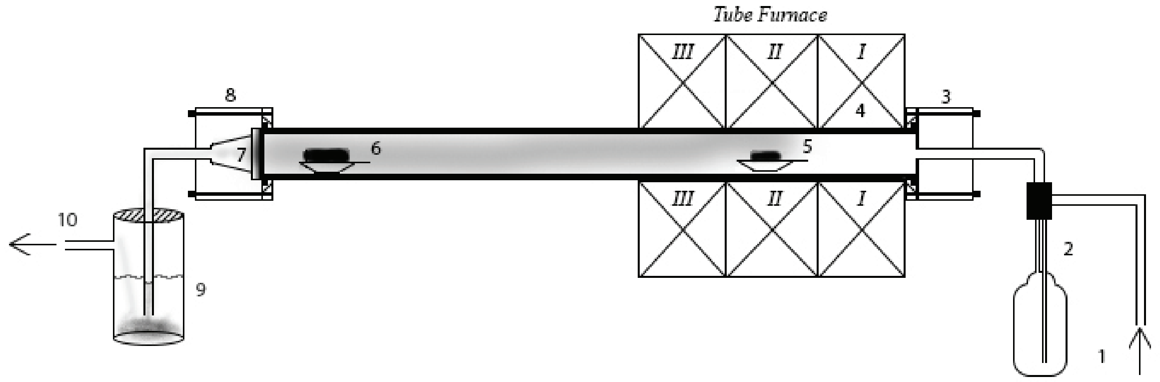

Figure 5.3.1 The experimental schematics: (1) gas inlet, (2) atomizer, (3) inlet, (4) Al2O3-tube, (5) the precursor location,(6) the metallic coupon, (7) cone-formed outlet, (8) connector, (9) a sodium hydroxide solution (0.1 M) trap, and a water trap, and (10) the gas outlet

5.3.2. Results

For all samples under inert conditions, two distinct different mass loss phases were observed from the TGA results. Both of these phases for all samples started at roughly the same temperatures, 690-710 K for the first mass loss phase and 920-1080 for the second mass loss phase. The TGA results are provided in Figure 5.3.*2*. Observing the pure tellurium reference (Reference 1), similar mass loss phases were seen. However, the pure sodium chloride reference (Reference 2) had only one mass loss phase, which started at roughly 1000 K.

Inert Conditions

By observing the behavior of the samples during heating, which can be seen in Figure 5.3.*2*, seemingly a higher ratio of tellurium resulted in a longer first mass loss phase. Once the first mass loss phase stopped, the gradient slowed down significantly. The degree that this occurred to, seemingly depended on the fraction of the tellurium in the sample, as a higher fraction resulted in a lower remaining total mass. The second mass loss phase start varied slightly between the different samples, as well as how the gradient of mass loss evolved. Following the second mass loss phase, the experiment continued until the end, ending at normalized masses of 7.6%, 12%, and 2.5% for samples 1, 2, and 3 as well as 5% and close to zero for Reference 1 and Reference 2, respectively. A summary of when the mass losses occurred and at what temperatures can be seen in Table 5.1.

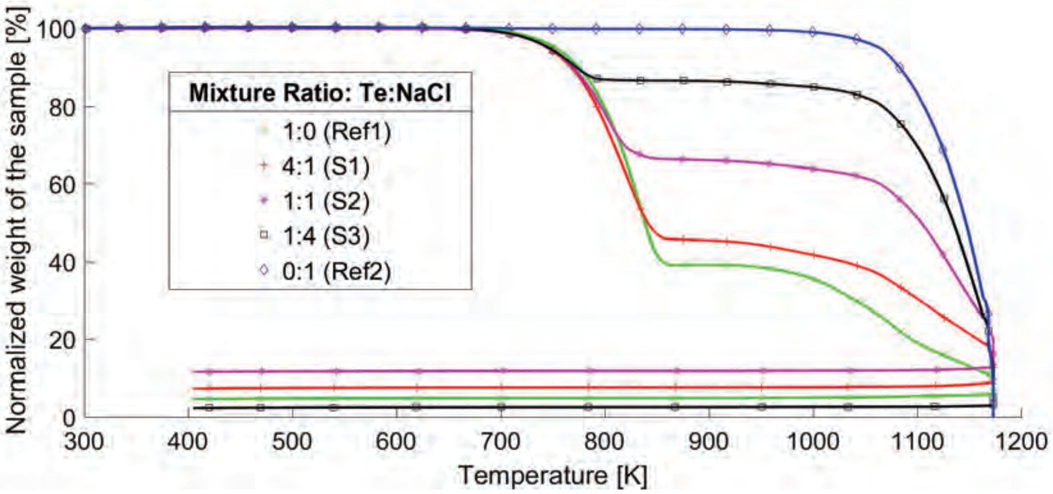

Figure 5.3.2 The thermogravimetric analysis results for the different Te:NaCl-ratios (weight basis) heated in inert conditions

Comparing the different Te:NaCl ratios to that of the pure tellurium reference, the temperature for when the different mass loss phases occur are similar. Thus, it is reasonable that similar volatilization of species is occurring, as the initial behavior is very similar. The first mass loss also starts close to the melting point of tellurium (722 K [RUM19]) and thus a phase change is occurring for tellurium. Based on the literature, it is likely that the species leaving the sample is Te_2 or possibly Te [MCF96b]. Furthermore, after the first mass loss phase, the normalized weights of the different samples stabilize at different values. This difference is reasonable as the normalized mass level increases with the content of sodium chloride and is hence correlated to it. Regarding the second mass loss of the samples, this starts roughly at the melting point of sodium chloride (1074 K [GRE97]) and thus most likely is correlated to it. Similarly, at the same temperatures the pure sodium chloride reference is also seen to experience a mass loss, which also supports this idea. Considering the tellurium part of the sample, it would also be volatilized at these temperatures as the pure tellurium reference is also losing mass.

Table 5.1 A summary of the thermogravimetrically analysis carried out under inert conditions

Sample	First main mass loss temperature range [K]	Second main mass loss temperature range [K]	Final normalized mass [$\%_{weight}$]
Reference 1 (Only Te)	690 to 870	920 to the end	~ 5
Reference 2 (Only NaCl)	1000 to the end	-	~ 0
Sample 1 (4:1 of Te:NaCl)	620 to 865	925 to the end	~ 8
Sample 2 (1:1 of Te:NaCl)	680 to 850	920 to the end	~12
Sample 3 (1:4 of Te:NaCl)	670 to 805	920 to the end	~ 3

Observing these results, no reactions seem to have occurred between tellurium and sodium chloride under inert conditions inside the pan. This is also supported by the observation that the main constituting part of the sample dictated the behavior of the mixture. However, these observations do not exclude that a gas phase interaction can take place between sodium chloride and tellurium after volatilization of the two components, or that a very rapid interaction takes place at high temperatures, since this would not be apparent in the TGA results.

Oxidizing Conditions

The TGA experiment under oxidizing conditions also clearly indicates two distinct mass loss phases. However, the mass loss never completely stops, and minor releases also occur between the two main mass loss phases. The beginning of the two main mass loss phases for all samples were at temperatures of 690-710 K and 1000-1030 K for the first and second phases, respectively. At a higher fraction of tellurium, the final normalized mass was lower and the time between the two mass loss phases were shorter. Comparing these to the references, noticeable differences can be observed. Both samples and references are shown in Figure 5.3.***3***. The pure sodium chloride reference (Reference 2) had only one mass loss phase (similar to the inert conditions reference) at circa 1000 K. In comparison, the pure tellurium reference (Reference 1) had two main mass loss phases and between them there was a mass increase phase, which was not observed at all for any of the samples. Similar to the samples, the first mass loss phase started roughly at comparable temperatures (around 700 K), whereas the second mass loss phase started earlier then the samples at roughly 900 K. At the end of the experiments, the normalized mass reached levels of 14%, 18%, and 8% for samples 1, 2, and 3 as well as 30% and close to zero for Reference 1 and Reference 2, respectively. A summary of when the mass losses occurred and at what temperatures can be found in Table 5.1.

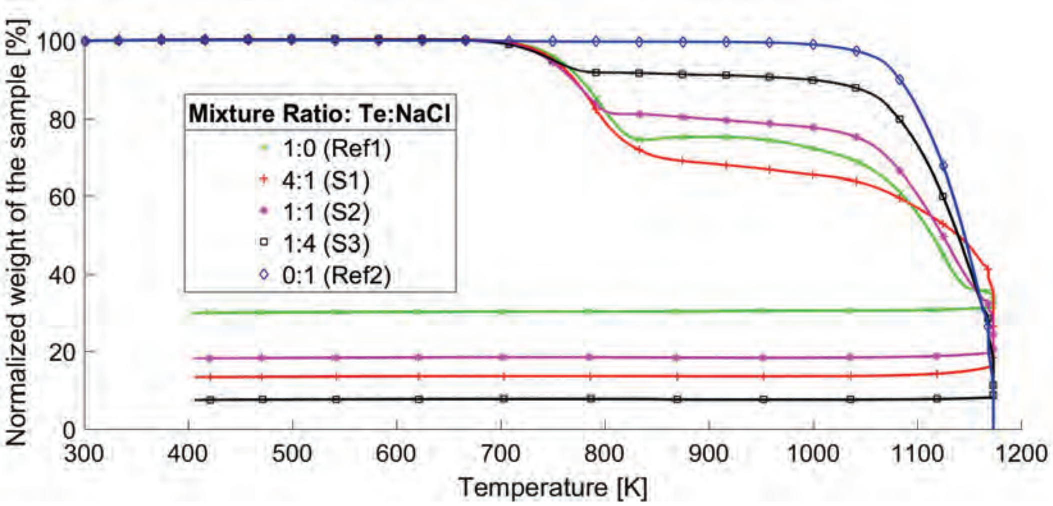

Figure 5.3.3 The thermogravimetric analysis results for the different Te:NaCl-ratios (weight basis) heated in oxidizing conditions

Considering the temperature when the first main mass loss phases of the samples start, this is close to the melting point of tellurium (722.66 K [RUM19]) and may be connected to it. The pure tellurium reference behaves in the same way and it is reasonable that the first mass loss phase of each sample is only due to the melting and volatilization of the tellurium. After the initial mass loss phases of the samples, the mass loss trend leveled out for all samples, except for the pure tellurium reference. For this reference, an increase in mass was observed and thus it diverged from the behavior of the samples. This mass increase could be correlated to the oxidation of tellurium to the alpha-TeO$_2$ according to the O-Te phase diagram [ITK96]. Since this mass increase did not occur for the different samples or the sodium chloride reference, the addition of sodium chloride may either have prevented or counteracted the mass increase. The final mass loss of all the different samples occurred around 920 K, which is close to the melting point of TeO$_2$ (1006 K [RUM19]). This means that a phase change likely occurred, and observing the phase diagram for the Te-O system [118], both liquid and gaseous state of the TeO$_2$ may exist above this temperature. The second mass loss phase could be explained by the volatilization of TeO$_2$. For the pure sodium chloride reference, the only mass loss phase observed was at around 1000 K.

Table 5.2 A summary of the thermogravimetrically analysis carried out under inert conditions

Sample	First main mass loss temperature range [K]	Second main mass loss temperature range [K]	Final normalized mass [%$_{\text{weight}}$]
Reference 1 (Only Te)	700 to 840	900 to the end	~ 30
Reference 2 (Only NaCl)	1000 to the end	-	~ 0
Sample 1 (4:1 of Te:NaCl)	700 to 870	1030 to the end	~ 14
Sample 2 (1:1 of Te:NaCl)	695 to 815	1020 to the end	~18
Sample 3 (1:4 of Te:NaCl)	680 to 785	1000 to the end	~ 8

Considering these results, the sodium chloride did affect the volatilization of tellurium as the observed mass increase for the pure tellurium reference did not occur for any of the samples. This could be explained by the sodium chloride simply preventing the oxidation of the tellurium in the pan by physically covering the tellurium, and therefore preventing the mass increase. Alternatively, a chemical reaction may have occurred between the tellurium and sodium chloride that prevented the oxidation of the tellurium or formed a more volatile species that suppressed the mass increase through the increased volatilization. Possible tellurium species could be with chloride, as these would be more volatile based on melting and boiling points and possible chlorides.

Regardless of what occurred, comparing the different samples the differences are minor and seem related to the content of sodium chloride, as increasing the ratio of sodium chloride increased the similarity of the samples to the pure sodium chloride reference. This means that even a small amount of sodium chloride affects the tellurium volatility.

To gain insight into what occurred during the oxidizing experiments, a mixture of 1-1 of tellurium and sodium chloride was heated to different temperatures, followed by rapid cooling. This was mainly done to obtain a visual observation of the mixture after being heated to the different temperatures. The samples produced for each temperature can be observed in Figure 5.3.***4***. The first image (A), resembles the initial appearance of the state of the samples; the black part is tellurium (black powder) and the white part is sodium chloride (white powder).
The eight individual samples were heated to temperatures starting at 473 K and reaching 1073 K, with an initial temperature step of 100 K, followed by temperature steps of 50 K. Observing the images in Figure 5.3.***4***, it was first at 673 K (D) that the sample changed as sodium chloride became more apparent. These changes continued as the temperature continued to increase, most likely due to the disappearance of the tellurium. However, at 873 K (H) the second main change was observed when a yellow phase started to emerge, covering both the mixture and the crucible. Reaching 923 K (I), the yellow color became more prominent and the integrity of the sample started to decrease. At 973 K (J), the sample as a whole started to melt, and a noticeable loss of volume had occurred after the experiment. Finally, at 1023 K (K) and onward only the yellow phase remained as well as a glaze covering the crucible.

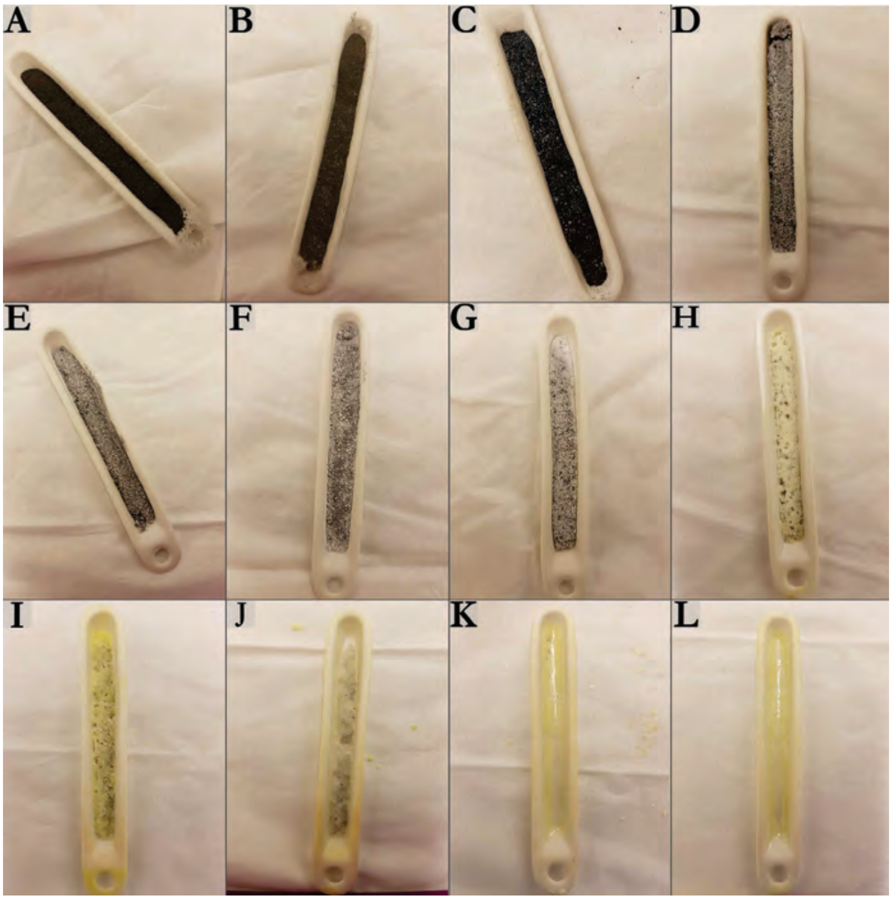

Figure 5.3.4 Crucibles containing the sample, as seen after the furnace experiment. The initial composition of the samples was 1:1 of tellurium and sodium chloride (2 g). In total eight, temperatures were investigated: (A) 473 K, (B) 573 K, (C) 623 K, (D) 673 K, (E) 723 K, (F) 773 K, (G) 823 K, (H) 873 K, (I) 923 K, (J) 973 K, (K) 1023 K and (L) 1073 K

The first three samples (A, B, C) seen in Figure 5.3.***4*** show only minor changes, whereas those following (D to L) all show noticeable changes from the initial state. Considering the temperatures, this trend is reasonable as the melting point of tellurium (722.66 K [cite_53]) is close to the fifth sample (E) and the melting point of sodium chloride (1075.2 K [cite_53]) is close to the eleventh sample (K). The reason for increasing visibility of the sodium chloride already at 600 K is not clear. As previously mentioned, the sample reaching 723 K (E) should have less tellurium, and therefore makes the sodium chloride more visible. This, considering that the melting point of tellurium has been exceeded. Reaching 873 K (H), a yellow phase did appear. Considering the coloration and the elements involved, two possible yellow species are; Te_4Cl_{16} or the orthorhombic-TeO_2 [GRE97]. Of these, only the first has a melting point below 1000 K. At a temperature of 1023 K (K), little remains of the samples. Considering the melting point (1075.2 K [RUM19]) and boiling point (1738 K [RUM19]) of sodium chloride, parts of this compound should remain at such a temperature, indicating that something has occurred which has resulted in more volatile species of the sodium chloride. Alternatively, a sodium-tellurium complex may have formed, a possibility for which is Na_2TeO_3. However, this is less likely as it is reported to have a white color [RUM19]. Nevertheless, from these results, no definite conclusion can be made about what species may have formed. However, it is clear that the sodium chloride did have an effect on the tellurium.

Comparing the two experimental methods used for oxidizing conditions, a consistency between the results exists. The observed decrease in tellurium mass from the furnace experiments occurs at the same time as the first major mass loss phase of the TGA experiment. In the period between the two major mass loss phases, the TGA shows as slow mass loss and concurrently in the furnace samples the yellow phase appears. This indicates a correlation between the slow mass loss phase and the build-up of the yellow phase. The second major mass-loss phase of the TGA experiment coincides with the significant reduction of the mass of the furnace sample. Simultaneously to this mass loss phase, the pure sodium chloride reference shows at best, minor amounts of mass released. This is an indication that something is occurring at these temperatures that results in the mass loss, which could be the formation of a more volatile species such as Te_4Cl_{16}. Considering both the TGA and furnace experiments it is a possibility that the sodium chloride affected the tellurium volatility during these experiments under oxidizing conditions. Thus, the use of seawater may enhance the volatility of tellurium under oxidizing conditions.

5.4 CsI-Te Experiments

Cesium-tellurium species are among the different tellurium species that have received attention in the context of nuclear accidents. However, in most cases predictions of formation and properties of cesium-tellurium species have been done using thermodynamic calculations or some experimental work which did not represent accident conditions.

Observing the existing literature, it has been found that several different cesium-tellurium complexes can form. Two possible species are CsTe and Cs_2Te, of which the latter has been suggested to form according to reaction 1 when cesium is present at large quantities.

$$2CsOH(s,l) + H_2(g) + Te(s,l) \leftrightarrow Cs_2Te(s) + 2H_2O(g) \quad (1)$$

CsTe is suggested to form at temperatures of 873 to 1073 K under steam atmosphere (H/H_2O-ratio larger than 0.1). Moreover, both oxidizing conditions and steam are likely to affect these two species by dissociating them. For instance, Cs_2Te dissociates at temperatures above 1400-1600 K [KAN15, MCF96a, MCF96b, BOW86, GAR82]. Additionally, during the nuclear research fission product programs of VERCORS and PHEBUS cesium and tellurium were observed to interact as they were deposited together [PON10, JON15, SAN15].

5.4.1. Experiment

To investigate the behavior of tellurium in the RCS, as well as possible chemical effects caused by cesium iodide, a dual furnace setup was used. The main details of this facility can be found elsewhere [KÄR06, KÄR17]. However, a schematic overview can be seen in Figure 5.4.***1***.

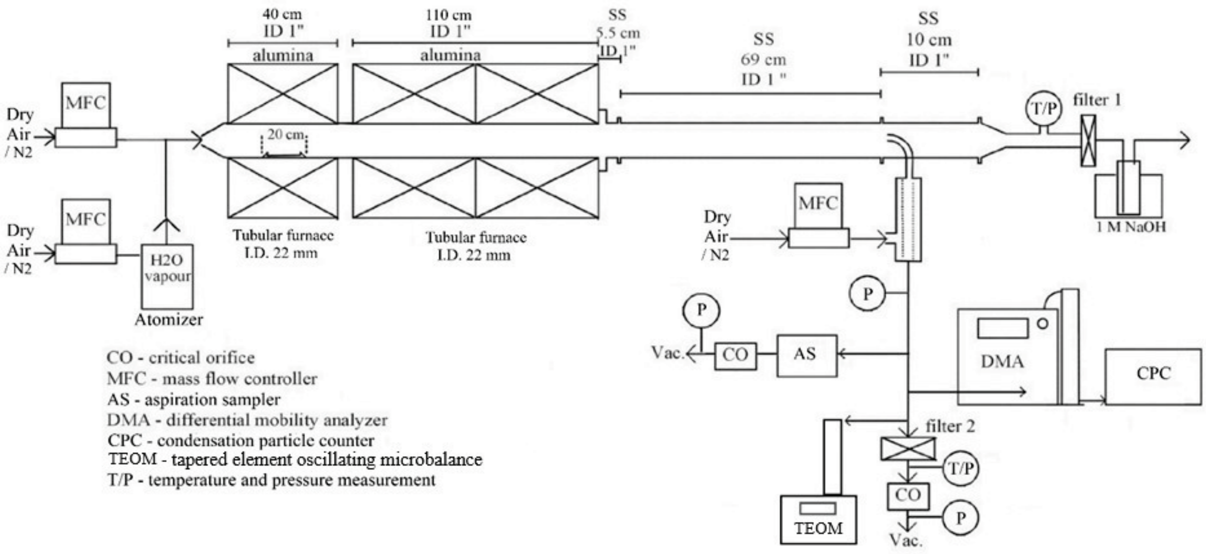

Figure 5.4.1 Schematics of the experimental facility for tellurium transport studies

Briefly, two furnaces were used, one of which was the main reaction furnace with a smaller one located upstream to vaporize the tellurium precursor (approximately 1 g). Through both furnaces, an aluminum tube with an inner diameter of 22 mm was located in which the experiments were carried out. At the end of the reaction furnace, a stainless steel tube was attached to the aluminum tube to transport the outgoing gas (temperature decreased to ca. 300 K) to either an online measuring device (1/5 of the flow) or a plane polytetrafluoroethylene (PTFE) filter followed by two sodium hydroxide liquid traps (0.1 M) (4/5 of the flow). Towards the end of each experiment, sampling of the gas phase aerosols was done using perforated carbon-coated nickel grid (400 mesh) with the aspiration sampler. Two conditions corresponding to oxidizing and inert atmosphere were investigated, both without and with humidity. Additionally, one experiment with cesium iodide added to the atmosphere under humid conditions was also performed. The flow through the system was 5 l/min. In the two experiments involving humidity and/or cesium iodide an atomizer was used, which was filled with either only water or cesium iodide (0.15 M) dissolved in water. The outgoing gas from the atomizer was channeled through a heated line (390 K) before entering the smaller furnace.

Table 5.3 Experimental matrix, showing the main different parameters

	Gas	Temperature* [K]	Humidity [ppmV]	CsI [M]**
RCS-1	Air	1500	Dry	
RCS-2	Air	1500	$2.1 \cdot 10^4$	
RCS-3	Air	1500	$2.1 \cdot 10^4$	0.15
RCS-4	Nitrogen	1500	Dry	
RCS-5	Nitrogen	1500	$2.1 \cdot 10^4$	
RCS-6	Nitrogen	1500	$2.1 \cdot 10^4$	0.15

**Temperature in the reaction furnace. **Concentration of the solution used in the atomizer.*

All experiments were carried out in the same way. First, the reaction furnace was heated (10 K/min) to the isothermal temperature (1500 K). Once the temperature was reached, the tellurium precursor located inside an alumina crucible was positioned inside the small furnace where heating (10 K/min) was started until the set-point temperature (810 K) was reached. Concurrently, a nitrogen gas flow (0.5 l/min) was maintained until reaching the temperature set-point of the small furnace and then stopped. Following this, the main gas mixture corresponding to the investigated experimental condition was started. An overview of the experiments can be found in Table 5.3.

5.4.2. Results

After each experiment the samples and the remaining precursor were visually inspected and weighed using a balance. Following the experiments, the precursors used under the oxidizing conditions (RCS-1, RCS-2, and RCS-3) all had a slight gray color, while from the inert experiments (RCS-4, RCS-5, and RCS-6) all the precursors remained black. The filters collected after the reaction furnace had white deposits under dry (RCS-1) and humid (RCS-2) oxidizing conditions. An initial yellow color was observed on the filter from the experiment (RCS-3) performed under humid oxidizing conditions with added cesium iodide. After storage and transport to the Instrumental Neutron Activation Analysis[9] (INAA) location the yellow color had faded significantly, and a white color remained. A black deposit with a white tone to it had formed on all filters from all three inert experiments. The liquid sodium hydroxide traps located after the filters from the three oxidizing and the three inert conditions showed no visible change after each experiment. The weights of the remaining precursor (i.e., released mass) and species trapped on the filter (i.e., transported mass) from each experiment were determined with the balance and are shown in Table 5.4

Table 5.4 Released mass of the precursor in the alumina crucible and the mass reaching the filter

	Released Mass, [mg]	Transported Mass to the filter, [mg]
RCS-1	56	50
RCS-2	44	20
RCS-3	25	20
RCS-4	283	63
RCS-5	296	35
RCS-6	275	53

From the color change of the precursors and the color of the deposit on the filter, an initial estimate of the speciation was made. For the oxidizing conditions, the gray color of the precursor indicates that the originally black tellurium has most likely undergone a slight oxidization to form e.g., tellurium dioxide. The white color on the filter indicates tellurium dioxide [RUM19]. The yellow color observed could be attributed to several species but considering that the color faded during storage and transport it most likely is iodine. An alternative could be the

---

[9] INAA is a nuclear process for determining the concentrations of elements in a material. The method is based on neutron activation and therefore requires a source of neutrons. The sample is bombarded with neutrons, causing the elements to form radioactive isotopes. The radioactive emissions and radioactive decay paths for each element are well known. Using this information, it is possible to study spectra of the emissions of the radioactive sample, and determine the concentrations of the elements within it.

yellow orthorhombic-tellurium dioxide [GRE97], however this is less likely as it is not as volatile as iodine and would not result in the yellow color fading away.

The weights recorded from the balance provides an initial estimate of the transported amounts under oxidizing and inert conditions. From these results alone, the highest transported mass occurred under inert conditions. However, under oxidizing conditions the precursor was oxidized, which would add mass to the precursor and therefore it appears as less of the precursor was volatilized. For the oxidizing experiment with cesium iodide (RCS-3), the released mass was noticeably lower than the other two (RCS-1 and RCS-2). The transported masses were lowest for the experiments involving humid oxidizing conditions without (RCS-2) and with cesium iodide (RCS-3) compared to dry humid oxidizing conditions (RCS-1).

To provide a more detailed mass determination as well as the individual distribution of the elements in the samples, INAA was performed on the filters and liquid sodium hydroxide traps. The elements determined were cesium, iodine, and tellurium, of which the amounts of the two first were only determined from the samples of two experiments (RCS-3 and RCS-6). The tellurium INAA-values were also compared to the released amounts presented in Table 5.5. For the values of the liquid traps, they correspond to the original solution volume (i.e., 250 ml) used in each experiment.

Table 5.5 Instrumental neutron activation analysis results of the tellurium, caesium and iodine transported to filter 1 and liquid traps in the experiments

	Te		Cs		I	
	Filter	Trap	Filter	Trap	Filter	Trap
RCS-1	32	1.1				
RCS-2	28	0.95				
RCS-3	13	0.71	1.7	<0.01	0.5	<0.003
RCS-4	46	0.99				
RCS-5	40	0.57				
RCS-6	42	0.94	1.6	0.04	1.1	0.03

From the INAA data, it can be seen that the largest transport occurred under oxidizing conditions compared to inert conditions for both the filter and trap. This was only when comparing the tellurium amounts from the filter with the released amounts from the precursor. Otherwise, actual determined amounts were higher under inert conditions for the filters. This indicates that under inert conditions most of the tellurium was deposited throughout the tube. It should be noted that the precursor under oxidizing conditions was most likely oxidized, as it turned from black to slightly gray. This resulted in an uncertainty of the released amounts, as the oxygen would add mass to the precursor. Still, during the handling of the precursors from the three oxidizing conditions experiments it seemed that it was mainly the surface of the remaining precursors that was oxidized. Therefore, the remaining precursor would still be largely tellurium metal. These results showed that under oxidizing conditions the increased humidity increased the amount of tellurium transported through the reaction furnace. Other experiments confirm this effect of tellurium transport under humid conditions [SEH12, DUT66, MAL70, KON90]. Both the decrease and increase in the tellurium amounts on the filters during inert humid conditions and humid with cesium iodide additive conditions can be explained by the formation of new species. In the former case, slight oxidization may have occurred of the gaseous tellurium, possibly to TeO. This species would then have been less mobile than other species or it might have deposited on the tube surface as the temperature decreased. The increase of the tellurium amounts in the second case (involving CsI) can be explained by the formation of a tellurium-cesium complex, similar to what has been suggested in the literature [SAN15]. However, this would require both cesium hydroxide and hydrogen to have formed. This would then also explain the ratio between cesium and iodine on the filters, as the iodine could have escaped as I_2, either during the experiment or during the transport.

Comparing the contents of the filters with the contents in the liquid traps, it is clear that the filters captured most of the transported particles. This indicates that at these temperatures the main transport mode was as aerosols. As for the filters, the highest tellurium fraction reaching the traps was under oxidizing conditions. This fraction was increasing, first when humidity was added and again when cesium iodide was added. For the three inert conditions, the values were very similar. The additionally used analytical method of ICP-MS did not detect any amount of cesium or tellurium in any of the traps. To determine the chemical speciation of what was trapped on the different filters, a small part of each filter was cut away and analyzed using X-ray photoelectron spectroscopy (XPS). Specifically, the aim was to identify species related to cesium, iodine, and tellurium. The outcome of the identification of each XPS spectra is presented in Table 5.6 and Table 5.7 for the samples from the oxidizing and inert conditions, respectively.

Table 5.6 The data from the X-ray photoelectron spectrometer analysis of the filters, used under oxidizing conditions

	RCS-1		RCS-2		RCS-3			
Element	O	Te	O	Te	O	Te	Cs	I
Shell	1s	$3d_{3/2}$	1s	$3d_{3/2}$	1s	$3d_{3/2}$	$3d_{3/2}$	$3d_{3/2}$
Binding energies	530.5	576.3	530.4	576.3	529.8	575.6	723.8	618.3
	532.0		531.6	574.3	531.7	577.5		
Chemical State of the element	TeO_2	TeO_2	TeO_2	TeO_2	TeO_2	TeO_2	CsI	CsI
				NN		TeO_3		

For oxidizing conditions, all three samples show clear indications for the species TeO_2. When the humid oxidizing condition was investigated a new, but very weak peak emerged. This peak was not successfully identified. When cesium iodide was added to the humid atmosphere, again a new peak emerged. This peak was correlated to tellurium in oxidation state +VI. According to the binding energy, possible species are either TeO_3 or $Te(OH)_6$. The peaks detected for cesium and iodine were both identified as cesium iodide.

The detection of TeO_2 in all the deposits from the filters at lower temperatures was expected. However, the observation of another peak that may be related to a new species as suggested by the literature [SEH12, DUT66, MAL70, KON90] was unexpected. It could be explained by the fact that the TeO_2 and water at high temperatures could result in new species, which could remain at lower temperatures. This could also be true for the humid conditions with added cesium iodide as well. In the latter case, the observed peak was different and more intense compared to the one observed from the humid oxidizing conditions. This indicates a possible interaction between tellurium bearing species and cesium iodide. According to the literature [MCF96b] cesium telluride is unstable in oxidizing conditions. However, no extensive experimental research exists on the cesium-tellurium compounds. Hence, further research is needed to verify possible reactions resulting in new species.

Table 5.7 The data from the X-ray photoelectron spectrometer analysis of the filters, used under inert conditions

	RCS-4		RCS-5		RCS-6			
Element	O	Te	O	Te	O	Te	Cs	I
Shell	1s	$3d_{3/2}$	1s	$3d_{3/2}$	1s	$3d_{3/2}$	$3d_{3/2}$	$3d_{3/2}$
Binding energies	530.6	576.3	530.4	576.3	530.1	575.9	723.7	618.5
	532.3	573.2	532.0	573.2	532.4	572.9	725.9	620.6
						578.3		
Chemical State of the element	TeO_2	TeO_2	TeO_2	TeO_2	TeO_2	TeO_2	CsI	CsI
		Te		Te		Te	Cs	I_2
						NN		

The outcome of the inert experiments showed the presence of both Te and TeO_2 in all of the filter samples. Observing metallic Te is reasonable considering the conditions as the potential for oxidation of tellurium is rather low under the dry inert conditions. First when the humidity is increased, oxidization should occur, initially from Te_2 to TeO, and then to TeO_2 at lower temperatures. It is also possible that some air may have leaked in during the experiment or that slight oxidation occurred during storage. When investigating the effect of cesium iodide, a new tellurium peak emerged. However, this peak was not positively identified using the reference data. For both cesium and iodine new peaks were detected and suggested species were Cs and I_2, respectively. From the speciation of the inert conditions filter samples, the main difference was that new peaks emerged for all the elements when humid inert condition with added cesium iodide was investigated. Of these, only one connected to tellurium was not positively identified. However, the identification attained for cesium is questionable, especially since metallic cesium is very unlikely to remain during the storage in air. It is possible that what is observed for cesium may be correlated to the unidentified tellurium peak, indicating a new tellurium-cesium species had formed There is also some support for the existence of this species in the literature [SAN15].

For the experiments, both the mass concentration of suspended particulate matter (all diameters) and the number size distribution were determined. In total, six of each were acquired and are presented in Figure 5.4.***2*** and Figure 5.4.***3***. However, for the experiment with humid oxidizing conditions with added cesium iodide (Experiment 3 in Figure 5.4.***2***, elsewhere called RCS-3) only the result for the later part of the experiment is available. This due to an initial malfunctioning of the measuring equipment.

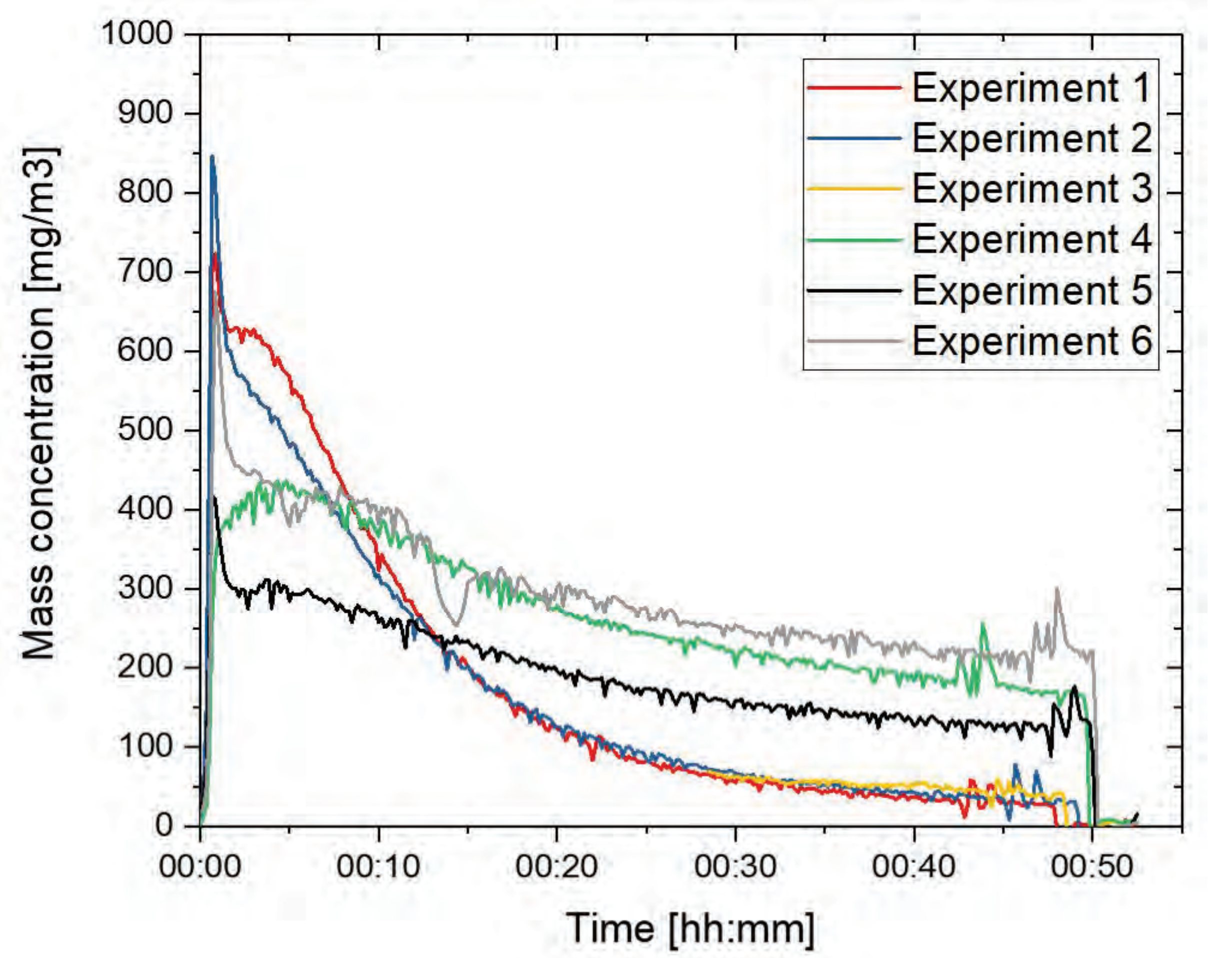

Figure 5.4.2 Evolution of the mass concentration of tellurium containing aerosol in the experiments

Observing these mass concentrations, the experiments performed under both oxidizing and inert conditions had an initial surge of mass concentration as the flow was started. Of these surges, the one occurring under inert conditions were the highest. Following the surge for all experiments, there was a decrease in the mass concentrations that eventually stabilized. The experiments performed under oxidizing conditions had generally a lower mass concentration when stabilized, compared to the inert conditions. This was likely due to the oxidation of the precursor, which slowed down the release rate.

The experiments performed under oxidizing conditions showed only a small increase in the aerosol mass concentration when humid oxidizing condition with added cesium iodide were used. The slight increase can be attributed to the addition of cesium iodide to the aerosols. For the experiments under inert conditions, a slight decrease was observed under the humid inert condition, and an increase when cesium iodide was added. The decrease may be due to added humidity resulting in tellurium oxide. The formed TeO would then deposit before reaching the tapered element oscillating microbalance (TEOM, an instrument used for real-time detection of aerosol particles by measuring their mass concentration, see Figure 5.4.*1*), as TeO is only stable at high temperatures. It could form tellurium dioxide as it was approaching room temperature, which would explain the observed tellurium dioxide on the filter. The mass increase observed when cesium iodide was present, could be explained by the already suggested possibility of a cesium-tellurium complex. This means that cesium iodide either increased the volatility of tellurium under humid inert conditions or added mass to the tellurium aerosol.

The number size distribution of tellurium bearing aerosols were also determined (particle diameter < 1 micrometer). The results for both oxidizing and inert conditions are presented in Figure 5.4.***3***.

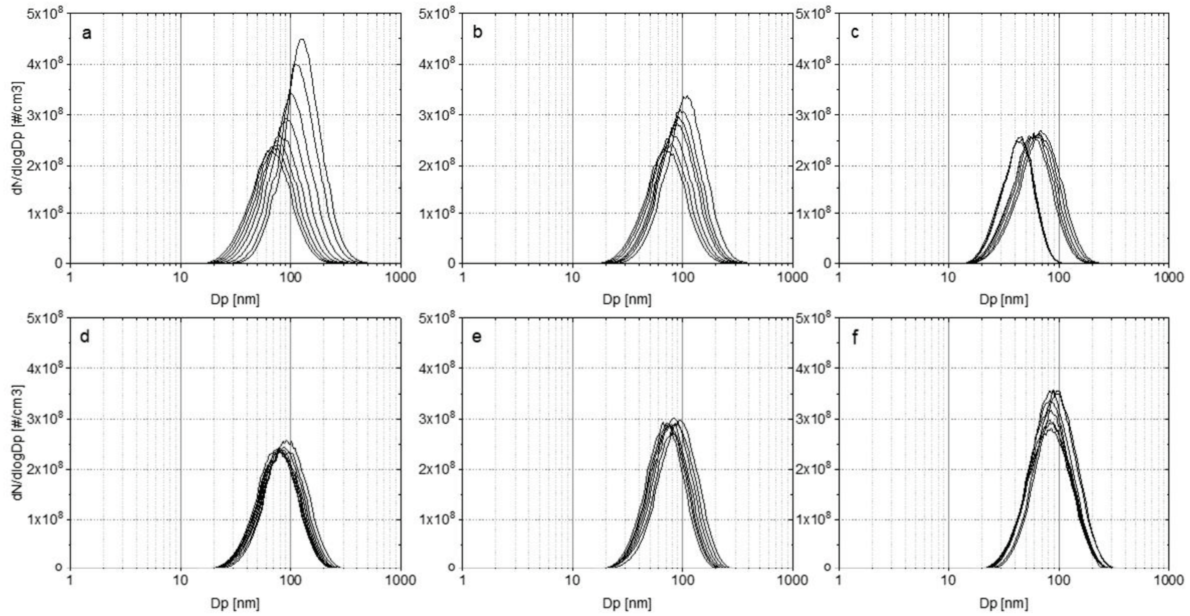

Figure 5.4.3 Evolution of the number size distribution of tellurium containing aerosol in the experiments. The diameter and number concentration of particles decreased in the course of experiments: a) RCS-1, b) RCS-2, c) RCS-3, d) RCS-4, e) RCS-5 and f) RCS-6

The number size distribution of tellurium bearing aerosols under both oxidizing and inert conditions showed decreasing trends of both the number and diameter during the experiments. For oxidizing conditions, the distribution remained unchanged when going from dry to humid conditions, even if the former had initially a higher number concentration. When adding cesium iodide to the system, a continuous decrease of the size distribution was observed, while the number concentration of the particles remained stable. The count median diameter (CMD) of tellurium-bearing particles for the experiments was estimated to decrease from 100 nm to 60 nm for both the dry and humid experiments, whereas the addition of cesium iodide measured a CMD decreasing from 70 nm to 40 nm. The size distribution from the three inert conditions was similar to one another. The number concentration increased when going from dry to humid conditions and became even higher when cesium iodide was added. The CMD for the inert conditions, changed from 100 nm to 70 nm and with the addition of cesium iodide the CMD range was from 100 nm to 85 nm.

In these results, a change in the particle distributions was observable from all the investigated conditions (oxidizing, inert) as well as a change in the particle distribution due to the addition of cesium iodide. Under oxidizing conditions, the size distribution decreases as a whole due to the addition of cesium iodide, whereas under the inert conditions the size distribution ended slightly higher (i.e., the CMD) compared to dry and humid inert conditions. The continuous decrease observed in all experiments is most likely related to the decrease in the mass being transported after the initial surge, and therefore less agglomeration of the tellurium aerosols occurs towards the end, due to less material in the gas. Under oxidizing conditions, the decrease observed when cesium iodide was investigated could be related to the cesium iodide particles reducing the agglomeration of the tellurium aerosols. This either by reaction with tellurium or reaction with oxygen (that prevents further reaction with tellurium). Another possibility could be that the cesium iodide increases the size of tellurium aerosols and therefore increases the tellurium deposition before reaching the measuring location. However, under inert conditions, the addition of cesium iodide slightly increased the final size distribution (i.e., CMD). Considering, that the initial surge of tellurium had faded towards the end of the experiment it is likely that the cesium iodide was promoting larger tellurium particles. This could occur by either reaction that forms larger particles (e.g., Cs_2Te) or an enhanced agglomeration due to the cesium iodide.

5.5 Containment surfaces

Inside the containment, several metallic and other surfaces exist, which may react with tellurium. The metallic surfaces of interest are aluminum, copper and zinc of which their surfaces areas inside the containment has been estimated to be in the order of thousands or tens of thousands square meters [GLÄ04, GLÄ06, HOL09, KAJ16]. Zinc and aluminum are present as metallic sheets and copper is available in electric cables that will melt during the accident and create aerosols that deposit inside the containment.

5.5.1. Experiment

To evaluate the behavior of tellurium and its reactions with or deposition on surfaces in a BWR containment, a single furnace setup was used. Positioned inside the furnace was the tellurium (1 g) precursor in either a porcelain or alumina crucible. The latter was used only during reducing conditions, due to heavy corrosion of the porcelain crucible under these conditions. A sufficiently long alumina tube was used, which extended far enough out from the furnace to ensure room temperature at the end of it. At this location and temperature, three metal surfaces representing parts of a BWR containment were located. These metals consisted of copper, zinc, and aluminum (positioned in a row) and were cut from a copper sheet, a zinc rod, and an alumina rod. Following the metal coupons, a filter and a sodium hydroxide liquid trap was located. A schematic of the system used can be found in Figure 5.5.***1***.

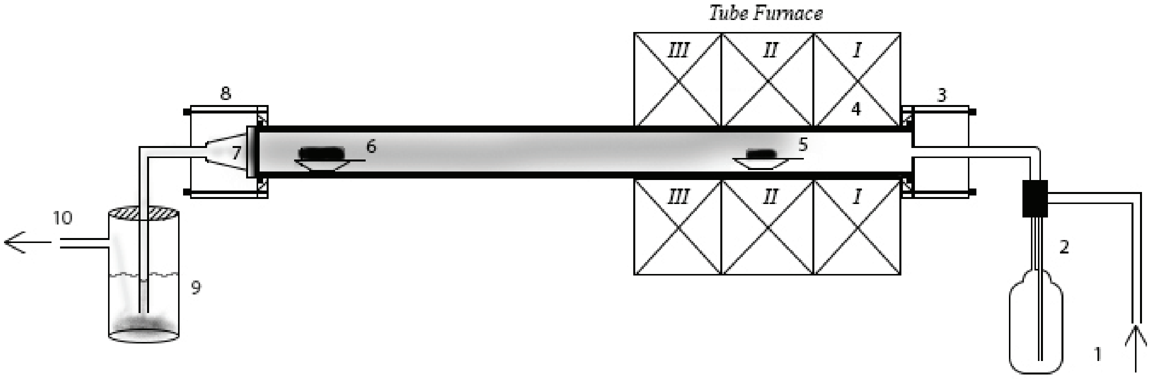

Figure 5.5.1 The experimental schematics: (1) gas inlet, (2) atomizer, (3) inlet, (4) Al2O3-tube, (5) the precursor location,(6) the metallic coupon, (7) cone-formed outlet, (8) connector, (9) a sodium hydroxide solution (1 M) trap, and a water trap, and (10) the gas outlet

During the containment experiments, three different conditions (oxidizing, inert, and reducing) both dry and humid were investigated. In the case of humid experiments, an atomizer was located before the furnace and filled with water. To establish the different conditions and transport the volatilized precursor, three carrier gases were used: compressed air (oxidizing), argon (inert), and argon with 5% hydrogen (reducing). Additionally, reference experiments were carried out with only the surfaces present. This in to determine how the conditions alone affected the different surfaces. An overview of these experiments with some of the parameters used can be found in Table 5.8.

Table 5.8 An overview of the experiments. Relative humidity (RH) determined at the outlet with the furnace heated to 1000°C) and a temperature of 27°C at the measuring location

Experiment	Atmosphere	Main gas	RH [%]	Surfaces
1	Oxidizing	Compressed Air	0.1	Cu, Zn, Al
2	Oxidizing	Compressed Air	99	Cu, Zn, Al
3	Inert	Argon	0.1	Cu, Zn, Al
4	Inert	Argon	99	Cu, Zn, Al
5	Reducing	Argon/5%hydrogen	0.1	Cu, Zn, Al
6	Reducing	Argon/5%hydrogen	99	Cu, Zn, Al

5.5.2. Results

To explore the behavior of tellurium in the containment, several experiments under three different conditions (oxidizing, inert, reducing) were investigated both dry and with increased humidity. The main aim was to observe any reaction or deposition on the surfaces found in a BWR containment. However, these experiments were only carried out as singlets and the experimental uncertainties of these results are unknown.

From a purely visual standpoint, the initial observations revealed little signs of any interaction between the tellurium and the surfaces located at room temperature. Only a thin (possible to see through the deposits) deposit had formed on each of the three surfaces with similar colors (i.e., within one experimental condition) under each condition. For the two oxidizing conditions, the appearance of the deposits was white, and for the deposits from the two inert and two reducing conditions they were black. To enable the scanning electron microscope (SEM) investigation, a small part of the deposits was removed with the adhesive side of a carbon tape.

During the experiments, particles were trapped on the filters. In the case of oxidizing conditions, mainly white-colored deposit with some hint of black had formed on the two filters. For the filters from both the two inert and the two reducing conditions, a back deposit with some white/gray coloration to it was observed.

After each experiment, the mass of the filters was weighed using a balance. The weight of the filter before and after each experiment is shown in Table 5.9.

Table 5.9 The mass of the filters used during each experiment. Weights are shown before and after the experiments

Condition		m_{before} [mg]	m_{after} [mg]
Oxidizing	Dry	0.15	0.26
	Humid	0.15	0.29
Inert	Dry	0.15	0.33
	Humid	0.15	0.3
Reducing	Dry	0.15	0.3
	Humid	0.15	0.32

Observing the weights of all the filters used in the experiments, the amounts trapped on the filters were similar at around 0.15 mg. However, under oxidizing conditions the oxidization of the tellurium would add to the mass, meaning that the mass increase observed of the filter will be a combination of tellurium and oxygen. This was not the case in the inert and reducing conditions where the main species reaching the filter would be metallic tellurium, assuming that no interaction occurred with any of the surfaces. To sum up, this indicates that more tellurium was trapped by the filters under inert and reducing conditions.

Oxidizing Conditions

The morphology of the particles observed in the deposits from all metal surfaces deposited during oxidizing conditions were smooth round spheres of different sizes. No apparent differences were noticeable, between dry and humid conditions. Micrographs of all deposits from oxidizing conditions are shown in Figure 5.5.***2***. In these micrographs, some locations have been indicated. These locations are where the element compositions were determined using energy-dispersive X-ray spectroscopy (EDX). The acquired spectra indicated tellurium, but also oxygen and carbon (likely source: carbon tape). In the deposits from the zinc surface under humid oxidizing conditions zinc was also detected.

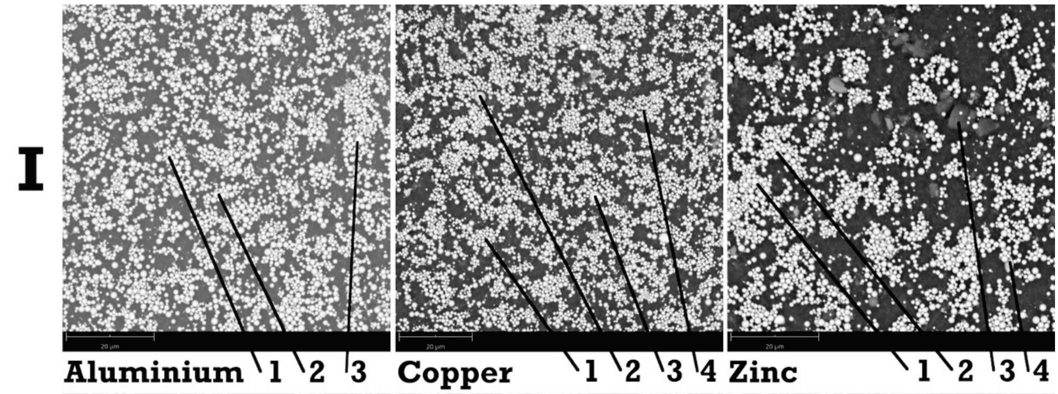

Figure 5.5.2 Six micrographs from dry (I) and humid (II) oxidizing conditions experiments, each showing the deposits from the aluminium (left), copper (middle), and zinc (right) surfaces

The elemental composition of the different deposits is to some degree as expected, meaning that both tellurium and oxygen were present considering the precursor and oxidizing conditions at high temperature. However, the fact that zinc was observed in the deposits is not as expected, as the temperature where the zinc surface was located would be to low to result in any reaction. Thus, finding zinc in the deposit would mean that something did result in the transportation of the zinc to the liquid trap. This could be due to the formation of a thin water film (i.e., humid oxidizing condition) that promotes reaction between zinc and tellurium, or that the tellurium species existing under this condition interacted with the surface. According to the literature

[ALO91, DUT66, MAL70], a transient tellurium species (e.g., $TeO(OH)_2$) exists at high temperatures when humidity is high under oxidizing conditions. If this new species remains in the gas phase at the location of the zinc surface, it may react with the zinc surface and be the cause of the zinc in the deposits. However, little research exists on the potential reactivity of this transient species.

The species in the deposits on all metal surfaces and on the filters were analyzed using X-ray diffraction (XRD) and are shown in the diffractogram in Figure 5.5.***3***. In all diffractograms, TeO_2 was identified. In the deposits under humid oxidizing conditions, two different crystal structures were detected: paratelluride and orthorhombic, of which only the latter was detected under dry oxidizing conditions. The species trapped by the filters from both dry and humid conditions, exhibited both crystal structures.

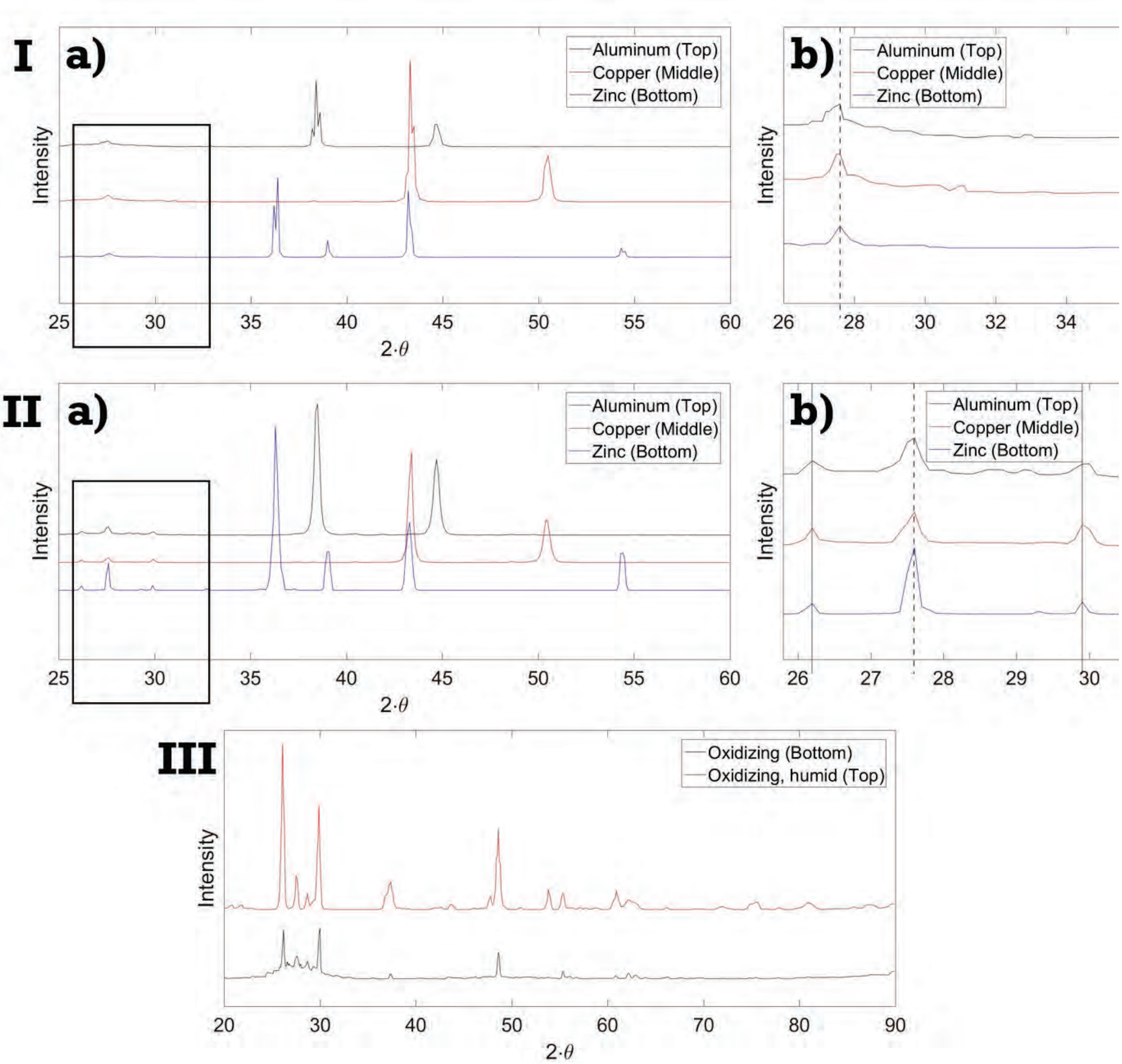

Figure 5.5.3 The x-ray diffraction analyses of the depositions formed on the metal surfaces from dry (I) and humid (II) oxidizing conditions experiments. Areas highlighted (I.a and II.a) by boxes are shown to the right (I.b and II.b). Diffractograms for the filter used during these experiments are also shown (III)

The main difference observed between the dry and humid conditions was the presence of two different crystal structures of the tellurium dioxide in the deposits on all metal surfaces. Observing the filters, both crystal structures were detected in the trapped particles under both conditions. From these observations alone, no clear explanation can be found. However, this indicates that the humidity may have increased the amount of paratelluride-TeO_2. Therethrough, more of it was able to deposit on the surface and increase its fraction in the deposit to such an extent that it was detected. A species that could be responsible for this alternative crystal structure is tellurium oxide (TeO). It is only stable at high temperatures and is formed under oxidizing conditions at high temperatures [ALO91]. It would then form the paratelluride-TeO_2 observed in these experiments as the temperature decreased. Alternatively, the transient species formed under humid oxidizing conditions at high temperatures could have a higher tendency for deposition on the surfaces. It would then also have formed the paratelluride-TeO_2 on the surfaces.

The liquid sodium hydroxide traps were also investigated for any amount of tellurium and metals (aluminum, copper, zinc). For the two oxidizing conditions, tellurium was detected in the traps from both dry and humid conditions at roughly $0.008\%_{wt}$ and $0.65\%_{wt}$ of the original precursor amount, respectively. The only metal detected in either trap was under humid oxidizing conditions, where around 0.3 mg of zinc was measured. These observations, which are consistent with the literature [ALO91, DUT66, MAL70], indicate a higher amount of tellurium transported to the liquid sodium hydroxide trap under humid oxidizing condition. However, detecting zinc in the trap was not expected, indicating that a reaction occurred on the zinc surface that transported zinc in a volatile form to the liquid traps under humid oxidizing conditions. From the reference experiments carried out, no signs of zinc in the trap was observed, which supports the idea that the tellurium species existing under humid oxidizing conditions affected the zinc surface. Additionally, literature [SAL84, ELR91] have shown that tellurium does react with different surfaces in the RCS (e.g., 304 stainless steel and Inconel-600, both with and without an oxide layer), therefore it is possible that other surfaces such as zinc may also react with tellurium.

Inert Conditions

Under inert conditions, the morphology of the particles under both dry and humid inert conditions were a mixture of smooth spheres, clusters of smaller round particles, spike-shaped, and rectangular objects. When comparing the morphology of the two depositions from the dry and humid inert conditions, little differences were noticeable. The relevant micrographs are shown in Figure 5.5.***4***, in which some locations have been highlighted. In these locations, the elemental composition was determined. Essentially, only tellurium and carbon were detected, with the occasional oxygen observed. The carbon most likely came from the carbon tapes used to remove the deposits from the metal surfaces.

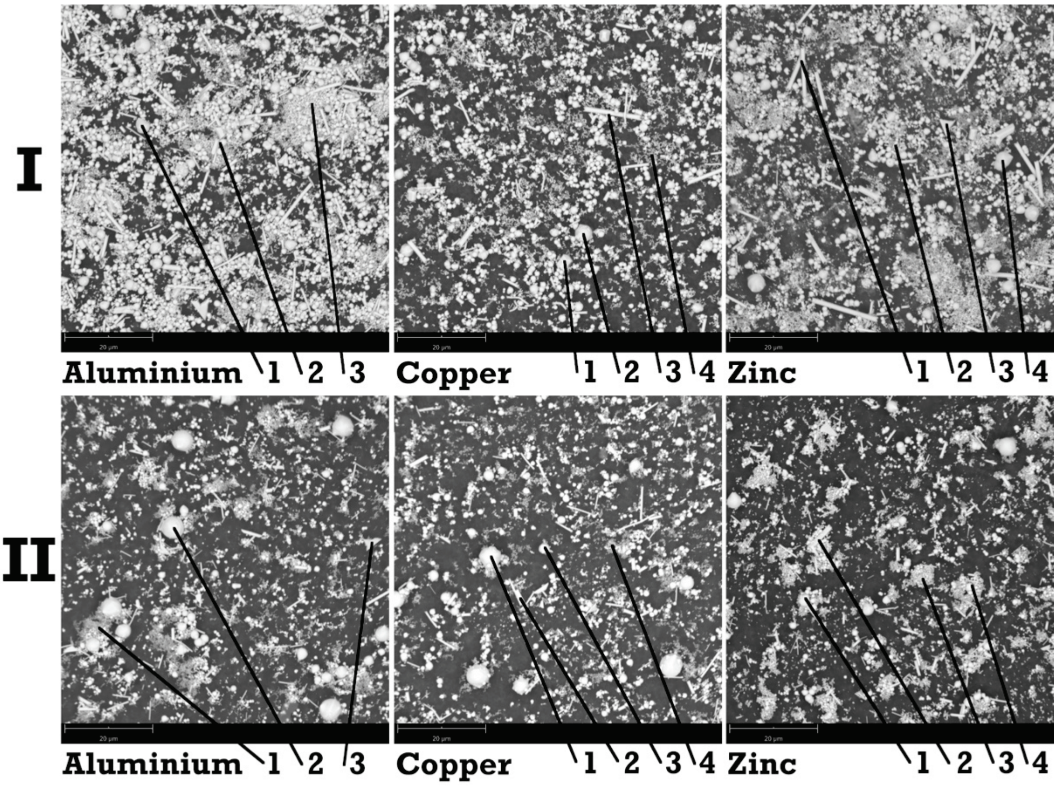

Figure 5.5.4 Six micrographs from dry (I) and humid (II) inert conditions experiments, each showing the deposits from the aluminium (left), copper (middle), and zinc (right) surfaces

The presence of tellurium is expected, considering the inert conditions at high temperatures. That oxygen present in the sample can be explained by oxidation of tellurium during storage/transport to the SEM/EDX or slight oxidation of tellurium due to the humidity in the humid inert condition. Alternatively, some air may have leaked in during the experiment. Determining the species of the deposits from the metal surfaces and the filters, showed that Te was the only species present. The diffractograms can be found in Figure 5.5.***5***.

The results shown in Figure 5.5.***5*** indicate that the addition of humidity to inert conditions had little effect on the species of tellurium that deposits and are stable at room temperature.

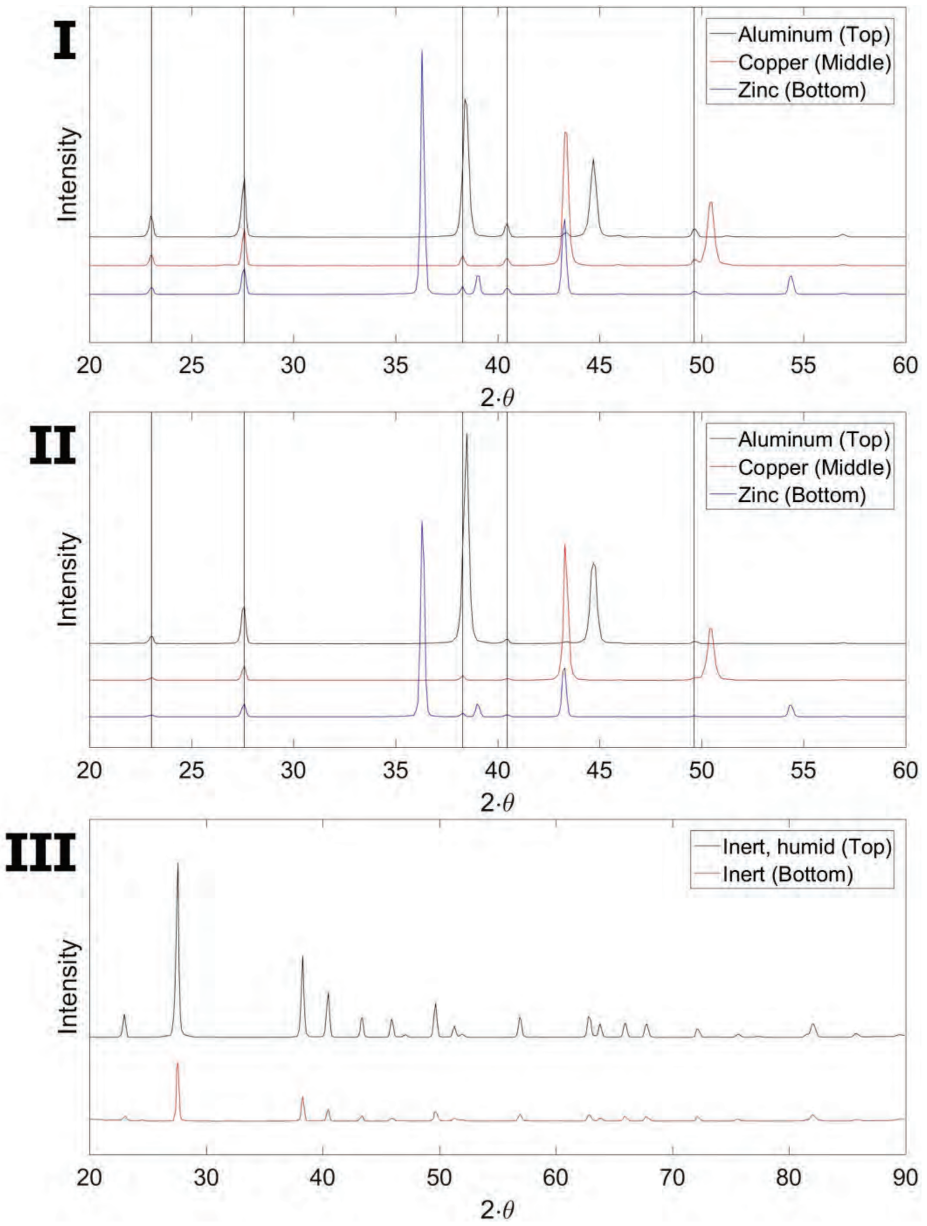

Figure 5.5.5 The x-ray diffraction analyses of the depositions formed on the metal surfaces from dry (I) and humid (II) inert conditions experiments. Diffractograms for the filter used during these experiments are also shown (III)

In the liquid sodium hydroxide traps, no detectable amounts of tellurium were measured. However, 0.2 mg of aluminum was observed in the trap from the humid inert condition.

Considering the weights of the filters, located just before the liquid sodium hydroxide traps, no significant increase in the mass was observed compared to the other two conditions. This indicates that the tellurium species formed are less volatile and not capable of reaching either the trap or the filter. As little remained in the crucible, it could however be that under both inert conditions larger particles formed that resulted in enhanced deposition on the tube walls. The presence of aluminum in the trap could be due to the tube itself being made from Al_2O_3 and small amounts being released from it.

Reducing Conditions

Investigating dry and humid reducing conditions resulted in deposits on the metal surfaces with a morphology consisting of smooth spheres, spike-shaped, and rectangular objects. Little differences were seen between the deposits acquired under the two reducing conditions. The micrographs of the deposits from the reducing conditions are shown in Figure 5.5.***6*** and some locations have been highlighted. The chemical composition of these locations were determined and only tellurium and carbon, with the occasional oxygen, was detected. The observed carbon most likely originates from the carbon tapes used to remove the deposits from the metal surfaces.

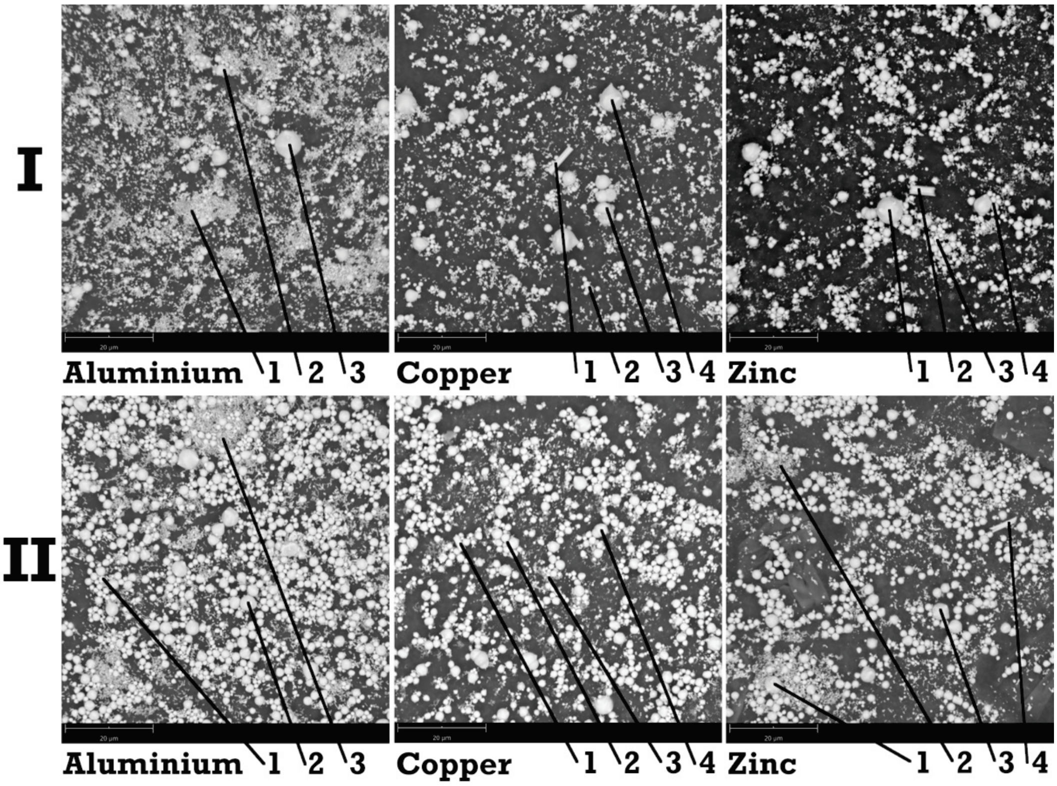

Figure 5.5.6 Six micrographs from dry (I) and humid (II) reducing conditions experiments, each showing the deposits from the aluminium (left), copper (middle), and zinc (right) surfaces

Tellurium was expected considering the temperature and reducing conditions at higher temperature. Similar to the inert conditions the presence of oxygen may come from slight oxidation during storage/transport to the SEM/EDX analysis, or that air leaked in during the experiment.

In the diffractograms produced from the deposits from the metals surfaces and filters under both reducing conditions, only metallic Te was detected. The corresponding diffractograms are shown in Figure 5.5.*7*.

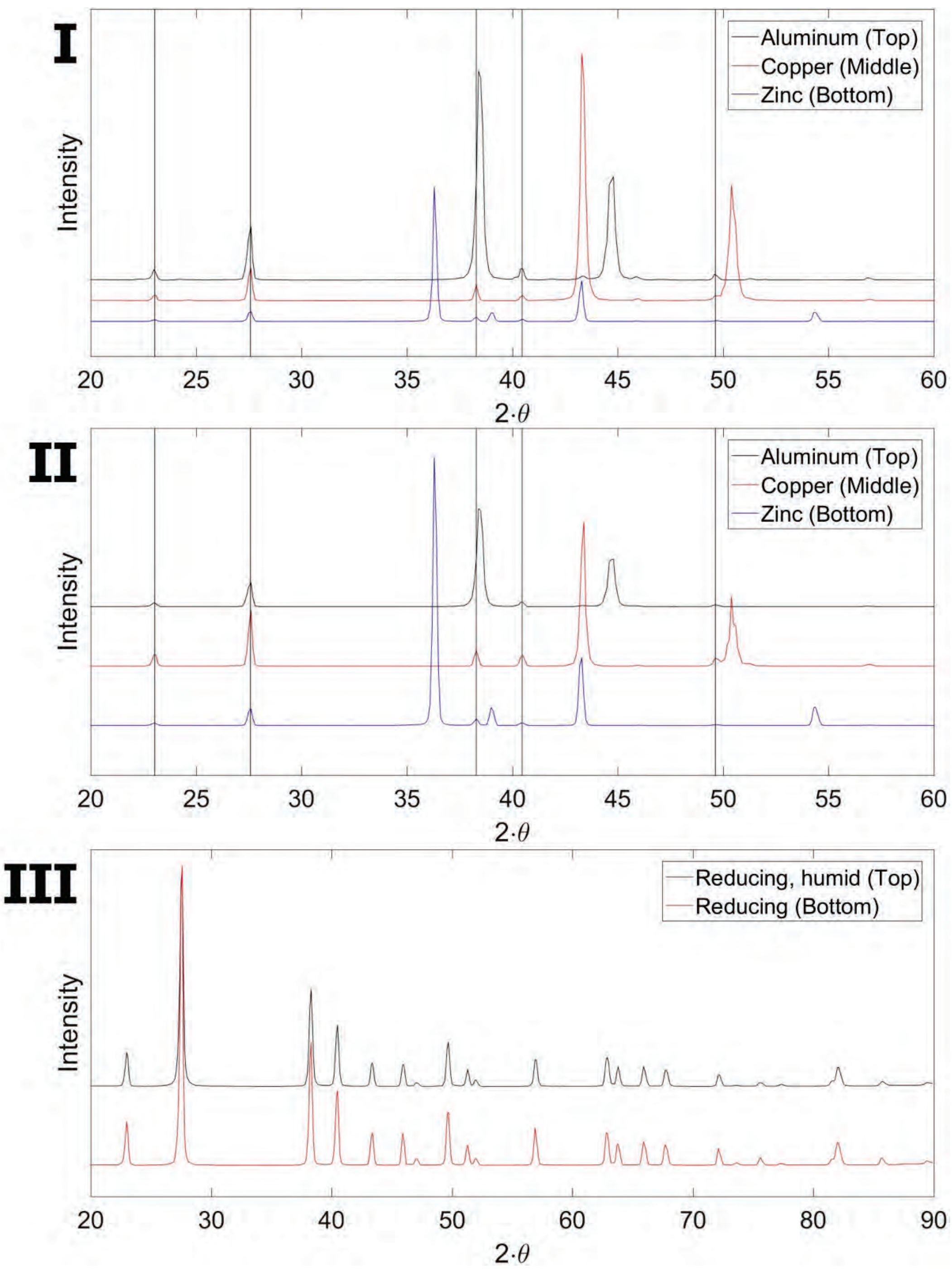

Figure 5.5.7 The x-ray diffracts analyses of the depositions formed on the metal surfaces from the dry (I) and humid (II) inert conditions experiments. Diffractograms for the filter used during these experiments are also shown (III)

Little difference between dry and humid reducing conditions can be seen in these diffractograms. These results are also similar to the result obtained for inert conditions. This indicates that neither the inert nor the reducing conditions or increasing the humidity of the two, had any effect on the speciation of tellurium at room temperature.

The content of the liquid sodium hydroxide traps under the two reducing conditions only showed detectable amounts of tellurium and aluminum under humid conditions. Around 1.1%$_{wt}$

of tellurium compared to the original precursor amount and 0.2 mg of aluminum were measured. Similar to the observed aluminum under humid inert conditions, the source may be the tube itself as no aluminum was detected in the deposits from the aluminum surface. Under reducing conditions, a possible species that could have reacted with the tube is H_2Te [ALO91]. Additionally, the formation of this species may also have promoted the transport of tellurium to the liquid sodium hydroxide trap.

5.6 Containment spray system (CSS)

One of the main engineered safety systems is the containment spray system (CSS). It has been designed to help maintain the containment building integrity by decreasing the pressure and temperature inside the containment as well as mitigate the release of radionuclides by removing fission products containing particles from the containment atmosphere into the sump. The removal happens via physical and chemical interactions and the efficiency of the CSS relates to the size of the aerosols in the containment atmosphere. The CSS has been found to be the most efficient way to remove particles larger than 1 μm or smaller than 0.1μm [OECD] Gaseous species can be removed by adjusting the chemistry of the spray solution to efficiently react with the gaseous compounds and convert them to a non-volatile form.

The chemical composition of the spray is primarily designed to mitigate iodine releases. Moreover, the main components of the CSS solution are generally a base (e.g. sodium hydroxide, potassium hydroxide or trisodium phosphate), boric acid and possibly an additive (e.g. sodium thiosulphate, hydrazine). The spray solution pH is generally kept alkaline to shift the disproportionation of volatile iodine to a more non-volatile iodate/iodide side [NEEB]. Similarly, the use of additives, usually reducing agents, reduces the amount of volatile iodine species by decomposing and trapping the gaseous species inside the droplets [PARSLY, JOYCE]. Finally, boric acid is used to maintain the subcriticality of the reactor core as well as buffer the pH with the base [NEEB]. The removal efficiency and the effect of the chemical composition of the spray have not been previously investigated towards tellurium species.

5.6.1. Materials and method

The containment spray experiments focused on investigating the removal efficiency of tellurium by the spray and the possible chemical effects of the spray solution. The experimental spray setup consisted of a spray chamber made of stainless-steel simulating a containment building. The inner walls of the chamber were coated with Teflon tape to passivate the surfaces and thereby decrease loss of material due to adsorption. The chamber was connected to a tubular furnace where the chosen tellurium precursor was vaporized. The schematics of the “VTT spray chamber” is shown in Figure 5.6.***1*** along with its dimensions. A spray nozzle simulating a containment spray system (CSS) was attached on top of the chamber. The spray droplets (ca. 10 µm in diameter) were generated from the solution in the spray supply bottle and the droplet feed rate was controlled with a pressurized air or nitrogen. The temperature of the spray solution and spray chamber was in room temperature. The aerosols not captured by the spray droplets exited close to the top of the spray chamber. Beyond of this exit, the aerosol flow was diluted and dried with hot gas flow of air or nitrogen (373 K). Aerosols were filtered out after the hot dilution. A filter was positioned at the end of the system to capture the aerosols not removed by the spray. After the filter, a 0.1 M sodium hydroxide trap was positioned to ensure retention of any gaseous tellurium species possibly released through the system. The spray droplets generated during the experiments were accumulated at the bottom of the chamber, forming the sump, which was collected for analysis along with the filter, trap and crucible. The filter samples were analyzed using Instrumental Neutron Activation Analysis (INAA), aerosols were monitored online with Electric Low-Pressure Impactor (ELPI) and the precursors were analyzed with X-ray Powder Diffraction (XRD).

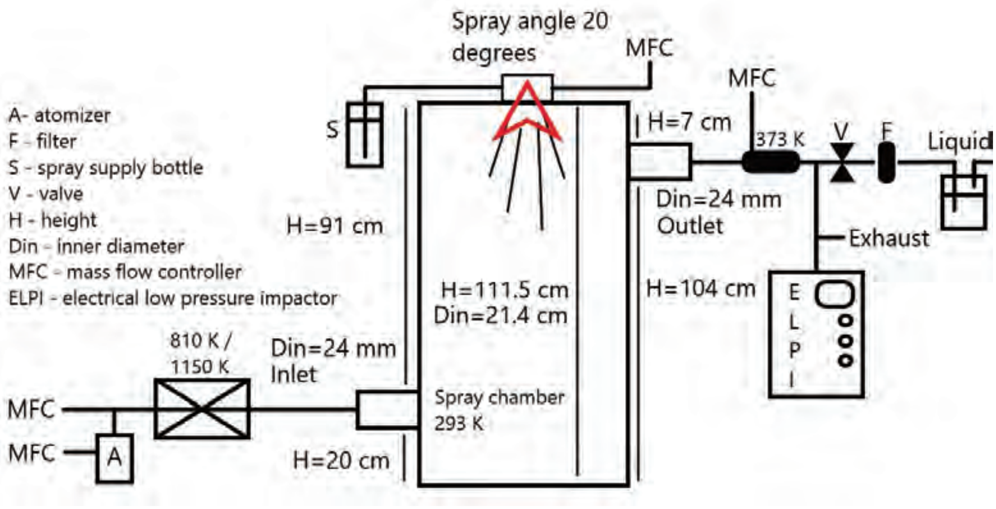

Figure 5.6.1 The experimental setup used in the spray experiments

The experiments were performed by placing the crucible with the precursor, either Te or TeO_2, in the alumina tube inside the furnace. The furnace was heated close to the boiling point of the chosen precursor; 810 K for metallic Te and 1150 K for TeO_2. First, a reference sample was collected in order to determine how much tellurium was generated and transported through the system when the spray was not on. After the collection of the reference sample, each solution was sprayed inside the containment unit for 20 minutes and samples were collected for analysis. Overall, nine experiments were performed in various conditions and using the two different precursors. The conditions investigated were dry and humid air and nitrogen. Moreover, the effect of cesium iodide (CsI) was also investigated in both conditions by dissolving solid CsI to the water sprayed into the system via the atomizer. The sample matrix and the changing parameters are shown in Table 5.10. In terms of the spray solution, three were investigated – water, alkaline borate solution and alkaline borate solution with sodium thiosulfate. The concentrations of the chemicals used in the solutions were 0.23 M H_3BO_3, 0.15 M NaOH and 0.064 M $Na_2S_2O_3$. The spray solutions were chosen to represent the chemical conditions relevant for accident conditions.

Table 5.10 Experimental matrix with the different parameters

Experiment#	Precursor	Temperature, [K]	Atmosphere	Added humidity[a]	CsI[b]
1	TeO_2	1150	Air	No	
2	TeO_2	1150	Air	Yes	
3	TeO_2	1150	Air	Yes	Yes
4	Te	810	Air	No	
5	Te	810	Air	Yes	
6	Te	810	Air	Yes	Yes
7	Te	810	Nitrogen	No	
8	Te	810	Nitrogen	Yes	
9	Te	810	Nitrogen	Yes	Yes

[a] Humidity content of the gas flow entering the spray chamber was 21000 ppmV

[b] CsI content of the atomizer supply bottle was 0.15

5.6.2. Results

The removal efficiency of tellurium species by the containment spray system was investigated in different atmospheric conditions. In addition, the effect of the spray solution composition was also analyzed. The results presented here show the analyses of the tellurium precursors, online particle size distribution and the spray removal efficiencies.

The crucible containing the tellurium precursor was weighed before and after each experiment and the mass differences were used to estimate the release behavior of tellurium under different conditions. The weighing results are presented in Table 5.11. In Experiments 1-3 performed with TeO_2 in air, the mass decreased 0.20, 0.26 and 0.30 g, respectively, from the initial mass of 1.26 g. Moreover, the volatilization and release were relatively consistent in each condition but with a slight increase when the conditions changed from dry to humid and humid with CsI. This indicated that humidity and CsI may have an effect on tellurium volatilization and release. However, a firm conclusion cannot be reached from these results alone due to the relatively small differences in the masses.

In the experiments performed with metallic Te in air, the mass of the precursor decreased 0.05 g in Experiment 4. Moreover, the mass of the tellurium precursor increased 0.009 and 0.070 g in Experiments 5 and 6, respectively. The low decrease or even the slight increase was suspected to occur due to oxidation of the metallic tellurium precursor under the experimental conditions. The precursors were later analyzed using X-ray Powder Diffraction (XRD), see below.

In Experiments 7–9 with metallic Te under nitrogen atmosphere, the mass decreased significantly during the experiments. In Experiment 7, the mass loss was 0.80 g, which corresponds to 80% of the initial 1.0 g of metallic Te precursor. Experiments 8 and 9 were performed back to back, which made it impossible to determine the mass difference in the individual experiments. However, overall the mass decreased 90% from the initial mass, indicating a large release.

Table 5.11 The initial mass of the tellurium precursor and the mass loss observed after each experiment. In Exp. 5 and 6 the negative value indicates mass increase instead of decrease

Experiment **[#]**	**Duration** **[min]**	**Initial Mass** **[g]**	**Mass loss** **[g]**
1	190	1.26	0.199
2	151	1.26	0.255
3	171	1.26	0.295
4	186	1.02	0.051[a]
5	182	1.00	-0.009[a]
6	231	1.01	-0.069[a]
7	197	1.00	0.789
8-9[b]	410	1.00	0.883

[a] Tellurium precursor oxidized during the experiment and therefore, the results are not reliable.

[b] Experiments 8 and 9 were performed back to back using the same precursor

Precursor analysis

As previously suggested, the metallic Te precursor may have oxidized when exposed to the oxidizing experimental conditions in Experiments 4–6. This was suggested by the increased mass of the precursor. The precursors were therefore analyzed using XRD after the experiments to determine whether the speciation of the solid material had changed during the experiments. The diffractograms for each sample from Experiments 4–6 are presented in Figure 5.6.*2*. All of the precursors after the experiments were found to be mixtures of elemental Te and TeO_2. This is in line with the assumption that Te had oxidized during the experiment. In addition, there were differences in the ratio between Te and TeO_2 between the precursors. Although each sample was found to be a mixture of the two tellurium species, it was observed that the precursor from Experiment 5 (Te in humid air) had more distinctive peaks for metallic Te compared to the precursors from Experiments 4 and 6. This indicates a lower degree of precursor oxidation, which could be the result of a different behavior of tellurium in humid air compared to dry air or humid air with CsI. However, inconsistent results were also observed with the INAA filter samples as well as the online aerosol measurements. Thus, an error in Experiment 5 cannot be ruled out. It should also be noted that comparing the peak intensities and their ratios is not a straightforward quantification technique, but it can be used for indication purposes.

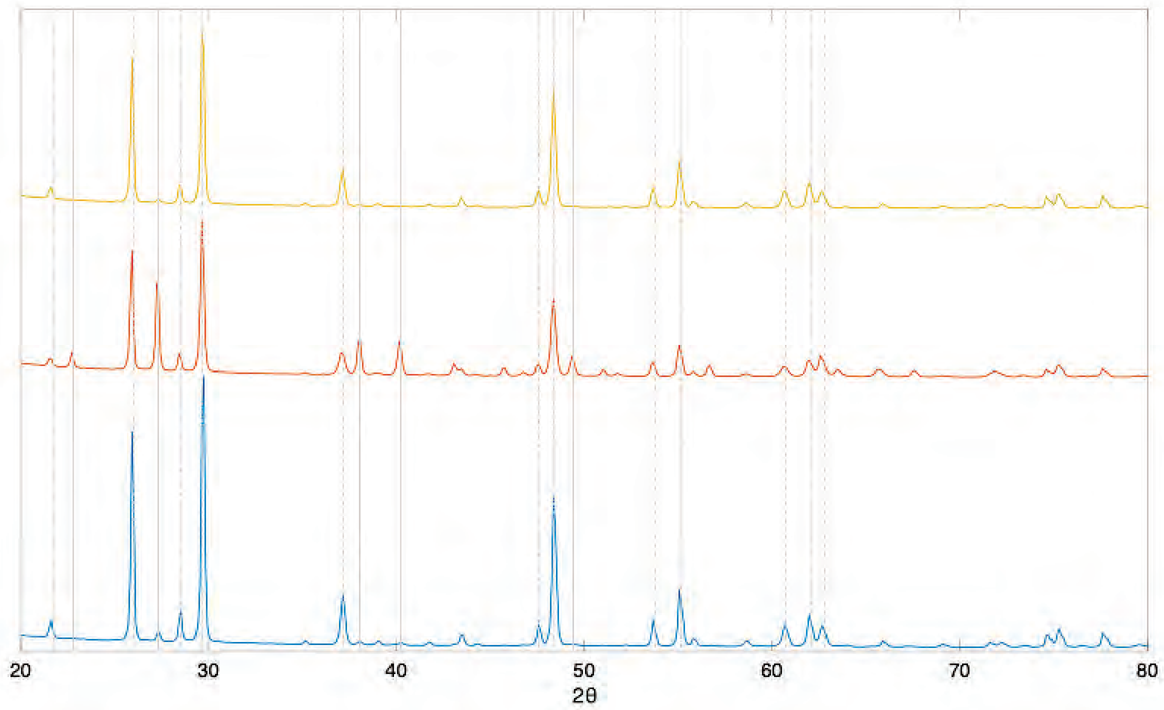

Figure 5.6.2 Diffractograms of the precursors from Experiments 4 (bottom), 5 (middle) and 6 (top). The solid lines mark the signals identified for elemental tellurium and the dashed lines the signals for TeO2

Filter analysis

Some observations regarding the release behavior of tellurium can be made from the reference filter samples taken in the beginning of each experiment without any spray. The filters placed at the end of the system were analyzed with INAA for their tellurium content. The results of the INAA measurements for each experiment are presented in Table 5.12.

The reference filters from Experiments 1, 2 and 3, where TeO_2 was used as a precursor in air, had an increasing tellurium content in the order dry to humid to humid with CsI. This is in line with the literature, which suggests that TeO_2 can react with steam to form a more volatile species, possibly $TeO(OH)_2$. However, the speciation during the experiments was not monitored. Thus, the exact reason for the higher volatility cannot be explained. The tellurium content on the filter from Experiment 2 with humid air had over twice the amount of tellurium deposition compared to the filter obtained in dry air atmosphere. Furthermore, a slight increase in deposition was observed when comparing experiments with humid air to humid air with CsI. However, taking into account the uncertainties, the results overlap and therefore it seems like CsI did not have any significant effect on tellurium release and transport.

In Experiments 4, 5 and 6 performed with metallic tellurium in air, there was more fluctuation in the filter results. The filter from Experiment 5 in particular had a very low amount of tellurium deposition compared to Experiments 4 and 6. This result is inconclusive and cannot be explained through literature or other means. As it was already previously mentioned, an experimental error cannot be ruled out when it comes to the low release obtained from Experiment 5.

Finally, the Experiments 7, 8 and 9, where metallic tellurium was used as a precursor in nitrogen atmosphere, the tellurium content on the filter decreased in order of dry to humid to humid with CsI.

Table 5.12 Filter results for reference filters from spray experiments

Experiment#	**Filter, Te [mg]**
1	0.240 ± 0.008
2	0.570 ± 0.018
3	0.588 ± 0.018
4	0.373 ± 0.011
5	0.023 ± 0.0007
6	0.283 ± 0.009
7	0.497 ± 0.015
8	0.348 ± 0.011
9	0.177 ± 0.005

Particle size distribution

The properties of tellurium aerosols entering the containment unit were monitored online using ELPI. The average mass size distributions describing the aerosol properties inside the spray chamber without spray operation are given in Figure 5.6.***3***. In general, the aerodynamic mass median diameter (AMMD) of tellurium aerosols was less than 1 µm. However, the particles formed larger agglomerates, which extended the mass size distribution towards the particle diameters of several µm. The fraction of agglomerates seemed to be more pronounced in the experiments with metallic tellurium precursor (Exp. 4-9). The mass concentration of tellurium aerosol particles varied between the experiments, with the highest concentration observed in the experiments with TeO_2 precursor. In Experiment 5 (metallic Te precursor in air), the mass concentration was very low. This strengthens the assumption of an experimental error since the results from previous measurements were also inconsistent compared to other experiments. The airborne CsI aerosol additive was fed together with tellurium aerosols in Experiments 3, 6 and 9. It was observed that the mass size distribution grew wider due to the addition of CsI particles.

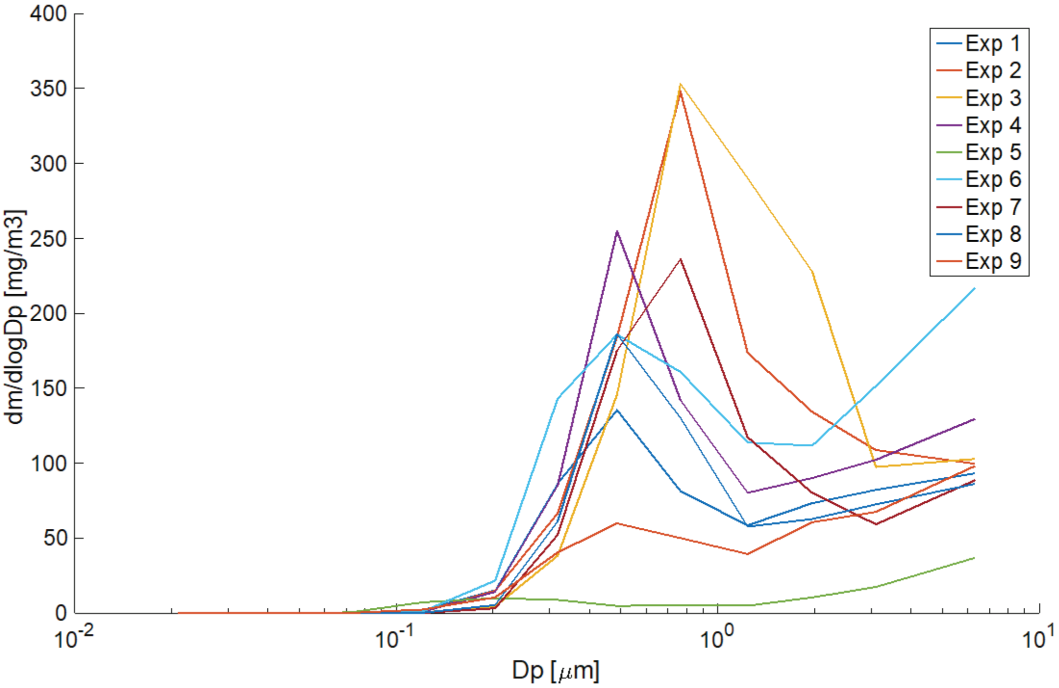

Figure 5.6.3 The average mass size distribution of the fed tellurium aerosols in the spray chamber in reference conditions

Removal efficiency

The spray removal efficiencies were calculated based on the analyses of reference and sample filters collected after each experiment. Tellurium content on the filters was analyzed with INAA. The filter results were used to calculate the removal efficiencies shown in Table 5.13. As seen in the table, the removal efficiencies were relatively high in all nine experiments. In Experiments 1–3, the efficiency was between 83 and 97 % in all conditions with each spray solution. The chemical sprays gave consistently higher removal results than the water spray.

In Experiments 4–6 the results had more fluctuation, especially, Experiment 5 had clearly lower removal efficiencies. However, as it was mentioned, an experimental error may have occurred, and the results therefore are not conclusive. In the two other experiments (4 and 6) the results were very high. The chemical sprays removed up to 99 % of all the tellurium species in the containment.

Lastly, the experiments performed with metallic tellurium in nitrogen atmosphere (Experiments 7–9) had significantly lower removal efficiencies compared to the other conditions. Here, a minimum efficiency was obtained at 63 % with water spray in dry nitrogen atmosphere. The addition of cesium iodide in the feed (Experiment 9) increased the removal efficiency again up to 94 %. This was possibly due to higher degree of agglomeration forming larger particles. Although the chemical effect of CsI cannot be fully excluded, it is more likely that the higher removal efficiency is due to higher degree of agglomeration.

Table 5.13 Removal efficiencies for each spray solution calculated from INAA filter results

	Removal Efficiency [%]		
Experiment#	**MilliQ water**	**ABS[a] without thiosulfate**	**ABS with thiosulfate**
1	83	96	97
2	89	97	97
3	91	97	97
4	83	99	99
5	74	73	73
6	92	99	99
7	63	72	75
8	70	65	60
9	89	93	94

[a] Alkaline Borate Solution

5.6.3. Conclusion

Based on all the filter results obtained from INAA analysis, the removal efficiency for TeO_2 and Te aerosols was high, above 80 %, using water spray droplets in the air atmosphere. The chemical spray droplets increased the efficiency above 95 %. Further addition of chemicals improved the efficiency slightly. The removal efficiency for Te aerosol decreased to 63 % in the nitrogen atmosphere. This significant drop in the removal efficiency should be further investigated. Whether the decrease is due to changes in the size distribution of the aerosols or the chemical interactions between the aerosol and the droplets, cannot be concluded. In all atmospheres, the additional airborne CsI particles increased the removal efficiency. The phenomenon was significant in the air atmosphere using water droplets, but it was less pronounced in the case of chemical droplets, which were likely increasing the removal efficiency already. The removal efficiency remained high regardless the chemical composition of spray droplets. This was possibly due to agglomeration of aerosols resulting in overall larger particles. Overall, the CSS was found to be efficient in removing tellurium species under various conditions.

5.7 Containment sump

The containment sump is the liquid phase that is collected on the bottom of the containment during a severe accident. The sump is a complex mixture of components originating either from accident management systems e.g. the containment spray system (CSS) or from events that take place during the accident e.g. leaks from the primary circuit, radiolysis of structural materials, water and air and corrosion and dissolution of materials from the surfaces. Due to the complexity of the sump, it is difficult to predict the behavior of FPs and possible release by re-volatilization. However, this must be considered since the sump formed during an accident will stay inside the containment and could be subjected to further chemical effects. Due to the complex chemistry of tellurium itself and the possibility of taking part in further reactions, it is necessary to gain knowledge of the behavior of tellurium in the sump especially under irradiation.

5.7.1. Materials and method

The samples for irradiation were prepared by weighing 30 mg of solid TeO_2 into a glass vial and adding 5 ml of alkaline borate solution with or without sodium thiosulphate. The air to liquid ratio was 0.4. Samples were irradiated for period of time ranging from 1 to 10 days. The maximum dose delivered to the sample was approximately 1.2 MGy. The reference samples were prepared in the same way but instead of irradiation, the samples were kept in a heating cabinet at 313 K. All samples were prepared as triplicates to obtain statistical significance. The sample matrix is presented in Table 5.14.

Both the irradiated and reference samples were filtered with 0.45 μm syringe filters and prepared for ICP-MS measurements by diluting with 0.5 M nitric acid. Rhodium (1ppb) was used as an internal standard in the ICP-MS measurements due to its rarity in most samples and relatively inert coordination chemistry. The tellurium standards were prepared by diluting from 10 ppm standard solution. The solid material remaining after the experiments in the samples was dried and ground to a powder before examination with XRD.

Table 5.14 Sample types used in the sump experiments

Sample ID	**ɣ-Irradiated**	**$Na_2S_2O_3$**
TeO_{2_w/o_thio_irrad}	Yes	No
TeO_{2_w/o_thio_ref}	No	No
$TeO_{2\_w/\_thio\_irrad}$	Yes	Yes
$TeO_{2\_w/\_thio\_ref}$	No	Yes

5.7.2. Results

The behavior of TeO_2 was investigated in alkaline borate solution (ABS) with and without sodium thiosulfate. The results presented below show the TeO_2 behavior in terms of solubility, speciation and redox chemistry.

Solubility

The results of the solubility experiments with TeO_2 in the alkaline borate solution (ABS) with (w/) and without (w/o) sodium thiosulphate are presented in Figure 4.1.*1*. Both irradiated and non-irradiated results are presented as well as the reference results. The main finding was that gamma radiation has a significant effect on tellurium solubility in the alkaline sump simulate solution. Without sodium thiosulphate additive, the solubility increased with increasing radiation dose. The solubility of tellurium in the non-irradiated samples reached an equilibrium at around 16 mM. In comparison, the concentration of tellurium after 10 d (1.2 MGy) irradiation in ABS without sodium thiosulphate additive was 26 mM and did not reach equilibrium during the experiment.

However, in the presence of the reducing thiosulphate additive, the concentration of tellurium decreased with increasing dose reaching a concentration of 6 mM after approximately 1.2 MGy dose. In addition, a change of color was observed in the solid material, from white to silvery black (Figure 4.20.), indicating that a possible reduction of initial precursor TeO_2 to elemental tellurium had occurred. The non-irradiated reference samples behaved similarly to the ones without the thiosulphate additive; solubility reached an equilibrium at 16 mM and no color change occurred. No significant change in pH was observed in any of the samples.

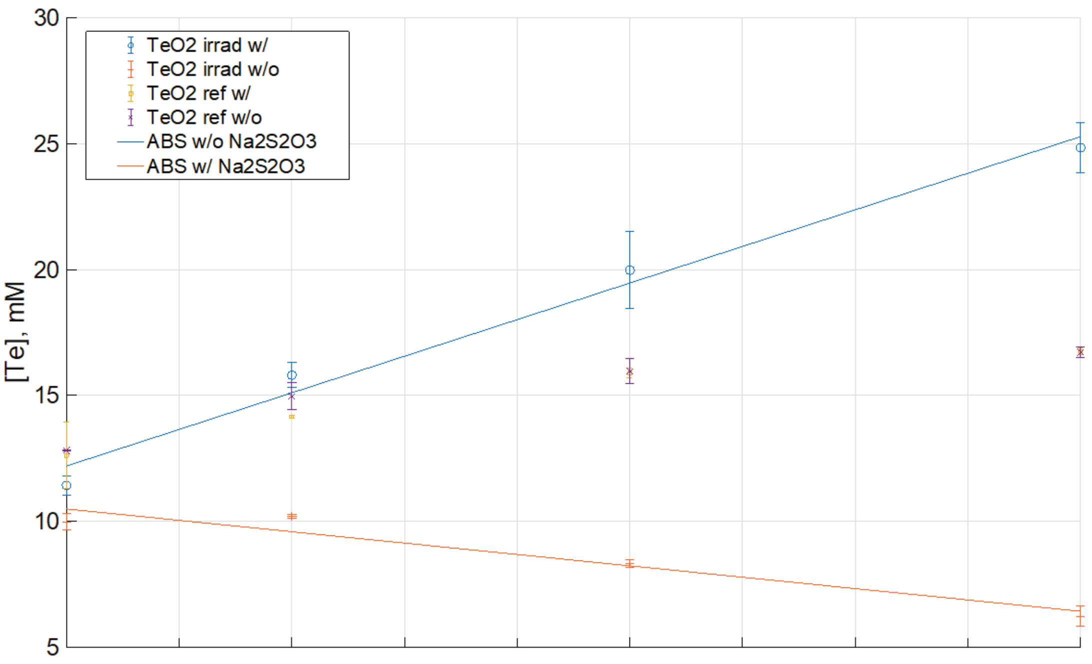

Figure 4.1.1 The solubility of tellurium in alkaline borate solution with and without sodium thiosulfate additive. Irradiated and reference samples are all presented. Maximum dose received after 10 days of irradiation was around 1.2 MGy. The solid lines represent the linear trend of the irradiated samples in the two different solutions

Liquid speciation

The speciation of tellurium in the simulated sump solutions was investigated with ion chromatography (IC). This method is suitable for differentiating between tellurium in oxidation states +4 and +6. However, the exact speciation might be affected by matrix effects while the samples pass through the column and thus, the exact speciation might be different. Hence, additional methods may need to be used for complete speciation analysis. The samples were run untreated and undiluted since the concentration of tellurium in the solution was relatively low. However, this caused high peaks for other anions present in higher concentrations in the solution (OH^-, $B(OH)_4^-$, SO_4^{2-}, $S_2O_3^{2-}$). Samples were compared with standard solutions prepared from analytical grade chemicals. Te(IV) standard was prepared from sodium tellurite (Na_2TeO_3) and Te(VI) from H_6TeO_6. Figure 4.1.*2* presents the main results from the IC measurements. Tellurate, Te(VI) has a retention time of around 6 minutes. Tellurite, Te(IV), has a slightly longer retention time, however, in the IC system used, Te(IV) was determined indirectly from the negative peak in the chromatogram (Figure 4.1.*2* right). This is possibly due to high positive hydration tendency of the TeO_3^{2-} species resulting in lower conductivity. Moreover, the method was suitable for speciation analysis since only one or the other of the species was present in the sample and therefore no separation was required.

The results suggest that without $Na_2S_2O_3$, Te(IV) is oxidized to Te(VI) species under irradiation. In the prevailing conditions the species formed is most probably $HTeO_4^-$The oxidation explains the increase in solubility, since the Te(VI) species have significantly higher solubility than TeO_2. Oxidation is most likely due to the oxidizing water radiolysis products (e.g. H_2O_2, •OH) formed by the gamma radiation. In the reference samples TeO_2 dissolved as TeO_3^{2-} species as expected in such alkaline pH.

With sodium thiosulphate present, TeO_2 dissolves as the TeO_3^{2-} species in both the irradiated and the reference samples. However, change in the solid material was observed as a color change (Figure 4.1.*3*). This was further investigated using XRD analysis, see below.

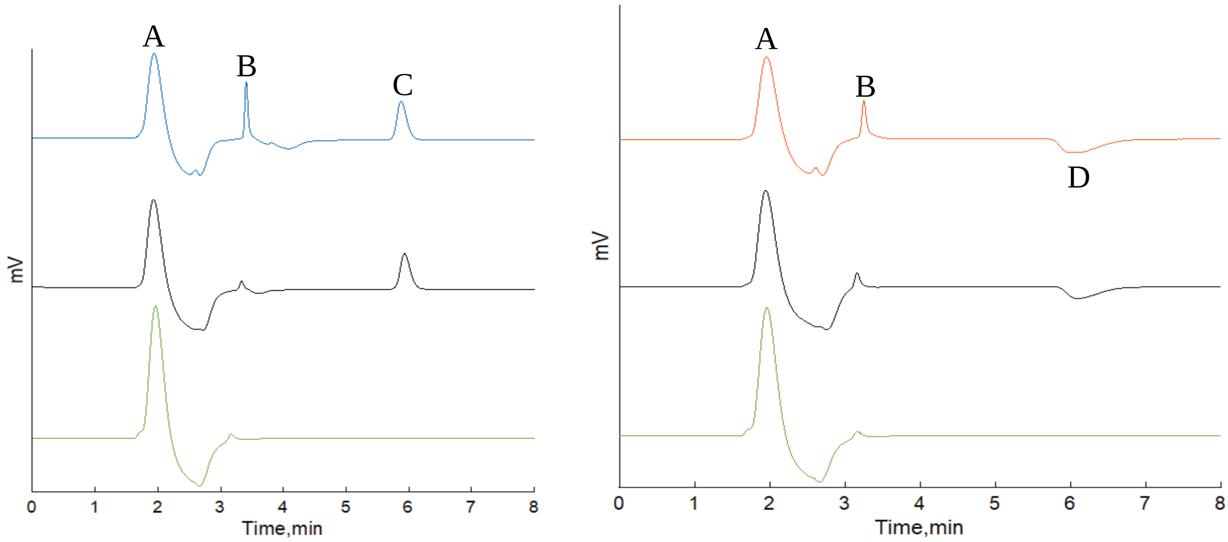

Figure 4.1.2 Ion chromatograms from tellurium speciation measurements in alkaline borate solution without (left) and ABS with (right) sodium thiosulphate. Bottom presents the solution matrix, middle is the respective tellurium standard and top is the irradiated TeO2 sample. Peaks: A. NaOH B. Borate C. Tellurate(VI) D. Tellurite(IV)

Solid speciation

The speciation of the solid material was investigated with XRD. The diffractograms for the irradiated sample in ABS with thiosulfate as well as for the corresponding reference sample are presented in Figure 4.1.*3*. The nonirradiated reference sample was identified as TeO_2, as expected. All of the main peaks and their intensities in the diffractogram corresponded to paratellurite TeO_2. The aforementioned color change can also be seen in Figure 4.1.*3*. The solid material in the irradiated sample with thiosulfate was silvery black in color and was identified as a mixture of paratellurite TeO_2 and elemental tellurium Te. The diffractogram of the irradiated sample had the same peaks corresponding to TeO_2 but had also signals characteristic to elemental Te. This indicates a reduction of Te(IV)O_2 to elemental Te(0) under irradiation in the presence of sodium thiosulfate.

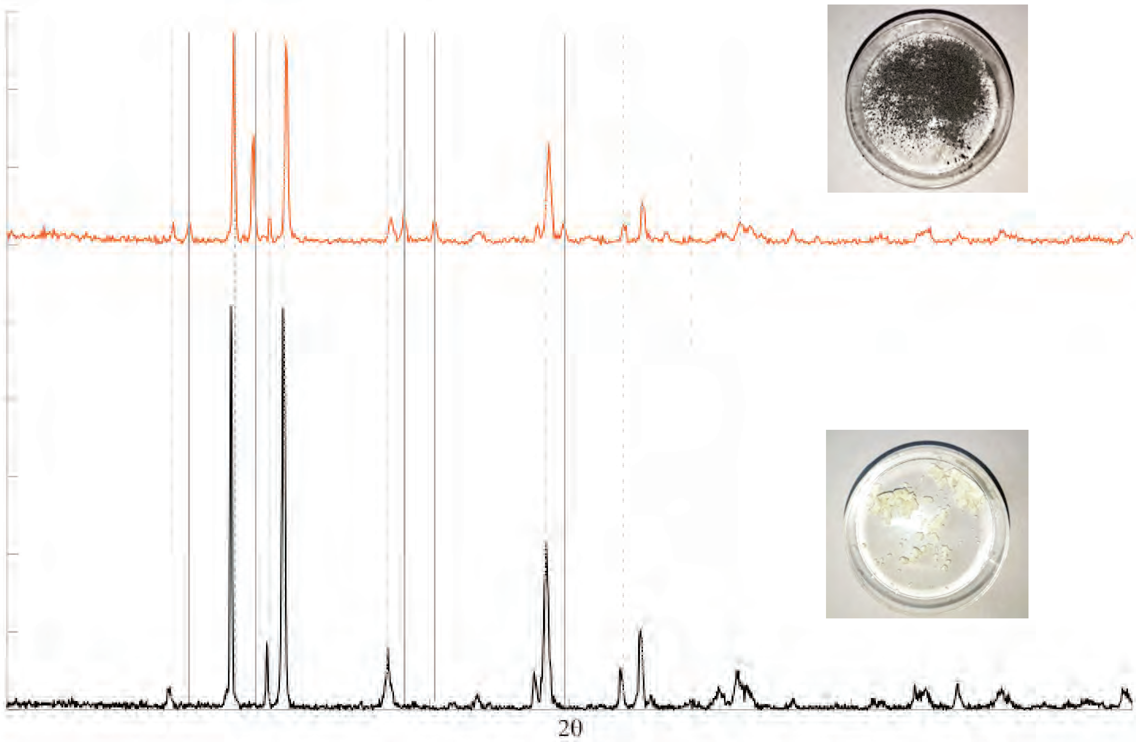

Figure 4.1.3 Diffractograms for TeO2 before (bottom) and after (top) irradiation. The solid lines mark the signals identified for elemental tellurium and the dashed lines the signals for TeO2

5.7.3. Conclusion

The containment sump chemistry was found to have an effect on tellurium solubility and speciation. Results show that tellurium dioxide solubility increased in alkaline borate solution under irradiation. This was due to oxidation of tellurium dioxide to more soluble telluric acid species. In alkaline borate solution with sodium thiosulfate, the solubility of tellurium dioxide decreased under irradiation. These results provide information on the behavior of tellurium during severe accident and guide the way to study possible further reactions of these tellurium species with for example other fission products and organic material that may be important for source term estimations.

5.8 Summary

The research at Chalmers during the APRI10 has been mainly focused on tellurium chemistry and behavior during severe nuclear accident. Experiments have aimed to provide information on the topics that have been previously overlooked, such as the effect of seawater cooling on the volatility, interactions with metal surfaces, effectiveness of the containment spray system and the radiation chemistry of tellurium in the sump. The results from all of the experiments have provided valuable data that has been compiled into scientific publications. Chalmers has also been active in collaborative research with other institutes and these collaborations has been successful and will potentially continue in the future.

5.9 References

[ALO91] A. Alonso and C González. Modelling the chemical behaviour of tellurium species in the reactor pressure vessel and the reactor cooling system under severe accident conditions. Report. EUR–13787. Commission of the European Communities (CEC), The Joint Research Centre, 1991.

[BEA86] E.C. Beahm. Tellurium behavior in containment under light water reactor accident conditions. Report. NUREG/CR–4338. Oak Ridge National Lab., TN (USA), 1986.

[BOW86] B.R. Bowsher, S. Dickinson, A.L. Nichols, R.A. Gomme, and J.S. Ogden. “The chemical form of fission product telluriumin a severe reactor accident”. In: Symposium on chemical phenomena associated with radioactivity releases during severe nuclear plant accidents; Anaheim, CA (USA); 8-12 Sep 1986. CONF-860938-. Washington DC, USA: American Chemical Society, Division of Nuclear Chemistry and Technology, 1986.

[BOE97] R. de Boer and E.H.P. Cordfunke. “The chemical form of fission product tellurium during reactor accident conditions”. In: Journal of Nuclear Materials 240.2 (1997), pp. 124 –130. ISSN: 0022-3115. DOI: 10.1016/S0022-3115(96)00600-9.

[BOE95] R. de Boer and E.H.P. Cordfunke. “Reaction of tellurium with Zircaloy-4”. In: Journal of Nuclear Materials 223.2 (1995), pp. 103 – 108. ISSN: 0022-3115. DOI: 10.1016/0022-3115(95)00005-4.

[NEA] CSNI, “Insights into the control of the release of iodine, cesium, strontium and other fission products in the containment by severe accident management.” NEA/OECD, Paris (2000).

[COL87] J.L. Collins, M.F. Osborne, and R.A. Lorenz. “Fission Product Tellurium Release Behavior Under Severe Light Water Reactor Accident Conditions”. In: Nuclear Technology 77.1 (1987), pp. 18–31. DOI: 10.13182/NT87-A33948.

[DUT66] W.A. Dutton andW.C. Cooper. “The Oxides and Oxyacids of Tellurium”. In: Chemical Reviews 66.6 (1966), pp. 657–675. DOI: 10.1021/cr60244a003.

[DÖR10] L.A. Ba, M. Döring, V. Jamier, and C. Jacob. “Tellurium: an element with great biological potency and potential”. In: Organic & biomolecular chemistry 8.19 (2010), 4203-4216. DOI: 10.1039/c0Ob00086h.

[GAR82] F. Garisto. Thermodynamics of Iodine, Cesium and Tellurium in the Primary Heat Transport System Under Accident Conditions. Report. AECL-7782.

[HIL&POST] Hilliard, R.K., Postma, A.K., McCormack, J.D. and Coleman, L.F., 1971. Removal of iodine and particles by sprays in the containment systems experiment. Nuclear Technology, 10(4), pp.499-519.

[IMO88] S. Imoto and T. Tanabe. “Chemical state of tellurium in a degraded LWR core”. In: Journal of Nuclear Materials 154.1 (1988), pp. 62 – 66. ISSN: 0022-3115. DOI: 10.1016/0022-3115(88)90119-5.

[JON88] I. Johnson and C.E. Johnson. “Mass spectrometry studies of fission product behavior: I. Fission products released from irradiated LWR fuel”. In: Journal of Nuclear Materials 154.1 (1988), pp. 67 –73. ISSN: 0022-3115. DOI: 10 . 1016 / 0022 - 3115(88) 90120-1.

[Joyce] W. E. JOYCE, “Sodium Thiosulfate Spray System for Radioiodine Removal,” Nucl. Technol. **10** 4, 444 (1971); https://doi.org/10.13182/NT71-A16254.

[JON15] A.V. Jones, R. Zeyen, and M. Sangiorgi. Circuit and Containment Aspects of PHÉBUS Experiment FPT0 and FPT1. EUR 27218. Publications Office of the European Union, 2015. DOI: 10.2790/740439.

[KAN15] Y. Kanai. “Geochemical behavior and activity ratios of Fukushima-derived radionuclides in aerosols at the Geological Survey of Japan, Tsukuba, Japan”. In: Journal of Radioanalytical and Nuclear Chemistry 303.2 (2015), pp. 1405–1408. DOI: 10.1007/s10967-014-3495-1.

[LOR83] R.A. Lorenz, E.C. Beahm, and R.P. Wichner. “Review of tellurium release rates from LWR fuel elements under accident conditions”. In: (1983). Proceedings of the International meeting on light-water reactor severe accident evaluation, Cambridge, Mass., Aug. 28-Sept. 1.

[MCF96a] J. McFarlane and J.C. Leblanc. “Fission-Product Tellurium and Cesium Telluride Chemistry Revisited”. In: Geochimica et Cosmochimica Acta (1996). (AECL–11333), Canada., pp. 851–866. ISSN: 0067-0367.

[MCF96b] J. McFarlane. “Fission product tellurium chemistry from fuel to containment”. In: Proceedings of the Fourth CSNI Workshop on the Chemistry of Iodine in Reactor Safety (1996). (PSI–97-02). Guentay, S. (Ed.). Switzerland, pp. 563–585.

[MAG15] J. Magill, G. Pfenning, R. Dreher, and Z. Sòti. Karlsruher Nuklidkarte, 7th ed. 2015.

[Moriyama] Moriyama, H., Fujiwara, I. and Nishi, T., 1980. Radiation-induced reactions of antimony and tellurium compounds in sulfuric acid solutions. The Journal of Physical Chemistry, 84(14), pp.1801-1805.

[NEEB] K-H. NEEB, The radiochemistry of nuclear power plants with light water reactors. Walter de Gruyter, (2011); https://doi.org/10.1515/9783110812015.

[PARSLY] L.F. PARSLY, “Spray Program at the Nuclear Safety Pilot Plant.” Nucl. Technol. 10 4, 472 (1971); https://doi.org/10.13182/nt71-a16259.

[POT85] P.E. Potter, M.H. Rand, and C.B. Alcock. “Some chemical eouilibria for accident analysis in pressurised water reactor systems”. In: Journal of Nuclear Materials 130 (1985), pp. 139 –153. ISSN: 0022-3115. DOI: 10.1016/0022-3115(85)90303-4.

[RUM20] “Composition of Seawater and Ionic Strength at Various Salinities”. In: CRC Handbook of Chemistry and Physics. Ed. by J. R. Rumble. 101st Edition (Internet Version 2020). Boca Raton, FL.: RC Press/Taylor & Francis.

[SAL84] R.A. Sallach, C.J. Greenholt, and A.R. Taig. Chemical interactions of tellurium vapors with reactor materials. NUREG/CR–2921. 1984.

[SAN15] M. Sangiorgi, A. Grah, and L. Ammirabile. Circuit and Containment Aspects of PHÉBUS Experiment FPT-2. EUR 27631. Publications Office of the European Union, 2015. DOI:10.2790/94418.

[TAY96] A. Taylor. “Biochemistry of tellurium”. In: Biological Trace Element Research 55.3 (1996), 231–239. DOI: 10.1007/BF02785282.

[PON10] Y. Pontillon and G. Ducros. “Behaviour of fission products under severe PWR accident conditions: The VERCORS experimental programme—Part 2: Release and transport of fission gases and volatile fission products”. In: Nuclear Engineering and Design 240.7 (2010), pp. 1853 –1866. ISSN: 0029-5493.

[GLÄ04] H. Glänneskog. “Interactions of I2 and CH3I with reactive metals under BWR severe accident conditions”. In: Nuclear Engineering and Design 227.3 (2004), pp. 323 –329. ISSN: 0029-5493. DOI: 10.1016/j.nucengdes.2003.11.008.

[GLÄ06] H. Glänneskog, J.O. Liljenzin, and L Sihver. “Reactions between reactive metals and iodine in aqueous solutions”. In: Journal of Nuclear Materials 348.1 (2006), pp. 87 –93. ISSN: 0022-3115. DOI: 10.1016/j.jnucmat.2005.09.004.

[HOL09] J. Holm, H. Glänneskog, and C. Ekberg. “Deposition of RuO4 on various surfaces in a nuclear reactor containment”. In: Journal of Nuclear Materials 392.1 (2009), pp. 55–62. ISSN: 0022-3115. DOI: 10.1016/j.jnucmat.2009.03.047.

[SEH12] “Fission Product Release and Transport”. In: Nuclear Safety in Light Water Reactors: Severe Accident Phenomenology. Ed. by B.R. Sehgal. 1st ed. Boston: Academic Press, 2012. Chap. 5, pp. 426–517. ISBN: 978-0-12-388446-6. DOI: 10.1016/B978-0-12-388446-6.00005-8.

[RUM19] “Physical Constants of Inorganic Compounds”. In: In CRC Handbook of Chemistry and Physics. Ed. by J.R. Rumble. 100 (Internet Version 2019. CRC Press/Taylor & Francis, Boca Raton, FL. Chap. 5.

[MAT94] Y. Matsuda, H. Anada, and H. E. Bishop. “^{18}O tracer study of the oxidation of zircaloy-4 in steam”. In: Surface and Interface Analysis 21.6-7 (1994), pp. 349–355. DOI: 10.1002/sia.740210605.

[MAL70] A. P. Malinauskas, J. W. Gooch Jr., and J. D. Redman. “The Interaction of Tellurium Dioxide andWater Vapor”. In: Nuclear Applications and Technology 8.1 (1970), pp. 52– 57. DOI: 10.13182/NT70-A28633.

[KON90] R.J.M. Konings, E.H.P. Cordfunke, and V . Smit-Groen. “The vapour pressures of hydroxides II. TeO(OH)2”. In: The Journal of Chemical Thermodynamics 22.8 (1990), pp. 751 –756. ISSN: 0021-9614. DOI: 10.1016/0021-9614(90)90066-Y.

[ELR91] R.M. Elrick and A.L. Ouellette. Interaction of Tin Telluride and Cesium Hydroxide With Reactor Materials in Steam. SAND-89-2504, UC - 501. 1991.

[KAJ16] I. Kajan, H. Lasseson, I. Persson, and C. Ekberg. “Interaction of ruthenium tetroxide with surfaces of nuclear reactor containment building”. In: Journal of Nuclear Science and Technology 53.9 (2016), pp. 1397–1408. DOI: 10.1080/00223131.2015. 1120245.

[GRE97] “16 - Kajan, Tellurium and Polonium”. In: Chemistry of the Elements. Ed. by N.N. Greenwood and A. Earnshaw. Second Edition. Oxford: Butterworth-Heinemann, 1997, pp. 747 –788. ISBN: 978-0-7506-3365-9. DOI: 10.1016/B978-0-7506-3365-9.50022-5.

[KÄR06] T. Kärkelä, U. Backman, A. Auvinen, R. Zilliacus, M. Lipponen, T. Kekki, U. Tapper, and J. Jokiniemi. “Experiments on the behaviour of ruthenium in air ingress accidents”. English. In: SAFIR: The Finnish Research Programme on Nuclear Power Plant Safety 2003-2006. VTT Tiedotteita - Research Notes 2363. Finland: VTT Technical Research Centre of Finland, 2006, pp. 253–262. ISBN: 951-38-6886-9.

[KÄR17] T. Kärkelä, I Kajan, U Tapper, A. Auvinen, and C. Ekberg. “Ruthenium transport in an RCS with airborne CsI”. In: Progress in Nuclear Energy 99 (2017), pp. 38 –48. ISSN: 0149-1970. DOI: 10.1016/j.pnucene.2017.04.019.

[ITK96] V.P. Itkin and C.B. Alcock. “The O-Te (oxygen-tellurium) system”. In: Journal of Phase Equilibria 17.6 (1996), pp. 533–538. DOI: 10.1007/BF02666000.

[Vlaev] Vlaev, L.T. and Georgieva, V.G., 2004. Activation energy for electroconduction of aqueous solutions of sulfuric and selenic acids and potassium tellurate. Russian Journal of Electrochemistry, 40(6), pp.674-678.

6. UPPFÖLJNING AV KÄRNKRAFTSOLYCKAN I FUKUSHIMA DAIICHI

Inom ramen för APRI-projektet ingår en bevakning och uppdatering av kunskapsläget och anläggningsstatus med anledning av de svåra haverierna i Fukushima Daiichi. Viktiga syften med bevakningen är en generellt ökad förståelse för svåra haverifenomen och frågor kopplade till detta, men även en utvärdering om ny kunskap från Fukushima påverkar den svenska haverihanteringsstrategin. Det har hittills inte framkommit något från bevakningen av Fukushimaolyckorna som har lett till någon förändring av den svenska haverihanteringsstrategin, utan snarare har strategin bekräftats av vad som framkommit från Fukushima.

Slutrapporten för APRI-9 [1] innehöll en beskrivning av anläggningsstatus för de skadade reaktorerna, bästa kunnande avseende haveriförloppen, provtagningar och status kring bränslebassängerna. Uppdateringen av händelserna i Fukushima i föreliggande rapport kommer att fokusera vad som har framkommit sedan APRI-9 avseende förnyad och fördjupad förståelse för haveriförloppet i de tre skadade reaktorerna med ugångspunkt från OECD-NEA:s rapport *Benchmark Study of the Accident at the Fukushima Daiichi Nuclear Power Plant (BSAF) phase 2* samt från aktuell information från TEPCO. Beskrivningen startar vid snabbstoppet till följd av jordbävningen och avslutas vid tidpunkten för ventilering av inneslutningen eller vätgasexplosionerna i reaktorbyggnaden, dvs. beskrivningen fokuserar på de inledande dygnen av händelserna.

6.1 Uppdatering haveriförlopp

6.1.1. Reaktor 1

I [1] diskuteras utestående osäkerheter i haveriförloppet för reaktor 1 och hit hör bland annat att ventillägena för hjälpkondensorn är oklara vid tidpunkten för elbortfallet samt att det råder osäkerheter huruvida operatörerna lyckades använda hjälpkondensorn i någon utsträckning alls. Ambitionen i följande stycke är att klargöra mer kring vad som är känt eller fortfarande okänt avseende haveriförloppet i reaktor 1 och hanteringen av hjälpkondensorn.

Fukushima Daiichi reaktorblock 1 (1F1) var vid tidpunkten för jordbävningen, fredagen den 11:e mars 2011 klockan 14:46, i full effekt, 460 MW elektrisk. Jordbävningen medförde snabbstopp av reaktorn och kraftförsörjning via reservkraft (dieselgeneratorer). Kylning av resteffekten sköttes via dubbla hjälpkondensorer och etablerades automatiskt. Enligt operatörsinstruktioner från reaktorleverantören skulle nedkylningen begränsas till 55 °C per timme vilket medförde att operatörerna cykliskt stängde av och på kylningen och snart övergick till att endast använda en hjälpkondensor (IC subsystem A). Cirka 40 minuter efter jordbävningen och snabbstoppet slog de första tsunamivågorna in över anläggningen som skyddades av tsunamivallarna. Ytterligare tio minuter senare slog en andra tsunamivåg in med våghöjd på upp till 14-15 meter in vilket överskred tsunamiskyddet och sköljde över anläggningen som beroende på utrymme dränktes i meterhögt vatten. Vattenmassorna slog ut bland annat ställverk, batteriskenor, dieselgeneratorer och reaktorn förlorade i samband med tsunamin både reservkraft och matningsvägar. En kort stund därefter förlorades även batterikraften och personalen förlorade möjligheterna att övervaka viktiga anläggningsparametrar som vattennivå i reaktortanken, tryck i primärsystemet, ventillägen och tillgängliga säkerhetssystem. Operatörerna hade inga instruktioner eller riktlinjer för den rådande situationen och fick börja improvisera den fortsatta haverihanteringen. Efter jordbävningen men innan tsunamin slog in kyldes resteffekten bort, som nämnts ovan, via hjälpkondensorn. Efter att batteriskenor och instrumenteringen slogs ut av vattenmassorna från tsunamin lyckades kontrollrumspersonalen via improviserade lösningar koppla in bilbatterier för att bevaka nyckelparametrar avseende reaktorns tillstånd och runt 18:00 observerades på så sätt att hjälpkondensorn var isolerad från primärsystemet via de från inneslutningen sett utvändiga skalventilerna MO-2A och MO-3A, som var stängda, se Figur 1. Ventilerna skulle enligt reaktorkonstruktionen få stängasignal vid elbortfall och sannolikt har ventilerna gått till stängt läge i samband med att tsunamin slog ut elmatningen. Det har i föreliggande avrapportering inte gått att kartlägga vad som var känt kring driften av hjälpkondensorn i kontrollrummet för reaktor 1 respektive i anläggningens krisledningscentral (ERC – Emergency Response Center). Det finns motstridiga uppgifter att kontrollrumspersonalen efter elbortfallet har fått bekräftat från ERC att det kom ånga från hjälpkondensorns utblåsningsrör (vilket skulle bekräfta drift av hjälpkondensorn) medan ERC menar att de har fått driften av hjälpkondensorn bekräftad av kontrollrumspersonalen [4]. Krisledningscentralen var försedd med system som bevakade anläggningsparametrar, men det systemet hade också slagits ut av tsunamin och kommunikationen kring anläggningsstatus och parametrar sköttes därför muntligt. Klockan 18:18 den 11:e mars, dvs. strax efter att operatörerna har uppmärksammat att ventilerna är stängda, öppnade de ventilerna och konstaterade att ånga strömmar ut från utblåsningsröret. Strax därefter avstannar dock ångflödet och operatörerna tror då att hjälpkondensorn är tömd på vatten och stängde därför ventil MO-3A. Det har efteråt konstaterats att tanken var fylld till ungefär 65% (initial nivå var 80%) och avkokningen bedöms ha skett efter stängningen av MO-3A [5]. Notera även att kylning via hjälpkondensorn degraderas när reaktortrycket sjunker samt om icke-kondenserbara gaser, som vätgas, finns i primärsystemet.

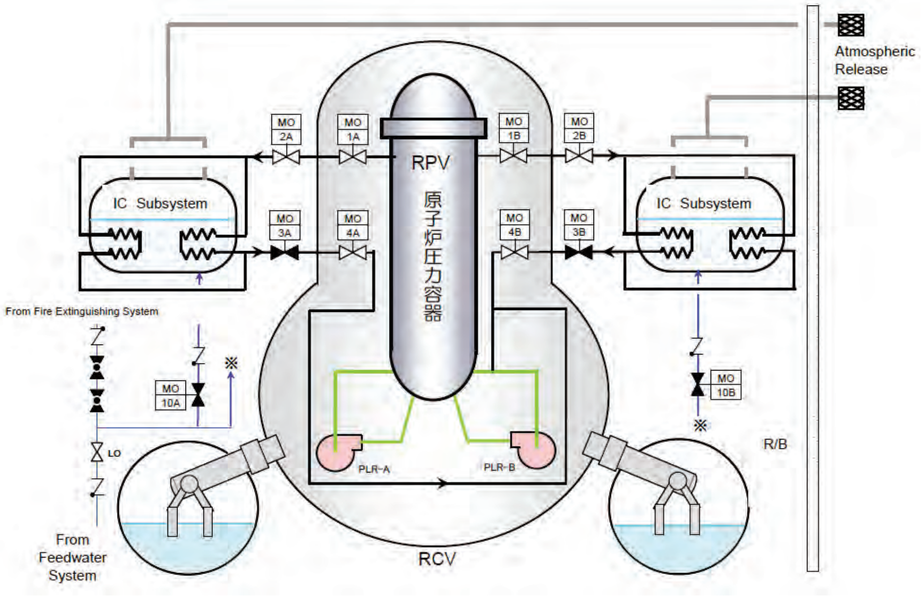

Figur 1 Hjälpkondensorsystemet 1F1 [4]

Ytterligare ett försök att kyla härden med hjälpkondensorn subsystem A gjordes kl. 21:30. Även denna gång strömmade ånga initialt ut, men ångflödet upphörde snart och ventilen stängdes åter. I detta läge bedöms härdskadorna vara ett faktum och vätgasproduktionen i primärsystemet kan förväntas ha degraderat hjälpkondensorns funktion. I samband med det andra försöket att etablera kylning via hjälpkondensorn uppmättes en hög strålnivå i reaktorbyggnaden, vilket indikerar att härdskador då hade påbörjats. Utöver möjligheterna att kyla härden via hjälpkondensorn fanns även en dieseldriven brandpump med egen vattenkälla (Diesel Driven Fire Protection, DDFP) ansluten till primärsystemet, samt möjligheten att ansluta en brandbil som via brandvattensystemet kunde kyla härden med hjälp av härdsprinklingen, se Figur 2.

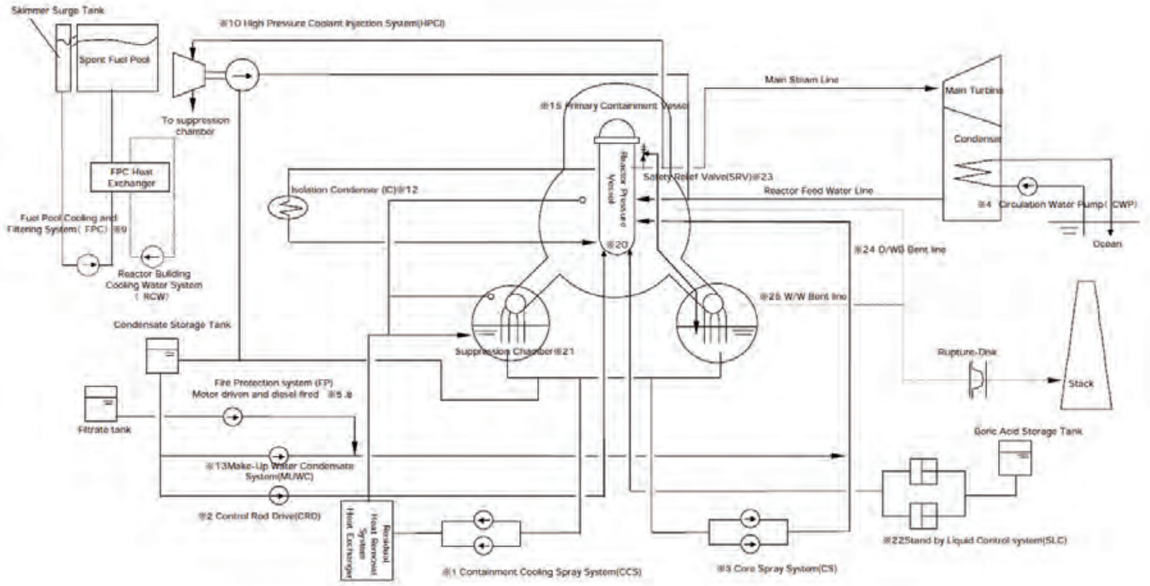

Figur 2 Schematisk skiss alternativa kylvägar Fukushima reaktor 1 [4]

På stationsområdet runt reaktor 1 fanns tre brandbilar, men efter ödeläggelsen visade sig endast en vara möjlig att använda. Parallellt med försöken att kyla härden via hjälpkondensorn beslutade krisledningscentralen kl. 17:12 om att förbereda vatteninpumpning till härden via brandbil. Ungefär samtidigt skickades personal ut till reaktorbyggnaden för att starta DDFP samt via manuella ventilmanövreringar förbereddes härdkylning genom vatteninpumpning från brandsystemet. Klockan 17:30 bekräftades att DDFP hade startat och klockan 20:50 rapporterades att nödvändiga ventilmanövreringar var genomförda för härdinpumpning med hjälp av DDFP. En förutsättning för att använda DDFP är dock att trycket i primärsystemet understiger 800 kPa, men vid tidpunkten för starten av DDFP var trycket runt 7,0 MPa vilket omöjliggjorde användandet av DDFP för härdinpumpning. Istället gjordes en tillfällig omläggning för påfyllning av hjälpkondensor subsystem A med vatten från DDFP vilket motiverade öppnandet av MO-3A kl 21:30, som nämnts ovan. Klockan 01:25 den 12:e mars skickas personal för att kontrollera driften av DDFP och det rapporterades 01:48 att DDFP hade stoppat. Försök att återstarta DDFP misslyckades och strategin att kyla härden via DDFP övergavs därmed. Den återstående strategin var att pumpa in vatten via brandbil och krisledningscentralen gav kl. 02:03 den 12:e mars order om att koppla in brandbil till reaktor 1. Cirka klockan 04:00 lyckades personalen vid reaktorn och kontraktsanställda ansluta vatteninpumpning till primärsystemet från den fungerande brandbilen via flänsar på utsidan av reaktorbyggnaden. Det hade då gått 12,5 timmar sedan tsunamin slog in mot anläggningen och elbortfallet som följde.

Den första inpumpningskampanjen medförde att cirka 1300 liter färskvatten pumpades in. En andra inpumpningskampanj påbörjades 05:46 och pågick i cirka 9 timmar med avbrott för påfyllande av färskvatten för inpumpning.

Figur 3 från [4] visar hur få mätdata som finns under förloppets första 12 timmar, då reaktortryck, inneslutningstryck och initialt vattennivå i härden uppmättes manuellt under stora svårigheter av operatörerna. Reaktortrycket kontrollerades två gånger (2011-03-11 kl. 20:07 samt 2011-03-12 kl. 02:45). Vid mätningen 2011-03-11 kl. 20:07 oscillerar visaren för trycket i primärsystemet kraftigt vilket har försvårat avläsning. Under tidsspannet 5 till 12 timmar efter att haveriet påbörjade skedde en trycknedtagning av primärsystemet. I BSAF2[10] diskuteras trycknedtagningen av primärsystemet och i studien ansätts antingen någon form av läckage från eller brott på primärsystemet. Sandia National Laboratory (SNL), som utvecklar Melcorkoden, har exempelvis utgått från ett ångledningsbrott vid 6,1 timmar till följd av heta gaser och högt reaktortryck vilket ger en momentan trycknedtagning, medan andra organisationer har antagit läckage i exempelvis genomföringar eller säkerhetsventiler på ångledningen, vilket medför en mer gradvis trycknedtagning av primärsystemet.

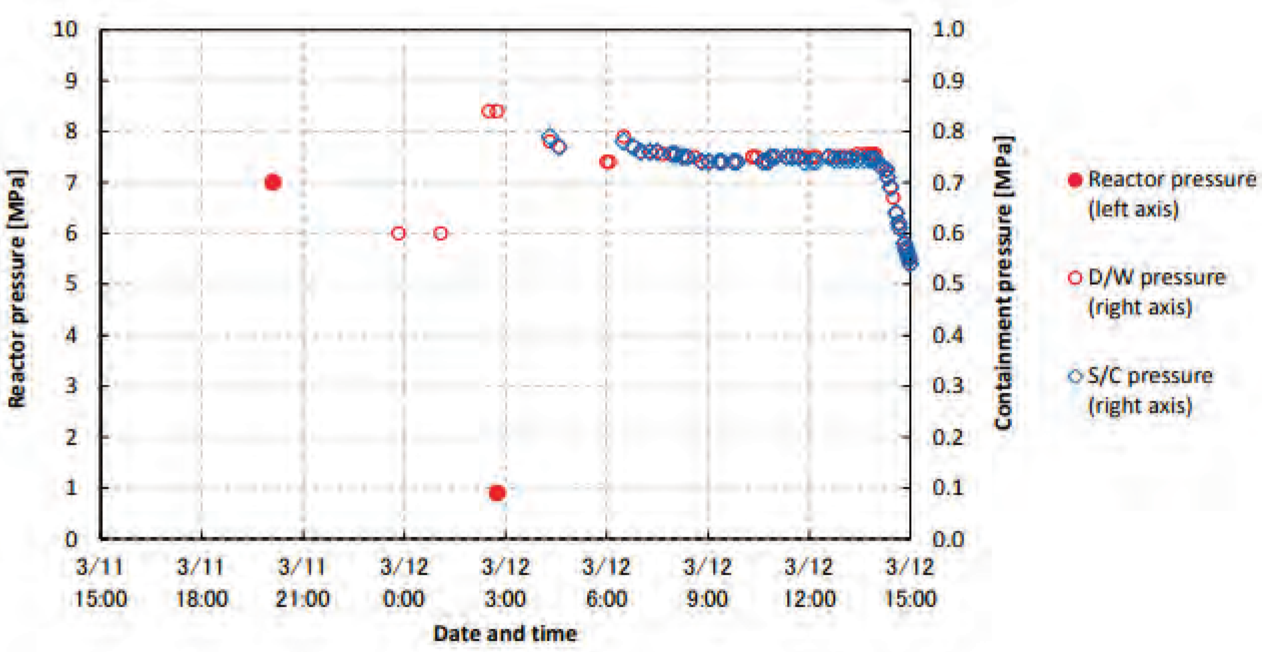

Figur 3 Tryck i primärsystemet 1F1 [4]

Den första avläsningen av trycket i reaktorinneslutningens primärutrymme gjordes klockan 23:50 den 11:e mars (dvs. 9 timmar in i förloppet), och det framgick då att inneslutningstrycket var på 0.6 MPa, vilket är högre än konstruktionstrycket 0,53 MPa [2]. I samband med avläsningen och konstaterandet att inneslutningstrycket översteg konstruktionstrycket gav områdesledaren order om att förbereda tryckavlastning av inneslutningen. Det högsta trycket i primärutrymmet i reaktor 1 uppmättes 02:30 och 02:45 den 12:e mars då trycket översteg 0,84 MPa och nästan låg i jämvikt med trycket i reaktortanken. Klockan 04:19 avlästes trycket igen i både primär och sekundärutrymmet och det framgick då att trycket hade

---

[10] BSAF2-studien är en internationell benchmark, som involverade 10 länder och 14 olika organisationer, avseende analyser av haveriförloppen i Fukushima Daichi 1-3 med olika integrala beräkningskoder

sjunkit utan några åtgärder från operatörerna sida. I BSAF2-studien kopplar finländska VTT och spanska CIEMAT de högsta uppmätta värdena i inneslutningstrycket till en genomsmältning av reaktortanken, medan franska IRSN och ryska IBRAE antar att tryckökningen beror på relokering av corium till nedre tankbotten. Japanska JAEA utgick ifrån att tankgenombrottet hade uppstått tidigare och att tryckökningen berodde på betongsmälta-reaktioner (MCCI) i inneslutningen. Det kan konstateras att stor osäkerhet råder kring när tankgenombrott kan ha uppträtt, vad som är orsaken till tryckhöjningen mellan första och andra avläsningen av inneslutningstrycket, samt när och hur effekterna av MCCI uppträder. Figur 4 visar simuleringar från BSAF2-studien.

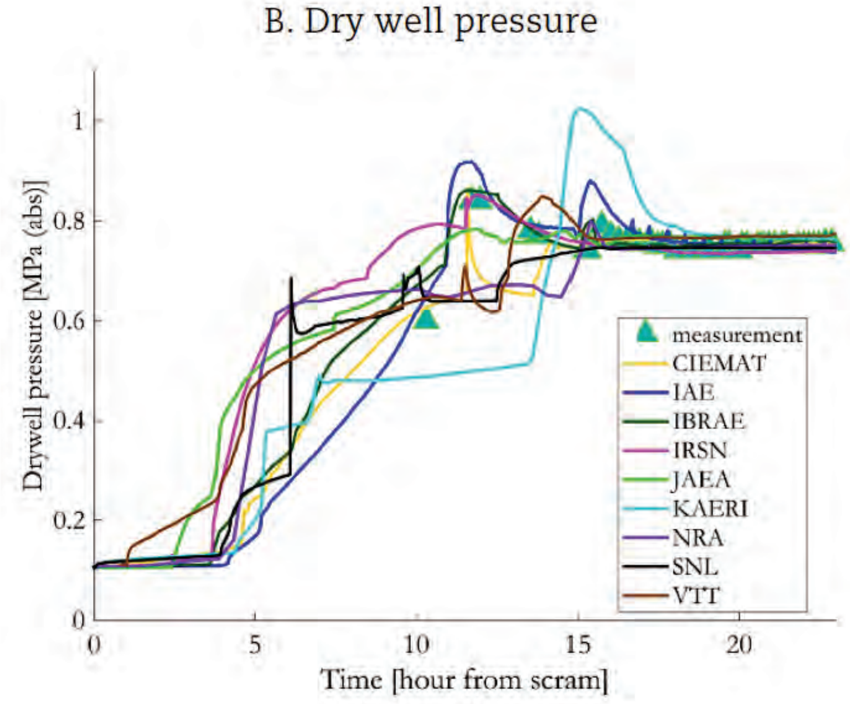

Figur 4 BSAF2-studien - tryck i primärutrymmet- 1F1 [2]

Den sänkning av trycket som skedde mellan klockan 02:45 och 04:19 den 12:e mars antyder att inneslutningens täthetsfunktion har brustit och att ett läckage har uppstått någonstans under förloppet, ett antagande som stärks av att aktivitet uppmättes vid huvudentrén strax efter. Även i BSAF2-studien antas att ett läckage har uppträtt, men att läckagets antal, storlek, placering och tidpunkt är okänt. Klockan 10:17, 10:23 och 10:24 den 12:e mars görs försök från kontrollrummet att manövrera den lilla ventilen till sekundärutrymmet för att ventilera inneslutningen, men personalen inte kunde nå fram till denna ventil (AO-90) pga. av höga strålnivåer. Däremot uppmättes en temporär aktivitetsökning vid huvudgrindarna runt kl. 10:40. Nya framgångsrika försök gjordes för att ventilera inneslutningen med hjälp att trycklyftstuber som kopplades till sekundärutrymmets stora ventil runt kl. 14:00 samma dag. Ånga som strömmade ur huvudskorstenen kunde observeras via kamera, och mellan kl. 14:30 och 14:50 sjönk inneslutningstrycket i primärutrymmet. Någon förhöjd aktivitet uppmättes däremot inte vid huvudgrinden, vilket antas bero på att vindarna låg ut mot havet. Nästan exakt ett dygn efter elbortfallet, kl. 15:36 den 12:e mars, förstördes reaktorbyggnaden i en våldsam vätgasexplosion. Även om läckagevägarna, mängden vätgas, huruvida det var en deflagration eller detonation och vad som triggade explosionen fortfarande är obekräftat finns analyser som väl beskriver vad som observerats, se exempelvis Attachment 1-10 till [4].

6.1.2. Reaktor 2

Fukushima Daiichi reaktorblock 2 (1F2) var vid tidpunkten för jordbävningen den 11:e mars 2011 i full effekt, 784 MW elektrisk. Jordbävningen medförde snabbstopp av reaktorn och kraftförsörjning via reservkraft (dieselgeneratorer). Kylning av resteffekten sköttes via RCIC som fick aktiveras manuellt två gånger eftersom systemet trippade automatiskt på hög nivå ”L-8” innan tsunamin. Den tredje och sista manuella aktiveringen av RCIC gjordes kl. 15:39 den 11 mars, bara två minuter innan tsunamin slog in. Logiken för RCIC var sådan att vid elbortfall så stannade ventiler i öppet läge, till skillnad från ventilerna till hjälpkondensorn i 1F1. Tack vare att RCIC hade startats precis innan tsunamin och elbortfallet kl. 15:41 var således RCIC i drift och inpumpning till reaktorn skedde via vatten från CST när batterikraft, reservkraft och kraftmatning föll bort (batterikraften försvann inte samtidigt som växelspänningen utan cirka 10 minuter senare i 1F2). Se Figur 5 för en schematisk bild över RCIC-systemet. Eftersom kraftförsörjningen hade slagits ut kunde dock RCIC inte kontrolleras eller nivåregleras. Vid kl. 22:00 den 11:e mars kunde de första avläsningarna av vattennivån i reaktortanken tillsammans med tryck i primärsystemet och inneslutningen göras vilket indikerade att vattennivån låg över högsta nivå L-8. Eftersom triplogiken inte fungerade pga. utebliven kraftförsörjning fortsatte driften av RCIC och det antas att vatten kan ha nått upp till ångledningarna och att RCIC:s turbin i så fall delvis har fungerat i tvåfasflöde. Vid drift i tvåfas kan RCIC ha självreglerat nivån i reaktortanken genom att sänka varvtalet då vatten blandats med ånga vilket gett lägre flöde på vatteninpumpningen och därigenom sänkt nivån. I samband med den första mätningen av anläggningsdata kl 22:00 den 11:e mars är trycket i primärsystemet strax över 6 MPa och vid en förnyad mätning runt 01:30 den 12:e mars har reaktortrycket sjunkit till 5,4 MPa.

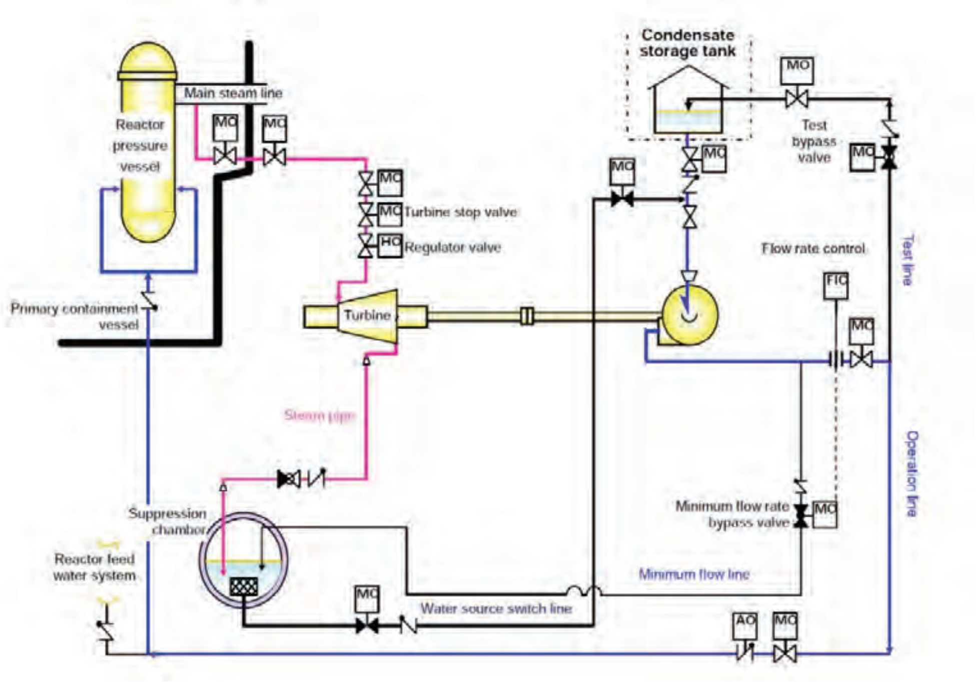

Figur 5 Schematisk bild över RCIC i 1F2 [4]

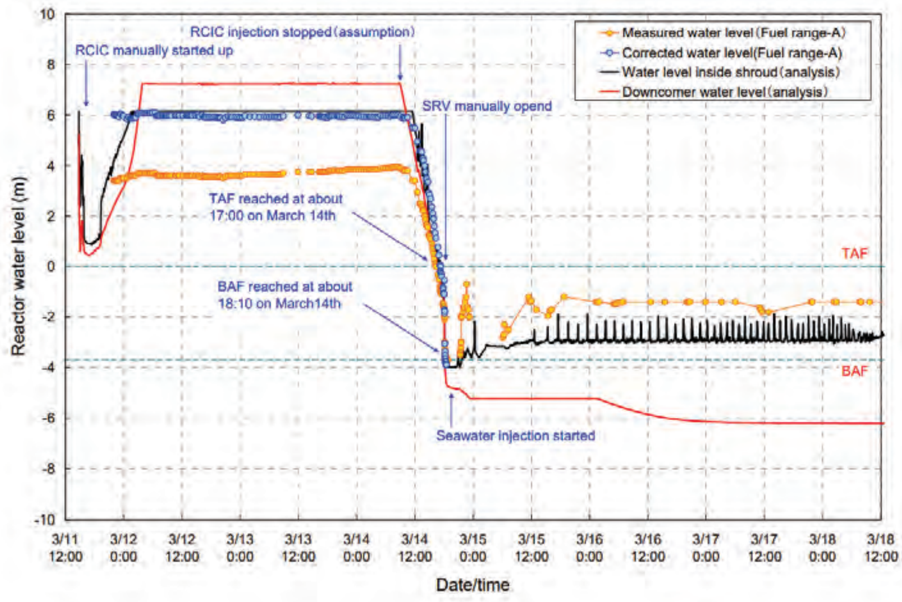

Figur 6 Vattennivå i reaktortanken 1F2 [2]

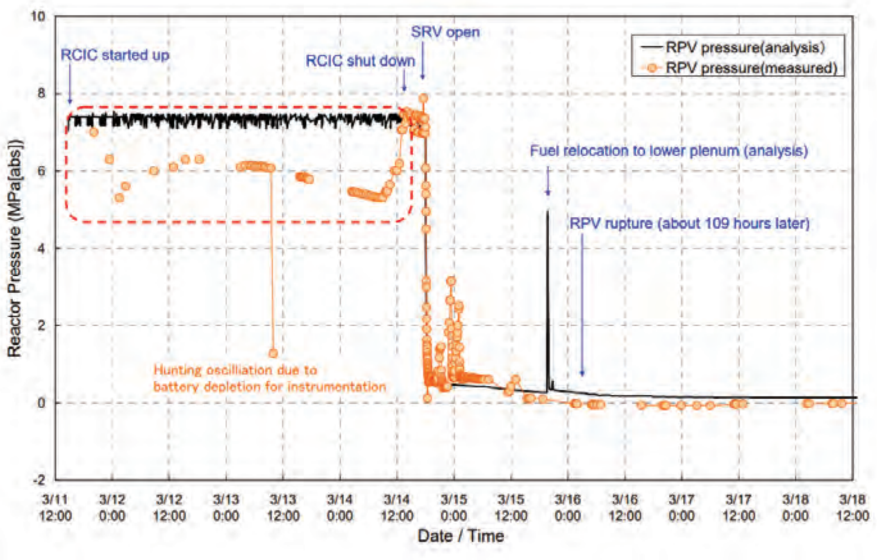

Figur 7 Tryck i primärsystemet 1F2 [4]

Möjliga orsaker till varför trycket i primärsystemet initialt hade en sjunkande trend och därefter stigande kan kopplas till att RCIC drevs okontrollerat och att det lägre trycket ledde till sänkt mättnadstemperatur. Energibalansen i reaktorn upprätthölls i detta skede utan att säkerhetsventilerna aktiverades. Strax efter klockan 03:00 den 12:e mars noterade operatörerna att CST hade låg nivå och det beslutas att koppla om RCIC från den betydligt kallare vattenkällan CST till recirkulation med kondensationsbassängen som vattenkälla. Omkopplingen görs klockan 04:20 samma morgon. Omkopplingen från CST till kondensationsbassängen bedöms inte ha med det stigande reaktortrycket att göra, och ligger dessutom fel i tid i förhållande till när reaktortrycket började stiga [4]. Trycket i reaktorinneslutningen uppvisade en långsammare tryckökning än vad som förväntades enligt analyserna. Resteffekten från reaktorn överfördes till inneslutningen via RCIC vilket förväntades leda till en tryckökning i reaktorinneslutningen eftersom kondensationsbassängen inte hade någon etablerad kylning. En teori som har förts fram är att torusrummet, dvs. utrymmet kring den torusformade kondensationsbassängen, vattenfylldes till halva kondensationsbassängens höjd i samband med att tsunamin slog in. Utrymmet har konstateras vara vattenfyllt och med hänsyn till läckage via kabelschakt etc. har det gjorts troligt att utrymmet blev vattenfyllt med en betydande höjd. Liknande observationer gjordes för övrigt i reaktor 4 (1F4), vilket stärker teorin. Vattenfyllningen av torusrummet tillförde en ytterligare värmesänka till inneslutningen som bidrog till en långsammare tryckuppbyggnad. Figur 8 beskriver inneslutningstrycket inklusive analysantaganden och kommentarer kring förloppet.

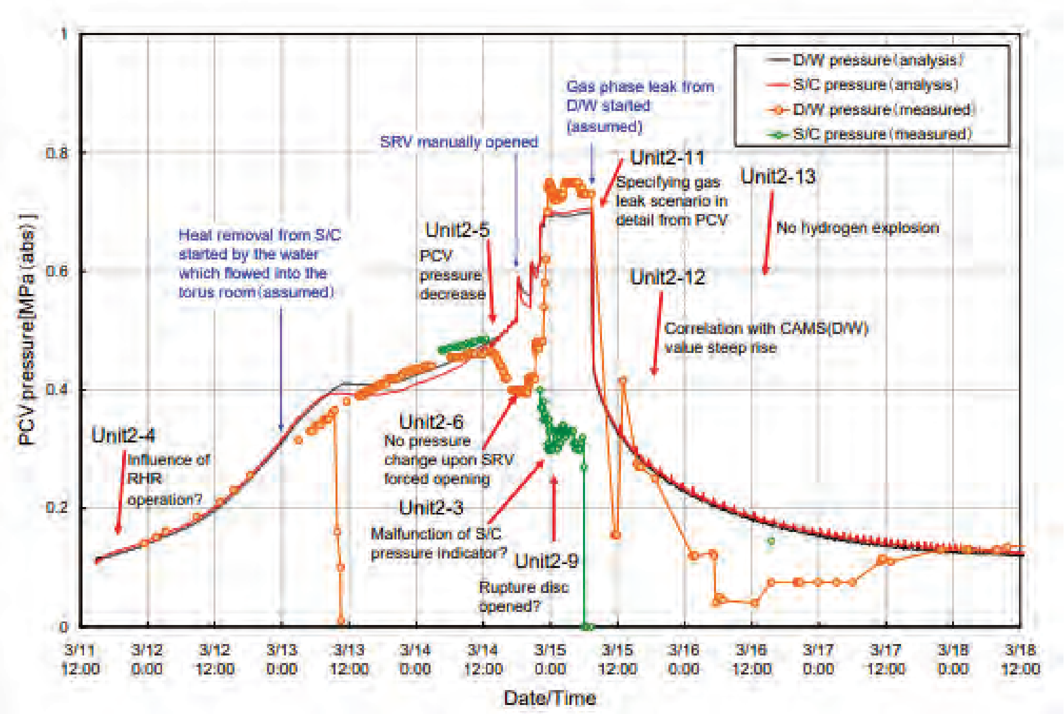

Figur 8 Inneslutningstryck 1F2 inklusive analys och kommentarer [4]

Runt kl. 06:00 den 13:e mars, knappt 40 timmar in i förloppet, började reaktortrycket sjunka igen. Fram till dess hade reaktortrycket varit stationärt genom den okontrollerade driften av RCIC. Det sänkta reaktortrycket i detta skede kan antas bero på den sjunkande resteffekten. Det lägsta reaktortrycket på 5,4 MPa uppmättes på morgonen kl. 09:00 den 14:e mars varvid trycket återigen började stiga. Samtidigt som reaktortrycket börjar stiga kan en sjunkande vattennivå i reaktortanken observeras. Runt 13-tiden den 14:e mars bedömdes RCIC ha stoppats efter över 70 timmars drift. Den exakta orsaken till varför RCIC avstannade är oklar, men en teori är att systemet trippade på högt varvtal. RCIC hade en mekanisk pådragsventil och tripfunktion som var kopplad till varvtalet. När RCIC hade avstannat steg reaktortrycket till 7,5 MPa och trycket låg sedan konstant på denna nivå genom cyklisk aktivering av en säkerhetsventil (SRV (A)). Inneslutningstrycket var vid denna tidpunkt under 0,5 MPa, dvs. ungefär i nivå med konstruktionstrycket på 0,48 MPa. Strax innan RCIC avstannar, kl 12:00, uppmättes en sänkning av trycket i inneslutningen. Orsaken till trycksänkningen är inte fastställd, men kan härröra från att RCIC slutade fungera och därigenom överföra energi från reaktortanken till inneslutningen i kombination med att vattnet i torusrummet ledde till ett sänkt tryck i inneslutningen genom att kyla kondensationsbassängen [4]. I samband med att RCIC konstaterades ha stannat gjordes istället försök att kyla härden genom inpumpning av havsvatten via brandbilar [6]. Försöken misslyckades då reaktortrycket var för högt och det beslutades därför att ta ner reaktortrycket med hjälp av trycknedtagningssystemet för att möjliggöra inpumpning via lågtrycksinpumpning. Nackdelen med trycknedtagning är att delar av vatteninventariet i reaktortanken går förlorat i ett redan mycket allvarligt tillstånd genom våldsam kokning då trycket tas ner. Klockan 18:00 den 14:e mars tas, efter svårigheter att samla ihop nödvändiga batterier, reaktortrycket ner genom öppnandet av en avblåsningsventil (oklart om en eller två ventiler har aktiverats) och sjunker snabbt till en nivå strax över trycket i reaktorinneslutningen. I samband med att trycket i primärsystemet sjönk startades inpumpning till reaktorn via brandbilssystemet. Ett uppehåll på cirka 30 minuter görs i inpumpningen kl. 19:20 för att fylla på bränsle till den dieseldrivna pumpen. Det är oklart hur mycket av det vatten som pumpades in som till slut nådde reaktorn, men med tanke på den fortsatta utvecklingen var inpumpningen uppenbarligen inte tillräcklig. Runt kl. 21:00, då avblåsningsventilen öppnas igen efter att tidigare ha stängts, noteras att vattennivån i reaktortanken har höjts, men det kan antas att mätningen i detta läge är opålitlig pga. kokning i referensbenet och att vattennivån visades ha för höga nivåer i förhållande till den faktiska situationen. I [2] är det konsensus att härdskador i 1F2 påbörjades 75 timmar efter snabbstoppet, dvs. i samband med trycknedtagningen kl. 18:00. I samband med att härdskador uppträder går förloppet i reaktortanken vidare in i ett skede som i [2] refereras till som ”three peak period”, se Figur 9 och Figur 10. Orsaken till tryckspikarna bedöms av deltagande organisationer ha olika orsaker men en gemensam bild är att det handlar om vätgasproduktion, härddegradering och nedsmältning, relokering av smälta till reaktortankbotten och tankgenomträngning.

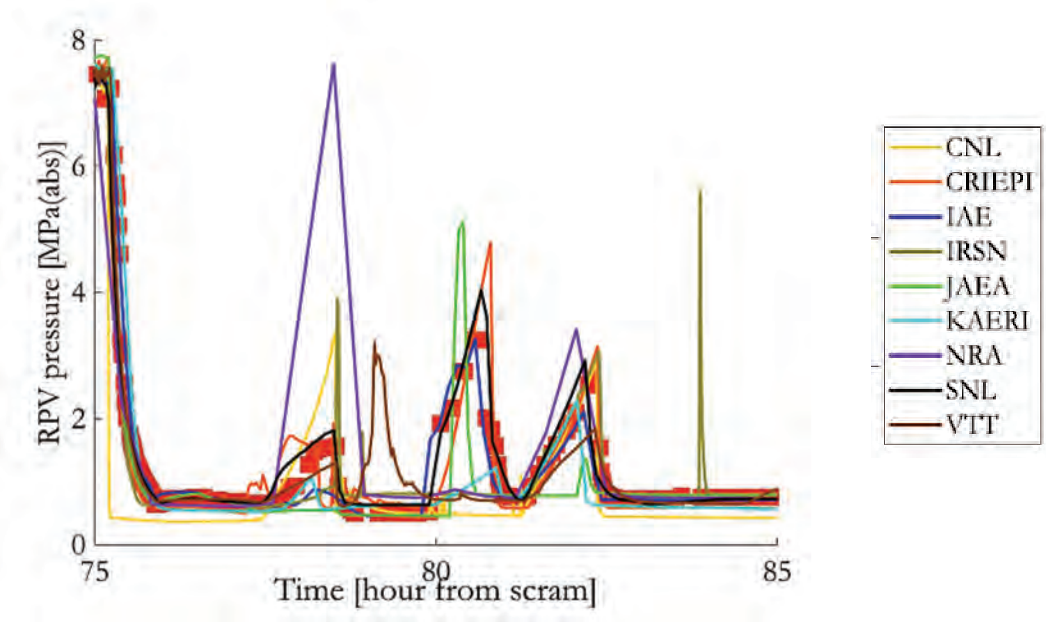

Figur 9 "Three peak period" i reaktortanken enligt BSAF2-studien [2]. 80 timmar motsvarar kl. 23:00 14:e mars.

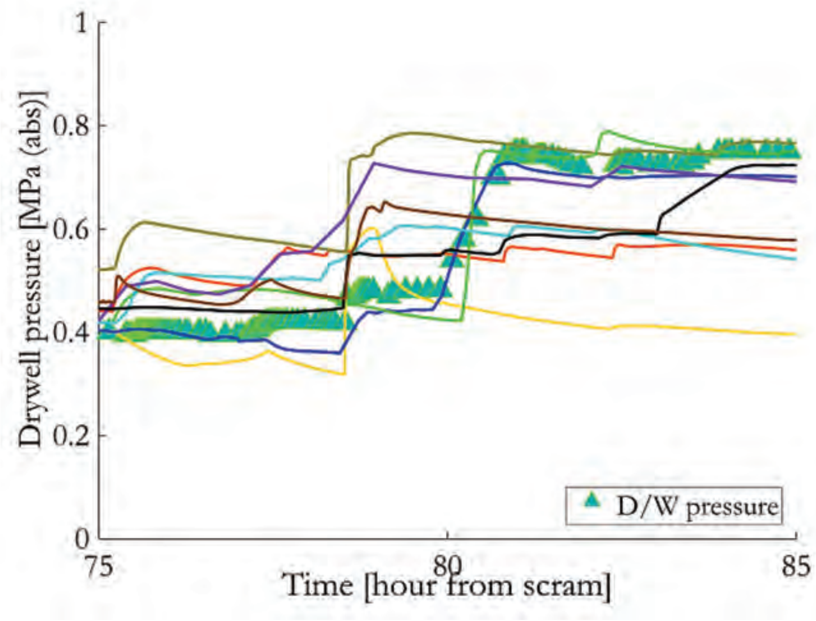

Figur 10 "Three peak period" i inneslutningen enligt BSAF2-studien [2]

Den första tryckspiken antas bero på vätgas- och ångproduktion och en motsvarande tryckökning kan även observeras i inneslutningstrycket. Den andra tryckspiken är betydligt högre och även i inneslutningstrycket noteras en motsvarande högre tryckspik. I simuleringarna har det antagits att avblåsningsventilen delvis har varit stängd. Tre organisationer (bland annat SNL) har i simuleringen lyckats fånga uppmätta värden förhållandevis väl och har antagit att tryckspiken beror på att härdsmälta faller ner i reaktortankbotten. Dock har den uppmätta tryckökningen i inneslutningen inte lyckats beskrivas i simuleringen. Den japanska teknikorganisationen CRIEPI antar att tryckökningen beror på vatteninpumpning till härden som antas vara i ett intakt skick. I den tredje tryckspiken har det antagits att avblåsningsventilen är helt stängd då någon motsvarande tryckspik inte kan observeras i inneslutningen. Nästan alla organisationer har lyckats fånga tryckspiken väl i simuleringarna. Tryckspiken antas bero på att härdrester har fallit ner i reaktortankbotten som var vattenfylld efter vatteninpumpning via brandbil. I detta läge bedöms reaktortanken fortfarande vara intakt. I ett led att kontrollera trycket i reaktortanken och möjliggöra vatteninpumpning så öppnades avblåsningsventiler kl. 21:00 den 14:e mars (som nämnts ovan) och kl. 01:10 den 15:e mars.

Det högsta inneslutningstrycket på 0,75 MPa uppmättes knappt 81 timmar efter snabbstoppet, dvs. runt midnatt mellan 14:e och 15:e mars. Dagen innan, klockan 13:00 den 13:e mars hade en tryckluftsstyrd ventil till inneslutningens tryckavlastning öppnats, sånär som på ett sprängbleck, för att möjliggöra tryckavlastning om behovet skulle uppstå. I samband med vätgasexplosionen i reaktor 3 runt kl. 11:00 den 14:e mars verkar ventilen ha gått till stänga-läge, även om det inte finns bekräftat att avlastningsledningen var korrekt uppställd med avseende på ventillägen innan explosionen. Efter midnatt och på morgonen den 15:e mars försökte personalen åter öppna avlastningsledningen från kondensationsbassängen och i ett senare skede även från inneslutningens primärutrymme utan att lyckas. Det förefaller som om sprängblecket i 1F2 inte har fungerat som avsett. Runt kl. 08:00 den 15:e mars, 89 timmar efter snabbstopp och när inneslutningstrycket låg runt 0,75 MPa så upphör tryckmätningarna i reaktortank och inneslutning. När mätningarna återupptas cirka 93 timmar efter snabbstopp (runt kl. 12:00 den 15:e mars) har inneslutningstrycket i primärutrymmet sjunkit till under 200 kPa. Någon timme därefter ökar trycket i primärsystemet igen tillsammans med en tryckökning i reaktortanken som påbörjats någon timme innan. Orsaken till den tryckökningen är oklar. Klockan 06:14 den 15:e mars hörs ett högt oidentifierat oljud och därefter sjönk trycket i sekundärutrymmet, och tryckgivaren i sekundärutrymmet visar efter ett tag 0 Pa vilket antyder att den har fallerat. Nästan samtidigt sker vätgasexplosionen i 1F3: reaktorbyggnad och det är oklart om oljudet som hördes i 1F2 härrör från den explosionen eller från en separat händelse. Trycket i primärutrymmet sjönk i samband med oljudet från 733 kPa till 155 kPa runt kl. 11:30.

6.1.3. Reaktor 3

Fukushima Daiichi reaktorblock 3 (1F3) var vid tidpunkten för jordbävningen den 11 mars 2011 i full effekt, 784 MW elektrisk. Efter snabbstopp av reaktorn som följde på jordbävningen sköttes kraftförsörjningen av reaktorn via reservkraft (dieselgeneratorer) och operatörerna försökte föra reaktorn till kallt avställt läge med hjälp av RCIC-systemet. När tsunamin sköljde in slogs yttre nät och reservkraften ut, dvs. totalt bortfall av all växelspänning. Till skillnad från reaktor 1 och 2 slogs inte batterimatningen ut och ventilmanövreringar etc. kunde utföras samt anläggningsdata övervakas. Således finns mätdata tillgängliga för hela förloppet som det utspelades i 1F3. Under de första 20 timmarna kyldes reaktorn med RCIC som överförde energin till kondensationsbassängen och inneslutningen. Tryckreglering sköttes via tryckavsäkringsventiler (SRV), se Figur 11, och vattennivån i reaktortanken hölls på en konstant nivå över härden. Under denna tid steg trycket i primärutrymmet monotont och mer än förväntat. Det antas att tryckökningen beror på termisk skiktning i kondensationsbassängen [2], se Figur 12. RCIC stoppade automatiskt kl. 11:36 den 12:e mars efter 20 timmars drift. RCIC har vid senare efterforskningar visats stoppa pga. hög temperatur i kondensationsbassängen, vilket i sin tur kan härledas till den termiska skiktningen som skedde i bassängen. Operatörerna försökte flera gånger återstarta RCIC, men lyckades inte. Eftersom kylning av reaktorn uteblev kokades kylmedel bort och vattennivån i reaktorn sjönk. Klockan 12:06 lyckades personalen etablera kylning av kondensationsbassängen med sprinkling via DDFP-systemet, vilket sänkte trycket i sekundärutrymmet så mycket att HPCI startades automatiskt på låg nivå ”L-2” vid kl. 12:35. För mer information om HPCI se Figur 13. Nödkylningssystemet HPCI lyckades etablera vattennivån och operatörerna övergick till manuell drift av HPCI för att inte utarma batterierna i onödan, en åtgärd som ingick i instruktionerna för elbortfall [6].

Trycket i primärsystemet sjönk efter att HPCI startades eftersom systemet förbrukar betydligt mer ånga än RCIC, och reaktortrycket hade sjunkit till ungefär 1 MPa kl. 19:00 den 12:e mars, se Figur 11. Set-värdet då HPCI trippar automatiskt pga. “low steam supply pressure” var 1,686 MPa, men systemet trippade aldrig. Det är oklart varför inte HPCI stoppades automatiskt på “low steam supply pressure”, men det antas att batterierna var slut vid tillfället. Nästan 36 timmar efter snabbstopp och 14 timmars drift stoppades HPCI manuellt kl. 02:42 den 13:e mars. En farhåga personalen hade och som, åtminstone delvis, motiverade stoppet av HPCI var att ett turbinhaveri skulle kunna leda till en utsläppsväg för aktivitet. Planen när HPCI stoppades manuellt var att istället använda DDFP för härdinpumpning. DDFP hade, som nämnts ovan, använts för att kyla kondensationsbassängen via sprinkling och skulle enligt planen kopplas om till härdinpumpning. På morgonen klockan 03:05 den 13:e mars fick kontrollrummet i 1F3 beskedet att omkopplingen av DDFP från sprinkling av kondensationsbassängen till härdinpumpning hade genomförts.

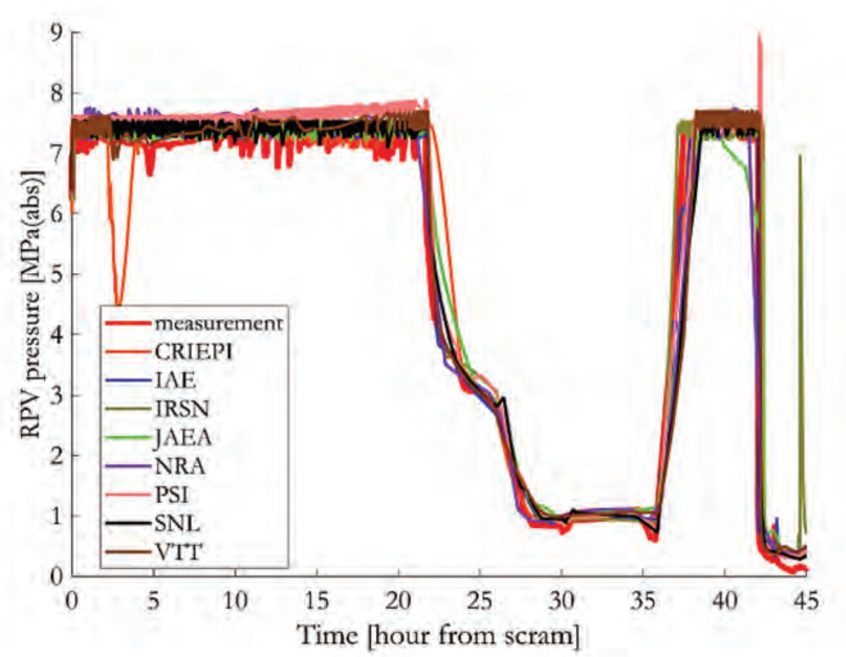

Figur 11 Reaktortryck 1F3 från BSAF2 [2]

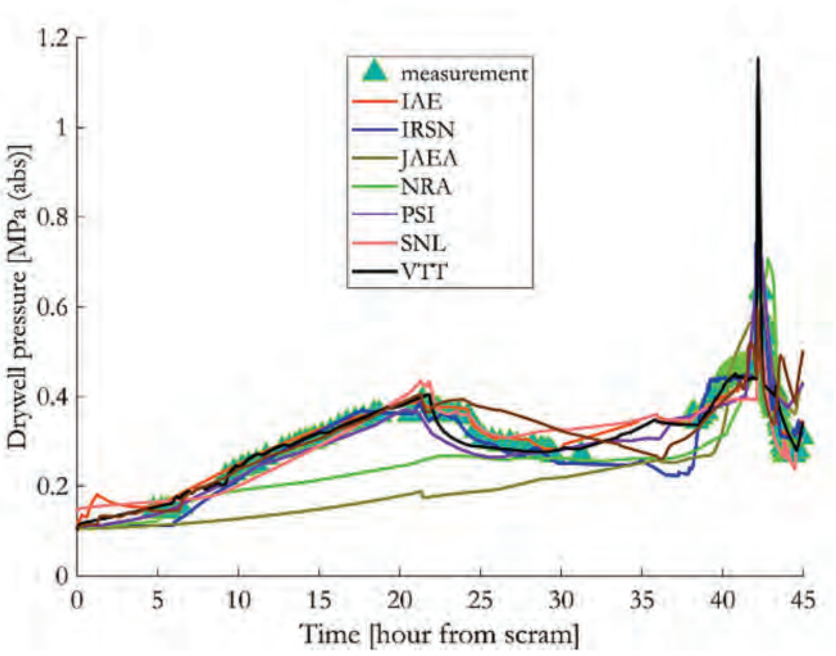

Figur 12 Inneslutningstryck 1F3 från BSAF2 [2]

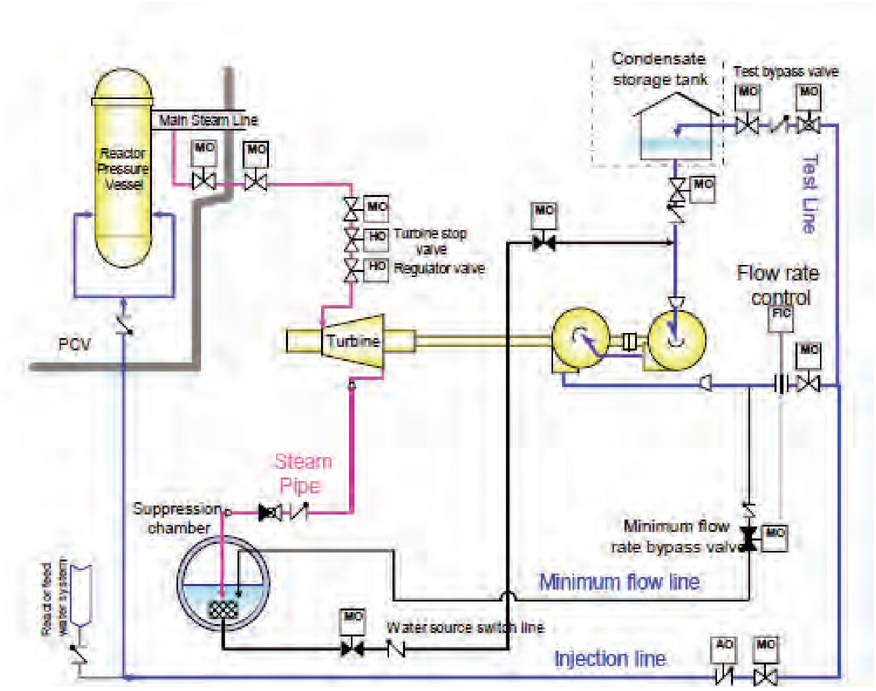

Figur 13 HPCI-systemet i 1F3 [3]

När HPCI stoppades steg reaktortrycket, se Figur 11. Operatörerna försökte sänka trycket med hjälp av trycknedtagningsventiler SRV, men misslyckades med dessa försök. Reaktortrycket fortsatte stiga över den nivå vid vilken DDFP-systemet kan pumpa in vatten i reaktorn vilket då omöjliggjorde kylning via alternativ vatteninpumpning AWI. Även flera försök att återstarta HPCI och RCIC gjordes utan framgång. HPCI gick inte att starta då batterierna var utarmade och i RCIC gick en trottelventil inte att lyfta från bottenläget vilket medförde att RCIC inte kunde startas upp. Personalen gjorde olika överväganden kring vilket system som borde prioriteras för att starta inpumpning i reaktorn och landade i att de bästa förutsättningarna fanns i att få igång DDFP och inpumpning via brandbil, men att detta krävde att reaktortrycket togs ner. Ett mödosamt arbete med att få tag i batterier som kunde användas för att aktivera avblåsningsventiler tog vid och vid en tidpunkt strax innan kl. 09:00 den 13:e april hade tillräckligt med batterier samlats ihop. Runt klockan 09:00 aktiverades trycknedtagningen och från kl. 09:25 etablerades härdinpumpning med färskvatten via brandbil. Det är oklart om aktiveringen av SRV berodde på operatörernas insats eller på tryckökningen i primärutrymmet som på något sätt kan ha aktiverat ADS och medfört att 6 ventiler öppnades [2]. Inpumpningen pågick till kl. 12:20 och fortsatte kl. 13:15 med inpumpning av havsvatten.

Redan runt lunchtid den 12:e mars hade den områdesansvariga beordrat förberedelser för att tryckavlasta inneslutningen eftersom trycket i inneslutningen kunde förväntas stiga då ingen inneslutningskylning var etablerad och resteffekten från reaktorn överfördes till inneslutningens kondensationsbassäng via RCIC och HPCI.
Runt 08:30 den 13:e mars meddelade berörd personal att tryckavlastningsledningen från inneslutningen var öppen sånär som på sprängblecket och klockan 09:20 kunde operatörerna se på instrumenteringen att trycket i inneslutningen började sjunka [3].
I samband med trycknedtagningen av primärsystemet kl. 09:00 ökade trycket i inne-

slutningen vilket ledde till att sprängblecket brast vid cirka 600 kPa inneslutningstryck och ånga samt icke-kondenserbara gaser ventilerades ut från sekundärutrymmet.

Tiden efter trycknedtagningen av primärsystemet och ventileringen av inneslutningen och innan vätgasexplosionen i 1F3 präglades av att operatörerna gjorde upprepade försök att pumpa in vatten i reaktorn via brandbil och upprepade ventileringar av inneslutningen genom att stänga och öppna ventilationsledningen. Vätgasexplosionen äger rum kl. 11:01 den 14:e mars, 68 timmar efter snabbstoppet. I samband med explosionen sjönk trycket i både reaktortank och inneslutningen kraftigt se Figur 14. Orsaken till tryckfallet är inte klarlagd.

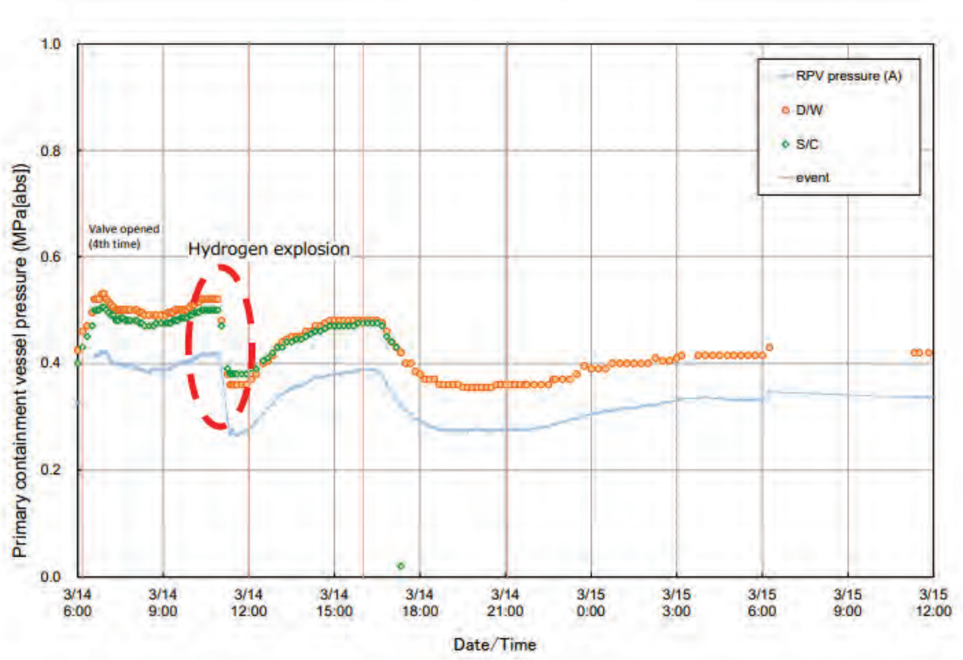

Figur 14 Trycksänkning i reaktortank och inneslutning 1F3 i samband med vätgasexplosion [4] Attachment 3-8

Efter att HPCI stannade kl. 02:42 den 13:e mars uppstod en period på ett flertal timmar innan inpumpning till reaktorn återupptogs. Kylmedlet kokades bort och trycket i reaktorn ökade. I BSAF2-studien så antas det att härdskadorna och haveriförloppet startade i detta tidsfönster. Två tryckspikar uppträder i både reaktortank och inneslutning vid 42 respektive 45 timmar (ungefär 08:40 respektive kl.12:00 den 13 mars), se Figur 15. I BSAF2 antas dessa tryckökningar vara kopplade till att härdrester faller till reaktortankbotten, och där en större mängd härdrester och smälta antas relokerat i den andra större tryckökningen.

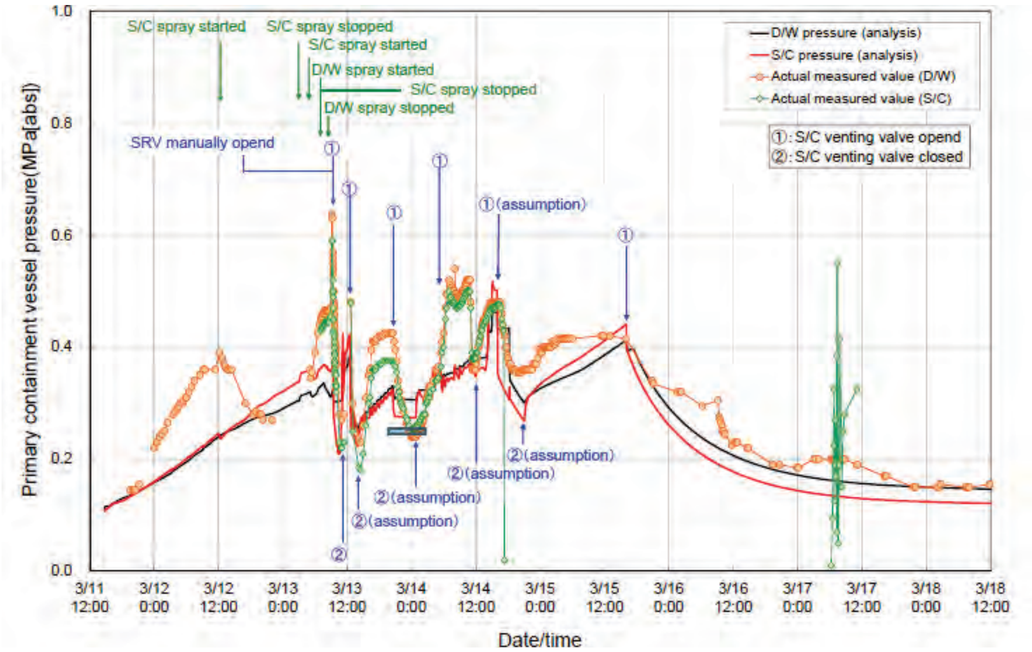

Figur 15 Tryckspikar i reaktortank 1F3 vid 42 timmar efter snabbstopp (runt 08:30 den 13:e mars) respektive 45 timmar efter snabbstopp (runt 12:00 den 13:e mars) [4] Attachment 3-8

Referenser

[1] APRI-9 Slutrapport, SSM Rapportnummer 2018:16, juni 2018

[2] Benchmark Study of the Accident at the Fukushima Daiichi Nuclear Power Plant, NEA No 7525, 2021

[3] Fukushima Nuclear Accident Analysis Report, Tokyo Electric Power Company (TEPCO), Inc., juni 2012

[4] The 5th Progress Report on the Investigation and Examination of Unconfirmed and Unresolved Issues on the Development Mechanism of the Fukushima Daiichi Nuclear Accident, Attachment 1-7, 2017, (tepco.co.jp)

[5] Fukushima Nuclear Accidents Investigation Report, Attachment

[6] IAEA, Fukushima Daiichi Accident, Gov/2015/26, Report by Director General

7. SLUTSATSER OCH REKOMMENDATIONER

7.1 Slutsatser av projektet

Det finns en substantiell kunskapsbas med avseende på riskdominerande fenomen under ett svårt haveri i en lättvattenreaktor. Kunskapsbasen har byggts upp genom forskning, både inom det experimentella området och genom analytiskt arbete. Denna forskning, studier och arbeten har bedrivits under decennier. Viktiga bidrag till denna state-of-the-art kunskap har levererats av KTH och Chalmers genom APRI-programmets stöd. KTH:s och Chalmers forskning har i sin tur dragit nytta av den internationella forskningen och samarbetet präglas av internationell ömsesidighet.

7.1.1. KTH:s avdelning för kärnkraftsäkerhet

Forskningen inom svåra haverier på KTH:s avdelning för kärnkraftsäkerhet har som mål och ambition att bidra till lösningen av säkerhetsfrågor med ett fokus på haverifenomen och de tekniska konsekvenslindrande lösningar som är relevanta för en effektiv haverihantering i de svenska kärnreaktorerna. Detta gäller både kokvattenreaktorer och tryckvattenreaktorer.

I det arbete som har bedrivits av KTH-NPS under APRI-10, och som har avrapporterats ovan, har varit inriktad på (i) in-vessel härddegradering och smältförlopp av corium sammansatt av flera komponenter och som ansamlas i reaktortankens botten (till exempel återsmältning av stelnat material och smälta som tränger in i stelnad grusbädd); (ii) studie av olika tankgenomsmältningsmoder (till exempel krypbrott i tankbotten versus genomsmältning av genomföring) som tillsammans med utvecklingen av härdrester och smälta i tankbotten kommer att vara avgörande för smältans frigörelse och övergång till ett ex-vessel scenario; (iii) stelning och oxidation av härdrester som är relevant för kylning av härdrester i inneslutningen; (iv) karaktärisering av den formation som en grusbädd av metallisk smälta antar i en vattenvolym; (v) grundläggande fysikalisk förståelse för de ingående mekanismerna i Fuel-Coolant Interaction (FCI) via experiment i MISTEE plattformen; (vi) utveckling av modeller och simuleringsverktyg för förståelse för fysiken i svåra haverifenomen samt för överföring av de studerade fenomenens betydelse för reaktorsäkerheten. Följande framsteg och resultat kan speciellt noteras:

- Testuppställningen SIMECO-2 är en transparent skivformad del av nedre tankbotten med simulering av resteffekt via induktion. Uppställningen är konstruerad för att studera torrkokning, återsmältning av stelnat material under vatten, formering av smältpöl och smältpölens värmeöverföring till tanken. Hittills har resultat från simuleringar av återsmältning i vatten presenterats.
- Experiment i REMCOD/MRSPOD har genomförts i olika skala och geometri för att ta fram en databas för både termohydraulisk och materialkaraktäristik av smält metall som penetrerar och infiltrerar partikulära härdrester (i experimentet små kulor). Resultaten ska användas för att utveckla en modell och för att validera förbättringar i simuleringskoder som exempelvis COCOMO-MEWA.
- Avseende studierna av tankgenomföringsmod har fokus kretsat kring utvecklingen av prediktiva förmågan. Detta arbete har inkluderat framtagandet av modeller och metodik för en kopplad termo-mekanisk analys av corium i tankbotten som angriper reaktortanken. Kopplingen avser en strukturmeka-

nisk kod med CFD, och har utvecklats i multifysikplattformen ANSYS Workbench. Validering av kopplingen har gjorts mot FOREVER-EC2 experimenten som genomförts på KTH tidigare. Två andra kopplingar har också genomförts där en strukturmekanisk kod har kopplats med bland annat Melcor för att snabbt (jämfört med CFD) kunna studera tankens uppträdande. Vidare så har en ny krypmodell utvecklats för stål från tankmaterialet 16MND5 för att kunna analysera alla tre stadier av krypning. Benchmark och valideringsstudier mot olika experiment har bidragit till att förbättra modeller och att hantera osäkerheter.
- COCOMO-MEWA koden, som används för att studera kylning/stelning och oxidation, har validerats mot det franska storskaliga experimentet PEARL och sedan tillämpats för att analysera kylbarhet av härdrester ex-vessel med beaktande av oxidation av metalliska härdrester.
- Fem stycken övergripande tester har genomförts för att studera karaktäristiken avseende formationen i samband med att en metallisk smälta bryts upp (”break-up”) i kontakt med vatten (break up-fenomenet har stor påverkan på formen härdresterna antar vilket i sin tur påverkar dess kylbarhet). De preliminära resultaten visar att egenskaperna hos metalliska härdrester skiljer sig på avgörande punkter från motsvarande oxidiskt material som har studerats i tidigare APRI-projekt. Egenskaperna hos en grusbädd som har formerats av smälta kommer att påverkas inte bara av materialsammansättningen (metallisk, oxidisk eller blandning), men också av var genomträngningen i reaktortanken är placerad.
- Experimentuppställningen MISTEE har uppgraderats för att möjliggöra experiment med prototypiska kompositioner av coriummaterial för att studera grundläggande fysikaliska mekanismer i samband med Fuel-Coolant Interaction (FCI). FCI är ett viktigt delmoment i förståelsen av både ångexplosioner och härdresters kylbarhet. Uppställningen har framgångsrikt kunna producera experiment med zirkonium och järn i en vattenbassäng samt studera de oxidationsprocesser som följer med experimentet. Vidare så har effekten av saltvattens påverkan på ångexplosioner samt filmkokning avseende studerats i MISTEE-plattformen.
- Avancerade turbulensmodeller som bygger på Algebraic turbulent Heat Flux Model (AHFM) och Direct Numerical Simulation har tillämpats för att utveckla simuleringskapaciteten avseende smältpölens uppträdande i tankbotten. Annan utveckling inkluderar dels en surrogatmodell för en snabb beräkning av härdresternas kylbarhet och dels koppling med COCOMO-MEWA och RELAP5 för att simulera kylningsprocessen av härdrester i tankbotten.

7.1.2. KTH:s avdelning för kärnteknik

Genom utvecklingen av ROAAM+ metodiken har exempel på hur deterministiska modeller tillsammans med känslighetsanalyser har används för att identifiera de viktigaste bidragen till den epistemiska osäkerheten i ramverket. Arbetet har visat att sannolikheten för inneslutningsbrott på grund av ångexplosioner eller ej kylbara härdrester kraftigt beror på modellosäkerheten i frigörelsemod från reaktortanken och frigörelsehastighet från tanken.

Arbetet under APRI-10 har visat att implementering av ROAAM+ i en storskalig PSA-modell är både möjlig och kan ge potentiella förbättringar avseende hur PSA-sekvensen definieras och ansenliga skillnader avseende frekvensen för oacceptabla utsläpp jämfört med referensfallet. I de resultat som har erhållits i den utökade PSA-modellen som har tillämpat ROAAM+ framkommer att frekvensen för oacceptabla utsläpp kan öka med 5 gånger vid ett antagande om att endast smält material frigörs från tanken (dvs. inte smält och stelnat material) jämfört med referensfallet för PSA-analysen. I de fall frigjort corium består av både smälta och stelnat material är den förhöjda frekvensen för oacceptabla utsläpp liten, endast cirka 10 %.

Ur PSA-synpunkt har arbetet i APRI-10 visat att:

- Det är både möjligt och fördelaktigt att höja växelverkan mellan deterministiska och probabilistiska analyser, speciellt inom PSA nivå 2.
- Sannolikheter i fenomen kan skattas genom att använda fysikaliska modeller i de termohydrauliska koderna.
- Osäkerheterna kan skattas och en korrelation mellan fenomen och osäkerhet kan hanteras.
- Det finns utrymme för förbättringar i den nuvarande modelleringen av PSA-nivå 2.

7.1.3. Chalmers avdelning för kärnkemi

Den forskning som Chalmers har bedrivit inom APRI-10 syftar till att kartlägga kemin hos tellur. Forskningen har syftat till att öka kunskapen bl.a. om hur tellur transporteras och interagerar med ytor av olika material som förekommer i inneslutningen. Studier har även genomförts som rör tellurs beteende i vattenlösning. Forskningen handlar om att förstå vilka processer som påverkar flyktigheten för dessa ämnen och hur de påverkas av de betingelser som kan råda vid haveriförhållanden, t.ex. höga temperaturer, varierande ånghalt eller oxidativ miljö. De experimentella resultaten utgör viktig kunskap för möjligheten att bygga beräkningsmodeller också för dessa ämnen.

Chalmers har utfört experiment för att studera tellurs uppförande under förhållanden som kan råda i samband med ett haveri. I en annan försöksserie har man sökt kunskap om hur metallernas flyktighet kan påverkas genom kemisk omvandling till andra ämnen såsom metallhalider eller s.k. metalloxyhalider. Studien har sin bakgrund i att man använde sig av havsvatten i Fukushima Dai-ichi för att upprätthålla kylning av härden vid haveriet. Det medförde att man fick in havssalt i anläggningen, vilket gör att det finns en misstanke om att kemisk interaktion mellan tellur och havssalt kan ha påverkat tellurs flyktighet. Preliminära resultat visar att det är möjligt att det kan uppstå betingelser i närvaro av havssalt som gynna kemiska processer som ökar tellurs flyktighet.

I ett samarbete med VTT i Finland har Chalmers medverkat i försök hos VTT för att studera tellurs beteende i gasfas samt inneslutningssprinklingens effekter på tellur. Chalmers har även undersökt om det förekommer någon kemisk interaktion mellan den deponerade telluren och metallytan. Metallytor av koppar, zink och aluminium har använts i försöken, vilka representerar de olika ytor som är vanliga i en reaktorinneslutning.

Chalmers har även inlett studier av tellurs vattenkemi i syfte att förstå tellurs beteende i kondensationsbassäng/sump, särskilt hur tellur kan medverka till bildandet av flyktig elementär jod. I försöken studeras hur radiolysprodukter som väteperoxid och hydroxyradikaler kan öka lösligheten hos tellurdioxid genom oxidation till tellursyra, som har en högre löslighet. Ett ytterligare syfte är att studera hur tillsatser till inneslutningssprinkling, t.ex. borsyra eller lut kan påverka tellurs löslighet. En annan tillsats är natriumtiosulfat, som används i haverifiltren för att minska tellurs löslighet genom reduktion till metalliskt tellur.

Resultaten från Chalmers forskning under APRI-10 har bidragit med ny kunskap om fissionsprodukters beteende i primärsystem och reaktorinneslutning under ett haveri. Detta kan ge utökade möjligheter att förutsäga bidraget till källtermen från nuklider som inte tidigare har ägnats mycket uppmärksamhet. Det kan också ge nya uppslag till hur man skulle kunna begränsa källtermsbidraget från dessa ämnen i utsläppen vid ett haveri.

7.2 Rekommendationer

Den framtida forskningen inom svåra haverier bör bibehålla fokus på att minska kunskapsgapet avseende kvantifieringen och bedömningen av risker kopplade till corium.

Det finns idag liten kunskap tillgänglig kring hur degraderingsförloppet för multikomponent corium går till i nedre tankbotten samtidigt som frågan har en stor betydelse för både in- och ex-vessel kylbarhet av härdresterna. Som en infrastruktur enligt första-av-sitt-slag och som präglas av hög arbetstemperatur, transparent visualisering och senaste instrumentering bör SIMECO-2 uppställningen tillämpas för att undersöka förloppet och värmeöverföringen av smälta i nedre tankbotten, där smältan består av flera ingående komponenter.

Givet de termiska och mekaniska lasterna från corium i reaktortankbotten bör den kopplade termo-mekaniska analysen som är utvecklad under APRI-10 fortsätta tillämpas för att försöka prediktera tankgenomträngning i reaktortankbotten och där en representativ modell av olika genomföringar ingår. Karaktäristiken på den resulterande smältfrigörelsen har en avgörande betydelse för bedömningen och kvantifieringen av den risk som en tankfrigörelse av härdsmälta innebär, kanske speciellt för svenska reaktorer med hänsyn taget till den svenska haverihanteringsstrategin.

Mer experiment rörande metallrik smälta som kyls och stelnar i vatten och formerar högar av härdrester och grusbädd bör genomföras, där ett mer systematisk testprogram genomförs. Exempelvis bör sammansättningen avseende Zr/Fe varieras för att få olika smältpunkter på blandningen. Syftet är att ta fram en databas över den karaktäristik som en grusbädd bestående av metall kan tänkas ha. Som ett komplement till den förhållandevis storskaliga uppställningen i DEFOR, bör experiment med prototypiska kompositioner av Zr/Fe/ZrO2 tillämpas i MISTEE-uppställningen för att minska kunskapsgapet avseende materialegenskaper.

De strukturer som finns under reaktortanken på BWR-reaktorerna (till exempel drivdon och styrstavar) har hittills inte ingått i de analyser av ångexplosioner och smältans kylbarhet som har studerats på KTH. En ökad vikt bör läggas på dessa strukturer i det fortsatta arbetet när det gäller att skatta och bedöma risken avseende svåra haverier. För PWR bör en ökad vikt läggas på de utmaningar kring smältans kylbarhet ex-vessel med tillämpning av de metoder och den kunskap som har byggts upp inom APRI och internationellt. Den kunskapen har i Sverige byggts upp mycket kring arbete med att värdera BWR, men bör således breddas till PWR.

Parallellt med den experimentella verksamheten är utvecklingen av modeler och simuleringskapacitet nödvändigt eftersom det är via simuleringskoder som experimentens betydelse för reaktorsäkerheten kommer in. En systematisk och konsekvent tillämpning av forskningsresultaten i reaktorsäkerheten via modell- och kodutveckling rekommenderas.

Nuvarande modellering som används i MELCOR-koden för analys av tankgenomsmältning och frigörelse av corium är förenklad i vissa aspekter och saknar en nödvändig valideringsdatabas. En mer mekanistisk modellering bör utvecklas för att hantera denna osäkerhetskälla.

Haveriscenarier med möjliga framgångsrika haveriåtgärder bör beaktas i PSA-analysen.

Högre upplösning av de olika formerna av inneslutningsbrott som potentiellt kan leda till olika konsekvenser när det gäller frigörelse av klyvningsprodukter och omgivningspåverkan bör utvecklas i PSA-sammanhanget.

Olyckan vid Fukushima visade på spridning av tellur i omgivningen och det arbete som påbörjades i APRI 10 avseende denna fissionsprodukt bör nu fortsättas.

Tellurkemin vid temperaturer som är representativa för primärkretsen bör studeras. Eventuella reaktioner med borsyra som då sker bör undersökas för att utröna om och på vilket sätt dessa påverkar flyktigheten för tellur.

Dessutom rekommenderas att reaktioner mellan tellur och organiska material samt jod i inneslutningen börjar undersökas. Avsikten är att kunna fastställa vilka stabila reaktionsprodukter som kan förväntas i inneslutningen och som kan få betydelse för källtermen till omgivningen.

8. FÖRKORTNINGSLISTA

AECL	Atomic Energy of Canada Limited
ANL	Argonne National Laboratory
ANN	Artificial Neural Network
APRI	Accident Phenomena of Risk Importance
ASTEC	Accident Source Term Evaluation Code
AWI	Alternative Water Injection
BET	Brunauer-Emmett-Teller theory
BIP	Behaviour of Iodine Project
BWR	Boiling Water Reactor
CCDF	Complimentary Cumulative Distribution Function
CCFP	Conditional Containment Failure Probability
CCI	Core-Concrete Interaction
CDF	Core Damage Frequency
CDF	Cumulative Distribution Function
CET	Containment Event Tree
CFD	Computational Fluid Dynamics
CHF	Critical Heat Flux
CRD	Control Rod Drive
CRGT	Control Rod Guide Tube
CSARP	Cooperative Severe Accident Research Program
CTH	Chalmers Tekniska Högskola
DABCO	1,4-diazabicyclo [2.2.2] octane (also known as triethylene diamine (TEDA))
DCH	Direct Containment Heating
DECOSIM	Code for Debris Bed Coolability Simulation
DEFOR	Debris Bed Formation
DEM	Discrete Element Method
DHF	Dryout Heat Flux
DDFP	Diesel Driven Fire Pump
EC	European Commission
ECM	Effective Convectivity Model
EDF	Electricité de France
EOP	Emergency Operating Procedures
ERMSAR	European Review Meetings on Severe Accident Research

ET	Event Tree
EXAFS	Extended X-ray Absorption Fine Structure analysis
FCI	Fuel-Coolant Interaction
FM	Full Model
FOMICAG	Facility for Online Measurements of I-131 labelled species Concentrations in Aqeous and Gaseous Phase
FP	framework programme
FPT	Fission Product Test
FT	Fault Tree
FTA	Fault Tree Analysis
GC-MS	Gas Chromatography – Mass Spectroscopy
HPCI	High Pressure Coolant Injection
HPGe	High Purity Germanium detector
IGT	Instrumentation Guide Tube
INCO	In-Vessel Coolability
IRSN	Institut de Radioprotection et de Sûrité Nucléaire
ISTP	International Source Term Project
IVR	In-Vessel Retention
KROTOS	a small-scale test facility for FCI (steam explosion) study at CEA
KTH	Kungliga Tekniska Högskolan/Royal Institute of Technology
LERF	Large Early Release Frequency
LET	Linear Energy Transfer
LIVE	Late In-Vessel Phase Experiments
LOCA	Loss Of Coolant Accident
LP	Lumped Parameter
LSC	Liquid Scintillation Counting
LWR	Light Water Reactor
MCCI	Melt Corium Concrete Interaction
MCSs	Minimal Cut sets
MELCOR	code for integral simulation of severe accident developed by Sandia National Labs on the mission from USNRC
MET	Melt Eruption Test
MISTEE	Micro Interactions of Steam Explosion Energetics
MSWI	Melt Structure Water Interactions
NCG	Non-Condensable Gas

NPP	Nuclear Power Plant
NRC	Nuclear Regulatory Commission
NROI	Nordic Research on Radiolytic Oxidation of Iodine
OECD	Organisation for Economic Co-operation and Development
OIPHA	Organic Iodide Partitioning and Hydrolysis Analysis model
PCV	Primary Containment Vessel
PDF	Probability Density Function
PDS	Particulate debris spreading
PDS	Plant Damage State
PECM	phase-change ECM
POMECO	Porous Media Coolability
PSA/PRA	Probabilistic Safety Assessment/Probabilistic Risk Assessment
PWR	pressurized water reactor
Pyro-IR	Pyrolysis – Infrared
RC	Release Category
ROAAM	Risk Oriented Accident Analysis Methodology
RPV	Reactor Pressure Vessel
RTF	Radioiodine Test Facility
SA	Severe Accident
SAID	Severe Accident Information Distillation
SAM	Severe Accident Management
SAMG	Severe Accident Management Guidelines
SARNET	severe accident research network of excellence
SBO	Station Blackout
SEE	Steam Explosion Energetics
SEM-EDX	Single Electron Miscroscopy – Energy Dispersive X-ray spectroscopy
SERENA	Steam Explosion REsolution for Nuclear Applications
SM	Surrogate Model
SRV	Safety Relief Valve
TEDA	TriEthylene DiAmine
TGA	Thermo Gravimetric Analysis
URF	Unacceptable Release Frequency
XPS	X-ray Photoelectron Spectroscopy

The Swedish Radiation Safety Authority has a comprehensive responsibility to ensure that society is safe from the effects of radiation. The Authority works from the effects of radiation. The Authority works to achieve radiation safety in a number of areas: nuclear power, medical care as well as commercial products and services. The Authority also works to achieve protection from natural radiation an to increase the level of ratiation safety internationally.

The Swedish Radiation Safety Authority works proactively and presentively to protect people and the environment from the harmful effects of radiation, now and in the future.
The Authority issues regulations and supervises compliance, while also supporting research, providing training and information, and issuing advice. Often, activities involving radiation require licences issued by the Authority. The Swedish Radiation Safety Authority maintains emergency preparedness around the clock with the aim of limiting the aftermath of radiation accidents and the unintentional spreading of radioactive substances. The Authority participates in international co-operation in order to promote radiation safety and finances projects aiming to raise the level of radiation safety in certain Eastern European countries.

The Authority reports to the Ministry of the Environment and has around 300 employees with competencies in the fields of engineering, natural and behavioral sciences, law, economics and communications. We have recieved quality, environmental and working environment certification.

Publikationer utgivna av Strålsäkerhetsmyndigheten kan laddas ned via stralsäkerhetsmyndigheten.se eller beställas genom att skicka e-post till registrator@ssm.se om du vill ha broschyren i alternativt format, som punktskrift eller daisy.

Strålsäkerhetsmyndigheten
Swedish Radiation Safety Authority
SE-171 16 Stockholm
Phone: 08-799 40 00
Web: ssm.se
E-mail: registrator@ssm.se

E-print AB, 2022